Master's thesis

NTNU
Norwegian University of Science and Technology
Faculty of Engineering
Department of Marine Technology

Emil Severin Moen Ramsvik

Numerical simulation of flow around a curved cylinder with varying diameter

Master's thesis in Marine Technology
Supervisor: Bjørnar Pettersen
June 2019

NTNU
Norwegian University of
Science and Technology

Emil Severin Moen Ramsvik

Numerical simulation of flow around a curved cylinder with varying diameter

Master's thesis in Marine Technology
Supervisor: Bjørnar Pettersen
June 2019

Norwegian University of Science and Technology
Faculty of Engineering
Department of Marine Technology

NTNU
Norwegian University of
Science and Technology

NTNU
Norwegian University of Science and Technology
Department of Marine Technology

MASTER THESIS IN MARINE HYDRODYNAMICS

SPRING 2019

FOR

Stud.techn. Emil Severin Moen Ramsvik

NUMERICAL SIMULATION OF FLOW AROUND A CURVED CYLINDER WITH VARYING DIAMETER.

The candidate shall investigate viscous flow around a curved cylinder with varying diameter using numerical simulation with MGLET.
Initially simple configurations such as straight cylinder and curved cylinder with constant diameter can be tested and results compared to existing published results.
The main study will be with a curved cylinder with a diameter a diameter ratio D/d =5. The choice of Reynolds numbers, numerical parameters, boundary conditions and computational domain shall be documented. How the end-conditions of the curved cylinder is treated and influence the results must be detailed documented.
Visualization and documentation of the fluid flow results are important.

In the thesis the candidate shall present his personal contribution to the resolution of the problem within the scope of the thesis work. Theories and conclusions should be based on mathematical derivation and logic reasoning identifying the various steps in the deduction. The original contribution of the candidate and material taken from other sources shall be clearly defined. Work from other sources shall be properly referenced. The candidate should utilize the existing possibilities for obtaining relevant literature.
The thesis should be organized in a rational manner to give a clear exposition of results, assessments and conclusions. The text should be brief and to the point, with a clear language.

The thesis shall contain the following elements: A text defining the scope, preface, list of contents, summary, main body of thesis, conclusions with recommendations for further work, list of symbols and acronyms, references and appendices. All figures, tables and equations shall be numerated.
It is supposed that Department of Marine Technology, NTNU, can use the results freely in its research work by referring to the student's thesis.
The thesis shall be submitted June 11th , 2019.

Bjørnar Pettersen
Professor/supervisor

Co-supervisor: Postdoc Fengjian Jiang, NTNU

Summary

In this master thesis, the flow around a concave curved cylinder with a change in diameter is presented. The study uses Direct Numerical Simulation to solve the Navier-Stokes equations without the use of turbulence modeling. The focus of this thesis is to investigate how the position of the change in diameter, or the step affects the fluid flow around the geometry and in the wake.

Different geometrical configurations were investigated, with the angle of the step being the main parameter investigated. In addition to the concave cylinder with a change in step, straight cylinders with a step both normal to and parallel to the flow direction was investigated.

The straight cylinder configurations showed distinct vortex structures forming. The horizontal cylinder had recirculation zones in front of the step and the vertical cylinder had junction and edge vortices around the step.

Uniform flow at a Reynolds number of 600 showed that the influence of the step has a large impact on the wake. The curvature induces a vertical flow, which can either be enhanced or reduced by the step. At the edge of the step, there was a decrease in pressure creating a suction zone which could either counteract or enhance the vertical flow from the step.

The parameter study showed that the step angles could be grouped into three categories. The first contained angles from a step normal to the incoming flow to a 45 degrees angle to the incoming flow. This group contained recirculation zones in front of and behind the edge of the step. The first group had similar vortex structures with the straight cylinder in parallel flow. The second group contained step angles between 45 degrees and 60 degrees. The flow field around those two configurations differed from all other simulations. The third groups contains configurations with step angles above 60 degrees. Vortex shedding occurs from both the small and large diameter cylinder. This group has similar vortex structures as the straight vertical cylinder with a change in step.

Sammendrag

I denne masteroppgaven utforskes strømning rundt en konkav buet sylinder med en endring i diameter. Studien bruker direkte numerisk simulering for å løse Navier-Stokes ligningene uten bruk av turbulensmodellering. Fokuset på denne oppgaven er å undersøke hvordan plasseringen av endringen i diameter, eller trinnet påvirker væskestrømmen rundt geometrien og i kjølvannet.

Ulike geometriske konfigurasjoner ble undersøkt, med trinnets vinkel som hovedparameteren. I tillegg til den konkave sylinderen med en forandring i diameter ble det undersøkt strøming rundt rette sylindere med et trinn både normalt på og parallelt med strømningsretningen.

De rette sylinderkonfigurasjonene viste forskjellige virvelstrukturer som dannes. Den horisontale sylinderen hadde resirkuleringssoner foran trinnet, og den vertikale sylinderen hadde kryss- og kantvirvler rundt trinnet.

Uniform strømning ved et Reynolds tall på 600 viste at påvirkning av trinnet har stor innvirkning på kjølvannet. Krumningen fremkaller en vertikal strøm, som enten kan forsterkes eller reduseres av trinnet. På kanten av trinnet var det en nedgang i trykket som skaper en lavtrykksone som enten kunne motvirke eller øke den vertikale strømningen fra trinnet.

Parameterundersøkelsen viste at vinklingen av trinnet kunne grupperes i tre kategorier. Den første inneholdt vinkler fra et trinn som er normalt til den innkommende strømmen til 45 degrees vinkel på den innkommende strømmen. Denne gruppen inneholdt resirkuleringssoner både foran trinnet og bak kanten av trinnet. Den første gruppen hadde lignende virvelstrukturer med den rette sylinderen i parallell strømning. Den andre gruppen inneholdt vinklinger av trinnet på 45 grader og 60 grader. Strømningsfeltet rundt disse to konfigurasjonene skiller seg fra alle andre simuleringer. Den tredje gruppen inneholder konfigurasjoner med vinklinger av trinnet over 60 grader. Virvelavløsning skjer fra både den lille og store sylinderen. Denne gruppen har lignende virvelstrukturer som den rette vertikale sylinderen med en forandring i diameter.

Preface

This master thesis is the culmination of my final semester at the five year integrated master program in Marine Technology at the Norwegian University of Science and Technology. The thesis is inspired by previous work done at the institute of marine technology, and is meant to be a gateway into further research. The thesis simplifies a riser with buoyancy elements into a 3D concave cylinder with a change in diameter and investigates how different geometrical parameters affected the flow field. The investigation was conducted numerically using the Direct numerical simulation tool MGLET.

My supervisor Professor Bjørnar Pettersen at the department of marine Technology, has inspired and motivated me to understand important aspects of hydrodynamics in my thesis. Bjørnar Pettersen has always been available to answer questions and provided insights and discussions. Fengjian Jiang, as my co-supervisor has been a huge resource during this work. His door has always been open and this thesis would not exists if not for his counsel, advice and help. He has been instrumental in helping with the software, the pre-process and post processing work and general understanding of computational fluid dynamics. I would also like to thank PhD student Cai Tian for valuable discussions and insights into the world of CFD. I would also like to express my gratitude to Phd student Håkon Strandenes for helping me with the post-processing computer which the Department of Marine Technology graciously loaned me for my research. The work has also received support from the Research Council of Norway (Program for Supercomputing, under project nn9191k) through a grant of computing time. A final thanks is in due to my family and my fellow students at Department of Marine Technology. Their support has been invaluable in both good and trying times. Writing this thesis has given me valuable insights into the world of numerical hydrodynamics as well as experience in conducting scientific work.

Trondheim
June 7, 2019

Emil Severin Moen Ramsvik

Nomenclature

Abbreviations

DNS	=	Direct Numerical Simulation.
CAD	=	Computer Aided Design.
FVM	=	Finite Volume Method.
VIV	=	Vortex Induced Vibration.
CFD	=	Computational Fluid Dynamics
CFL	=	Courant-Friedrichs-Levy number.
RMS	=	Root Mean Square
NTNU	=	Norwegian University of Science and Technology
PSD	=	Power Spectral Density
IBM	=	Immersed Boundary Method
MGLET	=	Multi Grid Large Eddy Turbulence

Symbols

α	=	Angle of step on the curved cylinder
θ	=	Angle of curvature
D	=	Diameter of the large cylinder. $[m]$
d	=	Diameter of the small cylinder. $[m]$
d/D	=	Diameter ratio between the large and small cylinder
R	=	Radius of the curvature on the curved cylinder
L_H	=	Length of horizontal extension
L_V	=	Length of vertical extension
s	=	Second $[s]$
U_0	=	Inflow velocity. $[m/s]$
P	=	Fluid pressure. $[N/m^2]$
C_L	=	Cylinder lift force coefficient. $C_L = F_y/\frac{1}{2}\rho U_0 S$
$C_{L,rms}$	=	Root mean square of the cylinder lift force coefficient.
C_D	=	Cylinder drag force coefficient. $C_D = F_x/\frac{1}{2}\rho U_0 S$
$C_{D,mean}$	=	Mean of the cylinder drag coefficient.
C_P	=	Pressure coefficient $C_P = \frac{p_0 - p}{\frac{1}{2}\rho U_0}$
ρ	=	Density of fluid
u	=	Velocity in x-direction
v	=	Velocity in y-direction
w	=	Velocity in z-direction
p	=	Pressure
u_{ax}	=	Axial velocity
f_i	=	Body force
τ	=	Tangential stress $= \mu\frac{\partial u}{\partial y}$
μ	=	Dynamic viscosity
ν	=	Kinematic viscosity $\nu = \frac{\mu}{\rho}$
f	=	Frequency of oscillations
f_v	=	Frequency of vortex shedding
T_v	=	Period vortex shedding
f_{beat}	=	Beat frequency $f_{beat} = f_L - f_N$
f_n	=	Natural frequency of the cylinder
St	=	Strouhal's number $St = f_n D/U$
St_L	=	Strouhal frequency L-cell (Large diameter cylinder)
St_S	=	Strouhal frequency S-cell (Small diameter cylinder)
St_S	=	Strouhal frequency S-cell (Small diameter cylinder)
St_N	=	Strouhal frequency N-cell
St_θ	=	Oblique Strouhal frequency

Γ	=	Circulation of fluid flow
δ_x	=	Axial coordinate of vortex core
δ_y	=	Vertical coordinate of vortex core
r	=	Reattachment length
a	=	Separation height
h	=	Height of the step
Re	=	Reynolds number. $Re = UD/\nu$
Re_D	=	Reynolds number based on the large cylinder diameter. $Re_D = UD/\nu$
Re_d	=	Reynolds number based on the small cylinder diameter. $Re_d = Ud/\nu$
Re_h	=	Reynolds number based on the step height $Re_h = Uh/\nu$
θ_S	=	Angle of oblique vortex shedding small diameter cylinder
θ_L	=	Angle of oblique vortex shedding large diameter cylinder
R_{sample}	=	Radius or length of the sampling line for streamlines
λ_2	=	Parameter for vorticity
ω	=	Vorticity vector.
ω_z	=	z-component of the vorticity
ω_y	=	y-component of the vorticity
ω_x	=	x-component of the vorticity
f_N	=	Frequency of vortex shedding N-cell region
f_L	=	Frequency of vortex shedding L-cell region
f_S	=	Frequency of vortex shedding S-cell region
$\delta_{0.99}$	=	Height of the boundary layer $u = 0.99U_0$
p_0	=	Ambient pressure
R/D	=	Aspect ratio curvature

Contents

Chapter 1

Introduction

1.1 Motivation

As new oil and gas fields are being developed, the need for designing risers capable of operating at large depths have arisen. To lessen the tension loads, different configurations are applicable. Some of these geometries, such as the Lazy-wave and Steep-Wave (see Figure 1.1) configurations employ buoyancy elements to lessen the tension loads at the top of the risers.

Slender offshore structures such as riser are subjected to current loads, which in turn may lead to dynamic phenomenon such as vortex-induced vibrations. As risers used in offshore applications are often made of steel and other metals they tend to be very heavy. Therefore they are often installed with buoyancy elements to help lessen the load on the riser tensioners. The normal practise for buoyancy elements is to place them in a staggered configuration, i.e. have them placed with a certain distance to each other. A change in section diameter will change the frequency of vortex shedding. Field experience suggest that the staggered buoyancy elements tend to suppress vortex induced vibration (Holmes et al., 2008). The phenomenon of vortex induced vibrations (VIV) is of great concern, as the phenomenon greatly increases the loads on the structures in question.

The consequences of vortex induced vibrations were according to Brooks (1987) threefold: Increased fatigue on the riser, increased drag on the riser and increased flex joint angles. The increased joint flex angles are of lesser importance than the increased drag.

By changing the dimensions of the cross section of the riser, the natural frequency modes of the riser changes as well. The change in geometry will also change the vortex shedding characteristics. However, these phenomenons have not been clearly investigated and a need for detailed studies of staggered buoyancy

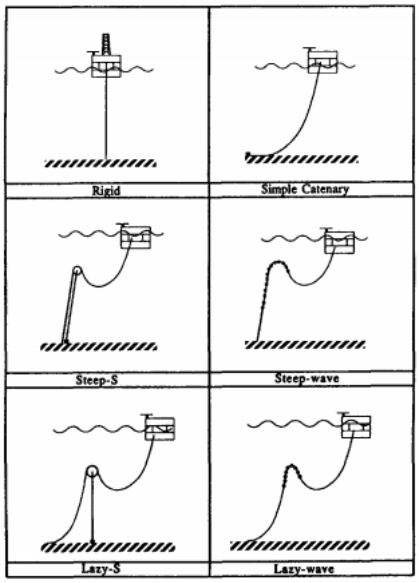

Figure 1.1: Different rigid and flexible riser geometries used in the offshore industry (Patel and Seyed, 1995)

elements is required.

1.2 Introduction to the Problem

In offshore applications the use of risers to extract hydrocarbons from the seabed to the surface is profound. Problems arise when ocean current and other hydrodynamic loads contribute to unsustainable responses in the risers. Of particular interests are viscous forces and dynamic phenomenon such as vortex induced vibrations.

As almost all flows in nature are viscous and turbulent, these fluid properties play a big part in the loads and flow phenomenons in hydrodynamics. To simulate realistic flows such as the flows around a ship in motion is extremely difficult and require enormous computational resources. As computers are not fast enough to simulate these flows, numerical models are used to simulate turbulence. However, solving less complex flows around less complicated geometries without the use of modeling is still of great importance. Direct numerical simulation, or DNS for short are complete simulations of the flows and serve as benchmarks for other simulations. Therefore it is of particular interest to investigate the flow around geometries commonly used in riser applications. One of these geometries is the

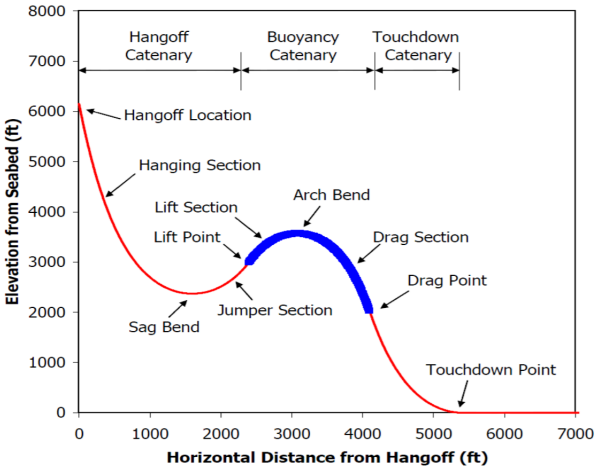

Figure 1.2: Example of Steel Lazy Wave Riser configuration. The buoyancy catenary section is of importance for this study. (Li and Nguyen, 2010)

curved cylinder.

As the the static forces on the risers increases with the depth and length of the riser from seabed to ocean surface, the need for buoyancy elements to lessen the gravitational tension loads arise. A riser in a curved configuration with buoyancy elements is displayed in Figure 1.3.

The introduction of a buoyancy element on a concave curved cylinder serves as the basic geometric configuration for this thesis. How the vortex shedding and drag and lift forces act on such a riser configuration is of great engineering interest as well as how the flow develops around the geometry and in the wake. Therefore this thesis focuses on the flow dynamics part of the problem.

1.3 Overview of the Chapters

Chapter 1 is the introduction to the problem. It covers the motivation and states the problem definition.

Chapter 2 contains a literature review and sums up previous research on the topic.

Chapter 3 covers the relevant background theory on fluid flow and dynamic phenomenons.

Chapter 4 dwells into the numerical analysis and assumptions of the numerical solver, covering the techniques used to simulate the fluid flow.

In Chapter 5 geometrical configurations investigated in other studies deemed

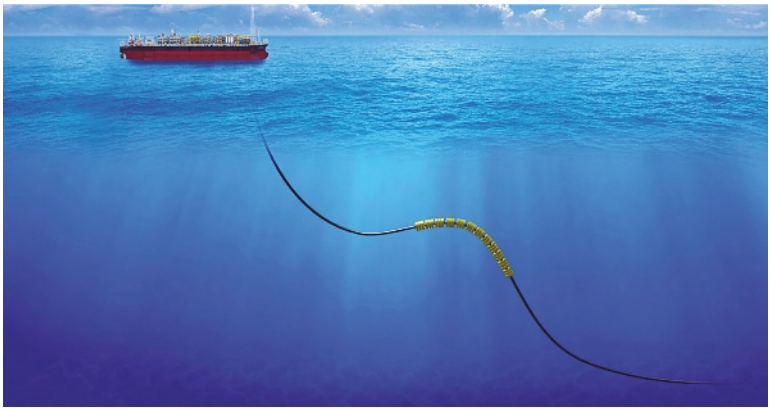

Figure 1.3: Illustration of a riser with buoyancy elements. The buoyancy modules are placed in staggered manner in a lazy wave configuration. (Hermas, 2017).

of interest to the parameter study is investigated.

The chapters 6 and 7 contains the grid convergence analysis and detailed discussion of different configurations of a concave cylinder with a change in diameter at the start of the vertical extension.

Chapter 8 contains a parameter study investigating how the change in diameter placed along different places along the curvature affects the fluid flow.

Finally, Chapter 9 discusses the results and what conclusions can be drawn ted in this report and lays the scope for further work to be conducted.

Chapter 2

Literature Review

As the need to develop risers that can extract hydrocarbons from the seabed at large depths have been increasing, the need to study fluid flow around more complex geometries have arisen. As conventional empirical means of modeling the forces on a cylinder like Morison's equation is not applicable on cross sections were the vortices are shed at directions not normal to the body, new means of modeling the fluid flow are important. Complicated geometries like a cylinder with a change in diameter and convex and concave cylinders have received much attention during the last years.

Furthermore, the use of buoyancy elements on riser have led to some initial studies on how a staggered buoyancy elements may contribute to dampen or reduce vortex induced vibrations.

As the main geometry studied in this thesis is a concave cylinder with a change in diameter from a chosen point at an angle to the flow, cases such as forward facing steps, a change in step normal to the flow and concave cylinders without a change in step is relevant to review. Previous cases may provide solid benchmark values for comparison and may also be used as a starting point for what should be investigated in this thesis.

2.1 Curved Cylinder

The use of curved cylinders is favoured in the offshore engineering community, as curved risers hanging from platforms down to the seabed and pipelines laying on the seabed and mooring lines all apply some form of curvature. As these configurations are used in subsea applications, there are considerable loads from the ocean currents which may introduce fluid flow phenomena such as vortex shed-

ding, which in turn may lead to vortex induced vibrations.

2.1.1 Effect of Boundary Conditions

It is important that the problem modeled is affected as little as possible by the boundary conditions. Therefore, the size of the domain is of importance. Gallardo et al. (2013) showed that for a curved convex cylinder a vertical extension of $6D$ is sufficient to separate the effects of the free slip boundary condition from the effects of the curvature of the cylinder. In cases with a vertical extension of $2D$ and no extension at all, the free-slip boundary condition suppressed the vertical velocity component.

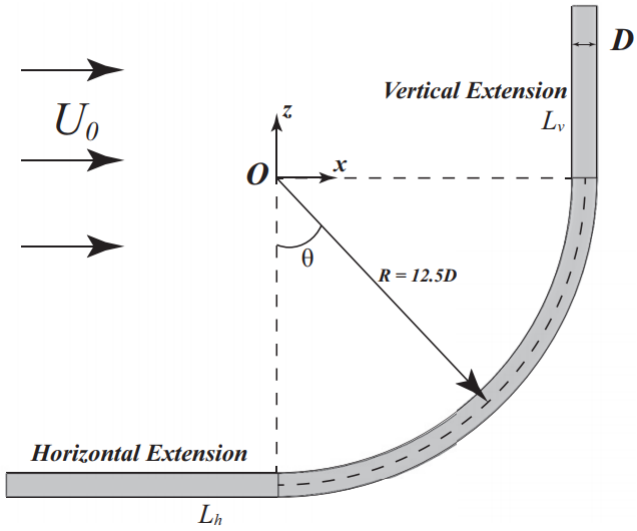

Figure 2.1: Geometry and flow configuration for the concave cylinder (taken from Jiang et al. (2018a)). The variables in the figure are described in the nomenclature and is also used throughout this thesis.

The geometry, as depicted in figure 2.1, has a radius of curvature of $R = 12.5D$, where D is the diameter of the cylinder. As shown by Bearman and Takamoto (1988) the wake patterns of flow perpendicular to the plane of a ring is approximate to that of a cylinder. As shown by Miliou et al. (2007), the aspect ratio of a quarter of a ring with an $R/D = 12.5$ would be 12.5.

Jiang et al. (2018b) investigated how long the horizontal extension must be in order to minimize the effect of the boundary conditions. They concluded that

a length of the horizontal extension $L_H = 5D$ is sufficient but that it is recommended with a length of at least $L_H = 10D$.

2.2 Concave Cylinder

Miliou et al. (2007) studied the flow around a concave cylinder at Reynolds numbers ranging from 100 to 500. At both Re = 100 and 500, the majority of the wake had become steady and generated a vertical velocity component w and an axially aligned flow. The flow is directed towards the top of the domain where the stagnation face flow becomes normal to the free-stream velocity. The peak in vertical velocity was found to be higher for the case Re = 500 ($\bar{w}_{Re=500} = 1.1U_0$) than for Re = 100 ($\bar{w}_{Re=100} = 0.77U_0$).

At Re =100, vortex shedding was completely suppressed, although some shedding at Strouhal frequency significantly lower than 2-D shedding was observed at Re = 500. The suppression of vortex shedding led to a reduction in total drag force. The suppression of vortex shedding was attributed to the stagnation face flow and production of streamwise vorticity in the shear layers of the cylinder.

Jiang et al. (2018a) studied the fluid flow around a concave cylinder at different Reynolds numbers ranging from Re = 100 to Re = 500. In this study, the effect of the vertical extension, i.e. the straight extension with its axis normal to the inflow turned out to be significant. The wake behind the cylinder was also investigated and is of importance when investigating the flow field and forces acting on the cylinder.. The wake consisted of several different flow regimes along the span of the curved cylinder. Flow phenomena such as oblique shedding, vortex dislocations and shedding at different frequencies was captured in the wake for different flow regimes. It should be noted that there are abrupt changes in flow regimes at $Re \leq 300$ but continuous changes at $Re = 500$ and $Re = 400$ and it is difficult to observe distinct changes between them. Jiang et al. (2018a) further suggest that the frequency band manifest itself in a three dimensional energy spectrum instead in a single dominating frequency.

In the concave cylinder wake vortex shedding is heavily suppressed by the axial flow on the leeward side. Furthermore, the concave wake is more complex than the convex wake.

Jiang et al. (2017) investigated the turbulent wake behind a concave curved cylinder at Re = 3990. A distinct difference in the upper and lower parts of the wake. The upper part, i.e. the area around the vertical extension showed typical turbulent topology. The lower part, i.e. behind the curved cylinder the width was considerably wider than for the upper part. A laminar like shear layer is observed in the upper part around the cylinder but is distorted in the lower part. finally, they concluded that the vortex structures in the wake of the curved cylinder is different

from that of a spheroid, suggesting different vortex dynamics.

2.3 Step Cylinder

The study of flow around a stepped cylinder is also of interest. Offshore platforms with SPAR-buoy hulls, wind turbine monopiles etc. all have similar configurations. In a flow past a step cylinder, the flow is governed by two important parameters, the Reynolds number $Re = UD/\nu$ and the ratio of the small and large diameter D/d.

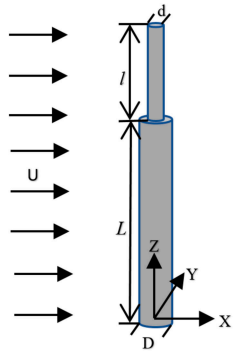

Figure 2.2: Step cylinder configuration (Tian et al., 2017b)

Dunn and Tavoularis (2006) did an experimental study on step-cylinders at different Reynolds number based on the largest diameter D. This study showed that vortices are formed in three distinct cells away from the far ends of the cylinder. The L-cells represents vortices shed from the largest cylinder while the S-cell represent those shed from the smallest. In the step, a junction vortex is formed in the front of the cylinder and the N-cell vortices are shed from the step, as can be seen in Figure 2.3.

The large cylinder will shed vortices at a lower rate than the small cylinder, therefore the connections will not be one-to-one. Vortex splitting can be represented as either two high-frequency vortices connecting into a single low-frequency vortex (Norberg (1992) or as two high-frequency vortices shed from opposite sides joining together.

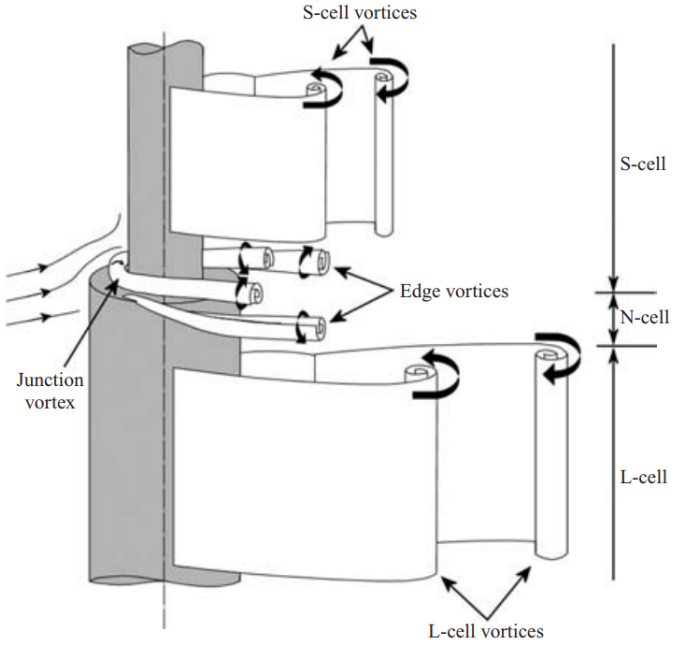

Figure 2.3: Different types of vortices near the step cylinder (Dunn and Tavoularis, 2006)

Moreover, Dunn and Tavoularis (2006) concluded that the vortices from the N-cell would connect with counterparts across the cell boundaries. The vortices were shed at different frequencies and therefore the vortices were shed increasingly out of phase at the cell boundaries. The junction and edge vortices were also observed to roll up at the sharp side edges and interact with the S-cell vortices. The N-cell shed vortices with a lower frequency than the S-cells.

Tian et al. (2017b) found that there were two kinds of N-cell shedding. N-cell vortex shedding defined by the Strouhal number for the N-cell St_N and one N-cell cycle defined by the beat frequency Strouhal number St_{beat}. Tian et al. (2017b) did not observe the junction vortex observed by Dunn and Tavoularis (2006). It was concluded that the junction vortex depend on the Reynolds number as the experimental study Dunn and Tavoularis (2006) had a considerably higher Reynolds number than the numerical study by Tian et al. (2017b). However, both studies contained edge vortices, which rolled up over the sides of the step towards the larger cylinder. Dunn and Tavoularis (2006) observed the junction vortex only under carefully controlled conditions. Furthermore, they used a much larger diameter than in previous cases.

Studies by Morton and Yarusevych (2010) observed that the frequency of the N-cell cycle can be estimated as the beat frequency $f_L - f_N$, which also corre-

sponds to the frequency of vortex oscillations at the N-L cell boundary. The beat frequency peaks are located in the regions where interactions between the L cell and N cell vortices take place. These results led Morton and Yarusevych (2010) to conclude that the vortex dislocations cause significant periodic fluctuations with a frequency equal to the beat frequency ($f_L - f_N$). They further state that the N-cell and L-cell vortices connect through both cross-boundary and half-loop connections. In the S-cell and N-cell boundary, the vortex dislocations manifests as half-loop connections of S-cell vortices with opposite signs.

The turbulent wakea behind a step cylinder was investigated by Tian et al. (2019). The S- and L- cell wake show signs of typical turbulent topology. The wake behind the N-cell is wider than the other regions, which Tian et al. (2019) notes may be attributed to vortex dislocations. Moreover, a junction vortex and edge vortices around the step was also captured in the study.

2.4 Flow around a Forward Facing Step

Another case worth exploring is the flow around a forward facing step. Although not as widely investigated as the flow around a backwards facing step, it is of importance due to the change in diameter size investigated in this master thesis may encounter phenomenon previously described in the forward facing step case.

In laminar flow, the identification of laminar flow separation was investigated by Stuer et al. (1999). It was concluded from this study that the laminar separation was found to be an open, three dimensional separation bubble. At decreasing Reynolds number, there was an increase of distance between breakthroughs in span, i e. the breakthroughs of fluid from the bubble along the step. Furthermore, the concluded that the flow separation along the step was unsteady and moved in the transverse direction.

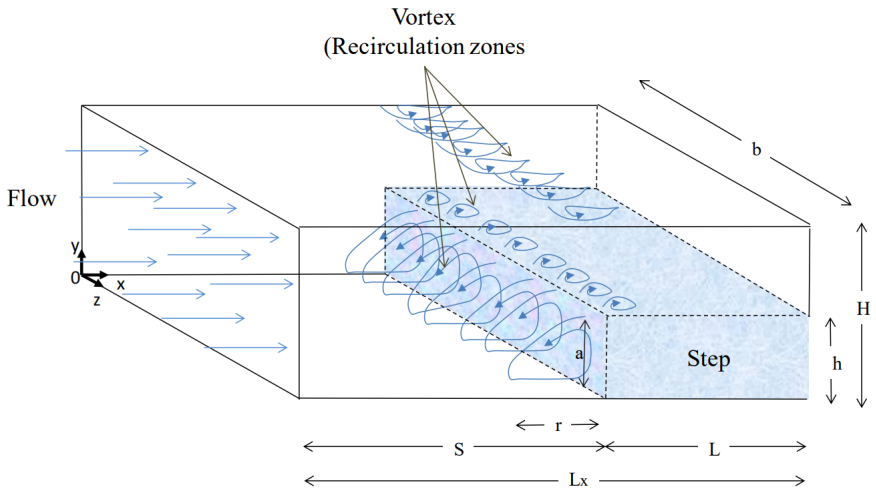

Figure 2.4: Visualization of flow through a forward facing step (Taken from Barbosa-Saldana et al. (2013)). The parameters H, L, S and L_x describes the dimensions of the duct. h and b is the height and width of the step respectively. The parameters r and a describes the recirculation zone length and height.

Barbosa-Saldana et al. (2013) investigated the flow around a forward facing step, both numerically and experimentally. Of main concern was the issues of flow separation and reattachment. Flow separation and reattachment leads to an increase in friction of the flow. These flow phenomena is inherently present in a whole range of industrial devices and is therefore of importance. However, the study of flow separation and reattachment is a complicated issue. To investigate these phenomena Barbosa-Saldana et al. (2013) used a rectangular duct with a forward facing step, as can be seen in Figure 2.4. It was found that a recirculation zone is attached to the step and that the flow in this region is highly three dimensional (Figure 2.4), which is associated with increasing Reynolds number. However, the size in the normal direction (parameter a in Figure 2.4) is largely unaffected by an increase in Reynolds number. It is therefore concluded that the length of the recirculation zone is largely affected by the Reynolds number while the height is dependent on the step height. The characterization of the vortex is achieved by means of the vortex core, where it is observed that the vortex core moves towards the bottom wall and upstream of the flow. The flow in the stepped zone is pushed to the side walls, where it jumps the step. The vortex at the side walls are also enlarged. Finally, Barbosa-Saldana et al. (2013) notes that the vertical w-velocity component has an important influence on the flow structures.

The characteristics of the separation bubble has also been investigated by Wilhelm and Kleiser (2002). They concluded that the height (a) and length (r) of

the separation bubble depends on the Reynolds number for flows with a Reynolds number below 1200. They also defined the length and height of the recirculation bubble as $r = Re^{0.6}$ and $a = Re^{0.2}$ respectively. The characteristics of the recirculation bubble is displayed in Figure 2.5. The vortex core is identified by the vertical (δ_y) and axial (δ_x) axes, which is also presented in Figure 2.5.

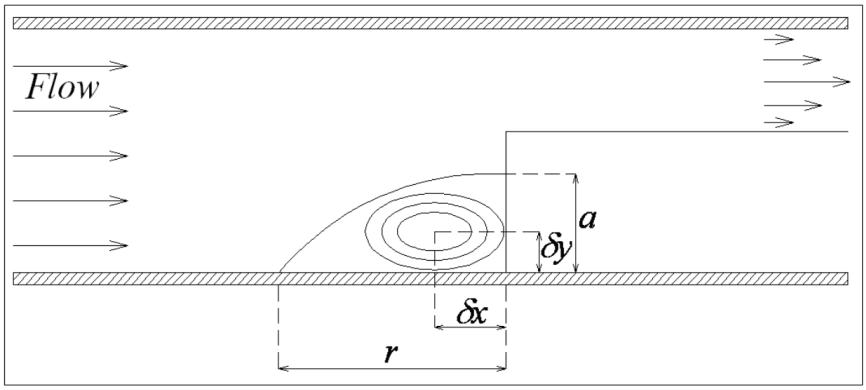

Figure 2.5: Characteristics of the recirculation zone defined by Barbosa-Saldana et al. (2013)

Flows normal to a circular disk is also of interest, as the flow field on the forward face of the disk may be used as a comparison case to the horizontal step with a sizable difference in diameter ($D/d < 2$). Tian et al. (2016) investigated the flow normal to a circular disk at Reynolds number $1.5 \cdot 10^5$. They found that toriodal vortices along the disk edges was introduced by the Kelvin-Helmholtz instability, which was not the case at lower Reynolds numbers (Shenoy and Kleinstreuer, 2008).

2.5 Risers with Staggered Buoyancy Elements

Both experimental and numerical investigations of risers with staggered buoyancy elements have been conducted over the years. Vandiver and Peoples (2003) in cooperation with MarinTek investigated the effect staggered buoyancy elements had on vortex induced vibrations. They concluded that with at least 50 % buoyancy coverage ratio the vortex shedding is dominated by the low frequency excitation from the buoyancy elements. The addition of buoyancy elements changes the ratio of mass per unit length to tension (m/T), which in turn affects the risers response displacement amplitude. A decrease in the frequency of vortex shedding decreases the loads on the structure and fatigue damage. An important parameter is the Strouhal relationship, $f_v = S_t U/D$. This relationship states that the

frequency of vortex shedding is inversely proportional to the diameter. A lower frequency results in lower modes being excited and therefore a reduction in fatigue damage rate. However, how the vortex shedding interacts in regions covered by both buoyancy elements and bare riser elements are not investigated properly. Lastly, Vandiver and Peoples (2003) concluded that in regions with high speed the ratio of buoyancy elements should not be less than 50 %.

Holmes et al. (2008) investigated what characteristics might be used to reduce VIV using numerical methods. They found out that the slick sections, i.e. the bare riser elements, acts as power-out sections and tend to damp out vibrations. However, the amount of damping is insufficient as a remedy to vortex induced vibrations. Furthermore, the use of CFD software with turbulence modeling requires validation from other sources, such as Direct Numerical Simulation or experimental studies. Therefore it is necessary to further investigate these results and conduct comparative studies. As of now, it is not known to this author whether any studies conducted on curved risers with staggered buoyancy elements have been conducted.

Chapter 3

Background Theory

This chapter covers the background theory used in this master thesis. The chapter contains the theory and assumptions behind the fluid properties used in the numerical model as well as an description of the flow phenomenons that occur in this thesis.

3.1 Fluid Dynamics

In fluid dynamics, how the fluid behaves in the spatial temporal domain is investigated. Some fluid properties, like viscosity and compressibility have a huge effect on the behaviour of the fluid flow and therefore the assumptions used are explained. In the engineering applications with riser, seawater is the fluid in question. Therefore the fluid properties used in the thesis is modeled after seawater.

3.1.1 Fluid Properties

The fluid used in simulations is a moving fluid with the following assumptions

- Single-component fluid
- Newtonian fluid
- The fluid is incompressible, with constant fluid density $\rho = constant$
- The fluid has a constant viscosity $\nu = constant$.

3.1.2 Fundamental Equations

The fluids investigated in this paper are incompressible Newtonian fluids. The dynamics of these fluids can be completely described by the time-dependent Navier-Stokes equations and the conservation of mass equation, expressed in tensorial form:

$$\frac{\partial u_i}{\partial x_i} = 0 \tag{3.1}$$

$$\frac{\partial u_i}{\partial t} + u_j \frac{\partial u_i}{x_j} = -\frac{1}{\rho}\frac{\partial p}{\partial x_i} + \nu \frac{\partial^2 u_i}{\partial x_j \partial x_j} + f_i \tag{3.2}$$

In equation 3.1 and 3.2 u_i stands for the velocity in the three-dimensional Cartesian space (i = 1,2,3), p stands for the pressure, ρ for the density and ν for the kinematic viscosity. It is assumed that both ρ and ν are constant. The term f_i represents the body forces.

This system of partial differential equations constitutes the core of modern fluid dynamics. The Navier Stokes equations are derived from Newton's second law of motion for a fluid.

3.1.3 Viscosity

The viscosity is a physical property of a fluid which defines its resistance to deformation from shear stresses. More generally speaking, one can describe viscosity as the fluid's resistance to flow. All fluids are, with some extreme exceptions, viscous and it is therefore important to understand viscosity in fluid dynamics.

The link between tangential stress τ and the variation of velocity u with respect to y can be written as

$$\tau = \mu \frac{du}{dy} \tag{3.3}$$

The coefficient of proportionality between the tangential stress and the velocity gradient is known as the dynamic viscosity. The kinematic viscosity ν is defined as the dynamic viscosity divided by the density

$$\nu = \frac{\mu}{\rho} \tag{3.4}$$

3.2 Fluid Phenomenon

A fluid flow can either be described as laminar, transient or turbulent. According to Cengel and Cimbala (2010), the laminar flow regime is characterized by smooth streamlines and highly ordered motion whereas the turbulent flow regime is characterized by velocity fluctuations and highly disordered motions.

The transition from laminar to turbulent flow occurs over some region in which the flow fluctuates between laminar and turbulent flow before it becomes fully turbulent.

3.2.1 Turbulent flow

In real life, most flows encountered in engineering are turbulent. A definition of turbulence was proposed by Lesieur (1987)

- A turbulent flow is unpredictable, in the sense that a small uncertainty as to its knowledge at a given initial time will amplify so as to render it impossible to have a precise deterministic determination of its evolution.
- It increases mixing properties when compared to a flow in which only the molecular diffusion processes are present.
- It involves a wide range of spatial and temporal scales

Turbulence, as described above is a particular characteristic of the fluid state. It is the amplification of small perturbations caused by the non-linear terms in the governing equations. To predict a turbulent flow, full knowledge of the flows detailed state at the initial time is required. If the flow is to be investigated isolated from its surroundings, full knowledge of the conditions prevailing on the boundaries is also required. Having exact knowledge of all the surroundings and conditions affecting the boundaries is an exercise in futility, so exactly predicting turbulence is impossible. However, even with the uncertainties relevant information for scientific and engineering purposes can be extracted from turbulence predictions.

As the last part of the definition in Section 3.2.1 mentions, turbulence involves a wide range of spatial and temporal scales. Turbulence is a chaotic but not a random process. In a turbulent flow, kinetic energy is transferred from large scales to small scales by the break up of the large structures. In the smallest scales, viscous dissipation transforms the kinetic energy into heat.

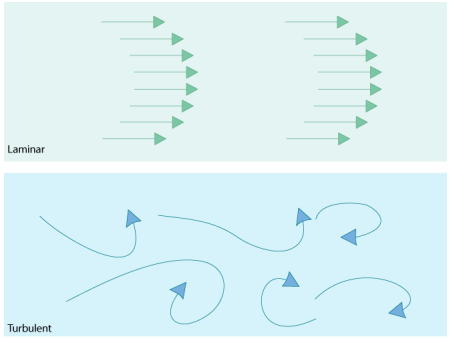

Figure 3.1: Depiction of laminar and turbulent flow.

3.2.2 Flow Parameters

One of the most important fluid parameters for viscous fluid flow is the dimensionless Reynolds number Re. It is defined as the ratio of inertial forces to viscous forces within a fluid. The difference between laminar and turbulent flow is characterized by the Reynolds number. Low Reynolds numbers describe laminar flow regimes and high numbers represents turbulent flow. The mathematical description of the Reynolds number is shown in Equation 3.5 where U is the fluid velocity, D is the characteristic linear dimension and ν is the kinematic viscosity of the fluid.

$$Re = \frac{UD}{\nu} \tag{3.5}$$

3.2.3 Flow Separation

Flow separation is a flow phenomenon that occurs for flow around fixed bodies. Flow separation is when the the flow breaks strongly away from the body. It occurs on the cylinder surface at a point where there is backflow on the downstream side of the point and no backflow on the upstream side. This means that the separation point lies on a point where $\frac{\partial u}{\partial y} = 0$ (Faltinsen, 1990). The separation points for a turbulent boundary layer differs from the laminar boundary layer in that it will separate more easily in laminar flow. This implies that with increasing Reynolds numbers, the separation point occurs further downstream on the cylinder. If the pressure gradient is strong enough, it will make the velocity gradient $\partial u/\partial y = 0$ at a certain point S, which is the separation point. This also implies that the tangential stresses from Equation 3.3 vanishes (Buresti, 2012). The occurrence of separation will lead to a drastic change in fluid features, with vortex shedding being one of the most important.

3.2.4 Vortex Shedding

Vortex shedding is a common phenomenon for all flow regimes. At Reynolds numbers above 48, vortices in the wake of the cylinder begin to shed alternately from the sides of the cylinder.

The non-dimensional vortex shedding frequency is described by the Strouhal's number St and defined by

$$St = \frac{f_v D}{U} \tag{3.6}$$

where $f_v = \frac{1}{T_v}$ is the vortex shedding frequency. It should be noted that in critical and supercritical flow there will be a spectrum of vortex shedding frequencies (Faltinsen, 1990). Roshko (1954b) showed that the Strouhal's number was related to the Reynolds number for a 2D circular cylinder, as shown in Figure 3.2. As the figure shows, the Strouhal's number is almost constant around 0.2 for Reynolds numbers in the range 10^3 to 10^4.

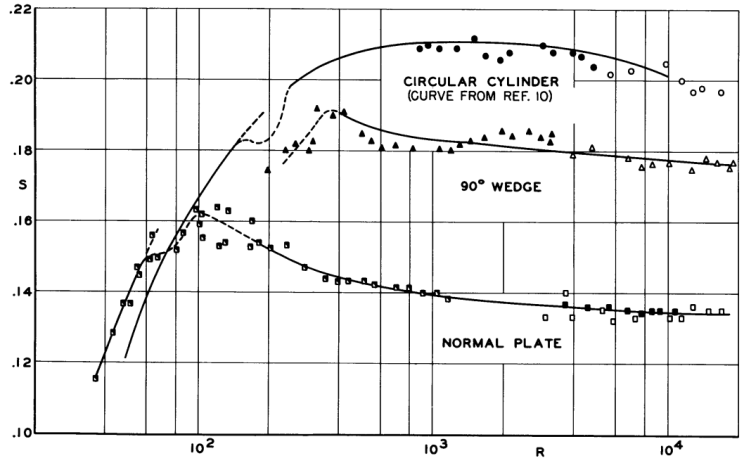

Figure 3.2: Strouhal's number for different Reynolds numbers (Roshko, 1954b)

In the wake of the cylinder, the vortex shedding creates eddies that can be mathematically represented as a point vortex of strength $|\Gamma|$. These eddies are formed in two parallel rows with uniform rotation in the row and with the opposite rotation to the other row (Lamb, 1945).

A consequence of vortex shedding is that pressure forces due to viscous effects are more important than shear forces (Faltinsen, 1990).

3.2.5 Definition of a Vortex

There has been some discussion in the fluid mechanics community of the question of what constitutes a vortex, specifically in regards to turbulent flows. Jeong and Hussain (1995) proposed a definition of a vortex in incompressible flow in terms of the eigenvalues of the velocity gradient ∇u. This definition captures the pressure minimum in planes perpendicular to vortices and also accurately defines the vortex cores at low Reynolds numbers.

The symmetric tensor $S^2+\Omega^2$ is the symmetric and antisymmetric parts of velocity gradient tensor $n\nabla u$. This tensor is the only parameter used to evaluate the local pressure minimum and define a vortex core. If λ_1, λ_2 and λ_3 are eigenvalues of $S^2+\Omega^2$ and $\lambda_3 \leq \lambda_2 \leq \lambda_1$, the definition from Jeong and Hussain (1995) is equivalent to $\lambda_2 < 0$ within the vortex core. Hunt et al. (1988) defined an eddy as the region with a positive second variant of ∇u, Q. The second variant is defined as

$$Q = \frac{1}{2}(||\Omega||^2 - ||S||^2) \tag{3.7}$$

The Q definition will incorrectly show a hollow core near the centre of a conically symmetric vortex (Jeong and Hussain, 1995). However, the Q and λ_2 values usually represent similar vortex cores.

Table 3.1: Possible choices of eigenvalues and the differences of definitions based on positive Q and on negative λ_2 (Jeong and Hussain, 1995)

λ_1	λ_2	λ_3	$\sum \lambda_i$	Negative λ_2	Positive Q
+	-	-	-	vortex core	vortex core
+	-	-	+	vortex core	not vortex core
+	+	-	-	not vortex core	vortex core
+	+	+	+	not vortex core	not vortex core

According to Jeong and Hussain (1995), only the λ_2 definition is found to represent the topology and geometry of a vortex core correctly. They also suggested that coherent structures be defined as domains of phase-correlated negative λ_2 instead of phase-correlated vorticity. Therefore the λ_2 criterion is used to identify coherent structures and vortex cores in this report.

3.2.6 Wake

According to Batchelor (2000), the term wake is commonly applied to the whole region of non-zero vorticity on the downstream side of a body in an otherwise uniform stream of fluid. The wake along with the boundary layer is usually the most

interesting part of the computational domain and therefore it is important to have a fine enough resolution in the wake to accurately describe the wake dynamics.

3.2.7 Boundary Layer

The boundary layer can be described as the layer from which the fluid makes the transition from the velocity of zero (relative to the body) at the boundary of the body to a finite value. This value should be appropriate to the value of an inviscid fluid. This means that the boundary layer $\delta(x)$ can be defined by a boundary layer thickness δ which ranges from the wall of the body to a point where the streamwise velocity component is 0.99 of the freestream velocity

$$u(y) = 0.99 \cdot U(x) \tag{3.8}$$

The boundary layer thickness can be roughly estimated with Equation 3.9 (White, 2006), which uses a flat plate as the surface.

$$\delta = \frac{D}{\sqrt{Re}} \tag{3.9}$$

3.2.8 Shear Layer

The shear layer describes a region were there is a significant velocity gradient. This implies that the viscous shear stresses τ are important. A common example of a shear layer is when a fluid moves over a solid body, and a boundary layer is formed.

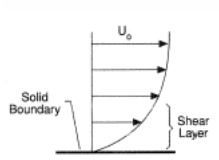

Figure 3.3: Development of shear layer from fluid passing over a solid boundary (Taken from Termopedia (2018))

A free shear layer is a shear layer that is not attached to a solid boundary. In the wake of a body in a uniform stream, a free shear layer develops between the the region of uniform flow and the wake region.

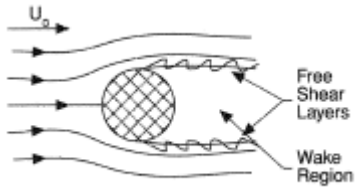

Figure 3.4: Free shear layer in the wake of a cylinder (Taken from Termopedia (2018))

3.2.9 Vortex Structures

Proper identification of types of vortical structures is one of the areas of interest in this thesis. It is therefore interesting to characterize the different vortical structures thought to appear in the thesis.

- **Junction Vortex** - A junction vortex is a vortical structure formed by the formation of a recirculation bubble that wraps around the small cylinder and forms a junction vortex (Morton et al., 2009).
- **Edge Vortex** - Edge vortices are vortex structures that are formed as flow is diverted over the large cylinder edge due to the presence of a junction vortex or a smaller cylinder (Morton et al., 2009).

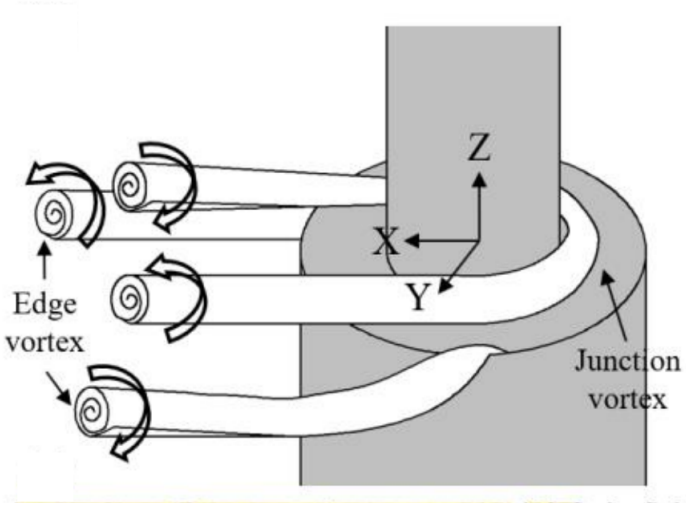

Figure 3.5: Sketch of the streamwise vortices shed from step cylinder. (Taken from Tian et al. (2019))

- **Helical Vortex** - An helical vortex is a vortex structure. Sonin (2012) described a helical vortex as a "straight vortex line with a circularly polarized Kelvin wave of arbitrary amplitude propagating along it". A Kelvin wave is a long scale perturbation mode of the vortex. The helical vortex consist of rolled up shear layers which are mostly laminar and does not shed.
- **Von Karman Vortex Street** - Von Karman vortex street is categorized by a swirling, asymmetric pattern of vortices. Von Karman vortex streets are caused by unsteady flow separation from blunt bodies i.e. vortex shedding.
- **Recirculation zone** A recirculation zone is a vortex that is stationary. Recirculation is a specific condition in which the flow separates from the body. This separation creates a low pressure area in the recirculation zone dragging fluid back into the zone creating a circulating vortex. A characteristic of the recirculation zone is the low velocity magnitude in the recirculation zone compared to the mean flow (Han, 2015).

3.2.10 Drag and Lift Forces

The forces acting on a body in a flow are separated into two components. The force the fluid flow exerts on a body in flow-wise direction is called the drag force. The forces in the direction normal to the incoming fluid flow is called the lift force. Both drag and lift force is a combination of pressure and wall shear forces and depend upon the fluid density ρ, velocity U and the size and shape of the body. For practical reasons, it is more convenient to operate with dimensionless numbers that represent the drag and lift characteristics of the body. These numbers are the drag coefficient C_D and lift coefficient C_L and are defined as

$$C_D = \frac{F_D}{\frac{1}{2}\rho U^2 A} \tag{3.10}$$

$$C_L = \frac{F_L}{\frac{1}{2}\rho U^2 A} \tag{3.11}$$

where A is the projected frontal area of the body.

The pressure was non-dimensionalized into the pressure coefficient C_P, which is defined as:

$$C_P = \frac{p - p_0}{\frac{1}{2}\rho U_0^2} \tag{3.12}$$

The pressure coefficient describes the relative pressure throughout the fluid flow field.

Chapter 4

Numerical Simulations of Fluid Dynamics

4.1 Computational Fluid Dynamics

Computational Fluid Dynamics (CFD) is the process of solving the equations of interest numerically, in this case the Navier-Stokes equations. The know-how of CFD has been known for quite some time but it was not until the implementation of high-speed computers that solving fluid dynamical problems became realistic. The advantage of solving fluid dynamic problems numerically compared to analytical and experimental methods its ability to treat complicated physics and obtain the time evolution of the flow. However, its disadvantages lie in its truncation errors, boundary conditions issues and high computational costs in terms of floating operations (Tannehill et al., 1997).

4.2 Direct Numerical Simulation

Direct numerical simulation (DNS) is a tool developed to give a complete description of the turbulent flow where the flow variables (pressure and velocity) can be obtained from the Navier-Stokes equations (Equations 3.1 and 3.2) for fluid flows. The numerical simulations in DNS have to account for all the different scales in turbulent flow, thereby making the computational time needed to solve engineering problems in DNS strenuous if not impossible. However, advances in computing power and numerical mathematics the last decades have made DNS a more viable tool in research problems. The main issue with DNS is the limited amount of computational power which limits DNS to simple geometries and low Reynolds

numbers.

In DNS the absence of a turbulence model requires that the computational grid is sufficiently fine to resolve all relevant flow scales. The smallest scales in a 3D homogeneous isotropic turbulent flow have been estimated by Kolmogorov in 1941. Kolmogorov suggested that there exist an equilibrium between the smallest flow scales and their destruction through viscous dissipation. The length scale is proportional to $Re_{ed}^{-3/5}\ell_{ed}$ and the time scale proportional to $Re_{ed}^{-1/2}\ell_{ed}/u_{ed}$ where ℓ_{ed} is the size of the largest eddies and u_{ed} their velocities. Re_{ed} is the Reynolds number based on the large eddies $Re_{ed} = \frac{u_{ed}\ell_{ed}}{\nu}$ and is approximately one order smaller than the "ordinary" Reynolds number (Veldman, 2012).

4.3 MGLET

The code MGLET[1] was developed for numerical simulation of turbulent flow with complex geometries. The code MGLET use a number of different techniques to save CPU time and computer memory. It is a code that will run efficiently a parallel computer with more than 2000 processes. (Strandenes et al., 2016). MGLET is based on a finite volume formulation of the Navier-Stokes equations. It is applied for an incompressible fluid and uses a staggered Cartesian non-equidistant grid.

4.3.1 Space Discretization

MGLET is based on a finite volume discretization of the integral form of the Navier-Stokes equations. The staggered Cartesian grid has the pressure nodes in the center of the control volumes, with the velocity components stored at the center of the control volume faces as displayed in Figure 4.1

[1]MGLET stands for Multi-Grid Large Eddy Turbulence and is a numerical Navier-Stokes solver for both Large Eddy Simulation and DNS.

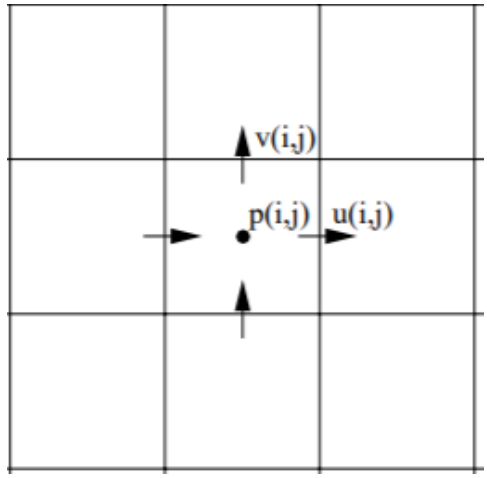

Figure 4.1: 2D representation of the control volume with pressure and velocity nodes. Taken from (Tremblay, 2015)

The equations to be discretized are the Navier-Stokes equations, i.e. the conservation of fluid momentum and the conservation of mass equation.

$$\int_S u_i \cdot \vec{n} dS = 0 \tag{4.1}$$

$$\frac{\partial}{\partial t} \int_\Omega \rho u_i d\Omega + \int_S \rho u_i \vec{u} \cdot \vec{n} dS - \int_S (\mu \nabla u_i - p) \vec{i_i} \cdot \vec{n} dS = 0 \tag{4.2}$$

The integration of the momentum equations are approximated numerically over the control volume using the midpoint rule. For the convective terms in the Navier-Stokes equations, the interpolations are done by central approximation of second-order accuracy. The diffusive terms are calculated by a central order method with second-order accuracy. (Tremblay, 2015)

4.3.2 Time Discretization

For the time discretization, the momentum equations are evaluated using an explicit second-order (leap-frog) time step (Manhart, 2004).

$$u^{n+1} = u^{n-1} + 2\Delta t[C(u^2) + D(u^{n-1}) - G(p^{n-1})] \tag{4.3}$$

Where the C represents the discrete convection, D the discrete diffusion and G the gradient operator. The leap-frog is unstable for the 1D convection-diffusion

equation in combination with central spatial discretization. Therefore, the diffusive term is calculated at time level $n + 1$. Time integration of Equation 4.3 is achieved by using a low storage explicit third order Runge-Kutta scheme proposed by Williamson (1980).

4.3.3 Solution for the Pressure

The pressure at time level p^{n+1} is found by solving the Poisson equation

$$Div[G(p^{n+1}] = \frac{1}{2\Delta t} Div(u^*) \tag{4.4}$$

Where u^* is an intermediate velocity field. The pressure field has to be updated for each of the three stages in the Runge-Kutta scheme. This implies that the Poisson equation for the pressure correction has to be solved for each of the three stages of the scheme until a divergence free velocity field is obtained. To find the divergence free velocity field the velocity correction equation is applied

$$u^{n+1} = u^* - 2\Delta t G(p^{n+1}) \tag{4.5}$$

4.4 Set up of Computational Domain and Fluid Flow Problem

By using a Cartesian grid in the space discretization, the savings in CPU time and memory is between 10-30 times when compared to a curvilinear coordinate system (Manhart et al., 1998). To represent complex geometries in the Cartesian grid, an immersed boundary method is implemented.

4.4.1 Immersed Boundary Method

The immersed boundary method (IBM) allows the effect of the body on the flow into account even while using a Cartesian grid (Peller et al., 2006). The distinguishing feature of this approach to solving the boundary conditions on the body is that the solver can perform the entire simulation on a fixed Cartesian grid thereby saving a lot of computational costs.

The immersed boundary method is applied by interpolating the boundary conditions from the body to the Cartesian fluid cells by direct forcing immersed boundary method. The surface of the geometry is represented by an unstructured triangular mesh, the fluid domain is represented by Cartesian grid cells. The geometry is applied directly by the immersed boundary method to the block cells (Tian et al., 2017a). The MGLET solver uses an algorithm to identify the body and construct

the least square interpolation for complex geometries. The main advantage of the IBM is that it is completely independent of the geometry. This implies that strenuous mesh generation around complex geometries are avoided unlike in body-fitted grids. Investigations on the accuracy by Peller et al. (2006) showed that the IBM method preserves the accuracy of the numerical solver. Furthermore, the IBM formulation in MGLET is created automatically in the pre-processing step and limits the numerical cost.

4.4.2 Grid Refinement

The grid is constructed by the use of cubic Cartesian grid boxes. Each of the boxes contains $N \times N \times N$ uniformly distributed grid cells. In regions were complex flows and boundary layers reside, the grid boxes can be locally refined by splitting each box into eight child boxes. The child box resolution is two times finer than the parent boxes. In the domain in MGLET, the grid may be divided into 4 to 6 levels depending on the minimum grid size Δ. This implies that the domain size must be the size of the coarsest grid box times an integer.

4.4.3 Boundary Conditions

In order to properly define a computational domain, the boundary conditions around the domain must be defined. The boundary conditions set constraints and restrictions for the velocities and the pressure. The boundary conditions have to be implemented at all the boundaries of the domain.

- The Dirichlet boundary condition prescribes the value of a variable at a boundary i.e. $u(x) = constant$.
- The Neumann boundary condition predicates that the gradient normal to the boundary of a variable at the boundary is constant. $\frac{\partial u(x)}{\partial n} = constant$
- The no-slip boundary condition predicates that the fluid velocity must be equal to the velocity of the object
- The impermeability condition states that no fluid particles may move through a solid body.

4.4.4 Boundary Layer Resolution

The boundary layer is of particular interest as the flow separation point and pressure distribution around the boundary layer are important parameters for the forces

and moments acting on the cylinder. The boundary layer and the wake can be refined by using refinement boxes, refinement boxes are manually selected to refine specific volumes in sections of interest. As the refinement around the cylinder is automatic, the grid generator will automatically refine the boundary layer to its finest level. However, it should be noted that additional refinement levels further away from the cylinder might be necessary.

4.5 Verification and validation

In numerical analysis, a code must be verified both as a numerical solver as well as with respect to the grid size. In fact, for each new problem, a CFD code must be verified by systematic grid convergence tests. This section will cover the procedure for the verification of the DNS code. For verification of CFD code the main procedure is to see if the grid results converge to a solution with decreasing grid size and if the grid size

In numerical studies, there is a distinct difference between the terms verification and validation. In general, the term verification can be described as solving the equations right, validation is solving the right equations (Roache, 1998). In verification, the specific partial differential equations are stated and defined how they are solved precisely. Then it must be stated convincingly that the equations are solved correctly and with what degree of accuracy the solution has. Validation is about whether the programs and equations bear any relation to the physical phenomenon they are trying to model. Validation is usually based on comparison to experimental data.

Chapter 5

Initial Comparison Studies

Before the main study started, initial studies of flow around cylinders with a change in diameter was conducted. The goal was to identify relevant flow phenomena which could be of importance in the main study, as well to get familiar with the basic cases presented in the literature study (Chapter 2) compared to the initial study results. The goal of the preliminary study was to get a clearer picture of the flow for the most extreme versions of the main case, and provide a pathway to choosing what values are best suited for the parameter study.

5.1 Flow around Cylinder with a Change in Diameter

Flow around a cylinder with a change in diameter has been investigated by Tian et al. (2017b) using the same software used in this thesis. To investigate how the flow patterns behave around a cylinder with a change in diameter a simulation was run with parameters as described in Table 5.1. One of the main differences in this analysis from the one run by Tian et al. (2017b) is the relationship between the large and small cylinder. In this analysis the diameter ratio is $D/d = 5$ instead of $D/d = 2$. The reason for this is that a diameter ratio of 5 is preferred in the industry and also the diameter ratio used in the main study.

Table 5.1: Domain size and grid refinement for the vertical cylinder with a change in diameter.

Δ	X Front	X Back	Y Right	Y Left	Z Bottom	Z top
$0.02D$	$-6D$	$20.88D$	$13.44D$	$-13.44D$	$-25D$	$15.32D$

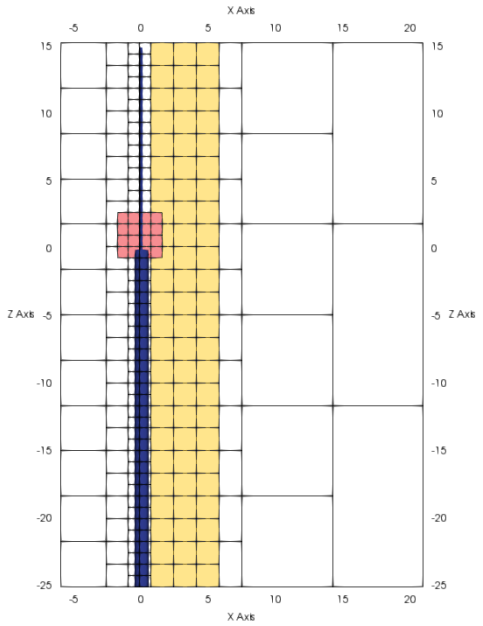

Figure 5.1: Domain and grid resolution for the vertical step-cylinder case. The red colored cells represent manual grid refinement around the step with a resolution equal to the finest grid resolution of the simulation i.e. Δ. The yellow colored sections represent manual grid refinement at two times the finest grid refinement i.e. $2 \cdot \Delta$

The geometric model used was with a ratio of d/D of 0.2 where D was put to one unit length. The Reynolds number was put to 600, as this was used in later studies and some other studies with similar geometry also apply this Reynolds number. The use of $Re_D = 600$ was to have vortex shedding around the smallest cylinder ($Re_d = 120$).

5.1.1 Results

In the simulation, vortex shedding is split into three regions or cells. The small region, or the S-cell region has a higher frequency than the region behind the large cylinder, the L-cell region. The N-cell region sheds vortices, according to Morton and Yarusevych (2010) with a frequency f_N. As seen in Figure 5.2, the different regions have distinct different vortex shedding modes coinciding with the spectrum peaks in Figure 5.3.
The visualizations of $\lambda_2 = -0.1$ displayed in Figure 5.2 illustrates the different vortex shedding regions in the wake of the stepped cylinder. The S-cell region sheds smaller and more compact 2-D vortices which are dragged down towards the wake of the large cylinder. The wake behind the large cylinder is more chaotic

and three dimensional, with a slower shedding frequency than behind the smaller diameter.
From Figure 5.2, downwash can clearly be seen. The vortex shedding in the wake can be divided into three regions, the first region is in the wake behind the small cylinder, the second region is behind the step, which is the N-cell region described in Morton and Yarusevych (2010) and Tian et al. (2017a). The last region is the L-cell region, which is behind the large cylinder. From Figure 5.3, the dominating

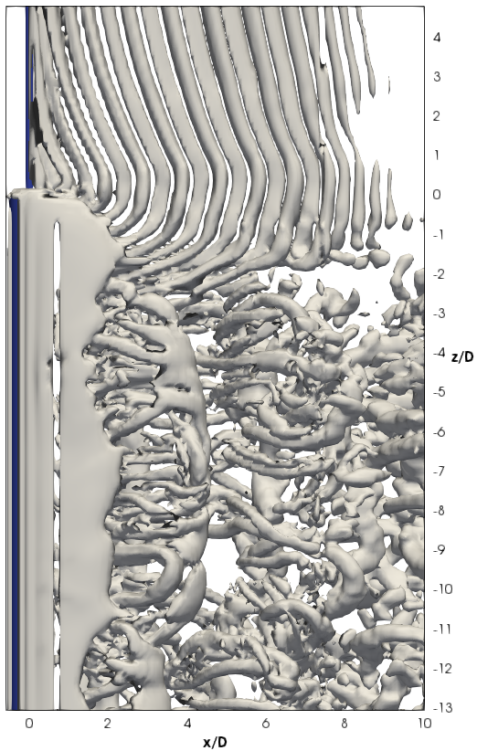

Figure 5.2: Visualization of the instantaneous iso-contour of $\lambda_2 = -0.1$, $Re_D = 600$ in the wake of the straight cylinder. The flow is fully developed.

frequencies along the vertical sampling line are the vortex shedding frequencies. The vortex shedding frequency in the wake behind the large has two dominating frequencies (f_L & f_N) and traces of another frequency of interest (f_{beat}). The wake behind the small cylinder shows only one dominating frequency (f_S).

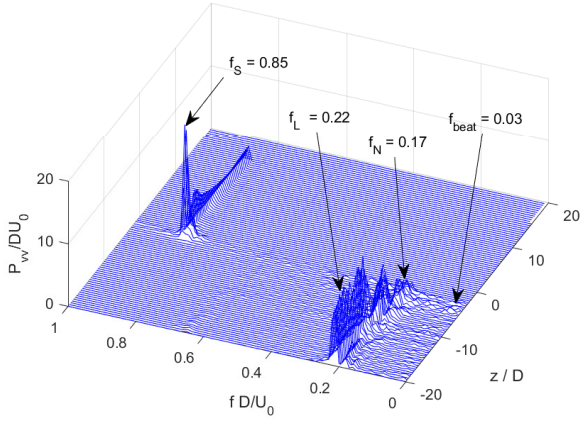

Figure 5.3: Power spectrum density distribution of the cross-flow velocity v along a sampling line $x/D = 3$ behind the cylinder at $y/D = 0$. $Re_D = 600$

Morton and Yarusevych (2010) noted that the oblique vortex shedding makes the Strouhal frequencies lower than values for Strouhal frequency past a uniform cylinder at the corresponding Re_D. Using evaluation methods from Tian et al. (2017b) the oblique angle for both the small and large cylinder were investigated. Williamson (1989) proved that the parallel vortex shedding is the universal one. The oblique vortex shedding St_θ can therefore be transformed into the universal one St by means of the trigonometric relationship $St = St_\theta / \cos\theta$. The vortex shedding behind the small cylinder has an oblique angle of $\theta_S = 22°$ as displayed in Figure 5.4. The L-cell vortices does not show any sign of oblique shedding below $z/D = -3$, which is the endpoint of the N-cell region. The parallel vortex shedding Strouhal number is compared to experimental results from Zdravkovich (1997) and the empirical formulas from Williamson (1989)

$$St = 0.2731 - 1.1129/Re^{0.5} + 0.4821/Re \tag{5.1}$$

and Roshko (1954a)

$$St = 0.212 \cdot (1 - 21.2/Re) \tag{5.2}$$

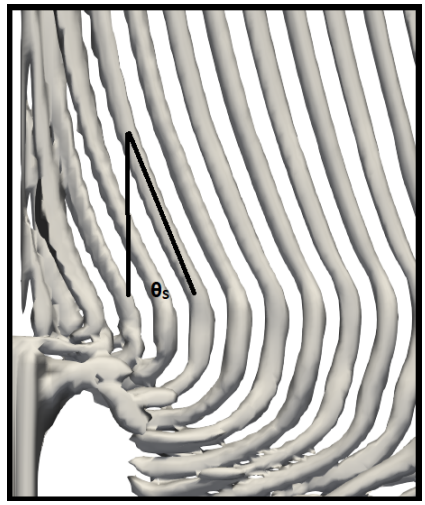

Figure 5.4: Close up display of the instantaneous iso-surfaces of $\lambda_2 = -1$ around the step. The oblique angle θ_S is found by investigating the angle of the vortices shed from the small cylinder.

Table 5.2: Strouhal numbers for the present case compared with empirical values. (It should be noted that St'_{θ_S} is based on the small cylinder diameter d and St_{θ_L} is based on the large cylinder diameter D)

	θ_L	θ_S	St'_{θ_S}	St_{θ_L}	St_S	St_L
Present	0 °	22 °	0.17	0.22	0.183	0.22
Equation 5.1	...	...	...	...	0.176	0.228
Equation 5.2	...	...	...	...	0.175	0.205

From Table 5.2 it is clear that the measured values shows good correlation to the empirical. Along the N-cell location, there are signs of a beat frequency $f_{beat} = f_L - f_N = 0.037$. The beat frequency are a result of the vortices in one of the cells moving out of phase with vortices in a neighboring cell. The beat frequency observed in the power density spectrum (Figure 5.3) is close to the beat frequency calculated from the S-cell and L-cell frequencies. Although the energy contained in the power density spectrum is small there is grounds to believe there is a beat frequency acting in the N-cell region.

5.2 Flow parallel to a Cylinder with a Change in Step.

Flow parallel to the length of the cylinder is of importance as how the flow develops behind a horizontal step can be used as an indicator and comparison for the main cases to be studied. It is to this authors knowledge, not any studies conducted on a stepped cylinder in parallel flow. For cases where the angle of the step α is close to zero and the step is normal to the flow direction, a comparison case would be advantageous. A direct numerical simulation of flow along a circular cylinder with a change in diameter is therefore conducted. The goal is to investigate how the flow develops around the change in diameter and compare the the circular forward facing step to cases of a forward facing step in a square channel flow. Also of note is to see if any flow patterns of note develops in the wake of the step, in particular recirculation zones is of interest.

The diameter of the large cylinder was used as a reference length, as have been done in the vertical cylinder with a change in diameter case (Section 5.1), and was put to one unit length. The Reynolds number for the large diameter cylinder was the same as in the other cases $Re_D = 600$, and the small cylinder had a Reynolds number of $Re_d = 120$. The height of the step between the cylinders was $h = 0.4D$. The Reynolds number based on the step was then $Re_h = 240$. The Reynolds number based on the step height h is used when compared to the channel flow studies reviewed in the literature study.

Table 5.3: Domain size and grid refinement for the horizontal cylinder with a change in diameter.

Δ	X Front	X Back	Y Right	Y Left	Z Bottom	Z top
$0.01D$	$-13.44D$	$26.88D$	$13.44D$	$-13.44D$	$-13.44D$	$13.44D$

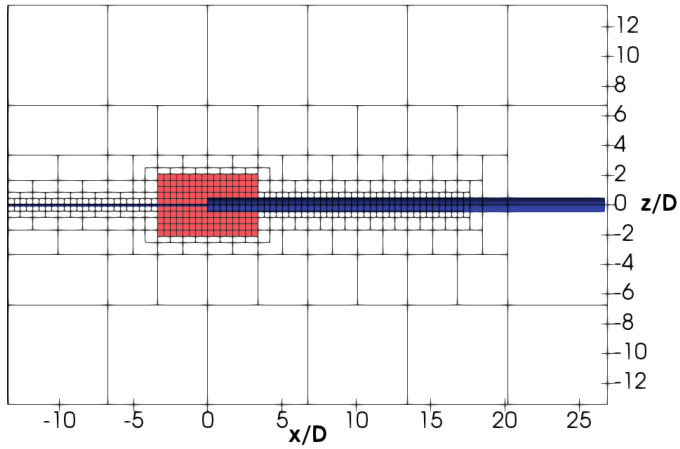

Figure 5.5: Domain and grid resolution for the horizontal step-cylinder case. The red colored cells represent manual grid refinement around the step with a resolution equal to the finest grid resolution of the simulation i.e. Δ. The blue sections represent the geometry of the cylinder in the domain.

5.2.1 Results

The flow field is symmetric in the $y/D, z/D$ planes. The velocity profiles of the u component along both the small and big cylinder boundary layers are plotted in Figures 5.6 and 5.7. The boundary layer along the small cylinder surface shows that the velocity turns into a negative value close to the step, which indicates backflow and separation. The boundary layer thickness is decreasing monotonously as the flow moves closer to the step, as indicated in Figure 5.6. Moreover, the boundary layer thickness does not exceed the step height, which may in addition to the low Reynolds number explain the lack of a recirculation zone behind the step.

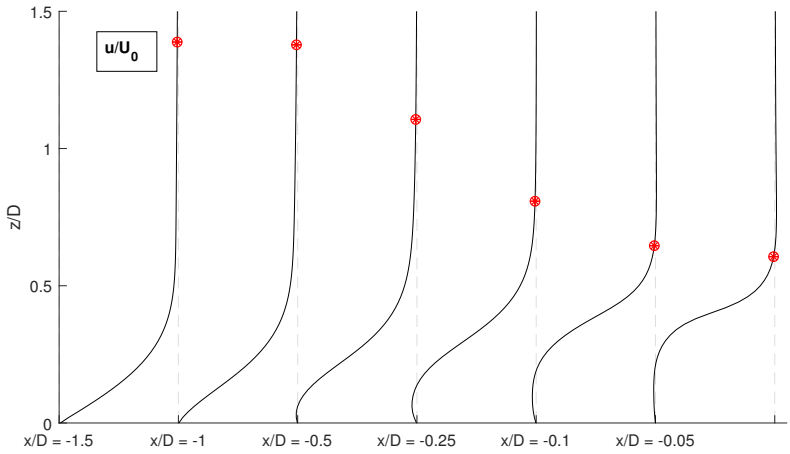

Figure 5.6: Profiles of the mean streamwise velocity component u along the small cylinder ahead of the step. The velocities are sampled from the cylinder surface at $y/D = 0$. The red dots indicates the thickness of the boundary layer ($u = 0.99U_0$).

The boundary layer in the immediate wake of the step decreases in thickness until approximately $x/D = 0.25$, where it starts to increase. The boundary layer thickness is significantly thinner along the the surface of the large cylinder surface than for the small cylinder surface.

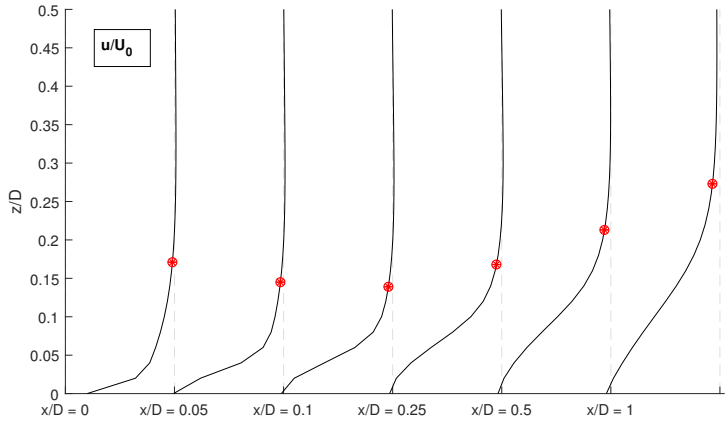

Figure 5.7: Profiles of the mean streamwise velocity component u along the big cylinder ahead of the step. The velocities are sampled from the cylinder surface at $y/D = 0$. The red dots indicates the thickness of the boundary layer $\delta_{0.99}$ ($u = 0.99U_0$).

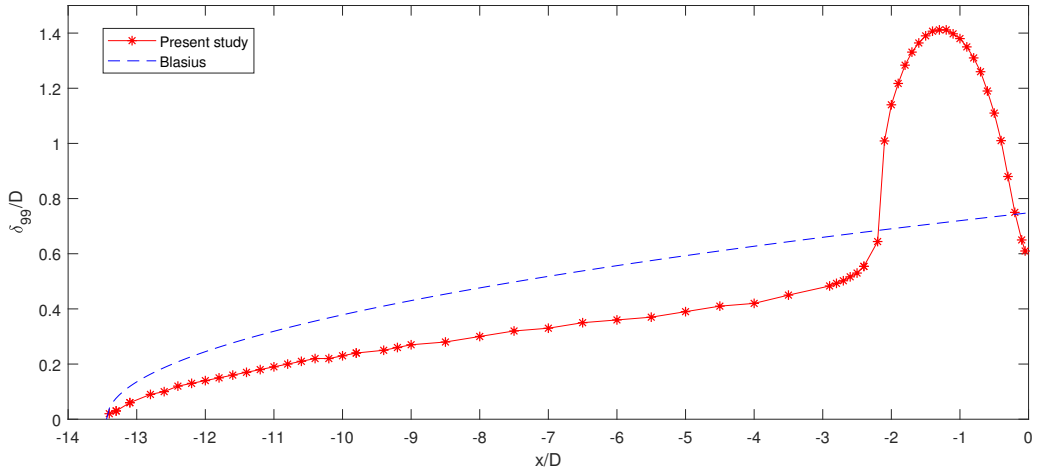

Figure 5.8: Boundary layer thickness δ_{99} along the small cylinder extension in the $y/D = 0$ symmetry plane. The Blasius equation for laminar flat plate flow is also presented for comparison. The length x/D represents the distance ahead of the step i.e. $x/D = 0$

To investigate how long the horizontal extension should be in order to have a fully developed flow before the influence of the step affects the flow. The boundary layer thickness δ_{99} from the edge of the domain along the small cylinder surface was investigated. The boundary thickness from the Blasius solution for a boundary layer over a flat plate, as defined by equation 5.3 in White (2006) [p.232] was used as a comparison.

$$\delta_{99} = 5.0(\nu x/U_0)^{1/2} \tag{5.3}$$

where ν is the kinematic fluid viscosity. Boundary layers development along horizontal cylinders at high Reynolds number have been studied by Tutty (2008) and at lower Reynolds numbers by Jiang et al. (2018b). They concluded that the laminar boundary layer along a circular cylinder is thinner than in a flat plate flow.

The boundary layer in the present study, displayed in Figure 5.8 develops in the same way as with present studies, where the boundary layer is thinner than for a laminar flat plate flow. However, at a distance of $3D$ ($x/D = -3$) ahead of the step the boundary layer thickness increases significantly until it reaches a maximum around $x/D = -1.5$ before it decreases again. It is clear that this sharp increase in boundary layer thickness is due to the influence of the step on the flow. This means that the influence of the step must be taken into account when deciding the proper length of the horizontal extension. Jiang et al. (2018b) recommended a distance of $L_H = 10D$ to properly develop a boundary layer. The

present study shows that in addition to the distance necessary for a fully developed boundary layer, an additional horizontal extension is required to account for the flow phenomena induced by the step. As the increase in boundary layer thickness occurs at a distance $3D$, at can reasonably be assumed that the horizontal extension must be at least $3D$ in addition to the length required to have a fully developed boundary layer.

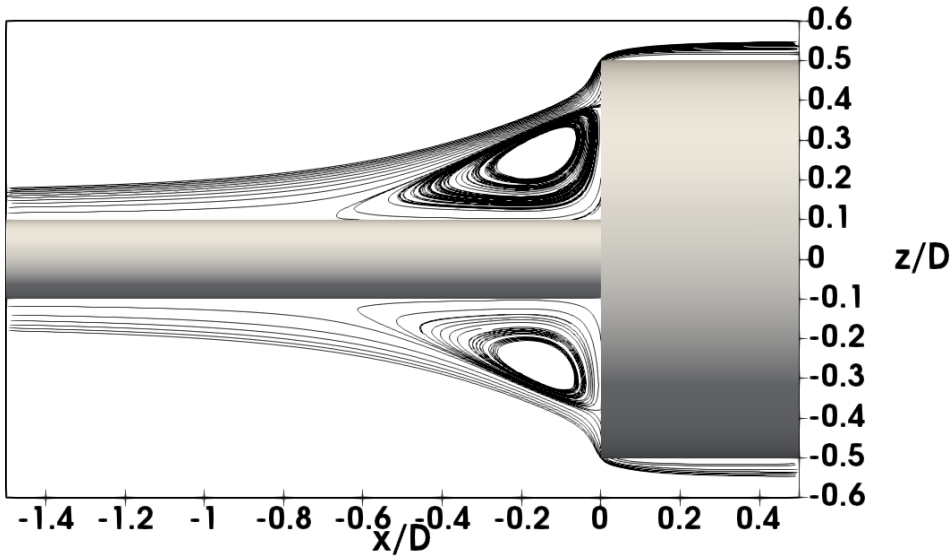

Figure 5.9: Streamlines calculated backwards from the step by a line probe, at a distance of $z/D = 0.1$ above and below the small cylinder surface in the $y/D = 0$ plane.

From Figure 5.9 there is no indication of a recirculation zone above the step, which has a height $h = 0.4D$. The studies done by Hattori and Nagano (2010) had a recirculation zone for the step at Reynolds numbers as low as $Re_h = 900$. However, in this case, $Re_h = 240$. This indicated that the flow presented is predominately a 2-D flow before the recirculation zone and at such a low Reynolds number there is no recirculation zone behind the step. The recirculation zone in front of step is presented along with characterization in Figure 5.10. As the previous studies reviewed in Chapter 2 are based on channel flows and a square step, it is difficult to make any quantitative comparisons. However, there are some particular similarities that should be noted.

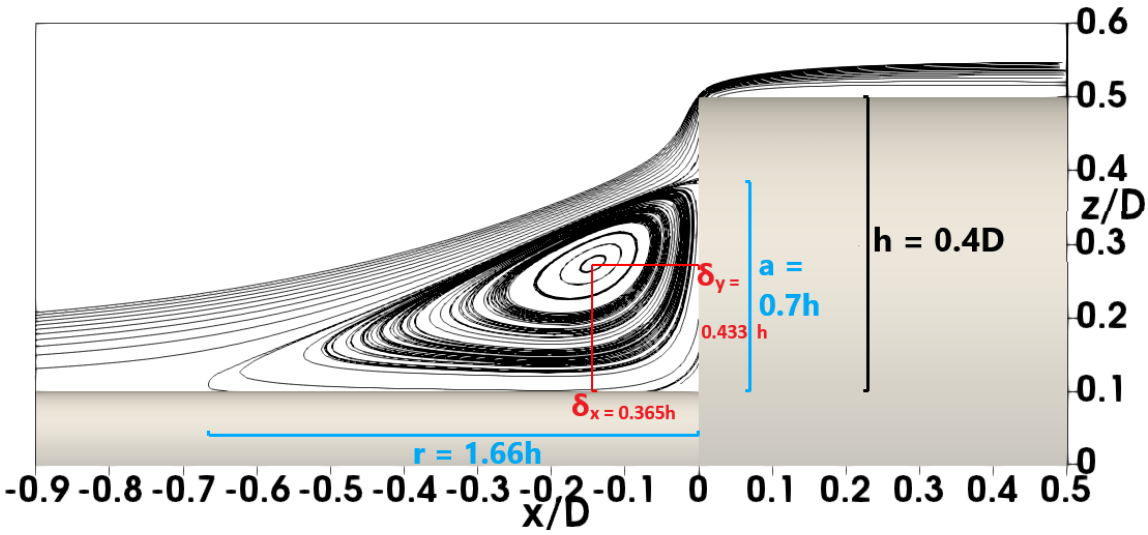

Figure 5.10: Streamlines calculated backwards from a line probe placed at the edge of the step and traced backwards. Measurements of the recirculation zone is also presented for ease of reading

The characteristics for the recirculation zone in front of the step is presented in Table 5.4. The recirculation zone height a has a value identical to the results from Barbosa-Saldana et al. (2013), which for Reynolds numbers from 269 to 475 had a height a/h between 0.68 and 0.7. Barbosa-Saldana et al. (2013) noted that the height does not experience a significant change although the Reynolds number almost doubles. Of note is the exact same value obtained in this present case, and the symmetry presented in Figure 5.9 indicates that the recirculation zone is symmetric along the x-axis. The value r/h is larger than values obtained by Barbosa-Saldana et al. (2013) at Reynolds numbers up to 475, but again lower than DNS results from Hattori and Nagano (2010). In regards to the discrepancy in the vertical location of the vortex core between the experimental values obtained from Barbosa-Saldana et al. (2013) and the present study, a key difference seems to be the structure of the recirculation zone, as the present case has triangular shape compared to the more square shape in Barbosa-Saldana et al. (2013). The boundary layer in the present case decreases as one moves closer to the step, this decrease may explain the triangular shape of the recirculation zone.

Table 5.4: Characteristics for the recirculation zone with values from experimental and numerical studies of flow around a forward facing step. It should be noted the differences in geometries makes direct comparisons inadvisable.

	r/h	a/h	δ_x/h	δ_y/h
Present case ($Re_h = 240$)	1.66	0.7	0.365	0.433
Hattori and Nagano (2010) (DNS -$Re_h = 900$)	1.91	-	-	-
Barbosa-Saldana et al. (2013) (Experimental - $Re = 269$)	0.95	0.73	0.4	0.32
Barbosa-Saldana et al. (2013) (Experimental - $Re = 365$)	1.09	0.76	0.42	0.30
Barbosa-Saldana et al. (2013) (Experimental - $Re = 475$)	1.25	0.74	0.41	0.29

5.3 Review of the Initial Study

The straight vertical cylinder with a change in diameter case showed how the different geometries influence the flow and how they can be separated into different regions. The influence of the step is of importance in the straight case, and many of the flow phenomena is directly related to fluid dynamics around the step.

As for the use of the horizontal cylinder preliminary case in regards to the main study of flow around a concave cylinder, the development of a recirculation zone at the step for lower angles α for the change in diameter is of interests. When does the recirculation zone cease to exist and flow phenomena relevant for the straight step cylinder case become more relevant? Furthermore, the formation of a recirculating zone behind the step could also be of interest, as the change in the angle of the step in regards to the horizontal flow direction may induce a recirculation zone behind the step at lower Reynolds numbers.

An investigation of the boundary layer thickness along the surface of the small diameter cylinder in front of the step showed that the step has an influence on the boundary layer thickness. The influence of the step on the boundary layer reached at least a distance of $3D$ upstream. Furthermore, studies from Jiang et al. (2018b) recommended a distance of at least $5D$ but preferably $10D$ for a concave curved cylinder with a diameter of D. In this case, it means that the recommended length should at a minimum be

$$L_H = L_{H,BoundaryLayer} + L_{H,Step} = 10d + 3D = 5D$$

and preferably be higher.

It should be noted that the horizontal cylinder with a change in diameter case did not have any comparative studies which could be used as a benchmark. The flow around step in horizontal is an interesting case, and further studies should investigate this case more thoroughly.

All of the cases investigated present a good base for investigating the main cases and a good background for comparisons in addition to the previous studies reviewed in Chapter 2.

Chapter 6

Grid Refinement Analysis

The choice of computational domain and grid size is a paramount part of a CFD study. The quality of the results from a CFD analysis is highly dependent on the quality of the grid (Cengel and Cimbala, 2010) and therefore it is important investigate how the grid quality and domain size affects the results.

This chapter investigates how the grid refinement affect the flow parameters, using a geometry where the increase in the diameter starts from the end of the curvature and extends the entire vertical extension.

6.1 Geometry and Computational Domain

The geometry in this study is a concave cylinder with a change in diameter at a certain angle. The geometry of this study is adapted as it can be seen as a merged between a previous study on concave curve cylinder by Jiang et al. (2018a) and a study of cylinder with a change in diameter by Tian et al. (2017b). The incoming flow is in the positive flow direction. As can be seen in Figure 6.1, the geometry parameters of interest are d, D, α, R, L_V and L_H. The parameters d and D are the diameters of the small and large cylinder respectively. The small cylinder goes parallel to the flow in the horizontal direction while the large cylinder is in the vertical position normal to the flow direction. The parameter α describes the angle between the start of the curve at the horizontal position and the step, which is the where the change in diameter occurs. The parameter R describes the radius of the curve. L_V and L_H are parameters that describes the height and length of the geometry inside the computational domain.

The geometry used in the grid convergence study was chosen as it has a clear split between the concave part with a small diameter and a larger diameter vertical

extension. This geometry also has the advantage of being similar with previous studies and therefore can be used to compare the results more accurately.

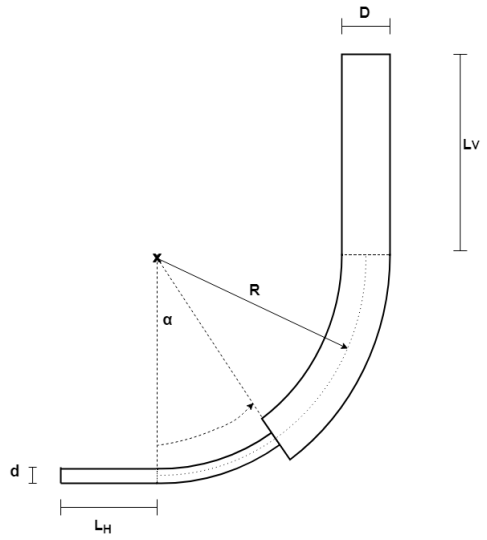

Figure 6.1: Set-up of the geometry, as seen from the positive y-direction. The parameters are the diameter of the small cylinder d, the diameter of the large cylinder D, the angle on the curvature were the change in diameter occurs α, the radius of curvature R, the length of the vertical extension L_V and the length of the horizontal extension L_H.

The flow and fluid parameters are all kept constant except the viscosity, which are applied to change the Reynolds number Re.

As mentioned in Section 2.1.1, the parameters for the length and height of the cylinder (L_V and L_H) and boundary conditions have an effect on the flow in the domain. They also provide a picture of the flow field in the wake of the cylinder.

6.1.1 Boundary Conditions

The problem defined is the effect of inplane flow around a concave curved cylinder with a change in diameter. The flow is a uniform flow in the x-direction with a constant velocity. As the boundary conditions may affect the results drastically it is important that they are chosen with care and in accordance with the physical problem modeled.

- At the inflow boundary, a uniform free stream condition was imposed ($u_i = (u, v, w) = (U_0, 0, 0)$.
- At the outlet boundary, a Neumann boundary conditions for the velocity

components ($\frac{\partial u}{\partial x} = \frac{\partial v}{\partial y} = \frac{\partial w}{\partial z} = 0$) and zero pressure condition ($p = 0$) was imposed.

- On the vertical side boundaries normal to the y-direction, a free slip boundary was imposed ($v = 0$, $\frac{\partial u}{\partial y} = \frac{\partial w}{\partial y} = 0$)
- On the two horizontal side boundaries normal to the z-direction, free slip boundary condition was also imposed ($w = 0$, $\frac{\partial u}{\partial z} = \frac{\partial v}{\partial z} = 0$)
- At the surface of the cylinder, the boundary conditions are no slip and impermeable wall.

These boundary conditions were used in all the grid convergence studies, as well as all the following simulations in the parameter study (Chapter 8) and more specialized studies (Chapter 7) By applying the same boundary conditions for all simulations, the amount of variables in the simulations are reduced and it would be easier to quantify the results.

6.2 Parameters used in the Grid Convergence Analysis

In order to get quantifiable results from the grid converge test, some output parameters should be investigated for each case and used for comparison of grid quality. The flow variables u, v, w and p forms the basis of a CFD solution. These output variables were used to determine the qulity of the grid for the simulation by means of comparison.

The following variables and statistical quantities were used to in the grid convergence study.

Velocities

- The time averaged flow velocity components u, a_{ax} and w in the immediate wake of the cylinder, from directly below the start of the horizontal extension to the a distance of $20D$ above the start of the vertical extension. The reason for the plotting over the entire vertical extension was to check how the flow variables behaved near the boundaries.
- The time averaged horizontal and vertical velocity components just below the step, at a distance $0.1D$ ahead of the the small cylinder surface and at $y/D = 0$.
- The dominating frequencies of the cross-flow velocity component v in the wake of the cylinder.

Pressure

- The time averaged pressure in the immediate wake of the cylinder, from directly below the start of the horizontal extension to the a distance of $20D$ above the start of the vertical extension.

Forces

- The time averaged drag force coefficient $C_{D,mean}$
- The root mean square of the lift coefficient $C_{L,rms}$

The variables for the velocities were chosen because they were easy to compare quantitatively for all the cases. The dominating frequencies are usually a very stable value while the velocity profiles can be used to assess where in the wake the largest discrepancies in values occur. By finding areas with large differences in the output values, the grid can be further refined at those locations.

6.3 Grid Quality

To investigate how the grid quality affects the final solution, five cases with specific grid refinements were run and investigated. The case information for the grid quality analysis is found in Table 6.1. The Reynolds number for all cases is defined in terms of the large cylinder. For all cases in the grid convergence study, the same domain size was used. to account for the influence of boundary conditions on the vertical and horizontal extensions, benchmark values from both Gallardo et al. (2013) and Jiang et al. (2018a). The dimensions for the domain can be seen in Table 6.2.

Table 6.1: Case information for grid quality analysis

Case	Re_D	Min grid spacing Δ/D	Total grid number
1	600	0.01	638.19 million
2	600	0.02	144.77 million
3	600	0.04	35.12 million
4	600	0.08	9.04 million
5	600	0.1	3.55 million

The grid generator in MGLET has the option to manually refine the grid in addition to the automatic refinement around the, namely at sharp edges around the geometry and in the wake of the body. To account for this manual refinement, the grid was increased with the same factor as the grid around the body. The grid was

refined by taking the iso-volume of the magnitude of vorticity $\omega_{mag} = 0.01$ and refining the grid in the volume, thereby ensuring all levels of the wake is properly refined. Furthermore, a symmetric grid was ensured by mirroring the instantaneous iso-volume of the magnitude of the vorticity. The symmetric iso-volume around the wake was refined at two levels. Firstly, the immediate wake behind the cylinder was refined with the finest grid Δ, while further behind the grid was refined at 2Δ. By applying the iso-volume of the magnitude of vorticity, the grid was refined at areas of interest. This approach was more efficient than by manually refining square volumes behind the cylinder as the number of grids in areas not pertinent to the flow field was reduced.

Table 6.2: Domain size for the grid quality analysis

X Front	X Back	Y Left	Y Right	Z Bottom	Z top
$-6.32D$	$34.0D$	$-13.44D$	$13.44D$	$-20D$	$20.32D$

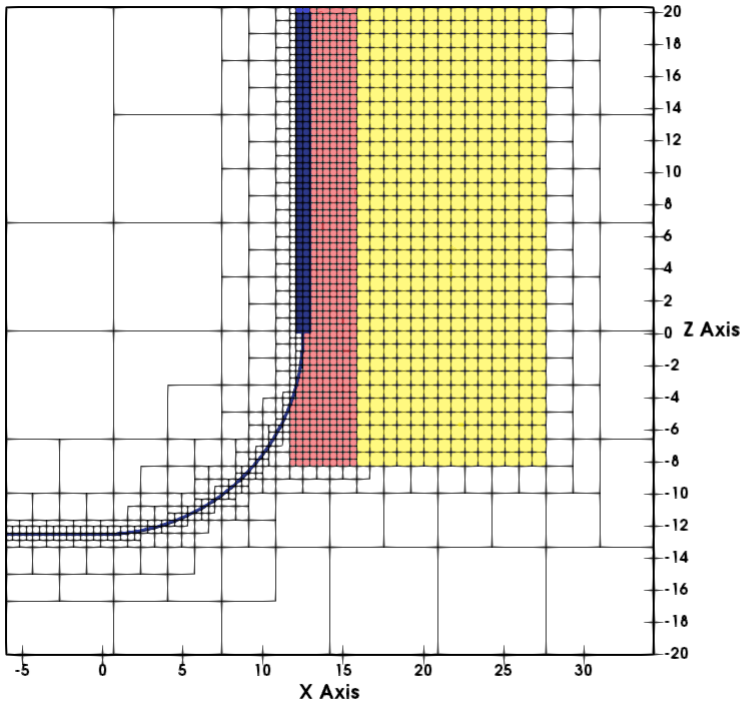

Figure 6.2: Grid refinement domain in the X-Z plane used for all cases in the grid refinement analysis. The colored sections represent the manual refinement. The red sections are refined at Δ and the yellow section refined at 2Δ. The blue sections represents the geometry.

6.3.1 Sampling of the Velocity and Pressure in the Wake

Due to the different aspects in the wake to be profiled, along with uncertainty regarding which cylinder would dominate the grid refinement study, 4 different sampling lines were used. The first three lines were used to investigate the velocity and pressure profiles in the wake of the cylinder. The fourth sampling line was applied in frequency analysis of the cross flow velocity component v. All sampling points were sampled in the $y/D = 0$ plane.

- The first line is sampled at a distance of $0.6d$ away from the small cylinder surface. It is used to compare the velocity and pressure profiles close to the small cylinder surface. The distance from the edge of the cylinder line was chosen due to similar results from previous studies. The vertical sampling line is not used.

- The second sampling line is sampled at a distance of $3d$ away from the small cylinder surface and $0.2D$ away from the large cylinder surface. This sampling line was used to measure the velocity and pressure profiles close to large cylinder surface and to investigate the effect of the step on the velocity and pressure.
- The third sampling line is sampled at a distance of $0.9D$ $(4.5d)$ away from the small cylinder surface and $0.5D$ away from the larger cylinder surface. It was applied for comparison of velocity profiles with previous studies.
- The fourth sampling line is a distance of $3.4D$ $(17d)$ away from small cylinder surface and $3D$ away from the large cylinder surface. It is used in frequency analysis of the cross flow.

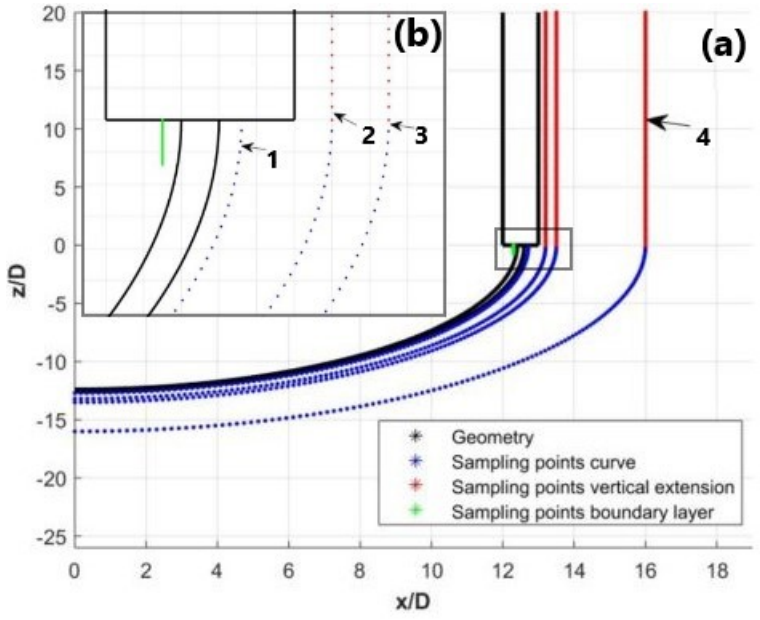

Figure 6.3: Sampling points for the velocities and pressure. The number indicate the sampling lines as described in Section 6.3.1. In the large plot (a), the area around the step is enhanced to further highlight the sampling close to the small cylinder surface (b). The geometry is not to scale.

6.4 Results

The flow was run until fully developed at all simulations. To check if the flow was fully developed, the force in x-direction was plotted in the time domain. From a fully developed state, the simulation was continued for another 100 UT/D. The pressure and velocity was sampled at points in the immediate wake, which is shown in Figure 6.3. The sampling point values and the time averaged values of the velocities and pressure were identified for all grid independence simulations.

Furthermore, the mean drag, root mean square of the lift force and the frequency was found and compared. The drag and lift coefficients were calculated by using Equations 3.10 and 3.11. The projected area was found to be $A_P = 22.80[D^2]$. The forces used in calculation of the forces coefficients were integrated over the body inside the domain.

Table 6.3: Drag and lift coefficients and dominating Strouhal frequencies for the grid independence study. St_1 is the Strouhal frequency in the domain behind the small curved cylinder and St_2 is the Strouhal frequency for the vertical extension.

Case	$C_{D,mean}$	$C_{L,rms}$	$St_1 = f_1 d/U_0$	$St_2 = f_2 D/U_0$
1	0.9788	0.0492	0.114	0.21
2	0.8896	0.0368	0.112	0.2
3	0.9867	0.0467	0.1054	0.199
4	1.1171	0.0679	-	0.19
5	1.6097	0.082	-	0.1

The velocity distributions for the vertical, and horizontal velocity components u and w can be found in Figures 6.4 and 6.5. The coarsest grid shows clear signs of having un-physical properties. The results show clear convergence for values of $\Delta = 0.4$ and smaller. However, it should be noted that the value of the velocities in the vertical extension have a much larger discrepancy in the results than the one behind the curvature. This is most likely a result of the wake dynamics behind the large cylinder affects the flow field more.

The dominating frequencies are for the 3 finest grids mostly stable, with a certain discrepancy in the Strouhal frequencies for the wake behind the small cylinder. For the two coarsest grids, there are just one frequency in which the cross-flow energy is present, which is behind the large cylinder. This implies that the coarsest grids does not accurately represent the flow field around the curvature.

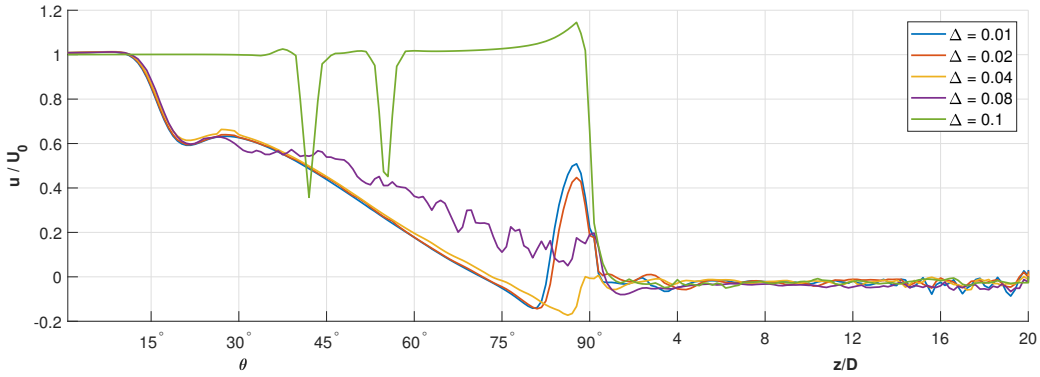

Figure 6.4: Average velocity profile of the horizontal velocity component u, sampled at $R = 13.2D$ i.e. $0.2D$ away from the large diameter cylinder surface ($0.6D$ from the small cylinder surface). The samples are located in the $y/D = 0$ plane along the the curvature from the start of the horizontal extension to the end of the vertical extension.

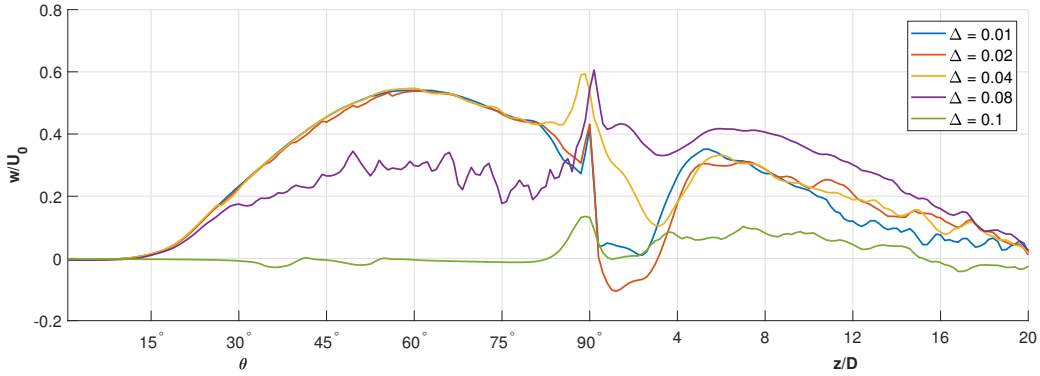

Figure 6.5: Average velocity profile of the vertical velocity component w, sampled at $R = 13.2D$ i.e. $0.2D$ away from the large diameter cylinder surface ($0.6D$ from the small cylinder surface). The samples are located in the $y/D = 0$ plane along the the curvature from the start of the horizontal extension to the end of the vertical extension.

The three finest grids show more or less coherent results at the curved part, with a discrepancy between Case 3 and the two finest grids at around 75 °, where the dip in velocity is not as profound in Case 3 (Figure 6.5) . Furthermore, even though the velocity values in the curved part are mostly identical for the two finest girds, the vertical extensions shows that the velocity profiles differ for all the cases. This can be attributed to the increase in Reynolds number from $Re_d = 120$ at wake behind the small cylinder to $Re_D = 600$ behind the large cylinder. This increase

in Reynolds number increases the disorder in the wake which is one possible explanation for the larger difference in results at the vertical extension.

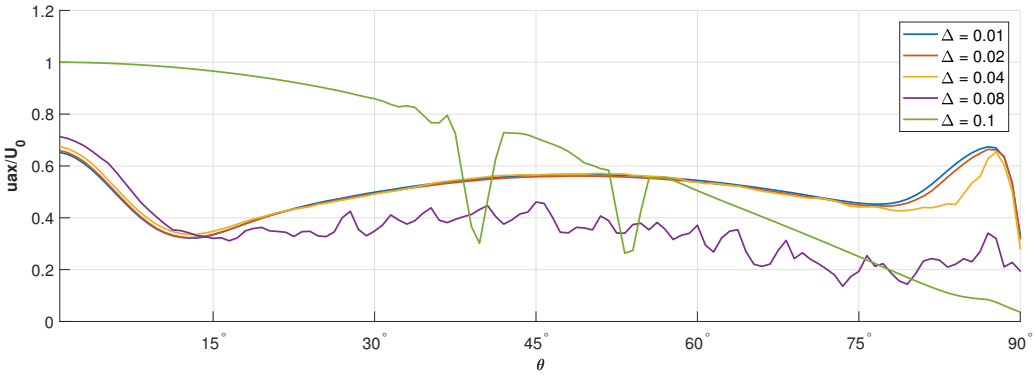

Figure 6.6: Average velocity profile of the axial velocity component u_{ax}, sampled at $R = 12.72D$ i.e. $0.6d$ from the small cylinder surface. The samples are located in the $y/D = 0$ plane along the the curvature from the start of the horizontal extension to the start of the vertical extension.

The axial velocity component close to the small cylinder surface was plotted along the curved part of the cylinder i.e. the wake behind the small cylinder. As displayed in Figure 6.6, the velocity converge for the three finest grid sizes but at the step only the two finest converge. The two coarsest grids show nonphysical values, indicating that the grid size is far too coarse to accurately depict the flow.

The velocity was also sampled at the step to find information about how the velocity components u and w behave in the boundary layer around the step. The velocities in the boundary layer behind the step are displayed in Figures 6.7 and 6.7.

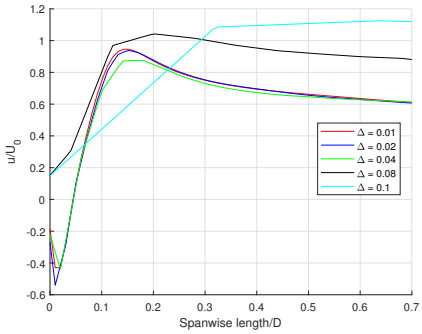

Figure 6.7: Velocity component u in the boundary layer for all five cases investigated in the grid independence study. The velocity was sampled at $y/D = 0, x/D = 12.3$ from $z/D = 0$ to $z?/D = -0.7$

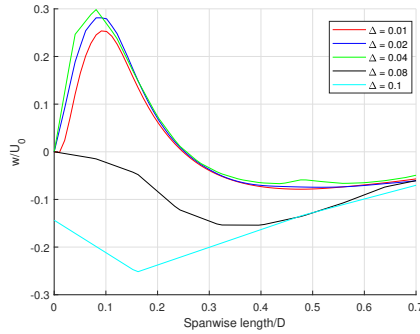

Figure 6.8: Velocity component w in the boundary layer for all five cases investigated in the grid independence study. The velocity was sampled at $y/D = 0, x/D = 12.3$ from $z/D = 0$ to $z?/D = -0.7$

The boundary layer depicted in Figures 6.7 and 6.8 shows that for the u component of the velocity, the results are starting to converge for Case 2. However, the discrepancy in the proximity of the cylinder surface is clear for the vertical velocity component w. For the two coarsest grid the results varies and the solution does not show any sign of converging in the boundary layer.

Accounting for the differences in velocity profiles, both in the boundary at the step and the wake behind the cylinder, the logical choice was to continue with the finest grid size. The increase in total grid points by a factor of 4.4 was not an issue due to sufficient computational resources. Therefore the computations in the parameter study was conducted with the same grid refinement as in Case 1, i.e. $\Delta = 0.01$.

One of the major issues with the choice of grid size is the relative difference in grid size in relation to the smallest cylinder. The relative gridsize is increased from $\Delta = 0.01$ to $\Delta = 0.05$ which is coarse and may affect the results. The initial study of a straight cylinder in horizontal incoming flow investigated in Section 5.2 showed that the development of the boundary layer is well resolved. However, the development of complex flow phenomenon around the step may not be resolved sufficiently. This issue should be investigated more clearly in further studies, and it should be noted that a different grid resolution along the small cylinder surface is a configuration that should be investigated.

Chapter 7

Simulation of Flow around a Concave cylinder with a Change in Diameter

The first simulations conducted in this thesis investigates different configurations of a concave curved cylinder with a change in diameter size at the vertical extension. The initial study had a much larger curvature than previous studies of a concave curved cylinder, thereby making a comparison of velocities and pressure along the curvature difficult. Therefore three geometrical configurations were investigated.

The first configurations has a radius of curvature of $R = 12.5D$ and a change from a small to large diameter at $\alpha = 90^{\circ}$ i.e. at the start of the vertical extension. This configuration is discussed in Section 7.1.

To compare with previous studies, the curvature was reduced from $R = 12.5D$ to $R = 2.5D$, which is equal to $R = 12.5d$. The results from this case is discussed in Section 7.2.

Finally, the diameter configuration was changed, such that the horizontal extension and curved part contained the large diameter cylinder which was reduced to the small cylinder diameter study at the start of the vertical extension. This case had similar configurations to previous studies by Jiang et al. (2018a) and Tian et al. (2017b), which detailed a concave curved cylinder and a straight cylinder with a step. The results of this case is discussed in Section 7.3.

7.1 Concave cylinder with a Radius of Curvature of 12.5 D

The first case investigated is flow around a concave cylinder with a change in diameter at $\alpha = 90°$, i.e. at the start of the vertical extension. The domain size is shown in Table 7.1. The grid was refined around the boundary of the cylinder and further refined in the immediate wake of the cylinder. It was also refined at the edge of the step, to more accurately depict the flow development at the edge of the step.

The grid generated is shown in Figure 6.2 and is the same used in the finest grid size for the grid refinement study (Chapter 6). The grid was manually refined in the immediate wake and at the step where the vertical extension begins. The horizontal extension stretches for 6.32 D, which is equivalent with 31.6 d. Jiang et al. (2018b) concluded that a diameter of 5 D was sufficient but 10 D recommended for the upstream extension of a concave curved cylinder with constant diameter. By both diameter standards, the upstream extension is sufficient. The vertical extension is 20.32 D. In accordance with results from Gallardo et al. (2013), it is long enough to diminish the effects of the free slip boundary condition on the flow at the top surface. The main concern stemming from a too short vertical extension is that the free-slip boundary condition affects the axial flow from the curvature. In a configuration with a change in diameter, the step might actually suppress some of the strong axial flows observed in Jiang et al. (2018a). It is therefore concluded that a vertical extension of 20.32 D is sufficient enough to accurately depict the flow.

Table 7.1: Domain size for the simulation. The grid refinement technique is the same as in the grid independence study and is shown in Figure 6.2.

Δ	X Front	X Back	Y Left	Y Right	Z Bottom	Z top
$0.01D$	$-6.32D$	$34D$	$-13.44D$	$13.44D$	$-20D$	$20.32D$

To measure the velocity and pressure profiles while simultaneously investigating the energy spectrum's of the cross-flow velocity, sampling points for pressure and velocities were put in the domain. The sampling points are the same as for the grid refinement study, described in Section 6.3.1.

7.1.1 Results

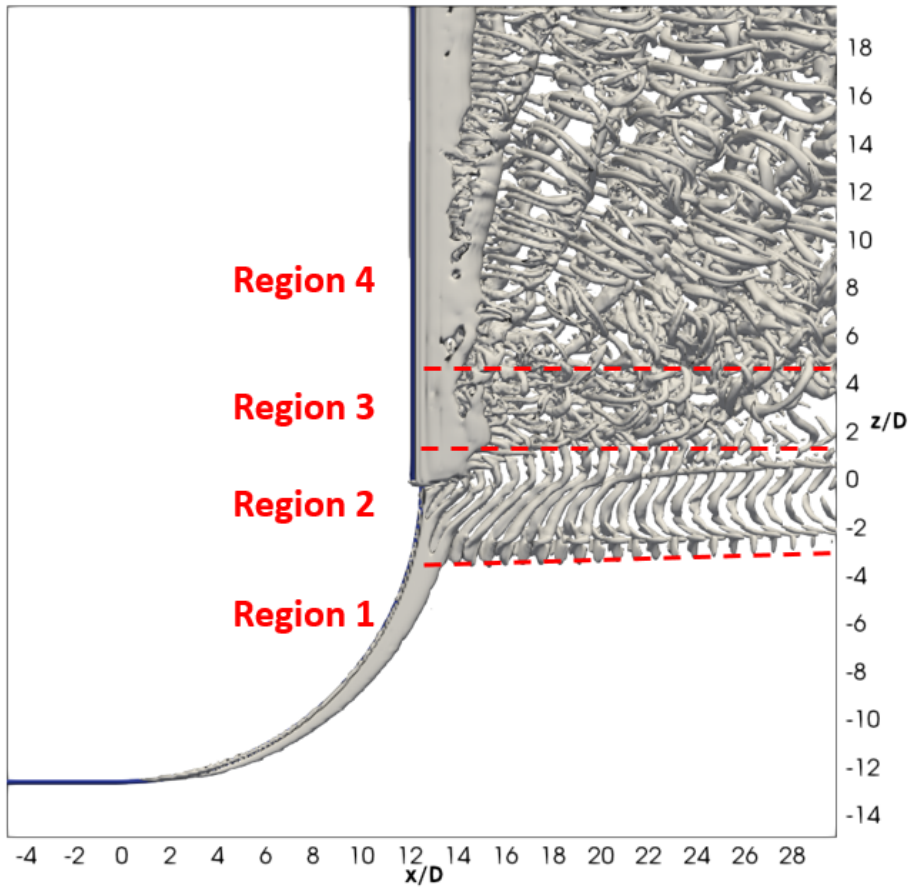

Figure 7.1: Snapshot of the iso-contour for $\lambda_2 = -0.1$ for a fully developed flow. The regimes are numbered from bottom to the top of the flow field and separated by a stippled red line.

Four regimes in the wake of the cylinder were identified and investigated. The first regime is laminar flow from the bottom of the curvature to around 80°. A helical vortex structure is formed along the curvature. The helical vortex structure shows no signs of dislocation. The second regime shows vortices shedding from the small cylinder. Figure 7.1 shows that oblique vortex shedding is occurring in regime 2 where the Reynolds number is $Re_d = 120$. The strong axial flow pushes the vortex structures upward towards the step and large diameter cylinder.

The third regime is the flow in the wake of the step. A indication of upwash from the lower part of the step can be seen. In the third regime, the vortices shed

from the smaller cylinder are moving upwards and interfering with the vortices shed from the large cylinder.

The fourth regime is characterized by vortex shedding from the large diameter cylinder. The vortex shedding is more chaotic, attributed to the five-fold increase in Reynolds number to $Re_D = 600$.

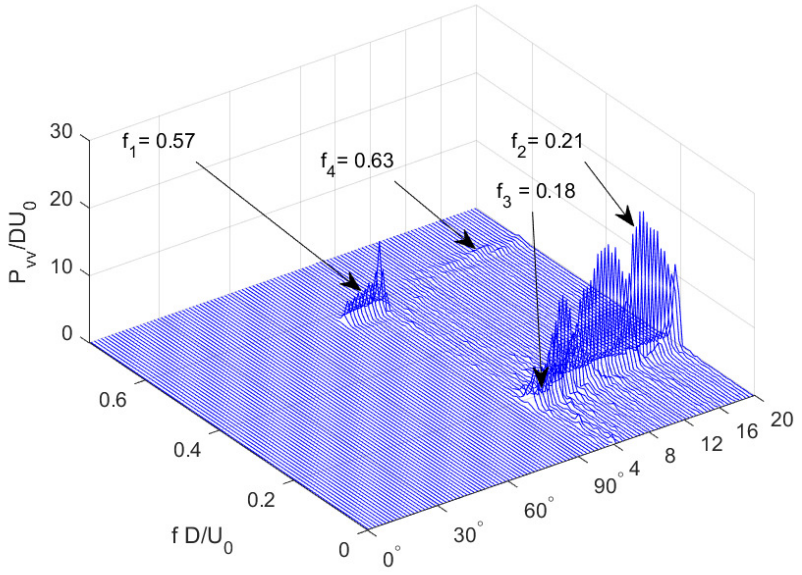

Figure 7.2: Power density spectrum of the wake behind the vertical extension of the top cylinder, measured at a distance of 3.5 D away from the cylinder surface. The text indicates the dominating frequencies at different regions in the simulation.

From Figure 7.2, three distinct frequencies and a harmonic frequency are observed. The first frequency is observed in Region 2, where the vortex shedding is acting with a frequency of $f_1 = 0.57fD/U_0$. From the Strouhal relationship (Equation 3.6), the Strouhal frequency is $St_1 = f_1U_0/d = 0.114$, where $Re_d = 120$. This value is in accordance with the value found in Jiang et al. (2018a), which at Re = 100 was a $St_1 = f_1U_0/d = 0.12$. One of the main differences between the spectrum's is the clear difference is over which lengths the frequency acts. At the case investigated in Jiang et al. (2018a), the upwash frequency acts f_1 is acting from $z/D = 0$ to just bellow $z/D = 10$. However, as can be seen from Figure 7.2, the small cylinder upwash vortex shedding frequency ends at around $z/D = 2$, i.e. $2D$ above the vertical step.

The second dominating frequency occurs in Region 3, and is characterized

by a slightly higher Strouhal frequency $St_2 = f_2 U_0/D = 0.18$. This frequency has similarities with both the N-cell frequency $f_N = 0.1538$ found in Tian et al. (2017b) and the lower frequency band $f_2 = 0.186$ found in Jiang et al. (2018a). The discrepancies in the frequencies are of interest, the introduction of strong vertical flow around the curvature in combination with the introduction of a step may include different vortex shedding frequencies, which may explain the smaller frequency of the vortex shedding at the curved part of the cylinder.

The final frequency identified is $f_4 = 0.63$ and is thought to be a harmonic frequency, as it is about three times larger than the dominating Strouhal frequency $f_2 = 0.21$.

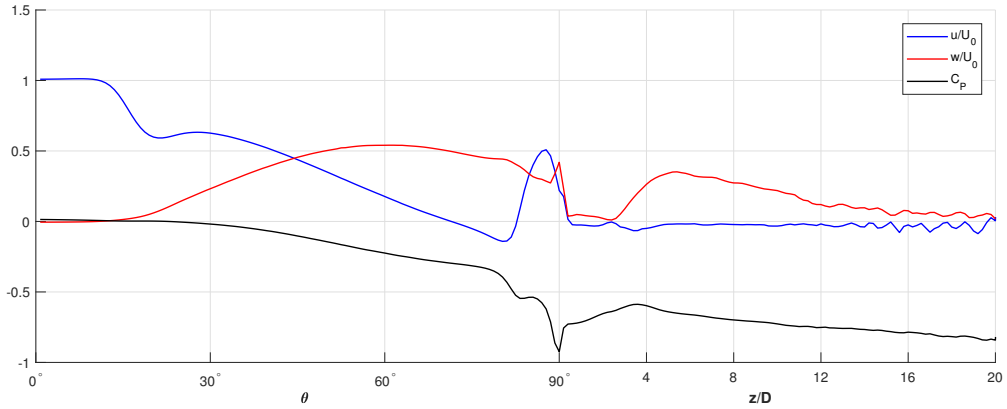

Figure 7.3: Average pressure and velocity profiles, sampled at $R = 13.2D$ i.e. $0.2D$ away from the large diameter cylinder surface ($0.6D$ from the small cylinder surface). The samples are located in the $y/D = 0$ plane along the the curvature from the start of the horizontal extension to at the end of the vertical extension.

From the velocity and pressure profiles in Figure 7.3, a sharp increase in the horizontal velocity u along with a sharp decrease in the pressure coefficient C_P at $\theta = 85°$ coincides with the step. In the vertical extension directly above the step, the horizontal and vertical velocities are more or less zero, which coincides with region 3 in Figure 7.1. Above region 3, there is an increase in the vertical velocity component w. This increase has a peak at $z/D = 6$, before it decreases to zero towards the top of the vertical extension.

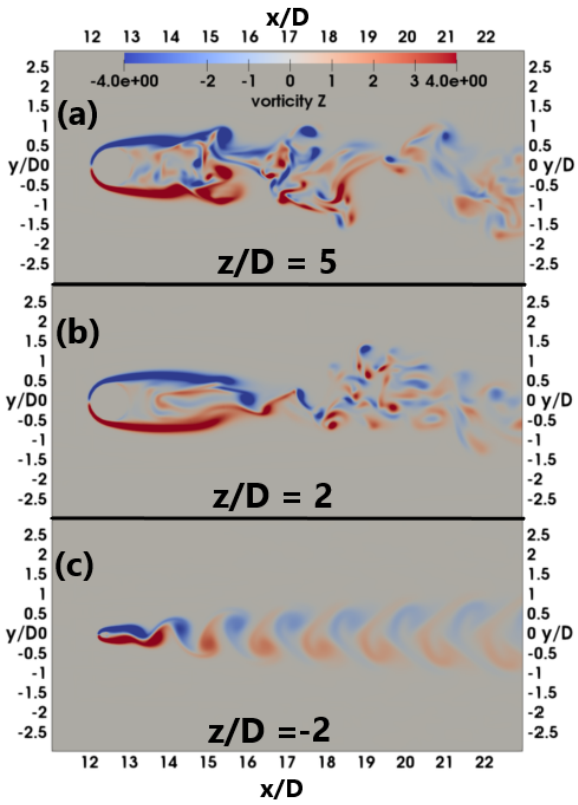

Figure 7.4: Instantaneous vorticity ω_z contour plot in the (x,y) plane. (a) is in the curvature at $z/D = 5$ behind the large diameter cylinder which is in region 4 described in Figure 7.1. Both the small and large cylinder affects the flow field. (b) Same as (a) but at $z/D = 2$ behind the large cylinder on the border line between region 3 and region 2. (c) same as in (a) but at $z/D = -2$ ($\theta = 80°$), which is behind the small diameter cylinder in region 2.

The vorticity contour plot of ω_z in the (x,y) plane is shown in Figure 7.4 for 3 different z-planes. In Figure 7.4 (a), which is in region 4, normal von Karman vortex shedding is observed. Jiang et al. (2017) observed laminar like shear layers behind the vertical extension, which is also the case in Figure 7.4 (a) and (b). Furthermore, this shear layer is also present in Figure 7.4 (c). Considering the low Reynolds number for the small diameter cylinder ($Re_d = 120$) this is assumed to be the laminar shear layer.

7.2 Reduction of Curvature to 2.5 D

To compare how the influence of a step affects the axial flow and vortex shedding, a concave cylinder with a bit smaller curvature was investigated. The radius of curvature was reduced by a factor of five from $12.5D$ to $2.5D$, which is equivalent to the radius of 12.5 d used in Jiang et al. (2018a).

To analyze the spectrum of frequencies in the wake as well as the velocity and pressure profiles in the immediate wake, sampling points were put at positions of interest. The sampling points can be seen in Figure 7.5.

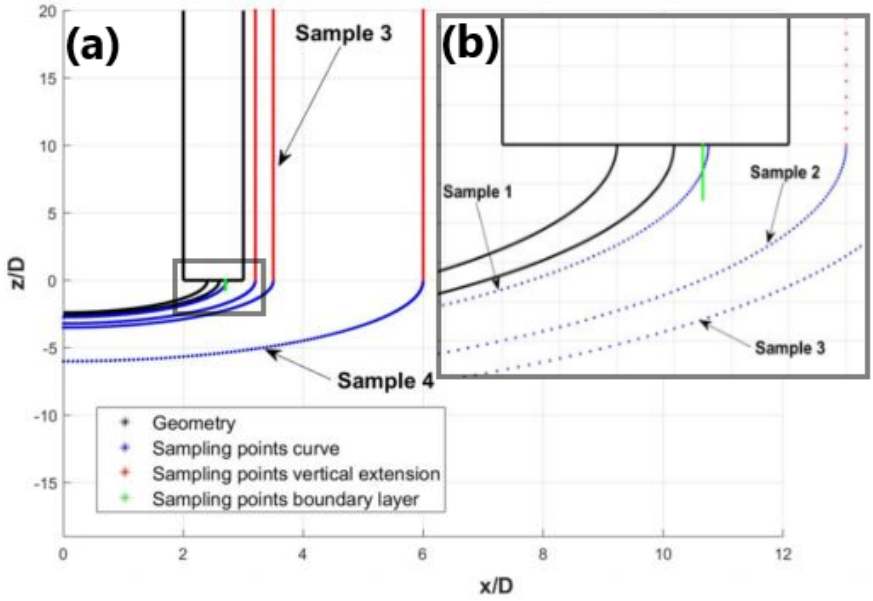

Figure 7.5: (a) Sampling points for the small curvature geometry. (b) Sampling points enhanced around the immediate vicinity of the step. The simulation was run with the sampling points for 100 TU_0/D, with a sampling frequency of 100 measurements per time unit TU_0/D. The geometry is not to scale.

The two sampling lines closest to the small curvature was used to measure the velocity and pressure profiles in the immediate wake of the small cylinder surface. The two further down in the wake was conducted to analyze the wake behind the largest diameter cylinder as well as for frequency analysis of the cross flow velocity v.

7.2.1 Results

The λ_2 iso-contours in Figure 7.6 the shows that vortices are shed from the large diameter cylinder, while there are no clear signs of vortex shedding from the curved extension of the small diameter cylinder. Furthermore, there are clear indications of upwash from the step, with vortex structures being formed regularly from $z/D = 2$ and upwards. The strong vertical velocity is affecting the wake and pushing the flow upwards. It is also reasonable to assume the flow is also pushed upwards by the step.

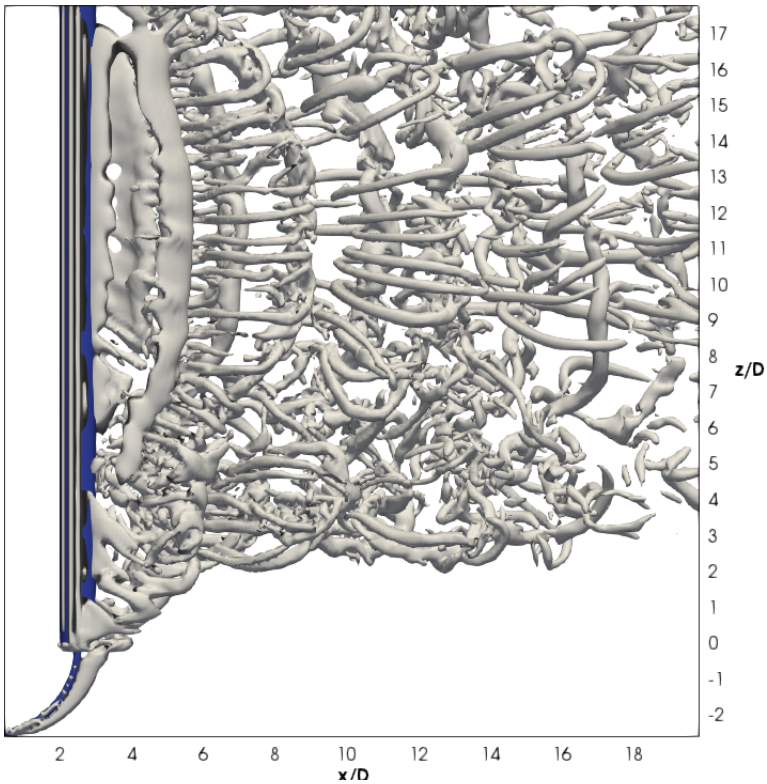

Figure 7.6: Snapshot of the iso-contour for $\lambda_2 = -0.5$ for the small curvature.

The maximal vertical velocity in the small curvature is significantly higher than for the larger curvature, with $w_{max} = 0.94U_0$ for the small curvature case and $w_{max} = 0.64U_0$ for the larger curvature case. Compared to results from Miliou et al. (2007), the maximum vertical velocity along the curvature for a concave cylinder without a step at $Re = 100$ was $w_{max} = 0.77$.

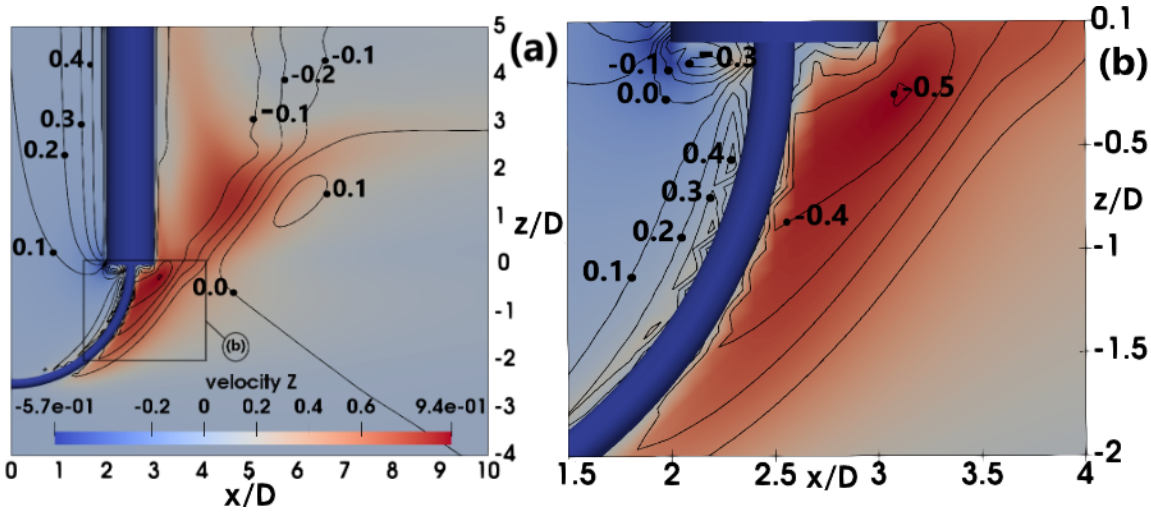

Figure 7.7: Illustration of the time averaged vertical velocity component w and contour lines of the time averaged pressure. (a) is in the wake and (b) is around the step. The black lines are contour lines of the pressure with numbers indicating the pressure value along the contour line. The velocity and pressure average was sampled for 100 TU_0/D.

The dominating narrow-band frequency is at $St_2 = 0.2$ from $z/D = 6$ to $z/D = 18$. At the downwards edge of the extension the there are no signs of energy indicating no vortex shedding below $z/D = 3$. This is in agreement with the λ_2 plot in Figure 7.6, which does not show any vortex structures below the $Z/D = 3$. From $z/D = 3$ to $z/D = 6$, the dominating frequency is slightly lower, at $St_1 = 0.17$.

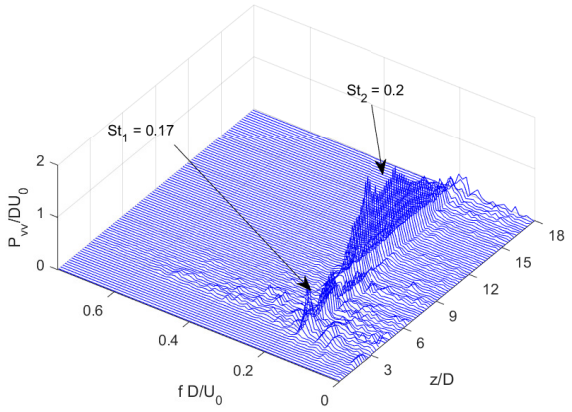

Figure 7.8: Power spectrum density distribution of the cross-flow velocity v along a sampling $4D$ away from the vertical extension in the symmetry plan ($y/D = 0$)

The streamlines in Figure 7.9 indicate that a junction vortex is formed in front of the small cylinder at the step. There is also indications of recirculation behind the small cylinder surface and right above the backward edge of the cylinder. There is also a helical vortex structure forming behind the curvature of the small cylinder. The helical vortex shows no indication of shedding before meeting the the step.

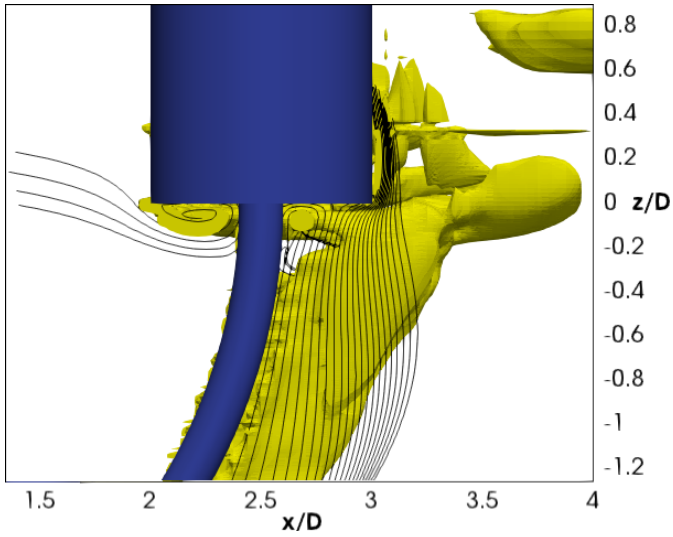

Figure 7.9: Iso-contour of $\lambda_2 = -1$ around the step of the small cylinder. Streamlines of the velocity in the $y/D = 0$ plane is also displayed. The streamlines indicate the formation of a junction vortex at the step just ahead of the the small cylinder surface.

The boundary layer in the $y/D = 0.25$, $x/D = 0$ plane was investigated by putting a sampling line from the step to a position of $z/D = 1.2$ bellow the cylinder surface (Figure 7.5). In Figure 7.9 the formation of vortices along the front end of the the cylinder is observable.

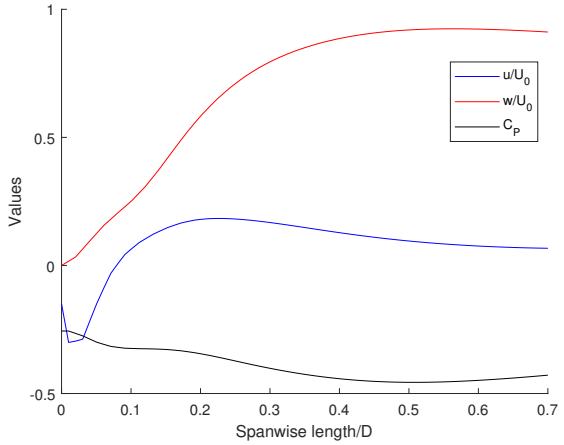

Figure 7.10: Pressure and velocity profiles from the bottom of the step $z/D = 0$ to $z/D = -0.7$. The the velocities and pressure was sampled in the $y/D = 0$, $x/D = 2.70$ plane, i.e. $0.1D$ behind the small cylinder surface.

The velocity and pressure was sampled at a distance of $0.5d$ away from the small cylinder along the curvature. The horizontal velocity component u is lower than the inflow velocity U_0 at at the bottom of the horizontal extension, due to the influence of the cylinder on the flow creating a boundary layer at the bottom. The axial and horizontal velocity, decreases from Point A to Point B, while the vertical velocity component increases monotonously. At Point B, the vertical velocity experiences a sharper increase and increases until Point C. The horizontal velocity experiences a sleight increase at around $35°$ in which afterwards it decreases until Point C. From Point C at approximately $80°$, the a horizontal velocity has a sharp increase until $85°$ where it has a drastic decrease The axial and vertical velocity components both experiences a sharp decrease from point C to the start of the step.

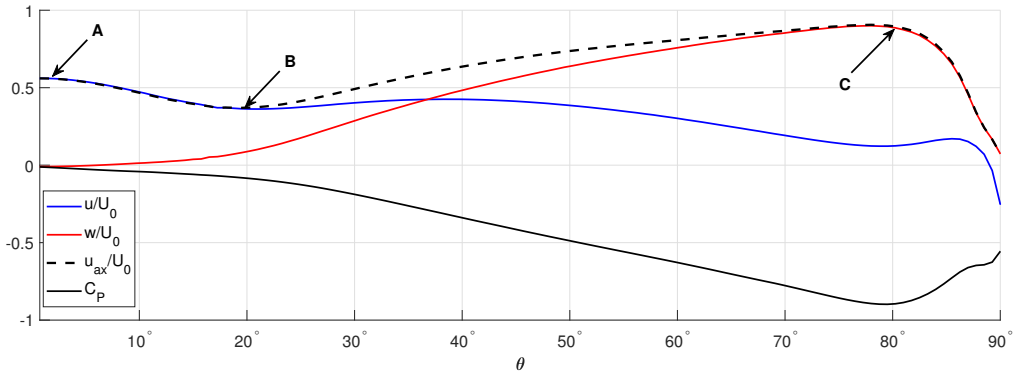

Figure 7.11: Velocity and pressure profiles along the curved part of the cylinder, measured $0.5d$ away from the cylinder surface. The sampling points are located in the $y/D = 0$ plane. The arrows represents points of interest on the curve.

The pressure decreases linearly from Point A to Point B, and at Point B it experiences a sharp linear increase until Point C, where it increases towards the step. The pressure and velocity profiles indicates that the introduction of a step has a profound influence on the pressure and velocity distribution close to the step. When comparing the values with those found in Jiang et al. (2018a), it seems reasonable to assume the introduction of a step influences the flow field from around $60° - 70°$.

7.3 Concave Cylinder with a Diameter Reduction at the Vertical Extension

A slight problem arising from the previous cases in this chapter was the difficulty comparing the cases with previous studies, in particular Jiang et al. (2018a) and Tian et al. (2017b). To further investigate the correlation between flow phenomenons and their relation to geometries, a simulation with large diameter D curved concave cylinder with a diameter reduction at the start of the vertical extension to $d = 0.2D$. The same grid resolution was applied and using the magnitude of the vorticity from previous cases as well as some manual grid refinement in the wake of the large diameter cylinder at the start of the curvature. The grid along with the geometry is displayed in Figure 7.12 and the domain size and finest grid resolution in Table 7.2.

A major advantage of this configuration is that it combines the curvature ratio of $12.5D$ along the curvature similar to Jiang et al. (2018a) with a change in step at $z/D = 0$, which, excluding the diameter ratio is similar to Tian et al. (2017b).

Although direct comparisons are not possible, qualitative comparisons of how the geometry and Reynolds number affect the fluid flow can be made.

Table 7.2: Domain size and grid refinement for the concave cylinder with a diameter reduction at $z/D = 0$

Δ	X Front	X Back	Y Right	Y Left	Z Bottom	Z top
$0.01D$	$-13.44D$	$40.32D$	$-13.44D$	$13.44D$	$-20.00D$	$20.32D$

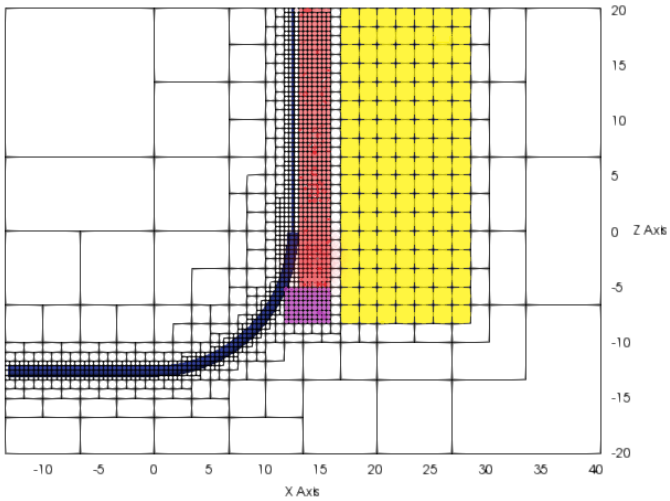

Figure 7.12: Domain and grid resolution for the step-cylinder case. The red colored cells represent grid refinement using vorticity from a previous simulation with a resolution equal to the finest grid resolution of the simulation i.e. Δ. The violet colored sections represent a manual square grid refinement equal to the finest grid resolution Δ. The yellow section represents a grid resolution of 4Δ using the vorticity of a previous simulation to refine the wake. The blue sections represent the geometry of the cylinder in the domain.

7.3.1 Results

The snapshot of the iso-contour for λ_2 in figure 7.13 and the power density spectrum of the cross flow velocity v in Figure 7.14 was investigated for the simulation. Vortex shedding starts to materialize at $z/D = -4$, or at a approximately 70° from the start of the curvature. The vortices are shed with a frequency of $fD/U_0 = 0.12$, which is the same frequency values identified in the wake of the curvature for a cylinder without a change in diameter in Jiang et al. (2018a). The frequency range for frequency domain 1 is from $z/D = -5.5$ to $z/D = 0$.

As can be seen in Figure 7.13, there are 4 distinct regions in which the dif-

ferent vortex regimes act. Region 1 acts from the start of the cylinder curvature to $z/D = -4.5$ or around $70°$. It is characterized by no signs of vortex shedding and a development of a strong axial flow. Region 2 acts from $z/D = -4.5$ until the change in diameter at $z/D = 0$. It is characterized by vortex shedding with a frequency lower than the Strouhal shedding frequency, and a strong negative pressure field sucking vortices from Region 3 and 4 downwards. In region 3, signs of a N-cell vortex shedding regime characterized by Tian et al. (2017b) is evident. Downwash is clearly seen, as the vortices are observed being dragged downwards and also has an oblique shedding angle $\theta_s = 14°$. Region 3 acts from the origin until approximately $z/D = 4$. Region 4 has an oblique vortex shedding regime, with a Strouhal frequency coinciding with theoretical values obtained by Williamson (1989) and Roshko (1954a). Region 4 starts at $z/D = 4$ until the end of the simulation domain at $z/D = 20$.

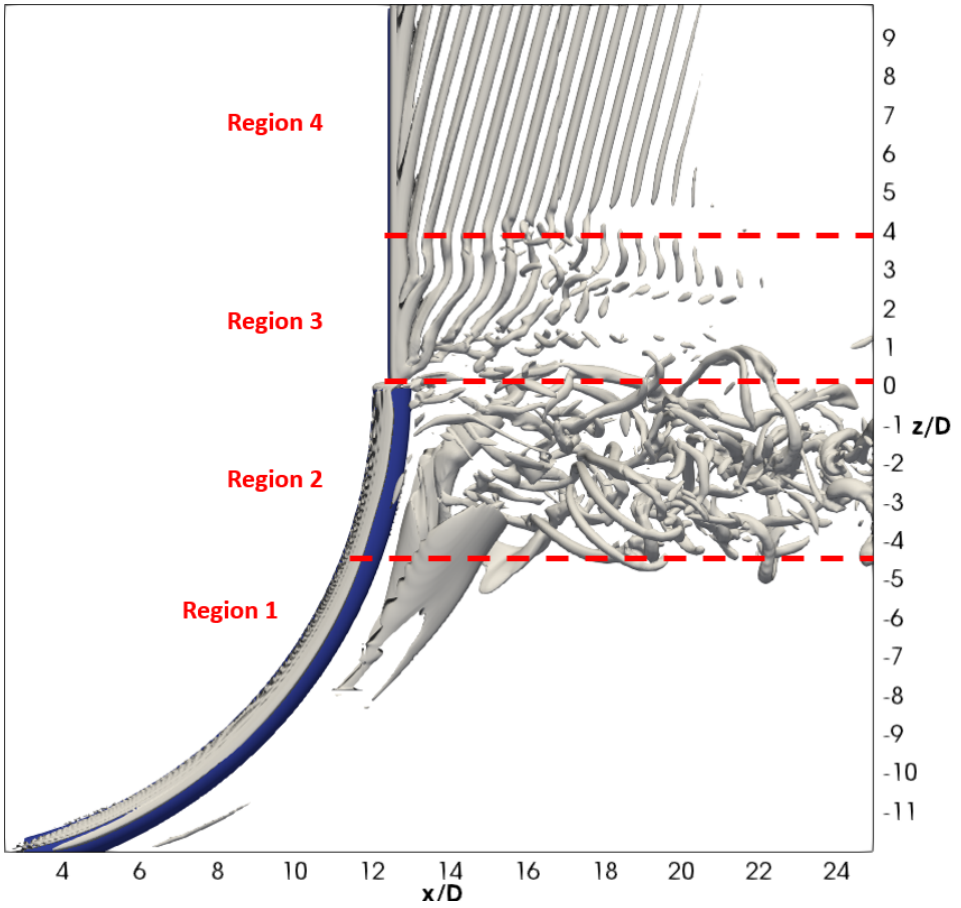

Figure 7.13: Snapshot of the iso-contour for $\lambda_2 = -1$ for a fully developed flow. The red dotted lines indicates regions in which different vortex shedding regimes occur.

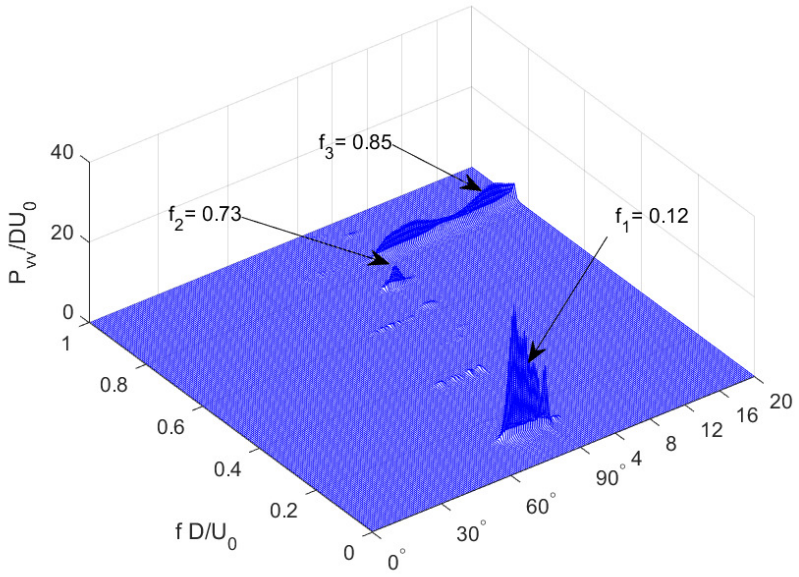

Figure 7.14: Power density spectrum of the cross flow velocity, sampled at a distance of 3.5 D behind the cylinder in the $y/D = 0$ plane. The text indicates the dominating frequencies at different regions in the simulation.

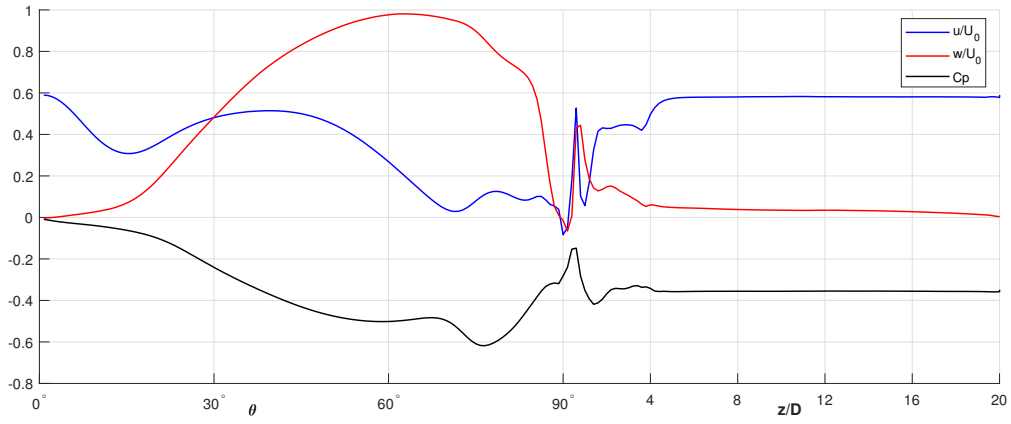

Figure 7.15: Average pressure and velocity profiles, sampled at $R = 13.2D$ i.e. $0.2D$ away from the large diameter cylinder surface ($0.6D$ from the small cylinder surface). The samples are located in the $y/D = 0$ plane along the the curvature from the start of the horizontal extension to at the end of the vertical extension.

The introduction of the curvature induces a strong vertical velocity, which peaks at $\theta = 60°$ before it experiences a sharp decline before the step and a sharp increase after the step. If the velocity and pressure profiles are examined together with the iso-contours of λ_2 in Figure 7.13, it is clear that the diameter reduction at the start of the vertical extension suppresses the vertical flow. In the straight cylinder case with a diameter reduction, the flow was pushed downwards towards the large cylinder wake. This reduction in velocity divides the vortex shedding from the large and small diameter cylinder along the a line parallel to the step (red dotted line between region 2 and 3 in Figure 7.13).

The vortex shedding from the small cylinder shows that the vortex shedding is oblique and has an oblique shedding angle of $14°$. The frequency of vortex shedding, as displayed in Figure 7.14, for the small cylinder is the same as empirical values for the Strouhal number (Williamson (1989) and Roshko (1954a) (numerical values in Table 5.2). Of importance is the drastic difference in the vortex shedding frequency behind the the large cylinder diameter for the present study and the empirical values. The large drop in frequency is due to the influence of the curvature, as the vortex shedding frequency for the present case matches with values from Jiang et al. (2018a).

Table 7.3: Strouhal numbers for the case with oblique shedding angles. (It should be noted that St'_{θ_S} is based on the small cylinder diameter d and St_{θ_L} is based on the large cylinder diameter D)

-	θ_L	θ_S	St'_{θ_S}	St_{θ_L}	St_S	St_L
Present	-	14 °	0.17	0.12	0.175	0.12
Equation 5.1	...	...	...	...	0.176	0.228
Equation 5.2	...	...	...	...	0.175	0.205

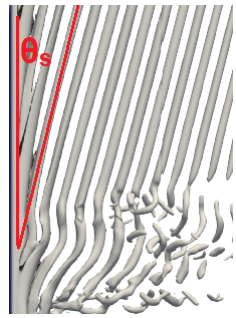

Figure 7.16: Identification of the oblique vortex shedding angle.

Figure 7.17 shows the streamlines and λ_2 around the step. On the back side,

the formation of a junction vortex is visible from the iso-volume of λ_2 and the streamlines indicate a recirculation zone ahead of the step.

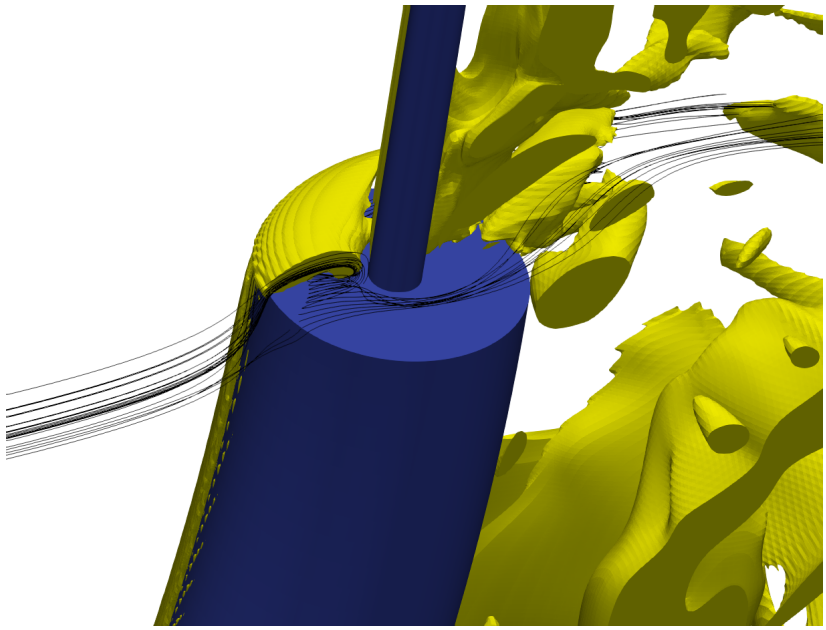

Figure 7.17: Streamlines of the velocity around the step for concave cylinder with a diameter reduction at the vertical extension. Iso-volume of $\lambda_2 = -0.1$ is shown in yellow color, indicating a junction vortex at the step. The streamlines ahead of the small diameter cylinder indicate the formation of a junction vortex.

The vorticity ω_z in the (x,y) plane for different Z/D values is shown in Figure 7.18. In Figure 7.18 (a), there is regular von Karman vortex shedding behind the small cylinder, which coincides with λ_2 values at region 4 in Figure 7.13. In Figure 7.18 (b), there is vortex shedding is more unsteady, and the wake field is larger in the y-direction behind the cylinder. Figure 7.18 (c), shows the wake behind the curved large diameter cylinder at $z/D = -2$ or $\theta = 80°$. Vortices are shed from the large cylinder, but the wake behind the cylinder is much larger compared to the results from the large diameter vertical extension in Figure 7.18 (a). By comparing the wake of the small diameter cylinder at the vertical extension and in the curved part, the wake is considerably larger at the curved part than at the vertical extension. For the small diameter cylinder, the wake at $x/D = 22$ is two times wider in the curvature than at the vertical extension. For the large cylinder, the wake at $x/D = 22$ is also about two times larger for the curved part than for the vertical extension. A possible influence on the wake is the can be the introduction of the step. Results from simulation around a straight step cylinder

with a diameter ratio of $D/d = 2$ by Tian et al. (2019) at $Re_D = 3900$ showed that the step influenced the wake, having wider wake in the area influenced by the step (N-cell area). Tian et al. (2019) suggested that the wider wake might be caused by vortex dislocations. However, the difference in diameter ratio and Reynolds number makes it difficult to suggest with any certainty how much the step influences the width of the wake in this case.

It therefore reasonable to suggest that both the curvature and change in diameter affects the width of the wake.

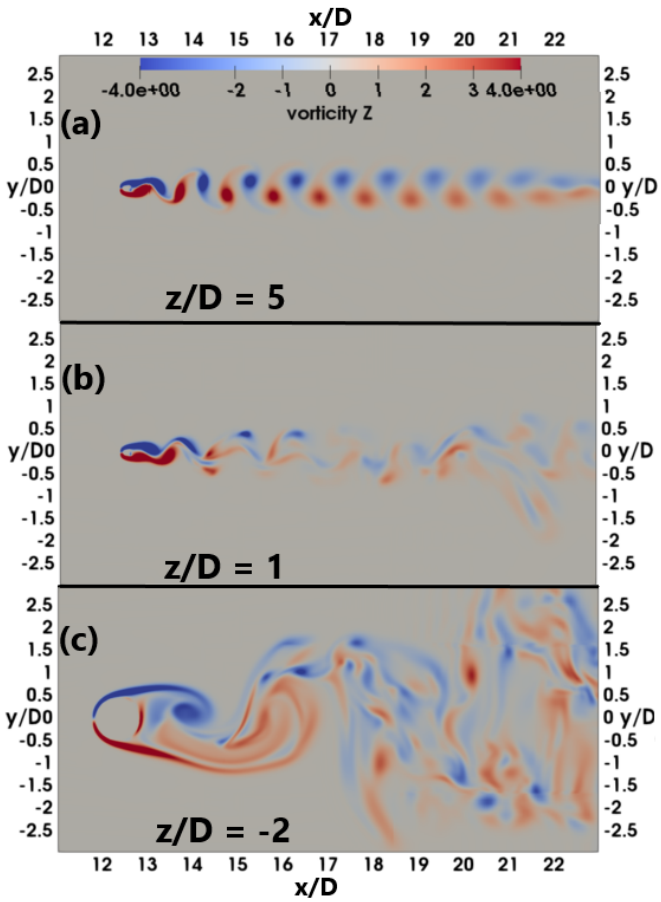

Figure 7.18: Instantaneous vorticity ω_z contour plot in the (x,y) plane. (a) is in the curvature at $z/D = 5$ behind the small diameter cylinder is in region 4 described in Figure 7.13. Both the small and large cylinder affects the flow field. (b) Same as (a) but at $z/D = 1$ behind the small cylinder in region 3. (c) same as in (a) but at $z/D = -6$, $\theta = 80°$ which is behind the large diameter cylinder in region 2.

At the curved part of the vorticity ω_z contour plot in Figure 7.18 (c), the lam-

inar like shear layer observed by Jiang et al. (2017), is much smaller and much more distorted than was the case for the wake behind the large diameter vertical extension (Figure 7.4 (a) and (b)). Following the results from this study and Jiang et al. (2017), the curvature as well as the Reynolds number have an influence on the shear layers behind the cylinder. Results from Tian et al. (2019) did not show any drastic changes in the shear layer in the wake influenced by the step, suggesting that this phenomenon is not affected by the step.

7.3.2 Discussion of results

By changing the diameter of the curvature and vertical extension to mirror the previous study, i.e. a large cylinder horizontal extension and curvature, small diameter vertical extension, some notable differences and similarities was observed. The simulation with an increase in diameter at the vertical extension from Section 7.1 is named Case A and the simulation with the decrease in diameter at the vertical extension from Section (7.3) is named Case B.

- The vortex shedding behind the curvature in Case B is not being pushed upwards in the vertical direction, but rather sheds in the horizontal direction with no oblique shedding angle. In case A the step influences the flow and pushes vortex shedding from the large diameter cylinder upwards.
- The vortices in case B which are shed from the vertical extension has an oblique angle to the vertical cylinder, which does not occur when the vertical extension has the large diameter D. Having a stronger pressure field in the top half of the curvature than case A has may explain why the vortex shedding is oblique in Case B. The negative pressure fields sucks the vortices downwards and creates an oblique vortex shedding angle.
- In case B, the vertical velocity component in the wake of the vertical extension is weaker than in case A. The introduction of a step, in which pushes the flow downwards may counter the vertical flow induced by the curvature. However, the vertical flow is significantly stronger behind the curvature in case B.
- In both cases, following the vorticity contour plots of ω_z in Figures 7.4 (A) and 7.18 (B), there is a clear indication that the wake behind the curvature is larger than at the vertical extension. This is true for both the small and large diameter cylinders.
- In the wake directly behind the step, there is a vortex shedding frequency in between the high frequency vortex shedding behind the vertical extension

and the low frequency vortex shedding behind the curve. This frequency is characterized by being slightly lower than the vortex shedding Strouhal frequency. This applies for both cases.

- By comparing the velocity and pressure profiles of both cases (Figures 7.3 (A) and 7.15 (B)), there are general trends which applies for both cases. There is a decrease in the horizontal velocity component u and a dip at around $\theta = 20°$. The vertical velocity component w is increasing in magnitude along the curvature to a maximum around $\theta = 65°$. Furthermore, there is a peak in vertical velocity at the step, in case A it is just before and in case B just after the step. The horizontal velocity at the step also experiences a sharp increase in magnitude.

- The velocity and pressure profiles have differences which should also be noted. In regards to the pressure, the pressure has its largest magnitude at the step for case A, while it decreases in magnitude for case B. The drop in the magnitude for the vertical velocity is much more sudden and drastic for case B than for case A. The vertical velocity also has a sharp increase in the vertical extension for case A, while it is approximately zero for case B. The horizontal velocity component u in the vertical extension is at a negative value just below zero for case A, while it is about 0.6 U_0 for case B. In the wake at A, $0.2D$ from the large cylinder surface there is backflow while at the same point in B the wake is influenced by the cylinder decreasing the horizontal velocity u.

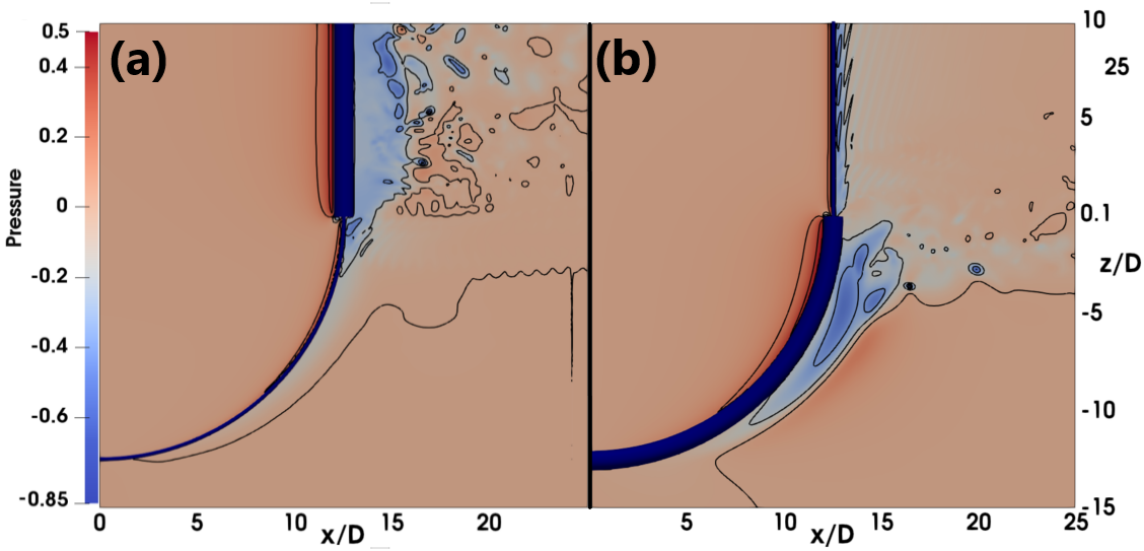

Figure 7.19: (a) instantaneous pressure field for Case A. (b) instantaneous pressure field for Case B. For both cases iso-contour lines of the pressure is also plotted.

Chapter 8

Parameter Study

The main goal of this thesis is to investigate how the introduction of a change in diameter affects fluid flow around a concave cylinder. To start, the parameters in question were the difference in diameter D/d, the angle of the step α, the direction and magnitude of the incoming flow U_0 and the Reynolds number. As previously mentioned, the ratio of diameters was chosen to be $D/d = 5$, which is based on the ratio most commonly used in ocean engineering. The flow direction was decided to be in the horizontal direction.

The variables to be considered was therefore the angle of the step α and the Reynolds number Re. The Reynolds number for the previous cases conducted in this thesis had been set to $Re_D = 600$. In light of the previous cases, the Reynolds number was kept at $Re_D = 600$ for the parameter study. By having the Reynolds number at a relatively high value, the flow and how it transitions from laminar to transitional to turbulent along the geometry could be investigated.

By setting all other parameters to constant values, this parameter study only concerns itself with the angle of the step α.

To investigate how the parameters affect the flow field and forces, certain variables were investigated and the flow field was plotted. The studies done in the previous part of this thesis serves as a background and comparison cases for the parameter study. Moreover, the flow phenomenons identified in the previous cases are applied as a comparison values. Vortex structures and recirculation zones are indicators about how the geometric configurations affect the fluid flow and therefore a detailed investigation was conducted for those flow phenomenons.

Table 8.1: Description of the different cases in the parameter study with computational information.

Case	α	Grid cells	Grid points
1	$0°$	9236	684.28 million
2	$15°$	8558	634.05 million
3	$30°$	6692	496.24 million
4	$45°$	6464	478.90 million
5	$60°$	6240	462.30 million
6	$70°$	5742	425.41 million
7	$75°$	5724	424.08 million
8	$80°$	5724	424.08 million
9	$85°$	5712	423.19 million
10	$90°$	8614	638.19 million

From Table 8.1 there is a marked difference in grid points between case 9 and 10 is more than 200 million number gird points. The reason for the discrepancy is due to the different grid refinement techniques used in the different simulations. In case 9 the use of vorticity in the wake to refine the plot was used, while in case 10 the use of square grid refinement blocks. As illustrated by the large increase in grid points, the block refinement technique is quite expensive and refines areas not necessary important for the simulation. Following this reasoning, the use of vorticity to define which areas in the wake to refine was applied in the parameter study.

8.1 Results

All simulations were run for 200 seconds and the instantaneous contours of the pressure and velocity components were visualized. Furthermore, the time averaged velocity and pressure profiles were plotted in the wake of the cylinder at the $y/D = 0$ plane. The velocity and pressure profiles were used to investigate velocity and pressure in the wake of the cylinder as well as the energy density spectrum of the cross flow velocity. The velocity and pressure profiles were time averaged for 100 seconds after the flow was deemed to be fully developed. The sampling interval was 100 samples per second. The position and application of the sampling points were the same as those described in Section 6.3.1.

For the first five cases, the velocities in the horizontal and vertical directions shows distinct changes in magnitude at the respective changes in diameter. The first case, with a change in diameter directly at the start of the curvature shows a similar behaviour as the horizontal cylinder with a change i diameter described

in Section 5.2. In the wake directly behind the step, there is a marked increase the horizontal velocity component u. The pressure drops and there is a negative vertical velocity directly behind the step. Furthermore, the behavior along the curvature resembles previous studies on a concave curved cylinder such as Jiang et al. (2018a). Of interest is the sharp increase in the horizontal velocity at 70° for $\alpha = 0°$ and $\alpha = 15°$. The increase in horizontal velocity coincides with a minor jump in the vertical velocity component. This jump may be attributed to the strong axial velocity induced by the curvature and is similar to flow around a concave cylinder at $Re_D = 500$ investigated by Jiang et al. (2018a). The introduction of vortex shedding at $z/D = -4$ may influence the flow in horizontal direction, creating a upwash directly behind the cylinder.

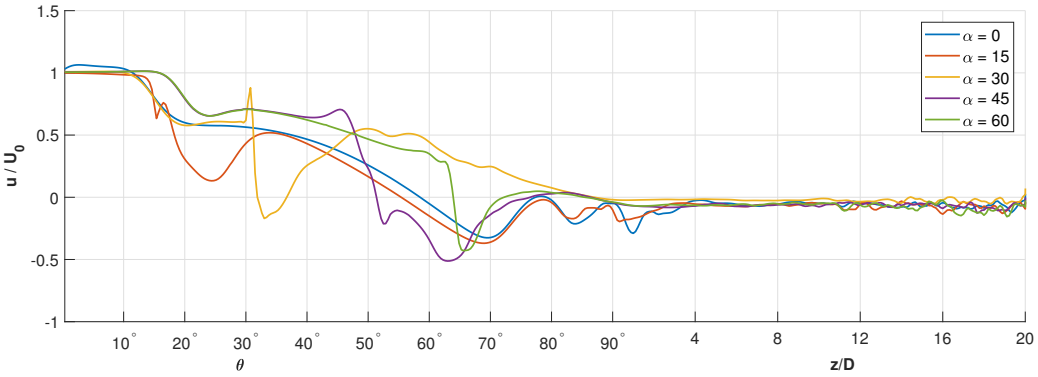

Figure 8.1: Velocity profiles of the average horizontal velocity for the first five cases ($\alpha = [0°, 15°, 30°, 45°, 60°]$). The velocities have been sampled at a distance of $0.2D$ away from the large cylinder surface ($0.6D$ away from small cylinder) in the $y/D = 0$ plane.

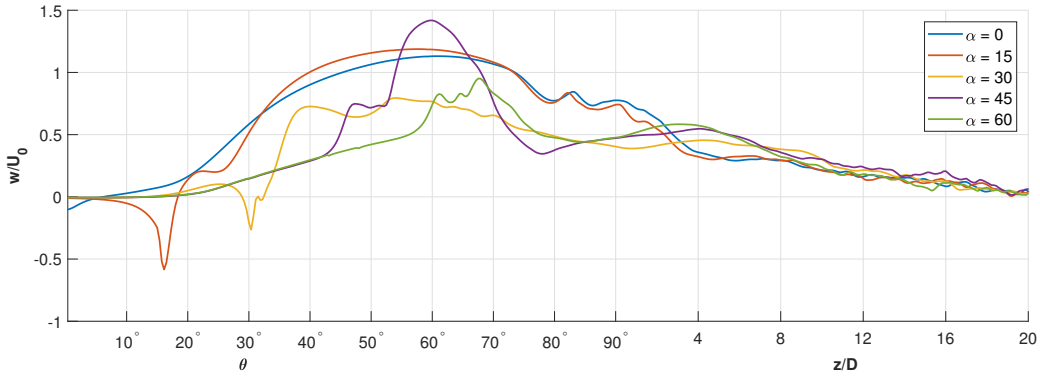

Figure 8.2: Velocity profiles of the average vertical velocity for the first five cases ($\alpha = [0°, 15°, 30°, 45°, 60°]$). The velocities have been sampled at a distance of $0.2D$ away from the large cylinder surface ($0.6D$ away from small cylinder) in the $y/D = 0$ plane.

For the last five cases, ranging from $\alpha = 70°$ to $\alpha = 90°$, some trends are apparent. There is a sharp increase in magnitude for the horizontal velocity component u near the step. This increase in magnitude near the step is also true for the vertical velocity component w.

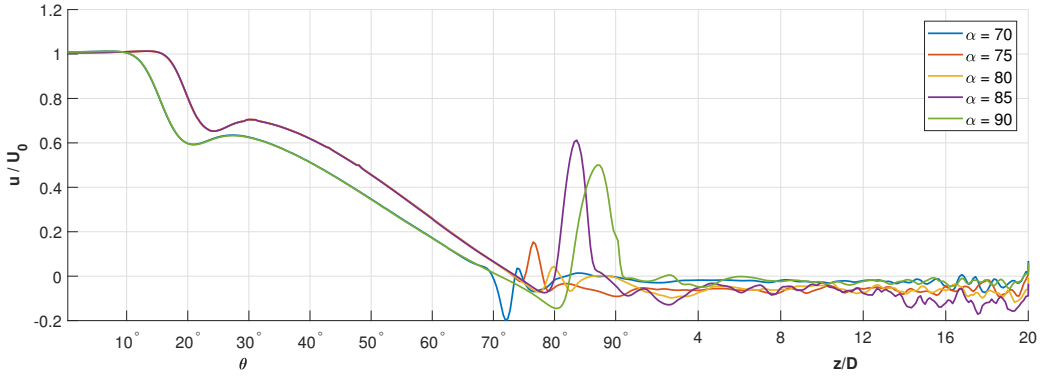

Figure 8.3: Velocity profiles of the average horizontal velocity for the last five cases ($\alpha = [70°, 75°, 80°, 85°, 90°]$). The velocities have been sampled at a distance of $0.2D$ away from the large cylinder surface ($0.6D$ away from small cylinder) in the $y/D = 0$ plane.

For case 6, 7 and 8, the there are two peaks in the vertical velocity (Figure 8.4). This is also true for case 5 in (Figure 8.2). The first peak is directly at the step and the second at angle just above the step. In the last two cases 9 and 10, the w component peaks at around $\theta = 60°$ followed by a drop in the velocity

around $5° - 7°$ ahead of the step. The corresponding peak in velocity at the step for case 9 and 10 restores the w component to the value it had before the drop. The horizontal velocity component u has a large peak just ahead of the step (Figure 8.3). This peak is higher than for the cases with a change in diameter at a lower angle α.

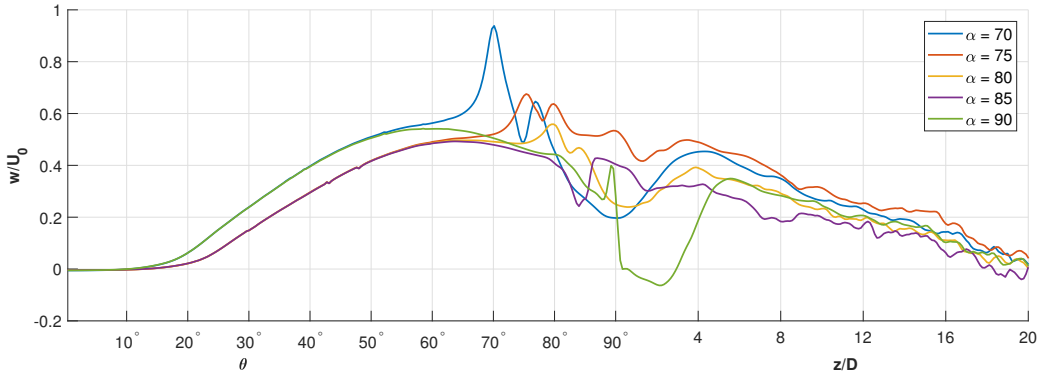

Figure 8.4: Velocity profiles of the average vertical velocity for the last five five cases ($\alpha = [70°, 75°, 80°, 85°, 90°]$). The velocities have been sampled at a distance of $0.2D$ away from the large cylinder surface ($0.6D$ away from small cylinder) in the $y/D = 0$ plane.

For the first five cases, the pressure profile has a distinct drop in pressure at the step, while for $\alpha = 15°$, $\alpha = 45°$ and $\alpha = 60°$ there is a peak in pressure directly behind the step. This drop and increase in the pressure coincides with the formation of a recirculation zone, which is investigated more in detailed later in this chapter. The peak at $\alpha = 60°$ has an almost negligible increase, and it is more reasonable to suggest that it shares more common traits with the simulations at higher α angles.

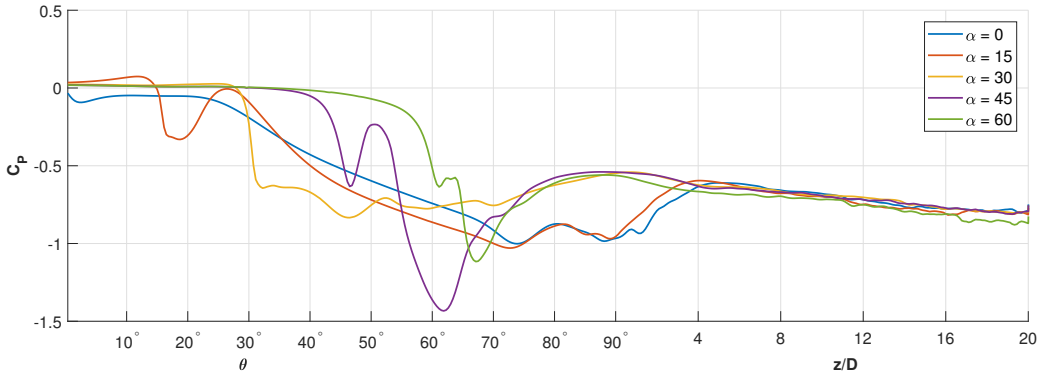

Figure 8.5: Pressure profiles of the average vertical velocity for the first five cases ($\alpha = [0°, 15°, 30°, 45°, 60°]$). The pressure have been sampled at a distance of $0.2D$ away from the large cylinder surface ($0.6D$ away from small cylinder) in the $y/D = 0$ plane.

For the five highest α angles (Figure 8.6), the pressure profiles are similar and have similar traits, following a pattern of slight decrease in pressure from $\theta = 30°$. Around $10°$ before the step, there is a strong decrease, where all pressures drops from -0.2 at $\theta = 60°$ to approximately -0.7 around the step. At cases 6 ($\alpha = 70°$) and 7 ($\alpha = 75°$), there is a small peak directly directly behind the step before the pressure falls further. this small peak is not present at higher angles. This small difference is further discussed in Section 8.1.1.

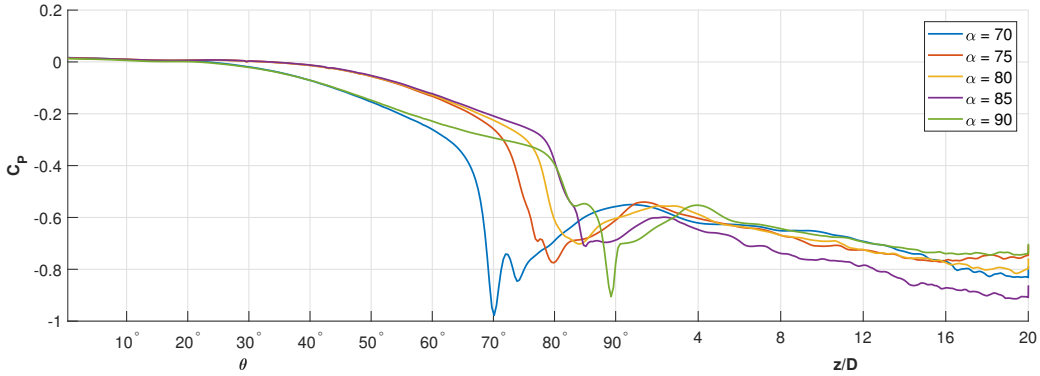

Figure 8.6: Pressure profiles of the average vertical velocity for the last five five cases ($\alpha = [70°, 75°, 80°, 85°, 90°]$). The pressure have been sampled at a distance of $0.2D$ away from the large cylinder surface ($0.6D$ away from small cylinder) in the $y/D = 0$ plane.

It is apparent that some trends apply for all the 10 cases. Along the vertical ex-

tension, the horizontal velocity is just below zero, with a negative value indicating backflow. The vertical velocity w decreases monotonously upwards the vertical extension towards zero at the top of the vertical extension. The strong vertical flow induced by the step and curvature is damped out by the vortex shedding along the vertical extension. Of interest is the fact that the vertical velocity component seems to have the same magnitude further upward the vertical extension $z/D > 8$ before decreasing towards at the top of the vertical extension.

8.1.1 Frequency Analysis

The frequency spectrum of the cross-flow velocity in the wake of the cylinders were investigated and the dominating frequencies were identified. From Table 8.2 some distinct trends were identified. The dominating frequencies along the vertical extension is the Strouhal frequency for the large cylinder $f_v = SD/U_0 = 0.2$. Furthermore, a higher frequency peak were identified for all the cases in the wake of the vertical extension. This frequency peak is assumed to be a harmonic frequency of the vortex shedding behind the vertical extension, with a frequency of oscillation about three times higher than the Strouhal frequency. The major difference in the frequency spectrum of the parameter study occurs at step angles of 45° and below.

Table 8.2: Frequency components of the cross flow velocity v in the wake for the different cases. The cross-flow velocity was sampled a distance of 3 D away from the cylinder surface. The V-cell describes the wake behind the vertical extension from $z/D = 0$ to $z/D = 20$. The C-cell describes the wake behind the curved part of the cylinder. The frequency domains are attached in Appendix C. The frequencies marked with an asterisks (*) are frequencies that contained negligible amount of energy, indicating no vortex shedding.

Case	C-cell frequency Large $[fD/U_0]$	V-cell frequency $[fD/U_0]$	C-cell Small $[fD/U_0]$	Harmonic $[fD/U_0]$
1 - $\alpha = 0^\circ$	0.13	0.19	0.38	0.62
2 - $\alpha = 15^\circ$	0.12	0.2	0.35	64
3 - $\alpha = 30^\circ$	0.08	0.2	0.29 & .39	0.62
4 - $\alpha = 45^\circ$	0.18	0.2	0.38	64
5 - $\alpha = 60^\circ$	0.18	0.2	0.45	0.62
6 - $\alpha = 70^\circ$	0.17	0.2	(0.49)*	0.62
7 - $\alpha = 75^\circ$	0.16	0.19	(0.57)*	0.64
8 - $\alpha = 80^\circ$	0.17	0.2	0.49	0.64
9 - $\alpha = 85^\circ$	0.18	0.2	0.59	0.64
10 - $\alpha = 90^\circ$	0.17	0.2	0.57	0.63

A dominating frequency occurs in the range of $\theta = 70°$ to a height of around $2D$ above the start of the vertical extension. For the cases $\alpha = 0°$ and $\alpha = 15°$ the frequencies coincide with values from a concave cylinder simulation from Jiang et al. (2018a). The vortex shedding is suppressed by strong axial flow lower down the cylinder ($\theta < 60°$).

The second frequency in the wake of the curved cylinder part is showing a tendency to increase with the with the angle of the step α. This may be an indication that the second C-cell frequency is affected by the dimension of the cylinder.

For the first three cases ($\alpha = 0°$, $\alpha = 15°$ and $\alpha = 30°$), the cross-flow power density spectrum indicates that the vortex shedding acts with different frequencies at the curved part, with a dominating low frequency peak followed by higher frequency peaks. The frequencies in question are displayed in Table 8.3. In the power density spectrum for $\alpha = 30°$ shown in Figure 8.14, the different frequency peaks and the range they act on is displayed. It should be noted that for all three cases, the range they act on is the same, as the peaks start at $\theta = 60°$ and stops at the start of the vertical extension, where the Strouhal frequency for the large diameter cylinder dominates.

Cases 6 and 7 has a small C-cell frequency which contains negligible amount of energy. The lack of energy in this frequency range concurrent with the lack of vortex shedding from the small cylinder, which occurs at higher α angles as well as case 5 ($\alpha = 60°$). This lack of frequency also occurs at angles where there is marked differences between case 6 and 7 and the other cases in pressure (Figure 8.6).

Table 8.3: Frequency peaks in the area from $\theta = 60°$ to the start of the vertical extension $\theta = 90°$. The frequencies are non-dimensional (fU_0/D).

Case	f_1	f_2	f_3	f_4	f_5	f_6
1 ($\alpha = 0°$)	0.13	0.38	0.62	0.88	-	-
2 ($\alpha = 15°$)	0.12	0.36	0.59	0.82	-	-
3 ($\alpha = 30°$)	0.08	0.23	0.39	0.52	0.66	0.83

These cases along with case 4 ($\alpha = 45°$) and 5 ($\alpha = 605°$) are assumed to affect the flow more significantly than the cases with higher step angles. Therefore the first fove cases were investigated in more detail.

8.2 Further Investigation of $\alpha = 0°$

Case 1 $\alpha = 0°$ is of special interest, as it has similarities with the the case investigated in Section 5.2. In particular the recirculation zone in front of step was

compared for both cases. As can be seen from Figure 8.7, a recirculating zone appears in front of the step above the small cylinder surface. The recirculation zone does not appear below the step, but the flow is dragged downwards towards the edge of the step.

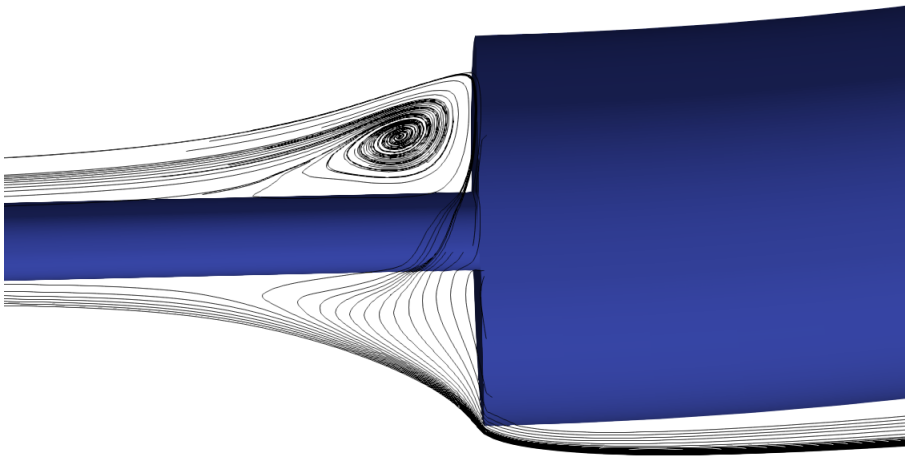

Figure 8.7: Streamlines of the velocity in front of the step for $\alpha = 0^\circ$ in the $y/D = 0$ plane. The streamlines were sampled in a straight line from the edge of the step in the middle of the cylinder i.e. $R_{sample} = 12.5D \pm 0.25D$ to $0.5D$ ahead of the step. The streamlines clearly show that the flow is asymmetric. Note the difference in streamlines with the horizontal cylinder in parallel flow case in Figure 5.9.

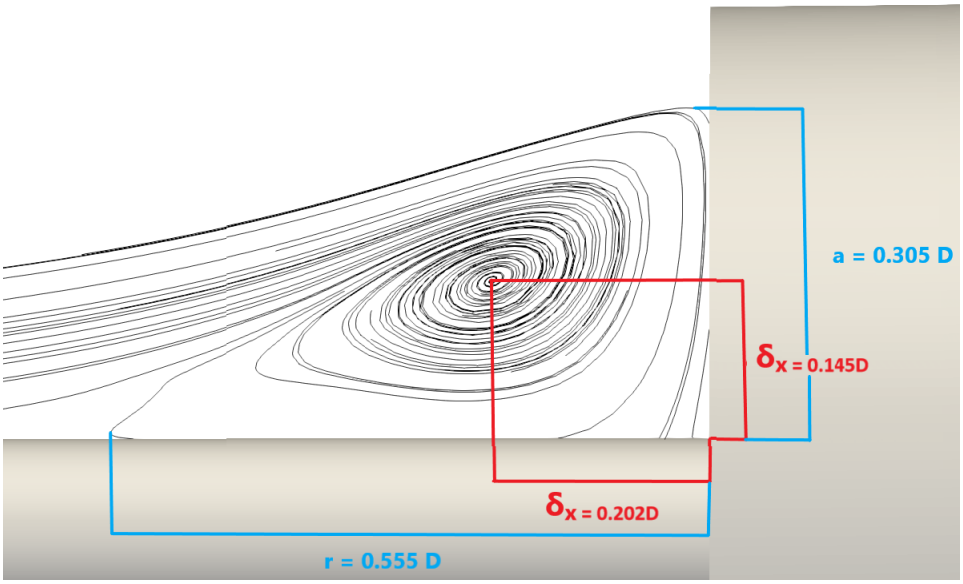

Figure 8.8: Recirculation zone in front of the step above the small cylinder surface. The lengths indicates the position and size of the recirculation zone. The change in diameter occurs at $x/D = 0$.

Table 8.4: Recirculation zone in front the step for case 1 ($\alpha = 0°$, Figure 8.8)and the horizontal cylinder with a step in parallel flow investigated in Section 5.2 (Figure 5.10). The value of the parameter h is 0.4D and represents the size of the step.

	δ_x	δ_y	r	a
Case 1	0.202 D	0.145 D	0.555 D	0.305D
($\alpha = 0°$)	0.505 h	0.363 h	1.388 h	0.763 h
Horizontal cylinder	0.146 D	0.173 D	0.664 D	0.280 D
parallel flow	0.365h	0.433 h	1.66 h	0.7 h

The boundary layer thickness directly ahead of the step was investigated above and below the small cylinder. The results displayed in Figure 8.9 shows that the increase in boundary layer thickness ahead of the step is larger above the small cylinder than bellow. Compared to the results in Section 5.2, the upper boundary layer thickness follows the same pattern but having a higher maximum thickness, while the lower boundary layer thickness have smaller maximum thickness. Further upstream all the boundary layers behave in the same way as results from Jiang et al. (2018b), having a smaller boundary layer thickness than the Blasisus equation for a flat plate. The influence of the step on the boundary layer is significant, with a sharp increase in the boundary layer thickness at a distance of $1.9D$ up-

stream of the step. The sharp increase is $0.1D$ further downstream compared to the boundary layer thickness in the straight horizontal case (Section 5.2). The recirculation zone identified in at the in front of the step above the small cylinder is shorter and reaches higher than for the straight cylinder case, by has vortex core further upstream and closer to the small cylinder surface. The recirculation zone characteristics for both simulations are presented in Table 8.8.

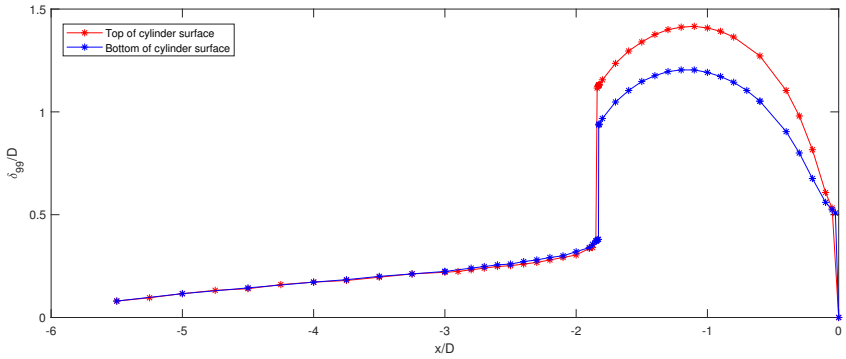

Figure 8.9: Boundary layer thickness $\delta_{0.99}$ along the small cylinder surface from directly behind the start of the simulation at $x/D = -5.5$ until the step at $x/D = 0$. The boundary layer is sampled in the above and bellow the small cylinder in the $y/D = 0$ plane. The increase at $x/D = -1.9$ is more profound than in Figure 5.8.

8.3 Further Investigation of $\alpha = 15°$

Of special interest is how a step at low angles affects the recirculation zones in front of and behind the step. Therefore a more thorough investigation of the vortices and flow characteristics in the $\alpha = 15°$ case was conducted. The horizontal and vertical components of the velocity are both sharply affected by the step. The velocity components u and w are displayed in Figures 8.10 and 8.11.

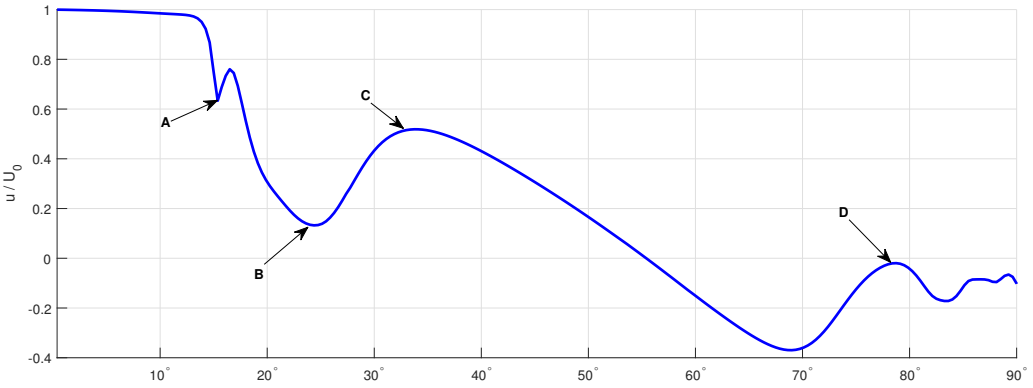

Figure 8.10: Average velocity profile of the horizontal velocity component u, sampled at $R = 13.2D$ i.e. $0.2D$ away from the large diameter cylinder surface ($0.6D$ from the small cylinder surface). The samples are located in the $y/D = 0$ plane along the the curvature from the start of the horizontal extension to at the start of the vertical extension.

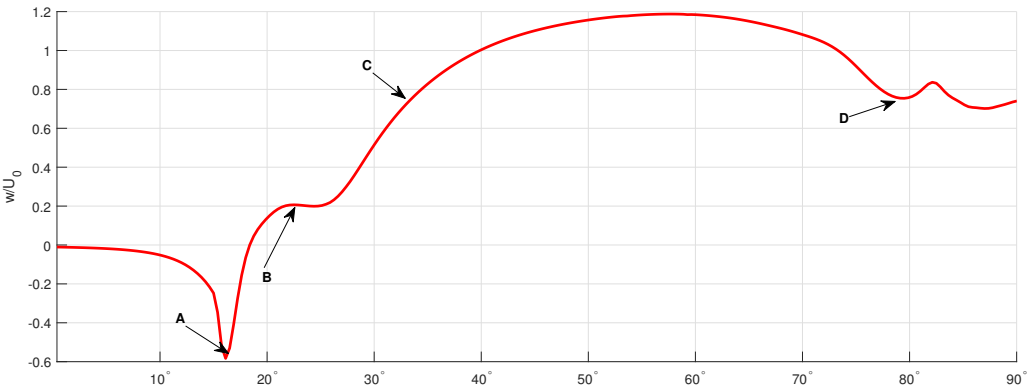

Figure 8.11: Average velocity profile of the vertical velocity component w, sampled at $R = 13.2D$ i.e. $0.2D$ away from the large diameter cylinder surface ($0.6D$ from the small cylinder surface). The samples are located in the $y/D = 0$ plane along the the curvature from the start of the horizontal extension to at the start of the vertical extension.

The vertical velocity component w experiences a sharp increase in the negative direction, going from around zero to $-0.6U_0$ at point A ($\theta = 15.4°$), while the horizontal velocity component u sinks down from $1U_0$ to $0.6U_0$ before it peaks up to $0.76U_0$ at $\theta = 16.5°$. At point B ($\theta = 24°$) there is a dip in the horizontal velocity component while the vertical velocity component starts to increase until

it reaches a maximum value of 1.187 U_0 at $\theta = 56^\circ$.

The horizontal velocity component starts to increase from point B to a local maximum at point C ($\theta = 33^\circ$). The velocity then decreases until $\theta = 70^\circ$. At point D ($\theta = 79^\circ$) the horizontal velocity experiences a peak while the vertical velocity dips. This change coincides with the formation of vortices at $z/D = -3$ as can be seen in Figure 8.17. The sharp decrease in both velocity components at point A is due to the influence of the step, and a recirculation zone is formed at the edge of the bottom step, as shown in Figure 8.12.

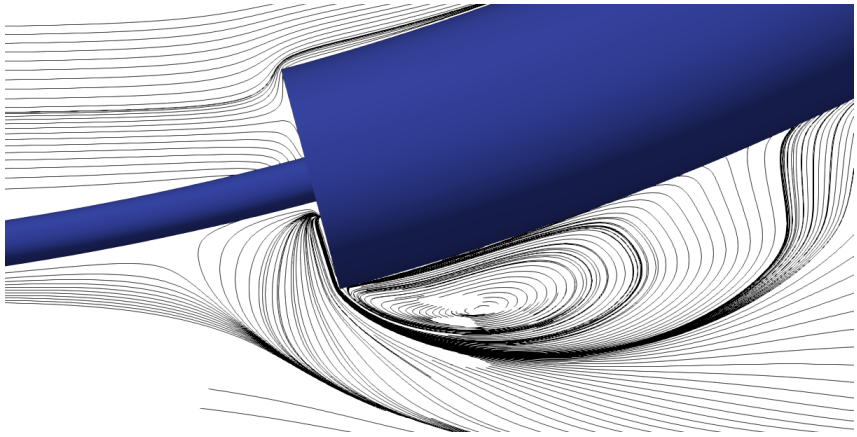

Figure 8.12: Streamlines of the velocity around the step of $\alpha = 15^\circ$ case. A recirculation zone is formed at the bottom edge of the step. There is no indication of a recirculation zone at the top of the step nor at the front of the step.

The formation of vortex structures start at the step, where a vortex structure is being formed at the bottom edge of the cylinder step. In Figure 8.12 a recirculation zone appears behind the bottom step. The formation of a helical vortex behind the bottom step creates large vortex structures in the wake of the large cylinder which in turn affects the formation of vortices at $\theta = 70^\circ$. The helical vortex is depicted in the snapshot of λ_2 in Figure 8.13, where a helical vortex is being formed directly behind the recirculation zone.

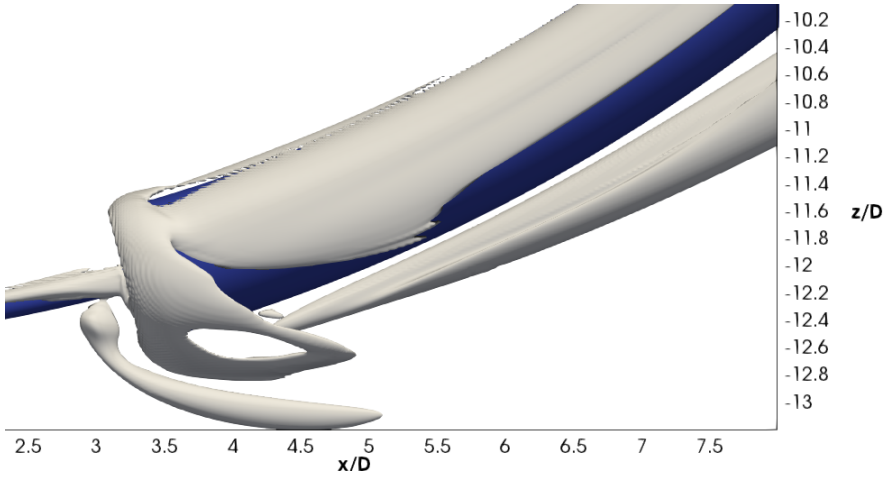

Figure 8.13: Iso-contour of $\lambda_2 = -1$ for case 2, $\alpha = 15°$ around the step. Vortex structures are formed in front of the step and in the wake of the bottom part of the step.

8.4 Further Investigation of $\alpha = 30°$

Case 3 $\alpha = 30°$ shows many of the same trends as case 2. As shown in the power density spectrum in Figure 8.14, the area behind the end of the curvature is characterized the vortex shedding being represented by a multitude of frequencies in the 60°-90° range.

Figure 8.15 shows the iso contour of λ_2 in the wake of the $\alpha = 30°$ case from $\theta = 35°$ to $\theta = 90°$. Large vortex structures are forming behind the step, and are mixed from with the vortices shed from the vertical extension. These elongated vortices are unique for case 3, and are the most likely cause for the different frequency peaks in the Power Density Spectrum (Figure 8.14). The long elongated vortices are shed from the helical vortex structure formed behind the step.

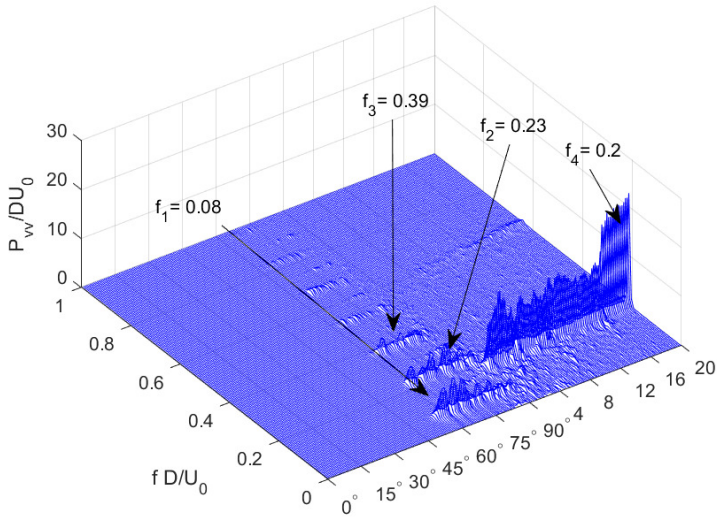

Figure 8.14: Power density spectrum of the cross flow velocity v for the $\alpha = 30^\circ$ case. Sampled at R = 16 D i.e. 3 D behind the large cylinder in the $y/D = 0$ plane.

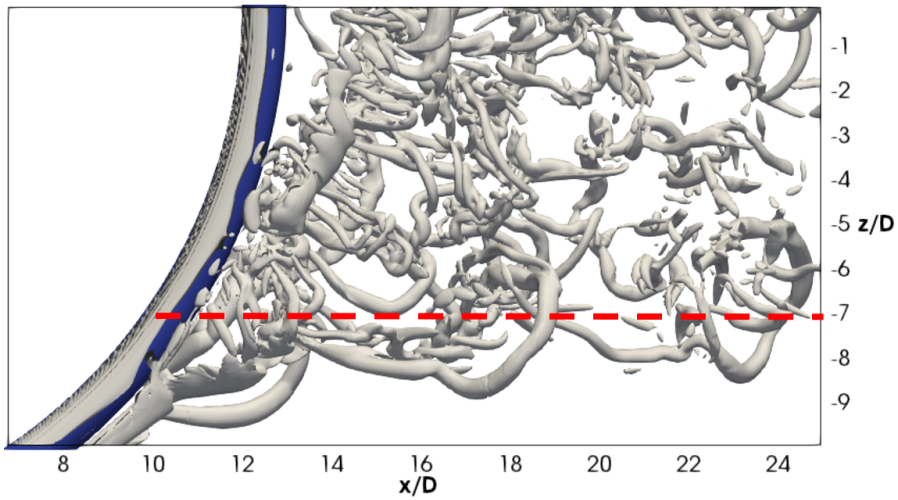

Figure 8.15: Iso-contour of $\lambda_2 = -1$ of the $\alpha = 30^\circ$ case. The red line marks the start of where the PSD of the cross-flow velocity v has energy (Figure 8.14).

Around the step, strong shear flow is observed. Behind the step, a recirculation zone is formed as can be seen in Figure 8.16.

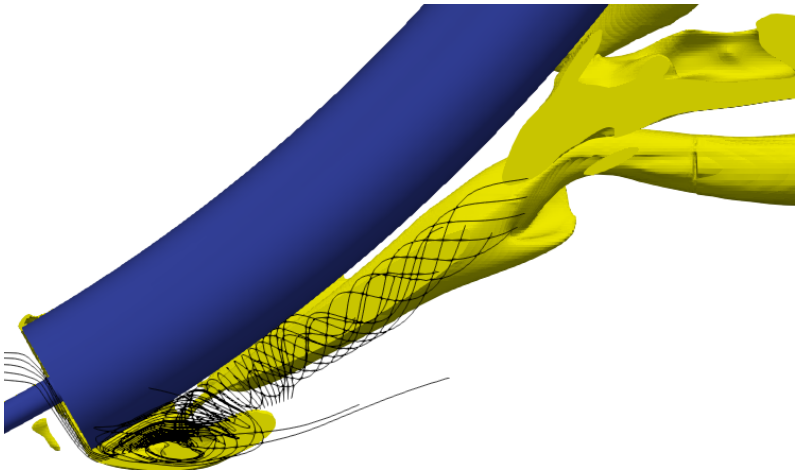

Figure 8.16: Iso-contour of $\lambda_2 = -1$ of the $\alpha = 30°$ case with streamlines of the velocity at the step and immediate wake. A recirculation zone is being formed in at the bottom edge and a helical vortex structure is being formed behind the recirculation zone.

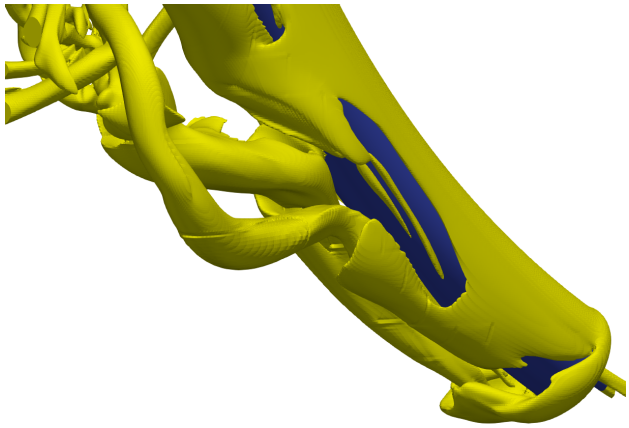

Figure 8.17: Snapshot of the iso-contour of $\lambda_2 = -1$ seen from behind the step. Notice the large vortex structures being formed behind the the recirculation zone and being shed further downstream.

At the step, a vortex is formed directly behind the edge of the bottom step. While a helical vortex is formed further behind at $\theta = 33°$. The helical vortex can be seen in Figure 8.16. The helical vortices separates from the cylinder surface at at $\theta = 47°$ and new vortex structures are also formed further up the cylinder wake. The the shedding of the helical vortices into elongated vortex structures coincides with a slight drop in the vertical velocity w and pressure (Figure 8.18). The hori-

zontal velocity component u has a small peak at the start of vortex shedding from the helical vortex. The vortex shedding from the helical vortex can be observed from Figure 8.17. The vortex structures being shed are longer than those shed further up the vertical extension.

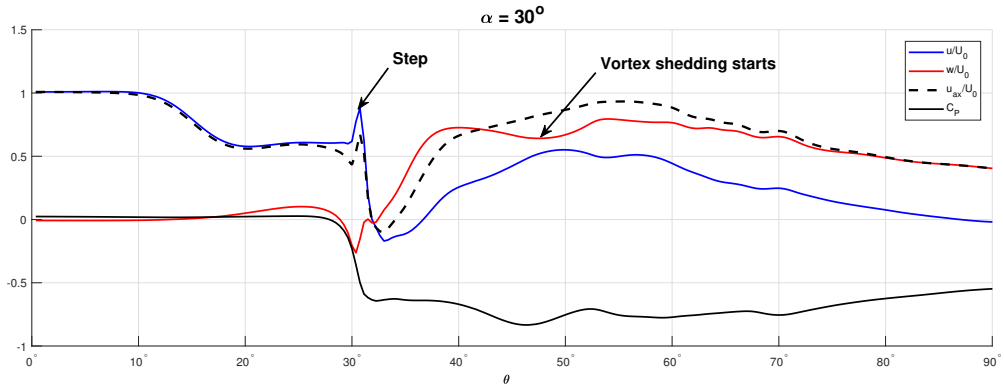

Figure 8.18: Profiles of the horizontal velocity component u, the vertical velocity component w and the pressure coefficient C_P for case 3, $\alpha = 30°$. The velocity and pressure was sampled at $R = 13.2D$, i.e. $0.2D$ behind the large cylinder surface and $0.6D$ behind the small cylinder surface. The samples are located in the $y/D = 0$ plane along the the curvature from the start of the horizontal extension to at the start of the vertical extension.

The contour plot of ω_z in the (x,y) plane at three different points in the vertical domain is shown in Figure 8.19. At (a) ($z/D = -11$) the introduction of the step creates a recirculation zone. just behind the step, a helical vortex structure is being formed (Figure 8.19 (b)), but no shedding is being observed. The vorticity in Figure 8.19 (b) has similar behaviour to flow around a straight cylinder at low Reynolds numbers. In Figure 8.19 (c), long elongated vortices are being shed from the cylinder, but there are no signs indicating that they are being shed at regular intervals. The Von Karman vortex shedding from the vertical extension affects the helical vortex sheets and forces vortex shedding from the curved cylinder. In Figure 8.15 the vortex shedding behind the curvature and vertical extension is shown, and the long elongated vortex structures correspond with the irregular vortex shedding shown in the ω_z contour plot.

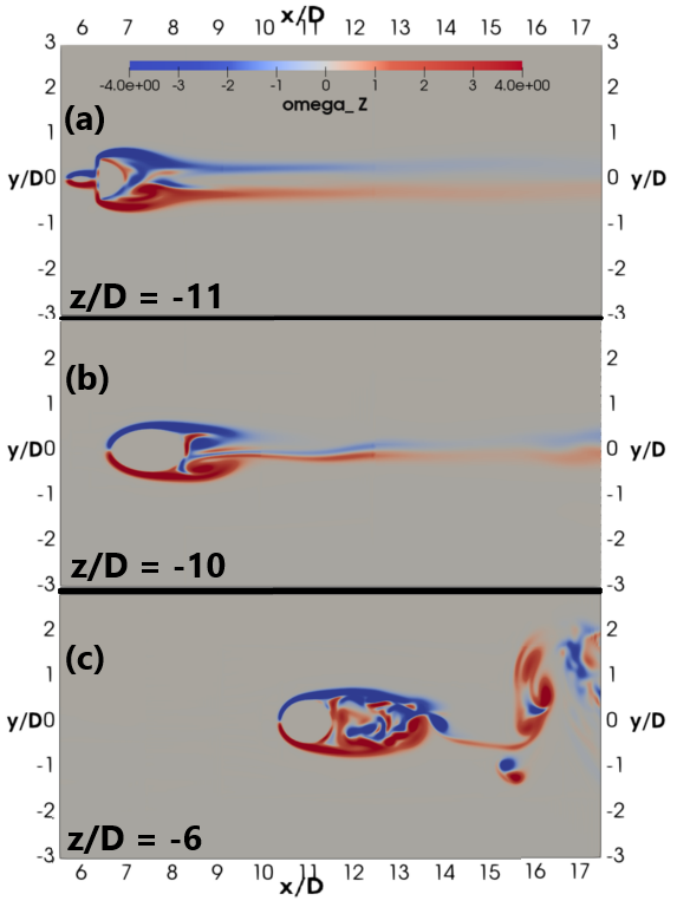

Figure 8.19: Instantaneous vorticity ω_z contour plot in the (x,y) plane. (a) is in the curvature at $z/D = -11$ which is where the center line of the cylinder is at $\theta = 28°$. Both the small and large cylinder affects the flow field. (b) Same as (a) but at $z/D = -11$, $\theta = 37°$ which i around the large cylinder directly above the step. (c) same as in (a) but at $z/D = -6$, $\theta = 61°$.

8.5 Further Investigation of $\alpha = 45°$

Further investigation of case 4, $\alpha = 45°$ showed a transition between the cases 2,3 and the case with higher step angles α. As in cases 2 and 3, there is no recirculation zone in front of the step. There is a recirculation zone directly behind the step, as shown in Figure 8.20. The size of the recirculation zone for case 4 is smaller than for case 2 and 3, and the vortex core is also positioned further upstream and closer

to the cylinder surface.

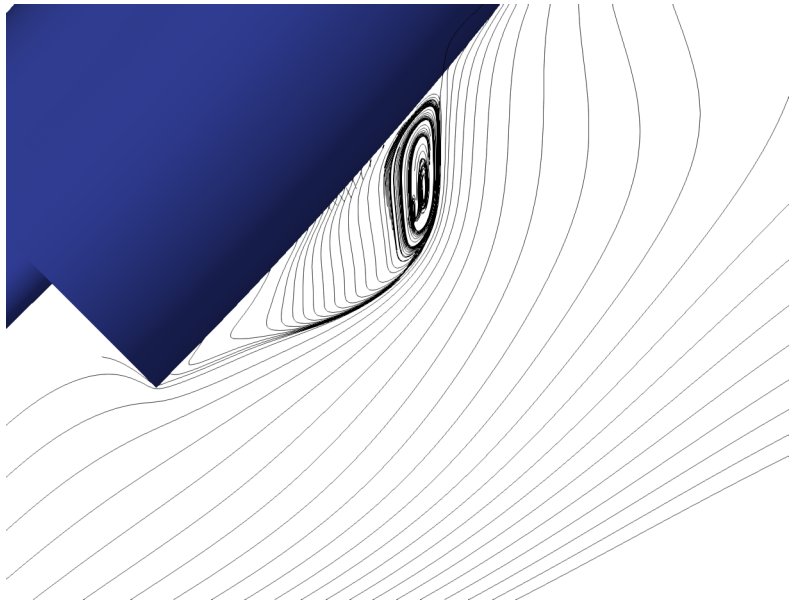

Figure 8.20: Streamlines of the velocity around the step for case 4, $\alpha = 45°$. Notice the formation of a vortex core at the region furthermost region of the cylinder, which differs from case 2 and 3.

The velocity and pressure was sampled in the wake of the cylinder and illustrated in Figure 8.21. The horizontal velocity starts to decrease at point A ($\theta = 17°$), which also marks the start of an increase in the vertical velocity component w. At point B ($\theta = 45°$), a sharp drop in u coincides with an increase of negative pressure. Point B lies in the recirculation zone identified in Figure 8.20. In point B, w stay more or less constant until Point C ($\theta = 55°$), where it experiences a sharp increase. The pressure coefficient experiences a small drop in magnitude before Point C and the starts to increase towards a maximum negative value at point D ($\theta = 62°$). The horizontal velocity u experiences a small drop and increase at point C before it further decreases towards point D. At point D, the maximum absolute value of the vertical velocity w and the pressure is observed. This point also marks where the first vortex structures starts to shed from the cylinder shown in the snapshot of the vortex structures in Figure 8.22.

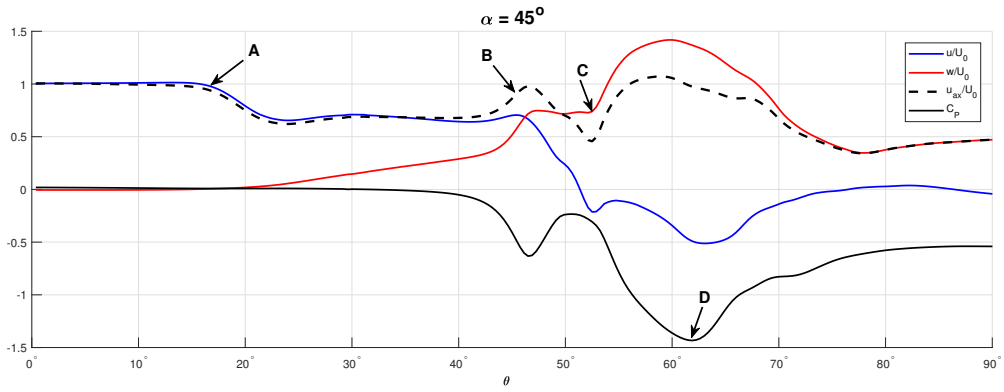

Figure 8.21: Profiles of the horizontal velocity component u, the axial velocity component u_{ax}, the vertical velocity component w and the pressure coefficient C_P for case 4, $\alpha = 45°$. The velocity and pressure was sampled at $R = 13.2D$, i.e. $0.2D$ behind the large cylinder surface and $0.6D$ behind the small cylinder surface in the $y/D = 0$ plane.

The iso-contour of $\lambda_2 0 - 2.5$ displayed in Figure 8.22 show the formation of a helical vortex behind the step. The helical vortex spans from the the start of the step at $\theta = 45°$ to $\alpha = 60°$. Vortex shedding from the cylinder starts at the end of the helical vortex structure at $\theta = 60°$. Studies by Jiang et al. (2019) and Jiang et al. (2018a) showed that for a concave curved cylinder at Reynolds numbers of 500 and 3900, the vortex shedding starts at $z/D = -5$ for $Re_D = 500$ with an increase to $z/D = -6$ for $Re_D = 3900$. This suggest that the influence of the step does not affect the vortex shedding from the curvature at $\alpha = 45°$.

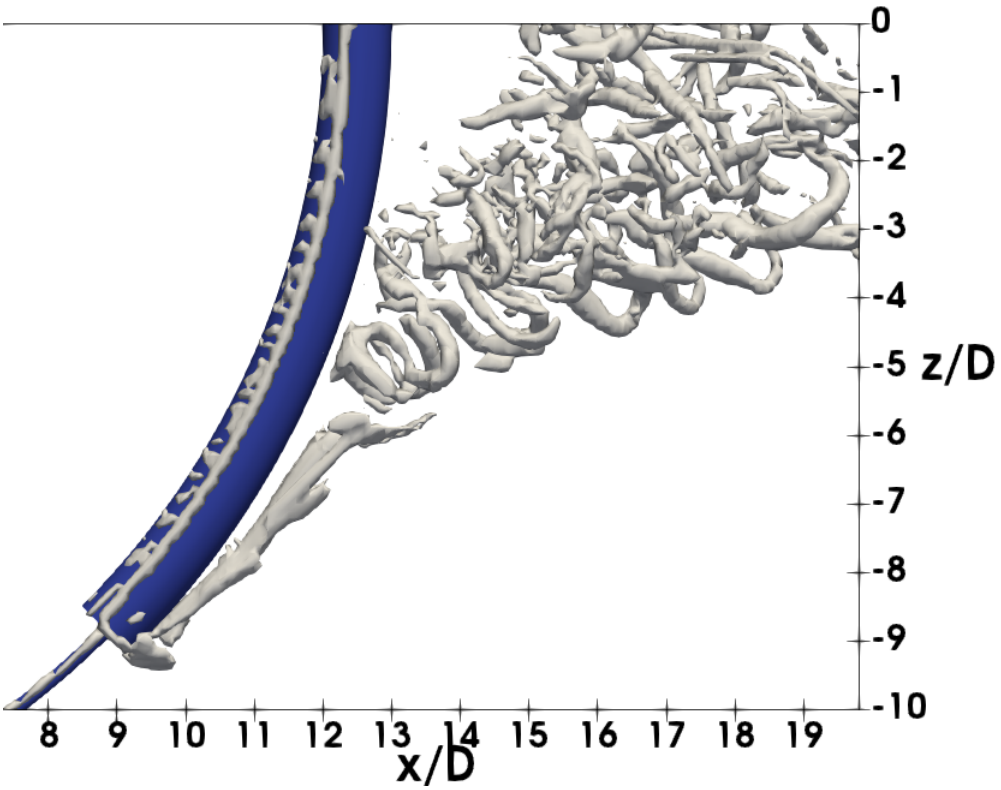

Figure 8.22: Snapshot of the iso-contour for $\lambda_2 = -2.5$ for case 4, $\alpha = 45°$. The vortex structures starts to shed at $z/D = -6.5$ which is equivalent to $\theta = 60°$.

In Table 8.5 the size of the edge recirculation zone and the position of the the vortex core in relation to the bottom step edge is listed. The edge recirculation zone is significantly smaller and positioned further behind the step for case 4.

Table 8.5: Comparison of the recirculation zone behind the bottom part of the step for cases $2 - \alpha = 15°$, $3 - \alpha = 30°$ and $4 - \alpha = 45°$. An illustration of the size parameters can be found in Figure 8.8

Case	2 ($\alpha = 15°$)	3 ($\alpha = 30°$)	4 ($\alpha = 45°$)
δ_x	0.585 D	0.426 D	0.889 D
δ_y	0.261 D	0.235 D	0.163 D
r	2.1 D	2.01 D	1.1 D
a	0.621D	0.61 D	0.275 D

8.6 Further Investigation of $\alpha = 60°$

For case 5 - $\alpha = 60°$ no edge recirculation zone was identified, with only edge vortices along the step. Furthermore, there was also no indication of a junction vortex around the small cylinder at the step. Of note is the formation of small vortex structures directly behind the step for case 6, displayed in Figure 8.23.

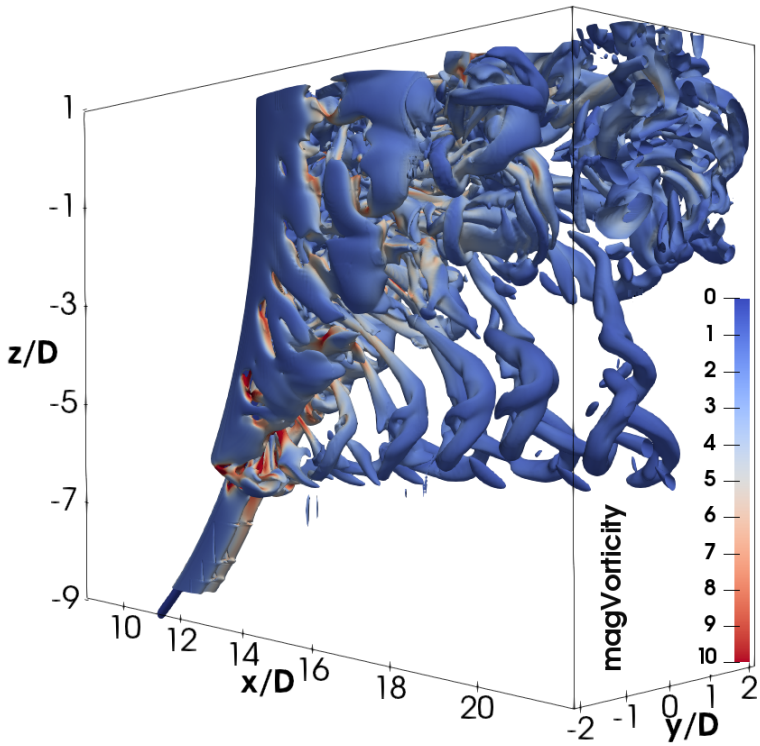

Figure 8.23: 3-D iso-volume of $\lambda_2 = -0.1$ for case 5, $\alpha = 60°$. The magnitude of the vorticity is shown as a color contour on the iso-volume.

The vortex dynamics of case 5 is interesting because of how the flow and shedding of vortex structures behave at other cases. In most other cases, vortex shedding starts around $\theta = 60°$. It is assumed that the strong vertical flow along the small cylinder, which suppresses vortex shedding along the bottom part of the cylinder is not present in the $\alpha = 60°$ case. Below the step, vortex shedding is suppressed by the small cylinder due to its low Reynolds number. For $Re_d = 120$, vortex shedding behind the curvature does not manifest itself before $\theta = 60°$ for all cases. Behind the large cylinder, the helical vortex structures manifested by the strong axial flow also act to suppress vortex shedding for angles below $\theta = 60°$. This makes case 5 unique, as the steps is placed in a position where it disrupts the

flow patterns for both the small and large cylinder, and thereby initiating vortex shedding which would otherwise have been suppressed.

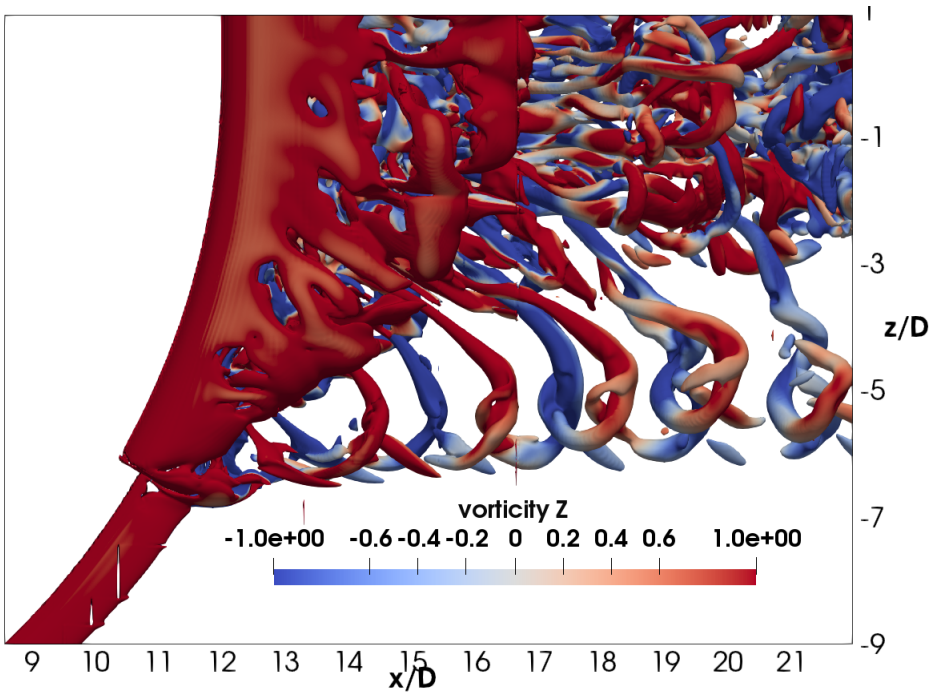

Figure 8.24: Iso-volume of $\lambda_2 = -0.1$ for case 5, $\alpha = 60°$, seen from the positive y-direction. The iso-volume has a coloring representing the vorticity component in the vertical direction ω_z.

The formation of the small vortex sheets behind the step is interesting, as this is the only case where small vortex sheets are being shed from the large cylinder surface. This indicates that some special phenomenon happens around the step at $\alpha = 60°$. Of note is the fact that vortices split from the large cylinder in case 5 is similar in frequency to those shed from the small cylinder at high α angles. The vortices have a somewhat similar frequency of oscillation (C-cell small frequency in Table 8.2). It should be noted that the shape of the vortex structures for case 5 is unique, and the vortices formed along the small diameter cylinder in higher cases resemble von Karman vortex shedding which case 5 does not. It should be noted that Levold (2012) discovered a similar vortex structures for the top of a free-end cylinder. This may implicate that the small diameter cylinder does not impact the vortex shedding from the edge.

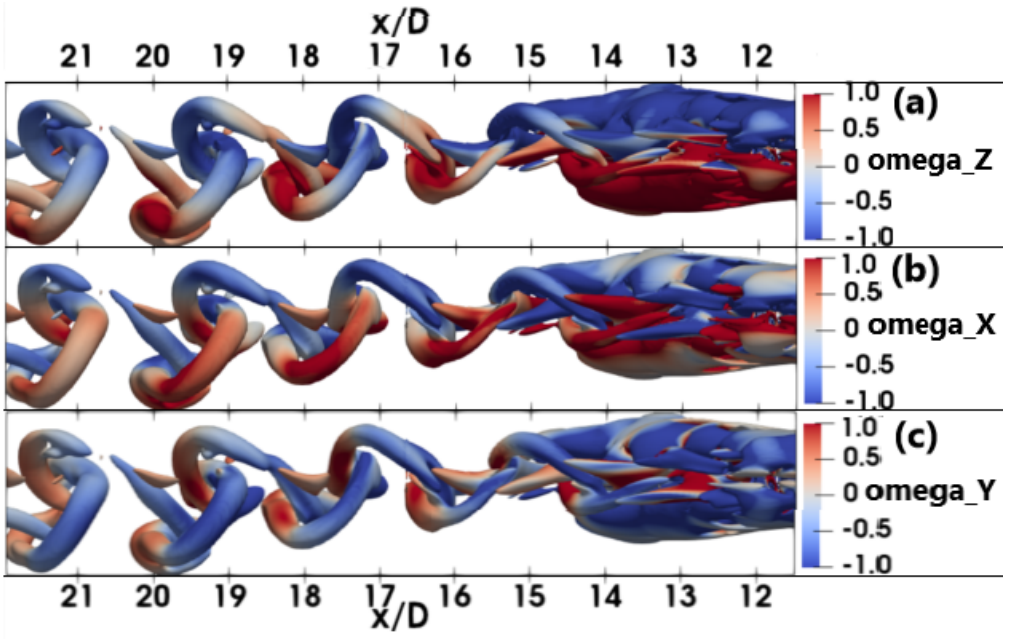

Figure 8.25: Iso-volume of $\lambda_2 = -0.1$ for case 5, $\alpha = 60°$, seen from the negative z-direction (bottom view). (a) has a coloring representing the vorticity component in the vertical direction ω_z. The red positive values indicating a the flow is rotating counterclockwise, the blue negative values indicates a clockwise rotation of the flow. (b) same as in (a) but the vorticity component ω_x. (c) same as in (a) but for the vorticity component ω_y

In Figure 8.25 the iso-volume of λ_2 with with colors representing the three different vorticity component. The vorticity plot indicates some trends. The flat vortex structure rotates counterclockwise which manifest itself in the bottom vortex sheet begin to twist around towards the top vortex. This twist causes the vortex sheets to resemble a chain-link. These ”chain-link” vortex structures does not occur in any of the other cases. The chain-link vortices are shed in the area from the edge of the cylinder and spreads upwards before it is suppressed by the normal vortex shedding behind the large cylinder close to the top of the curvature.

8.7 Investigation of Diameter Changes at Higher Angles

This section investigates how the introduction of a step at angles higher than $\alpha = 60°$. The flow patterns were similar for a lot of cases and therefore all the remaining cases were investigated in this section.

For case 6 - $\alpha = 70°$ no edge circulation zone or junction vortices were found. but edge vortices were seen forming along the step edge. At the step, two peaks

in the average vertical velocity occurs at the step, and directly after the step. From Figure 8.27, the vertical velocity is strong at the edge of the step, and a second concentration beginning at $z/D = -3.6$ or $\theta = 75°$. The pressure and velocity profiles are displayed in Figure 8.26. The second peak in the velocity plot at $\theta =$

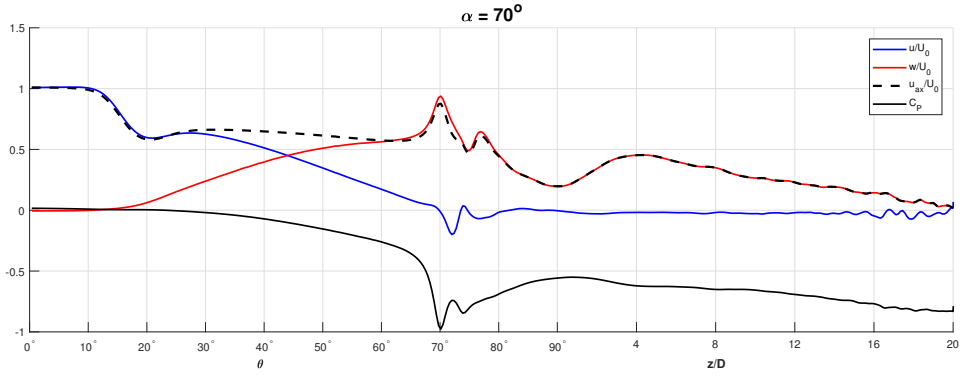

Figure 8.26: Profiles of the horizontal velocity component u, the axial velocity profile u_{ax}, the vertical velocity component w and the pressure coefficient C_P for case 6, $\alpha = 70°$. The velocity and pressure was sampled at $R = 13.2D$, i.e. $0.2D$ behind the large cylinder surface and $0.6D$ behind the small cylinder surface in the $y/D = 0$ plane.

$75°$ is where the vortex shedding from the large cylinder starts to occur, and the vortex structures are dragged upwards in the domain.

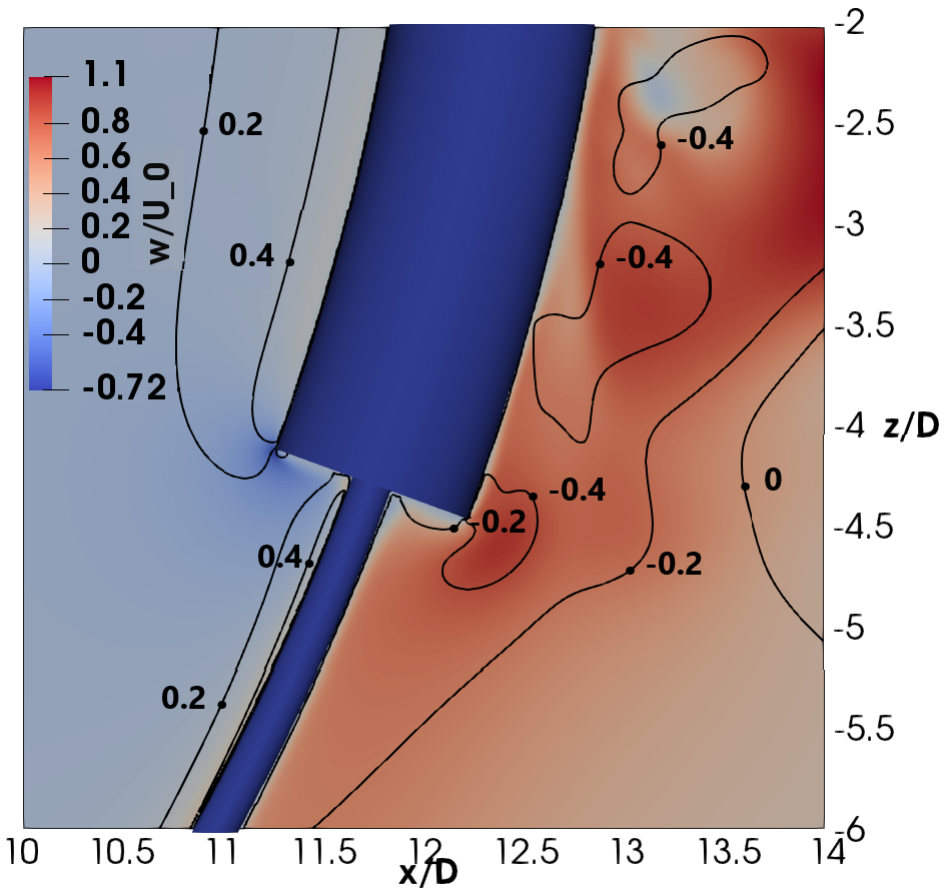

Figure 8.27: Snapshot of the instantaneous contour of the vertical velocity component w for case 6 - $\alpha = 70°$.Two high velocity zones can be observed directly behind the cylinder at $z/D = -4.6$ and $z/D = -3.6$. The velocity contour is sampled in the $y/D = 0$ plane. Iso-contour lines of the pressure along with the pressure values are depicted as well.

In Figure 8.28, the iso-volume of $\lambda_2 = -1$ and the streamlines of the vorticity shows the formation of a junction vortex ahead of the small cylinder and the lack of a helical vortex behind the large cylinder for case 6. Furthermore, edge vortices are also formed along the cylinder surface and vortex structures are being shed directly above the step.

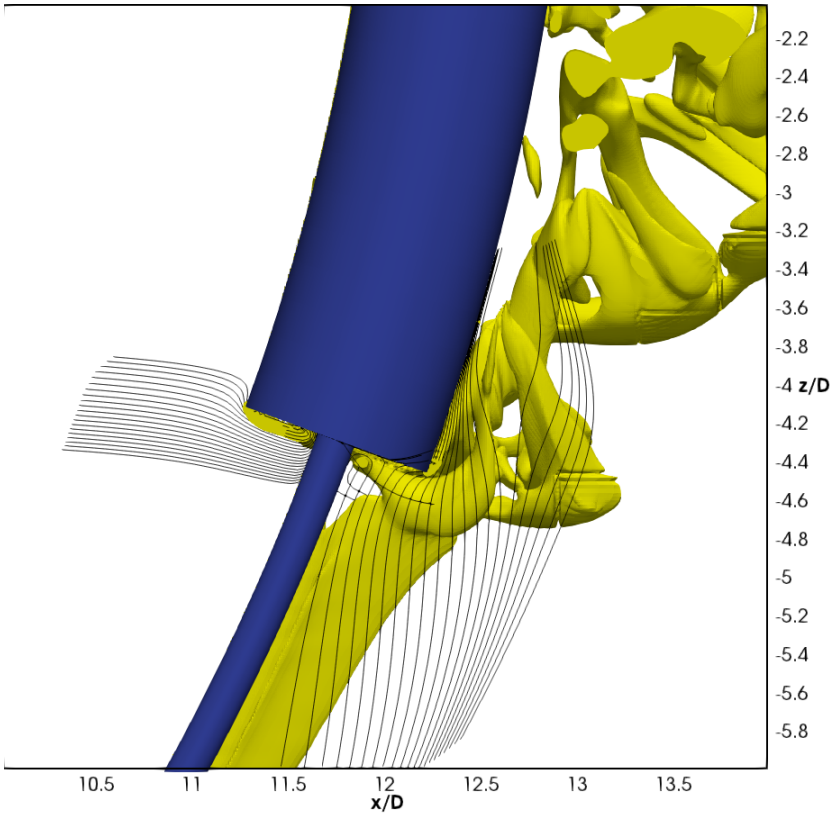

Figure 8.28: Streamlines of the velocity and iso-volume of $\lambda_2 = -1$ for case 6 - $\alpha = 70°$. In front of the small cylinder surface directly below the step a recirculation zone belonging to the junction vortex can be observed

The peaks in the frequency domain along with the Snapshot of the iso-contour for λ_2 shows a distinct difference between case 6, 7 and 8, 9, 10. At α lower than $80°$ there are no clear signs of vortex shedding from the small cylinder, and the flow has a strong vertical flow pushing the vortex structures upwards. At $\alpha = 80°$ and higher vortex shedding from the small cylinder occurs. Therefore, it is reasonable to suggest that a vortex shedding from the small cylinder starts at some point between $\theta = 70°$ and $\theta = 80°$.

The peaks in velocity in cases 6, 7 and 8 may indicate that at the angles in question, the incoming horizontal flow is induces a strong vertical flow at the backward edge of the step, creating a strong vertical velocity concentration directly at the step.

In case 9 and 10, there is no peak in the vertical velocity component w at the step, but a drop in velocity just ahead of the step followed by a spike in velocity

directly at the step. Further up the vertical extension there is yet another drop in vertical velocity, much more profound for case 10 than any other case. This drop in velocity for case 10 - $\alpha = 90^\circ$ is investigated in Section 7.1.

8.8 Discussion of the Parameter Study

The area around the step for all cases were investigated to identify the what types of recirculation zones and vortex structures appears for the different geometric configurations. Table 8.6 shows which vortex structures appear for the the different configurations.

The different vortical structures and recirculation zones appearing in the different cases is catalogued in Table 8.6.

Table 8.6: Table describing which different recirculation zones and vortical structures appear in the different cases in the parameter study. In the helical vortex column, large and small indicates if the helical vortex is formed behind the large diameter or small diameter cylinder respectively.

Case	Recirculation zone front	Recirculation zone edge	Junction Vortex	Helical Vortex
1 ($\alpha = 0^\circ$)	Yes	No	No	Large
2 ($\alpha = 15^\circ$)	No	Yes	No	Large
3 ($\alpha = 30^\circ$)	No	Yes	No	Large
4 ($\alpha = 45^\circ$)	No	Yes	No	Small & Large
5 ($\alpha = 60^\circ$)	No	No	No	Small
6 ($\alpha = 70^\circ$)	No	No	Yes	Small
7 ($\alpha = 75^\circ$)	No	No	Yes	Small
8 ($\alpha = 80^\circ$)	No	No	Yes	Small
9 ($\alpha = 85^\circ$)	No	No	Yes	Small
10 ($\alpha = 90^\circ$)	No	No	Yes	Small

For the different cases, case 1 is unique with respect to the geometric configurations. It is the only case with a recirculation zone in front of the step. This case is similar to the horizontal cylinder in parallel flow although the introduction of a curvature affects the recirculation zone ahead of the step. It can be assumed that the introduction of a curvature, even though the angle is small at the start have a profound impact on flow ahead of the of the step.

For cases 2-4, a recirculating zone behind the bottom edge appears, with a helical vortex structures appears behind the recirculation zone. Case 6 is unique in that a recirculation zone is not present but also has a helical vortex. The forma-

tion of helical vortex structures changes to start from behind the large cylinder to the small cylinder at $\alpha = 45°$, which has indications of helical vortex structures forming behind both the small and large cylinder surface. Case 3, $\alpha = 30°$ has some indications of a helical vortex forming from behind the small cylinder but the formations were not clear enough to state a helical vortex is formed.

Recent studies by Jiang et al. (2018a) and Jiang et al. (2017) showed that for higher Reynolds number, vortex shedding along a concave curved cylinder manifests itself further downwards than for lower Reynolds numbers. The vortex shedding for the different cases showed similar trends in regards to the angles vortex shedding starts at. There are two notable exceptions however, as case 3 ($\alpha = 30°$) and 5 ($\alpha = 60°$) showed unique vortex structures which dislocated behind the step. These two cases may have a geometrical configuration which at that particular Reynolds number have a step at points were vortex shedding usually occurs and creates a disturbance in the vortex suppressing mechanisms.

With changes of diameter at angles $\alpha = 70°$ and above a junction vortex appears before the small diameter cylinder. The formation of a junction vortex is not present for smaller angles and therefore it is reasonable to conclude that junction vortex structures start to appear between a step angles $\alpha = 60°$ and $\alpha = 70°$.

As the parameter study shows, the geometrical configurations have a profound impact on the fluid flow. The fluid flow phenomenon appear to follow a pattern, with recirculation zones appear at lower angles and junction vortices appear at higher angles.

Chapter 9

Conclusion

This thesis presents an investigation of fluid flow around different geometries at a constant Reynolds number using Direct Numerical Simulation. The parameter study was conducted to investigate flow phenomenon in the wake of the geometry. The variable used in the parameter study is the angle in which the change in diameter occurs (α). Ten different cases were investigated starting from a change in diameter at the bottom of the curve at $\alpha = 0^\circ$ to the start of the vertical extension at $\alpha = 90^\circ$.

After investigating the geometrical configurations with a change in diameter at $\alpha = 90^\circ$, it was revealed that the curvature and the change in diameter both affects the flow field significantly. The studies done in Chapter 7 shows that the wake is drastically influenced by the curvature, with a much wider wake behind the curved part than the vertical extension. This was the case for both the small and large diameter cylinder. The strong vertical flow around the large diameter cylinder in Section 7.3 is suppressed by the diameter reduction at the start of the vertical extension. The pressure and velocity are heavily influenced by the step.

The geometrical configurations follow a pattern where the change in diameter drastically affects the flow in the wake of the step. The results show that at small angles the formation of different vortex structures are apparent. For even the first case, $\alpha = 0^\circ$ have strong differences from the straight horizontal cylinder in parallel flow, as the recirculation zone in front of the step is not symmetric in case 1. The formation of recirculation zone in front of the cylinder disappears at $\alpha = 15^\circ$ and does not appear in any of the other cases than $\alpha = 0^\circ$. For cases 2,3 and 4 a recirculation zone appears behind the downward edge, but disappears for $\alpha > 45^\circ$.

At high α angles, the introduction of a step creates a low pressure zone behind

the large cylinder, which drags the flow towards the large cylinder. This phenomenon can cancel out the strong vertical flow induced by the curvature if the step changes from large to small diameter at the vertical extension.

The different angles investigated in the parameter study showed some interesting similarities and differences. The angles can be split into three categories. The first category contains the cases with angles $\alpha <= 45°$. In this group is categorized by recirculation zones around the step, and vortex structures forming at the edge of the step and in some cases the helical vortex structures shed from the cylinder. The second group contains the cases between $\alpha >= 45°$ and $\alpha < 70°$. This group shows some interesting phenomenons. At the step and above small there is vortex shedding which behaves similarly to von Karman vortex shedding behind the small cylinder.

The last group is the cases containing $\alpha = 70°$ and above. This group has a helical vortex forming along the curvature of the large cylinder. At cases where $\alpha >= 80°$ vortex shedding from the small cylinder is also observed. From the results and observations in this thesis, it is clear that the geometrical configurations affect the flow field and wake drastically. The curvature of the cylinder and the change in diameter affect the flow in its own way, and the angle of the step relative to the incoming flow changes the effect of the step.

In the parameter study, two cases showed vortex structures forming which differed significantly from the other cases. In case 3, $\alpha = 30°$ long elongated vortex structures formed directly behind the step and shed at a higher angle. In case 5, $\alpha = 60°$ vortex structures formed directly at the step. The vortex structures intertwined in a chain-link like fashion, and those vortex structures did not occur in any other cases.

9.1 Further Work

This master thesis is one of the first studies concerning flow around a concave curved cylinder with a change in diameter using Direct Numerical Simulation. The parameter investigated have been the geometry of the cylinder. And the different geometrical configurations have been tested and compared with previous studies with relate-able geometries.

From the initial geometrical simulations in Chapter 5, the horizontal cylinder with both a change in step and parallel flow should be investigated further. The Reynolds number was kept at a constant value of $Re_D = 600$. Previous studies with a square step from Barbosa-Saldana et al. (2013) among others found interesting results with higher Reynolds number. As the results from Chapter 5 showed

interesting similarities in the development of flow induced phenomenons such as the recirculation zone in front of the step, it would be interesting to investigate if an increase in Reynolds number have a produces a recirculation zone behind the step, as is the case with the square step. Furthermore, an experimental study for validation purposes is also in order, and the experimental study may also show how the flow develops at even higher Reynolds numbers.

Following some interesting results from the initial case with a switch from a large diameter cylinder at the vertical extension to a small diameter cylinder at the vertical extension showed some interesting similarities with previous studies. A parameter study with a a change from large diameter to small diameter is an interesting case and how the different geometrical configurations affect the flow field is of interest.

Building on the parameter study in thesis, a more thorough study of the flow at α angles close to zero. The cases with α values below 45° showed some interesting trends and while there was not enough time to conduct ores simulations at lower angles, the results of the cases in this thesis can provide a starting point for further investigating, and the results found can be used as an a guideline to what flow phenomenons occur and how they change with the different angles. As the cases presented in this study have changes the angle with a ratio of 15° at angles lower than 60°, it is difficult to deduce at what angles the different flow phenomenons change behaviour. A more thorough study can give more concrete results.

A single case with the horizontal extension and curvature consisting a change in diameter to the small cylinder at the start of the vertical extension was conducted. The introduction of the step suppressed the strong vertical velocity induced by the curvature. A more thorough study containing with steps at different angles on the curvature should be investigated to see how the step counteracts the vertical flow. Furthermore, as the change from large to small diameter along the curvature is the opposite what this thesis have investigated, it could be very interesting to see what configuration is optimal for the application of seabed risers.

Staggered buoyancy elements on risers have a large diameter ratio in relation to their length. A more realistic scenario could therefore be changing the diameter at small sections in a staggered manner, modeling a buoyancy elements on the riser and investigating small buoyancy elements affect the flow.

Bibliography

Barbosa-Saldana, J., A. Morales-Contreras, , Jiménez-Bernal, J., Gutiérrez-Torres, C., A. Moreno-Pacheco, L., 05 2013. Numerical and experimental results for flow through a forward facing step channel. IJRRAS 15, 177.

Batchelor, G. K., 2000. An introduction to fluid dynamics. Cambridge university press.

Bearman, P. W., Takamoto, M., 1988. Vortex shedding behind rings and discs. Fluid Dynamics Research 3, 214,218.

Brooks, I., 01 1987. A pragmatic approach to vortex-induced vibrations of a drilling riser.

Buresti, G., 2012. Elements of fluid dynamics. Vol. 3. World Scientific Publishing Company.

Cengel, Y. A., Cimbala, J. M., 2010. Fluid Mechanics. McGraw-Hill.

Dunn, W., Tavoularis, S., 2006. Experimental studies of vortices shed from cylinders with a step-change in diameter. Journal of Fluid Mechanics 555, 409–437.

Faltinsen, O., 1990. Sea Loads on ships and offshore structures. Cambridge.

Gallardo, J. P., Andersson, H. I., Pettersen, B., 2013. Effects of free-slip boundary conditions on the flow around a curved circular cylinder. Computers & fluids 86, 389–394.

Han, L., Feb. 2015. Recirculation zone developing downstream of an expansion in a shallow open-channel flow. Theses, INSA de Lyon.

Hattori, H., Nagano, Y., 2010. Investigation of turbulent boundary layer over forward-facing step via direct numerical simulation. International Journal of Heat and Fluid Flow 31 (3), 284 – 294, sixth International Symposium on Turbulence and Shear Flow Phenomena.

Hermas, M., 2017. Installing a welded riser on a pipeline with a piggyback cable. Offshore Engineer Guide.

Holmes, S., Oakley, O., Raghavan, K., Constantinides, Y., 01 2008. Using cfd to study the effects of staggered buoyancy on dilling riser viv.

Hunt, J. C. R., Wray, A. A., Moin, P., 1988. Eddies, stream and convergent zones in turbulent flows. Center for Turbulence Research Report CTR-S88, 193.

Jeong, J., Hussain, F., 1995. On the identification of a vortex. Journal of Fluid Mechanics 285, 69.94.

Jiang, F., Pettersen, B., Andersson, H., Kim, J., Kim, S., 09 2018a. Wake behind a concave curved cylinder. Physical Review Fluids 3, 094804.

Jiang, F., Pettersen, B., Andersson, H. I., 08 2017. The turbulent wake behind a concave curved cylinder at re = 3900.

Jiang, F., Pettersen, B., Andersson, H. I., 2018b. Influences of upstream extensions on flow around a curved cylinder. European Journal of Mechanics - B/Fluids 67, 79 – 86.

Jiang, F., Pettersen, B., Andersson, H. I., 2019. Turbulent wake behind a concave curved cylinder. Journal of Fluid Mechanics (under review).

Lamb, H., 1945. Hydrodynamics. Dover Books on Physics. Dover publications.

Lesieur, M., 1987. Turbulence in Fluids. Kluwer Academic Publishers.

Levold, P., 6 2012. Viscous flow around finite length circular cylinder. Master's thesis, Norwegian University of Science and Technology.

Li, S., Nguyen, C., 2010. Dynamic response of deepwater lazy-wave catenary riser. Deep Offshore Technology International.

Manhart, M., 2004. A zonal grid algorithm for dns of turbulent boundary layers. Computers Fluids 33, 435–461.

Manhart, M., Deng, G., Huttl, T., Tremlay, F., Segal, A., Friedrich, R., Piquet, J., Wesseling, P., 1998. The minimal turbulent flow unit as a test case for three different computer codes. Notes on numerical fluid mechanics 66.

Miliou, A., De Vecchi, A., Sherwin, S., Graham, J., 2007. Wake dynamics of external flow past a curved circular cylinder with the free stream aligned with the plane of curvature. J. Fluid Mech. 592, 89–115.

Morton, C., Yarusevych, S., 08 2010. Vortex shedding in the wake of a step cylinder. Physics of Fluids - PHYS FLUIDS 22.

Morton, C., Yarusevych, S., Carvajal, I., 08 2009. Study of flow over a step cylinder. Applied Mechanics and Materials 15, 9–14.

Norberg, C., 12 1992. An experimental study of the flow around cylinders joined with a step in diameter.

Patel, M., Seyed, F., 1995. Review of flexible riser modelling and analysis techniques. Engineering Structures 17 (4), 293 – 304, the structural mechanics and service life predictions of marine cables, umbilicals and flexible pipes.

Peller, N., Le-Duc, A., Tremblay, F., Manhart, M., 2006. high-order stable interpolations for immersed boundary methods. International journal for numerical methods in fluids 54, 1175.1193.

Roache, P. J., 1998. Verification and Validation in Computaional Science and Engineering. Hermosa Pub.

Roshko, A., 01 1954a. On the development of turbulent wakes from vortex streets. NACA Report, Printed in USA 1191.

Roshko, A., 1954b. On the drag and shedding frequency of two-dimensional bluff bodies. National Advisory committee for Aeronautics 3169.

Shenoy, A. R., Kleinstreuer, C., 2008. Flow over a thin circular disk at low to moderate reynolds numbers. Journal of Fluid Mechanics 605, 253–262.

Sonin, E. B., Feb 2012. Dynamics of helical vortices and helical-vortex rings. EPL (Europhysics Letters) 97 (4), 46002.

Strandenes, H., Manhart, M., M, A., Pasichnyk, I., Schanderl, W., 2016. Improving scalability for the cfd software mglet.

Stuer, H., Gyr, A., Kinzelbach, W., 07 1999. Laminar separation on a forward facing step. European Journal of Mechanics B-fluids - EUR J MECH B-FLUID 18, 675–692.

Tannehill, J. C., Anderson, D. A., Pletcher, R. H., 1997. Computational Fluid Mechanics and Heat Transfer. TaylorFrancis.

Termopedia, 11 2018. Shear layer, taken from Termopedia.com/shear Layer.

Tian, C., Jiang, F., Pettersen, B., Anderson, H. I. (Eds.), 2019. Turbulent wake behind a step cylinder at Re 3900. Vol. 17.

Tian, C., Jiang, F., Pettersen, B., Andersson, H., 05 2017a. Numerical investigation of flow around a step cylinder.

Tian, C., Jiang, F., Pettersen, B., Andersson, H. I., 2017b. Antisymmetric vortex interactions in the wake behind a step cylinder. Physics of Fluids 29 (10), 101704.

Tian, X., Ong, M. C., Yang, J., Myrhaug, D., 2016. Large-eddy simulations of flow normal to a circular disk at re=1.5105. Computers Fluids 140, 422 – 434.

Tremblay, F., 2015. Numerical studies of viscous flow around bluff bodies. Ph.D. thesis.

Tutty, O. R., 2008. Flow along a long thin cylinder. Journal of Fluid Mechanics 602, 1–37.

Vandiver, J., Peoples, W, W., 01 2003. The effect of staggered buoyancy modules on flow-induced vibration of marine risers.

Veldman, A., 1 2012. Computational fluid dynamics. University of Groningen, Faculty of mathematics and natural sciences, lecture notes in applied mathematics.

White, F. M., 2006. Viscous Fluid Flow. McGraw-Hill.

Wilhelm, D., Kleiser, L., Dec 2002. Application of a spectral element method to two-dimensional forward-facing step flow. Journal of Scientific Computing 17 (1), 619–627.

Williamson, C. H. K., 1989. Oblique and parallel modes of vortex shedding in the wake of a circular cylinder at low reynolds numbers. Journal of Fluid Mechanics 206.

Williamson, J., 1980. Low-storage runge-kutta schemes. Journal of Computational Physics 35, 48.56.

Zdravkovich, M., 1997. Flow around circular cylinders. Oxford science publications.

Appendix A

Grid Independence Study

A.1 Power Density Spectrum of cross-flow velocity v

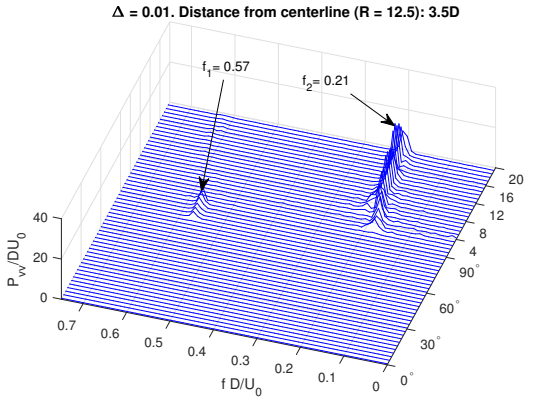

Figure A.1: Power density spectrum of the cross flow velocity at $[R/D, y/D] = [16, 0]$ stretching from the start of the horizontal extension to the end of the vertical extension in the domain. The dominating frequencies at the curve and vertical extension are displayed if they exist. $Re_D = 600$, finest gridsize $\Delta = 0.01$.

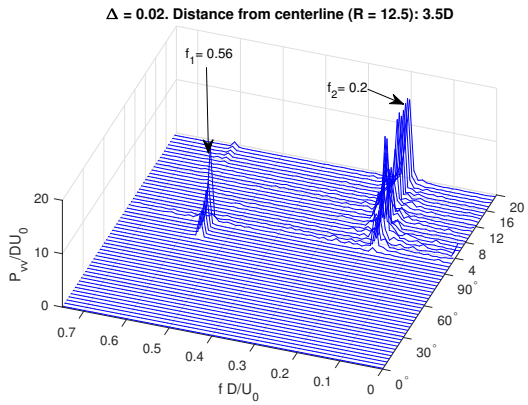

Figure A.2: Power density spectrum of the cross flow velocity at $[R/D, y/D] = [16, 0]$ stretching from the start of the horizontal extension to the end of the vertical extension in the domain. The dominating frequencies at the curve and vertical extension are displayed if they exist. $Re_D = 600$, finest gridsize $\Delta = 0.02$.

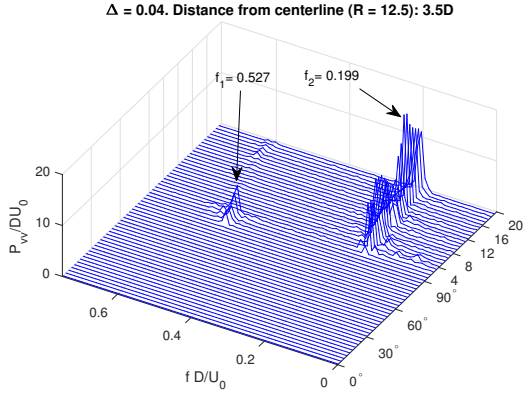

Figure A.3: Power density spectrum of the cross flow velocity at $[R/D, y/D] = [16, 0]$ stretching from the start of the horizontal extension to the end of the vertical extension in the domain. The dominating frequencies at the curve and vertical extension are displayed if they exist. $Re_D = 600$, finest gridsize $\Delta = 0.04$.

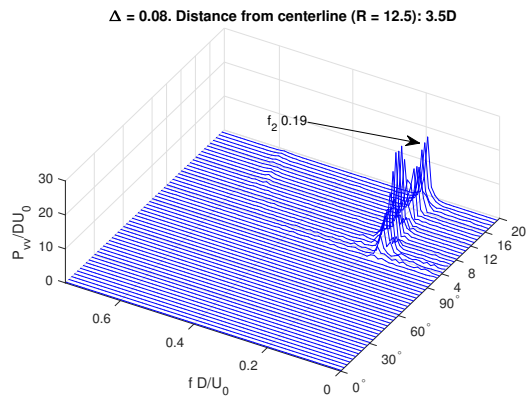

Figure A.4: Power density spectrum of the cross flow velocity at $[R/D, y/D] = [16, 0]$ stretching from the start of the horizontal extension to the end of the vertical extension in the domain. The dominating frequencies at the curve and vertical extension are displayed if they exist. $Re_D = 600$, finest gridsize $\Delta = 0.08$.

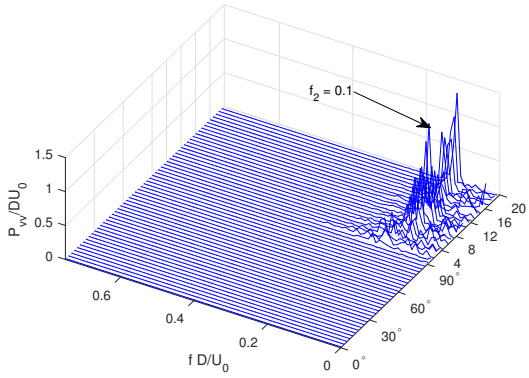

Figure A.5: Power density spectrum of the cross flow velocity at $[R/D, y/D] = [16, 0]$ stretching from the start of the horizontal extension to the end of the vertical extension in the domain. The dominating frequencies at the curve and vertical extension are displayed if they exist. $Re_D = 600$, finest gridsize $\Delta = 0.1$.

A.2 Velocity and pressure profiles

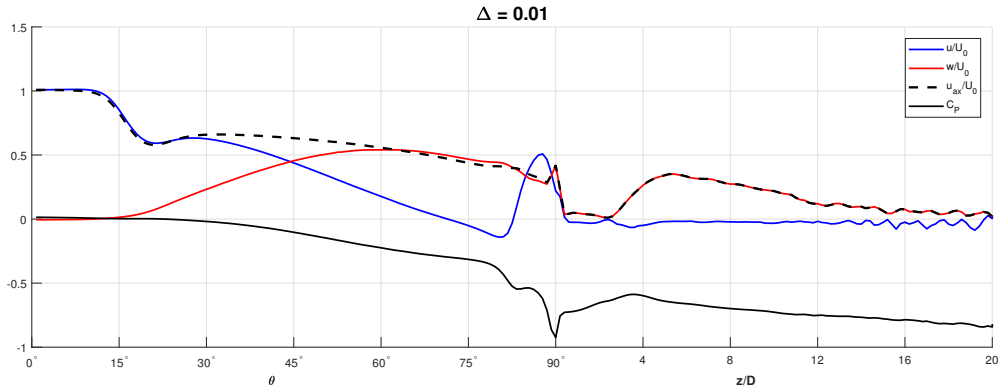

Figure A.6: Profiles of the horizontal velocity component u, the vertical velocity component w and the pressure coefficient C_P for for the grid refinement study. The velocity and pressure was sampled at $R = 13.2D$, i.e. $0.2D$ behind the large cylinder surface and $0.6D$ behind the small cylinder surface. The samples are located in the $y/D = 0$ plane along the the curvature from the start of the horizontal extension to at the start of the vertical extension. $Re_D = 600$, finest gridsize $\Delta = 0.01$.

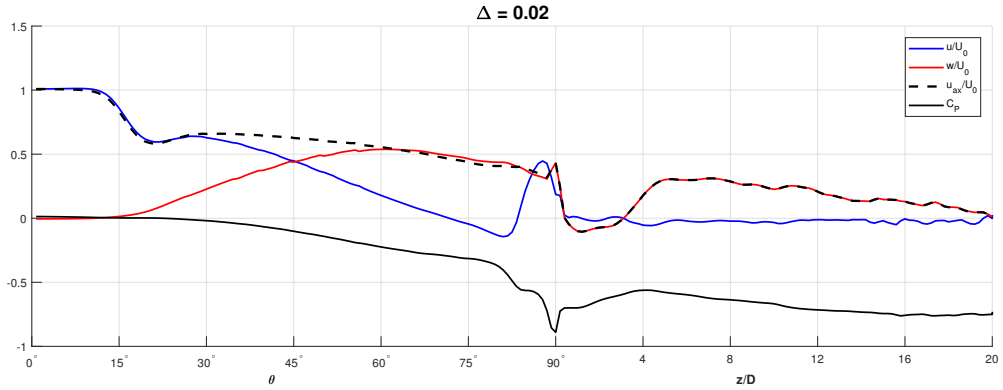

Figure A.7: Profiles of the horizontal velocity component u, the vertical velocity component w and the pressure coefficient C_P for for the grid refinement study. The velocity and pressure was sampled at $R = 13.2D$, i.e. $0.2D$ behind the large cylinder surface and $0.6D$ behind the small cylinder surface. The samples are located in the $y/D = 0$ plane along the the curvature from the start of the horizontal extension to at the start of the vertical extension. $Re_D = 600$, finest gridsize $\Delta = 0.02$.

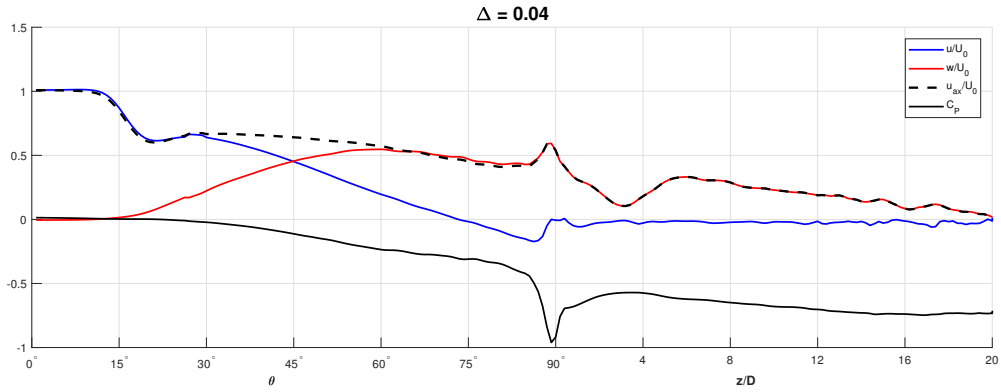

Figure A.8: Profiles of the horizontal velocity component u, the vertical velocity component w and the pressure coefficient C_P for for the grid refinement study. The velocity and pressure was sampled at $R = 13.2D$, i.e. $0.2D$ behind the large cylinder surface and $0.6D$ behind the small cylinder surface. The samples are located in the $y/D = 0$ plane along the the curvature from the start of the horizontal extension to at the start of the vertical extension. $Re_D = 600$, finest gridsize $\Delta = 0.04$.

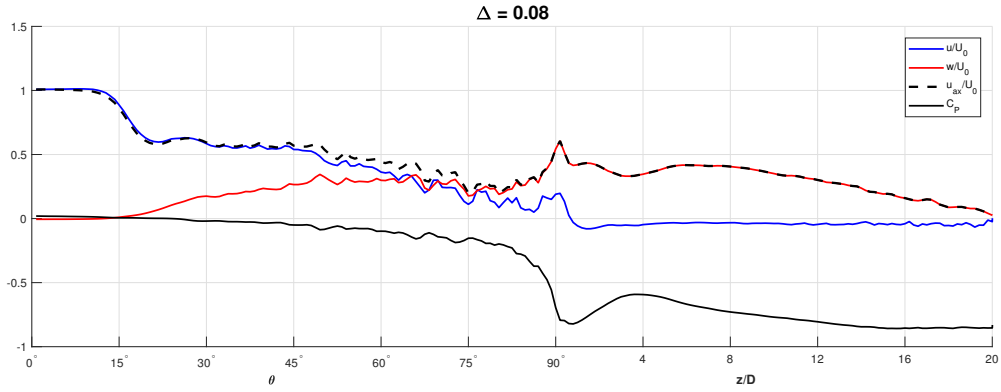

Figure A.9: Profiles of the horizontal velocity component u, the vertical velocity component w and the pressure coefficient C_P for for the grid refinement study. The velocity and pressure was sampled at $R = 13.2D$, i.e. $0.2D$ behind the large cylinder surface and $0.6D$ behind the small cylinder surface. The samples are located in the $y/D = 0$ plane along the the curvature from the start of the horizontal extension to at the start of the vertical extension. $Re_D = 600$, finest gridsize $\Delta = 0.08$.

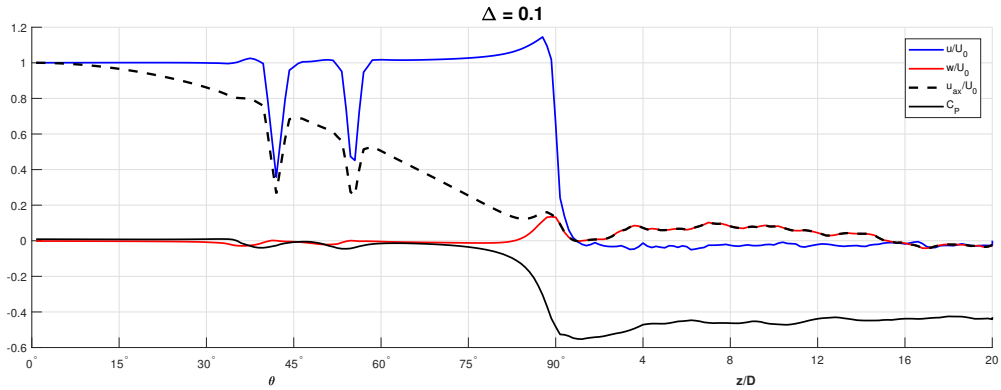

Figure A.10: Profiles of the horizontal velocity component u, the vertical velocity component w and the pressure coefficient C_P for for the grid refinement study. The velocity and pressure was sampled at $R = 13.2D$, i.e. $0.2D$ behind the large cylinder surface and $0.6D$ behind the small cylinder surface. The samples are located in the $y/D = 0$ plane along the the curvature from the start of the horizontal extension to at the start of the vertical extension. $Re_D = 600$, finest gridsize $\Delta = 0.1$.

Appendix B

Cylinder with a large diameter curvature and reduction in diameter at the start of vertical extension.

B.0.1 Pressure

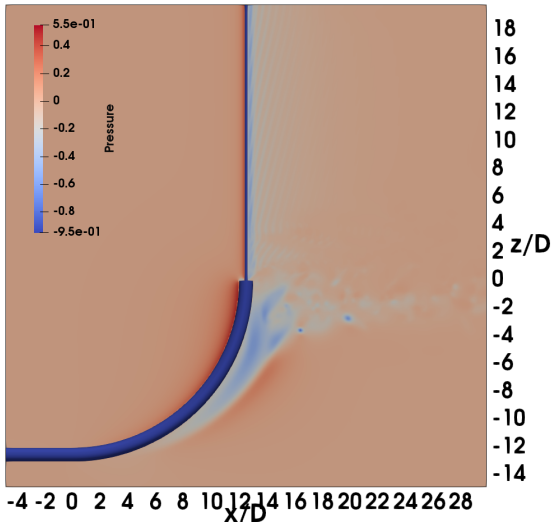

Figure B.1: Instantaneous pressure distribution in the $y/D = 0$ plane for the cylinder with a large diameter curvature and reduction in diameter at the vertical extension. The distribution is sampled at Re = 600 at time instant $t = 300s$. The values in the legend is the same as the parameter study cases.

B.0.2 Velocity

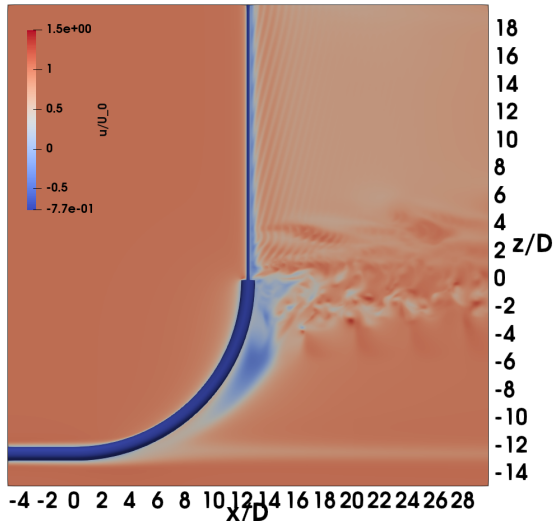

Figure B.2: Instantaneous distribution of the horizontal velocity component u for the cylinder with a large diameter curvature and reduction in diameter at the vertical extension. The distribution is sampled at Re = 600 at time instant $t = 300s$. The values in the legend is the same as the parameter study cases.

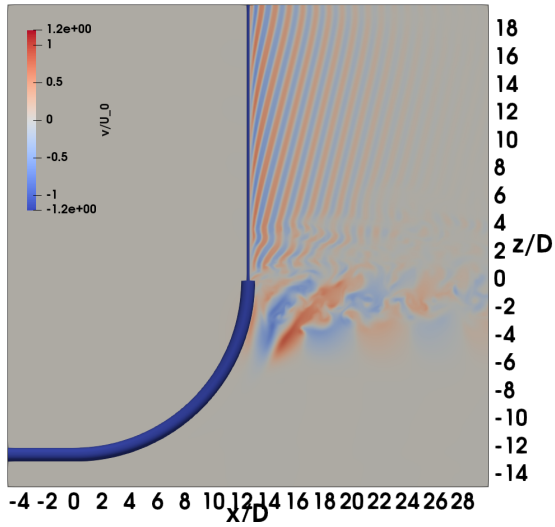

Figure B.3: Instantaneous distribution of the cross-flow velocity component v for the cylinder with a large diameter curvature and reduction in diameter at the vertical extension. The distribution is sampled at Re = 600 at time instant $t = 300s$. The values in the legend is the same as the parameter study cases.

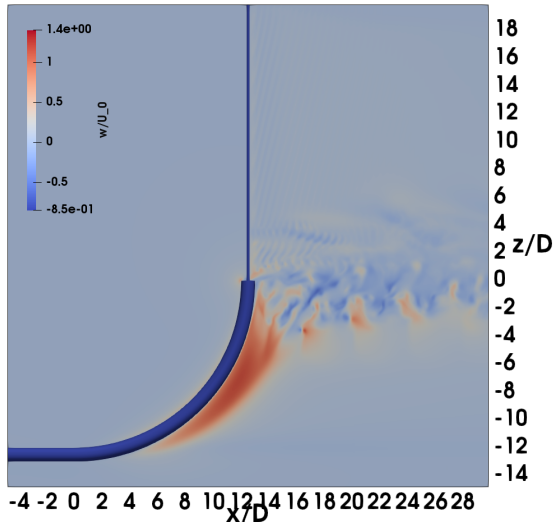

Figure B.4: Instantaneous distribution of the vertical velocity component w for the cylinder with a large diameter curvature and reduction in diameter at the vertical extension. The distribution is sampled at Re = 600 at time instant $t = 300s$. The values in the legend is the same as the parameter study cases.

B.0.3 Iso-volume of λ_2

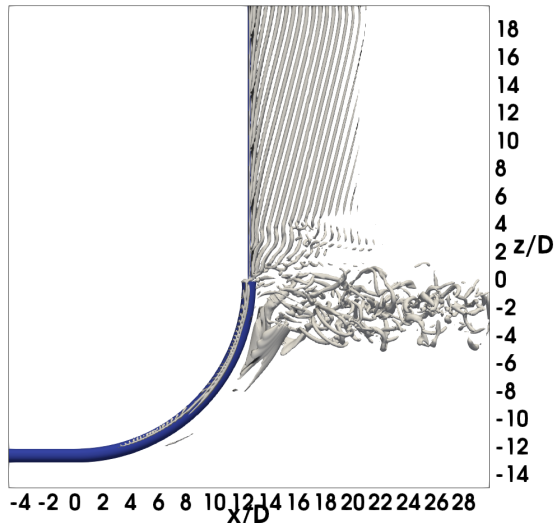

Figure B.5: Iso-contours of $\lambda_2 = -1$ for a fully developed flow for the cylinder with a large diameter curvature and reduction in diameter at the vertical extension. The distribution is sampled at Re = 600 at time instant $t = 300s$.

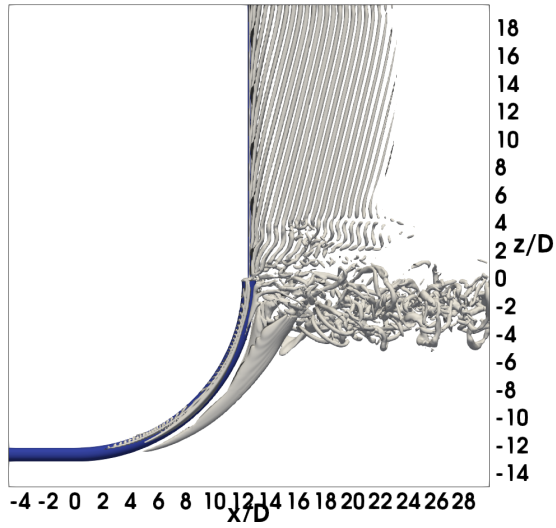

Figure B.6: Iso-contours of $\lambda_2 = -0.5$ for a fully developed flow for the cylinder with a large diameter curvature and reduction in diameter at the vertical extension. The distribution is sampled at Re = 600 at time instant $t = 300s$.

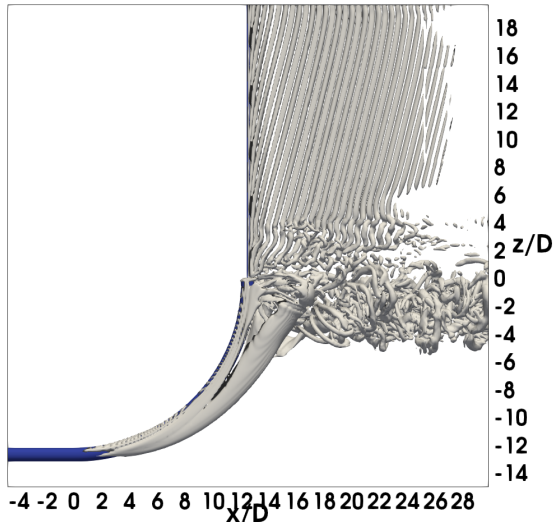

Figure B.7: Iso-contours of $\lambda_2 = -0.1$ for a fully developed flow for the cylinder with a large diameter curvature and reduction in diameter at the vertical extension. The distribution is sampled at Re = 600 at time instant $t = 300s$.

B.0.4 Vorticity

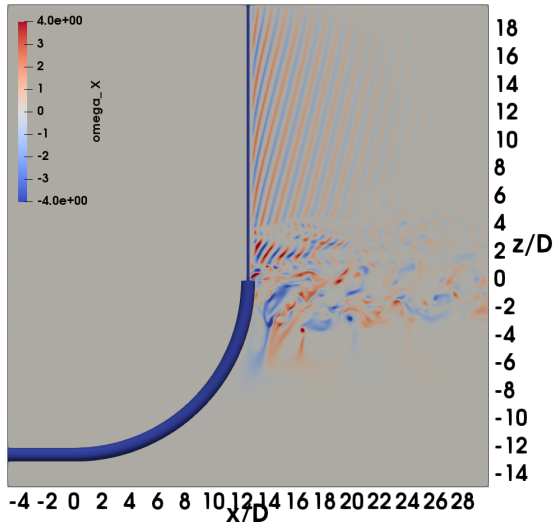

Figure B.8: Instantaneous distribution of the vorticity component ω_x for the cylinder with a large diameter curvature and reduction in diameter at the vertical extension. The distribution is sampled at Re = 600 at time instant $t = 300s$. The values in the legend is the same as the parameter study cases.

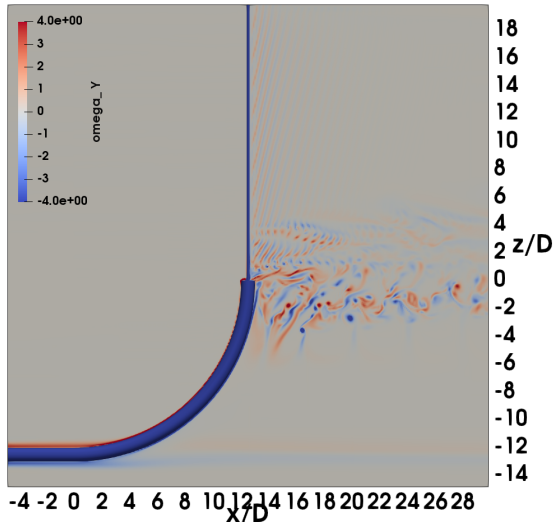

Figure B.9: Instantaneous distribution of the vorticity component ω_y for the cylinder with a large diameter curvature and reduction in diameter at the vertical extension. The distribution is sampled at Re = 600 at time instant $t = 300s$. The values in the legend is the same as the parameter study cases.

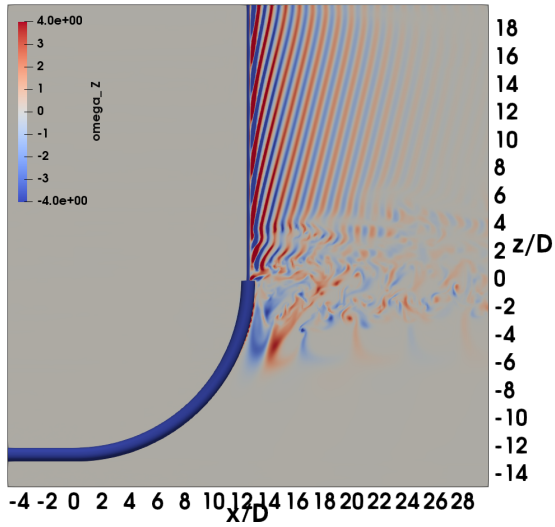

Figure B.10: Instantaneous distribution of the vorticity component ω_z for the cylinder with a large diameter curvature and reduction in diameter at the vertical extension. The distribution is sampled at Re = 600 at time instant $t = 300s$. The values in the legend is the same as the parameter study cases.

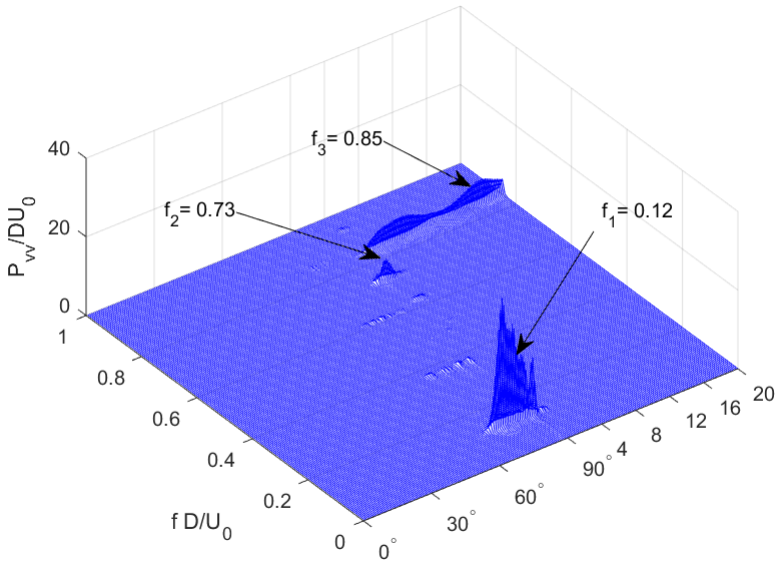

Figure B.11: Power density spectrum of the cross flow velocity.The cross flow velocity is sampled at a distance of 3.5 D behind the cylinder in the $y/D = 0$ plane for the cylinder with a large diameter curvature and reduction in diameter at the vertical extension. The text indicates the dominating frequencies at different regions in the simulation.The distribution is sampled at Re = 600 for 100 time units.

B.0.5 Velocity and Pressure Profiles

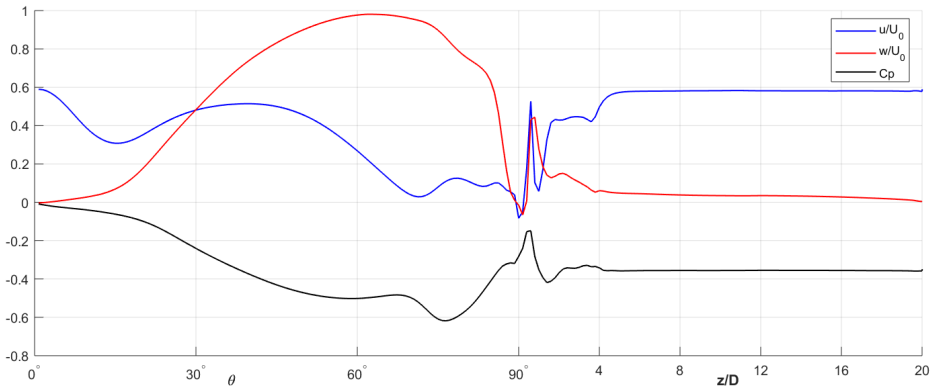

Figure B.12: Time averaged pressure and vertical, horizontal and axial velocity profiles, for for the cylinder with a large diameter curvature and reduction in diameter at the vertical extension. The values were sampled at $R = 13.2D$ i.e. $0.2D$ away from the large diameter cylinder surface ($0.6D$ from the small cylinder surface). The samples are located in the $y/D = 0$ plane along the the curvature from the start of the horizontal extension to at the end of the vertical extension. The velocities and pressure were time averaged for 100 seconds after the flow was fully developed

Appendix C

Parameter study

C.1 Case 1 - $\alpha = 0°$

C.1.1 Pressure

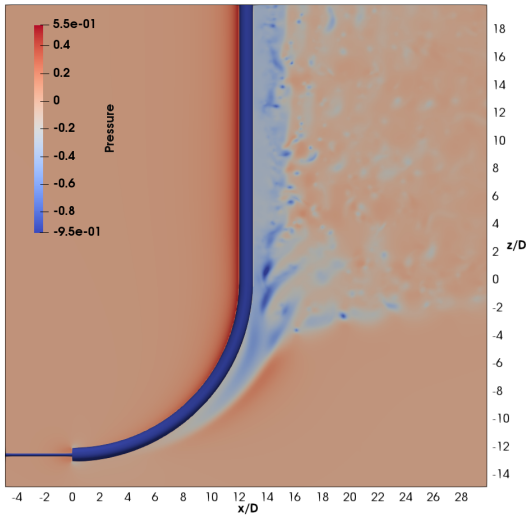

Figure C.1: Instantaneous pressure distribution in the $y/D = 0$ plane for case 1, $\alpha = 0°$. The distribution is sampled at Re = 600 at time instant $t = 300s$. The values in the legend is the same for all cases.

C.1.2 Velocity

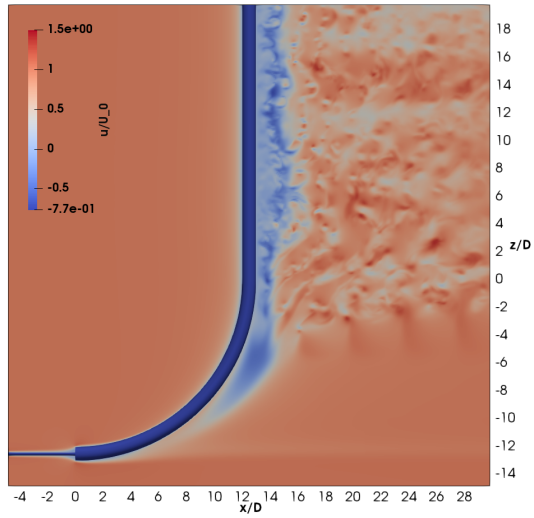

Figure C.2: Instantaneous distribution of the horizontal velocity component u for case 1, $\alpha = 0°$. The distribution is sampled at Re = 600 at time instant $t = 300s$. The values in the legend is the same for all cases.

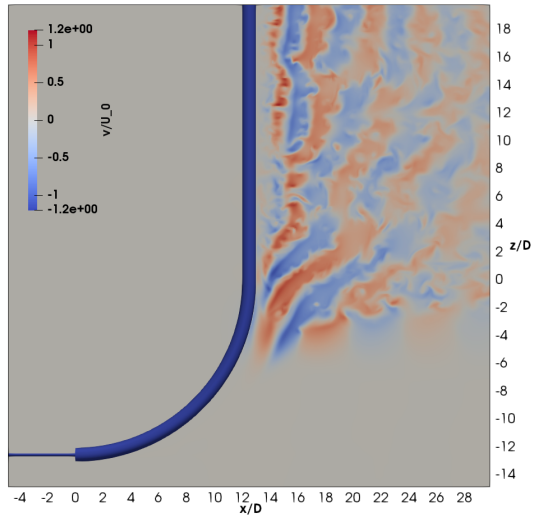

Figure C.3: Instantaneous distribution of the cross-flow velocity component v for case 1, $\alpha = 0°$. The distribution is sampled at Re = 600 at time instant $t = 300s$. The values in the legend is the same for all cases.

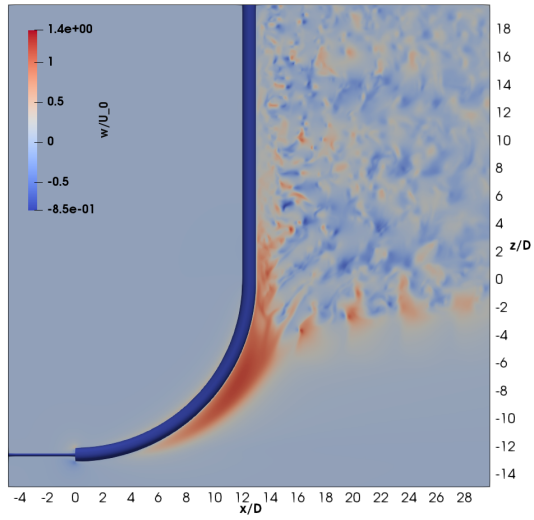

Figure C.4: Instantaneous distribution of the vertical velocity component w for case 1, $\alpha = 0°$. The distribution is sampled at Re = 600 at time instant $t = 300s$. The values in the legend is the same for all cases.

C.1.3 Iso-volume of λ_2

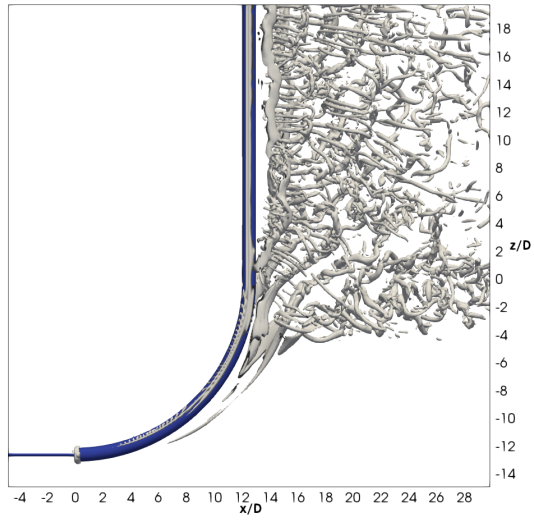

Figure C.5: Iso-contours of $\lambda_2 = -1$ for a fully developed flow for case 1, $\alpha = 0°$. The distribution is sampled at Re = 600 at time instant $t = 300s$.

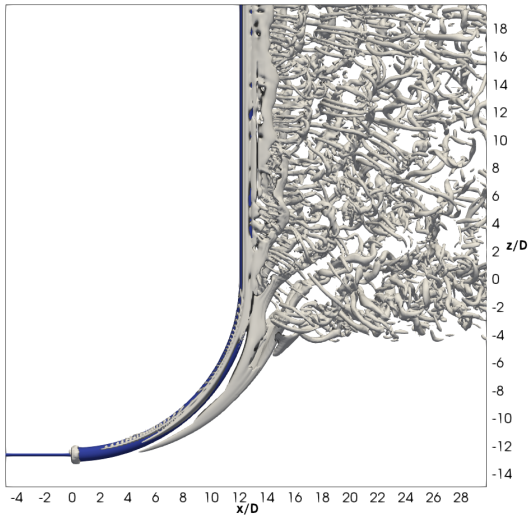

Figure C.6: Iso-contours of $\lambda_2 = -0.5$ for a fully developed flow for case 1, $\alpha = 0°$. The distribution is sampled at Re = 600 at time instant $t = 300s$.

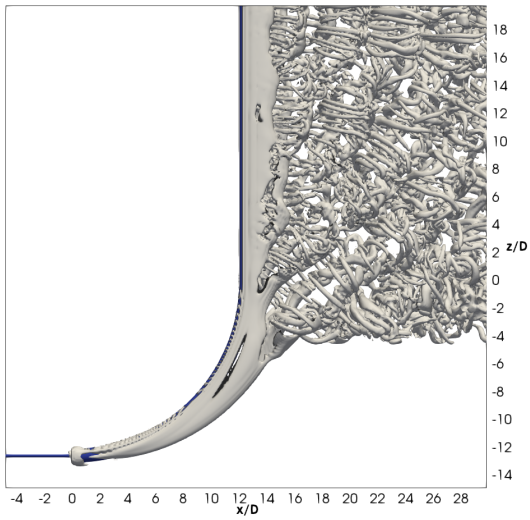

Figure C.7: Iso-contours of $\lambda_2 = -0.1$ for a fully developed flow for case 1, $\alpha = 0°$. The distribution is sampled at Re = 600 at time instant $t = 300s$.

C.1.4 Vorticity

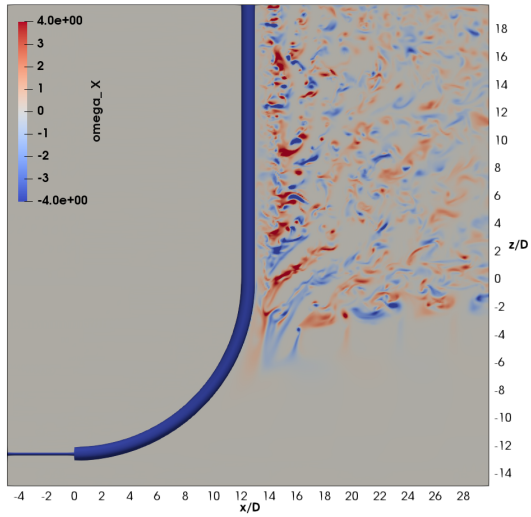

Figure C.8: Instantaneous distribution of the vorticity component ω_x for case 1, $\alpha = 0°$. The distribution is sampled at Re = 600 at time instant $t = 300s$. The values in the legend is the same for all cases.

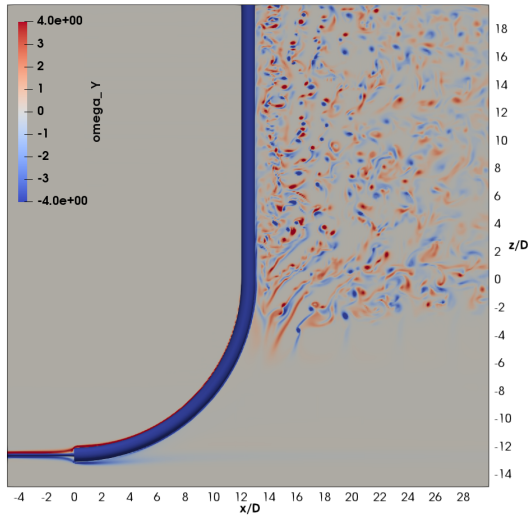

Figure C.9: Instantaneous distribution of the vorticity component ω_y for case 1, $\alpha = 0°$. The distribution is sampled at Re = 600 at time instant $t = 300s$. The values in the legend is the same for all cases.

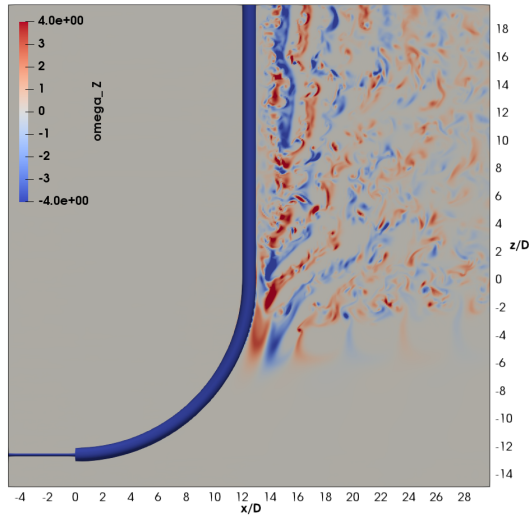

Figure C.10: Instantaneous distribution of the vorticity component ω_z for case 1, $\alpha = 0°$. The distribution is sampled at Re = 600 at time instant $t = 300s$. The values in the legend is the same for all cases.

C.1.5 Power Density Spectrum of Cross Flow Velocity v

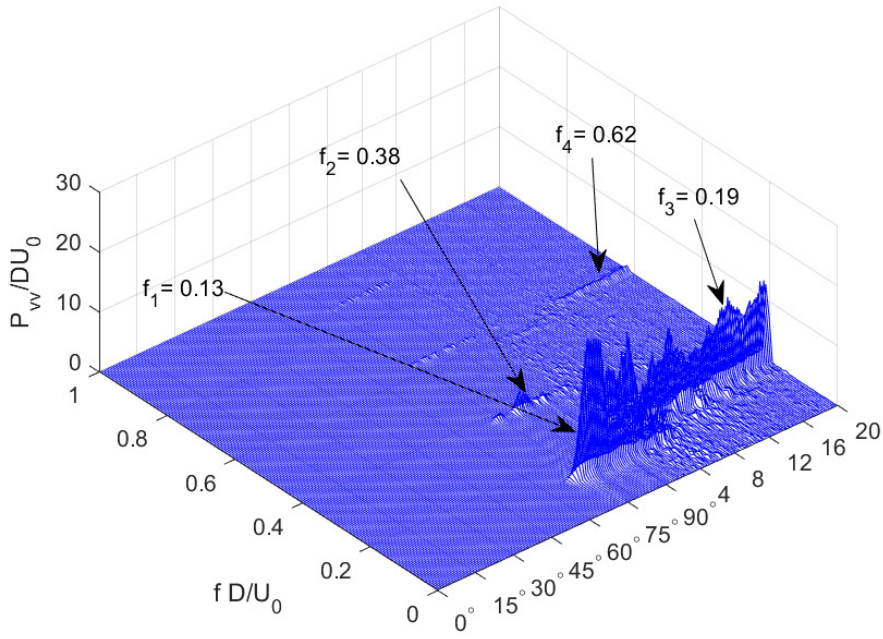

Figure C.11: Power density spectrum of the cross flow velocity.The cross flow velocity is sampled at a distance of 3.5 D behind the cylinder in the $y/D = 0$ plane for case 1, $\alpha = 0°$. . The text indicates the dominating frequencies at different regions in the simulation.The distribution is sampled at Re = 600 for 100 time units.

C.2 Case 2 - $\alpha = 15°$

C.2.1 Pressure

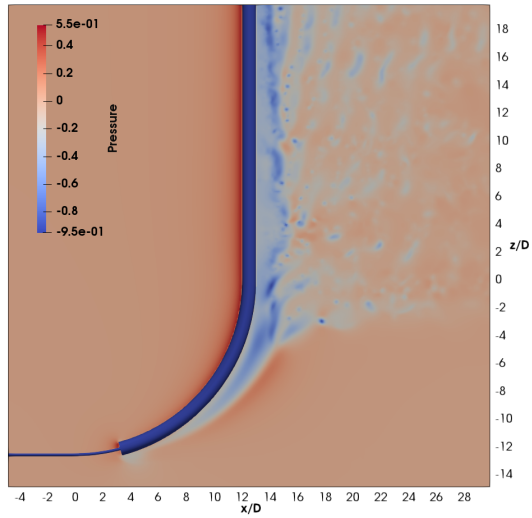

Figure C.12: Instantaneous pressure distribution in the $y/D = 0$ plane for case 1, $\alpha = 15°$. The distribution is sampled at Re = 600 at time instant $t = 300s$. The values in the legend is the same for all cases.

C.2.2 Velocity

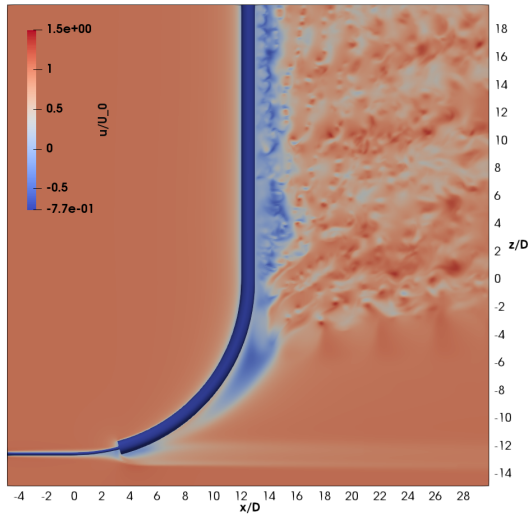

Figure C.13: Instantaneous distribution of the horizontal velocity component u for case 1, $\alpha = 15°$. The distribution is sampled at Re = 600 at time instant $t = 300s$. The values in the legend is the same for all cases.

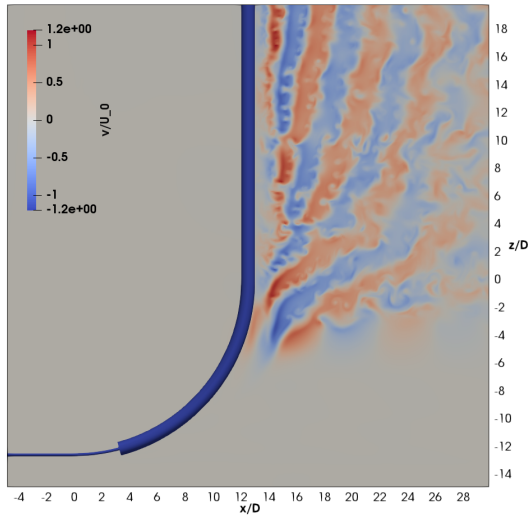

Figure C.14: Instantaneous distribution of the cross-flow velocity component v for case 1, $\alpha = 15°$. The distribution is sampled at Re = 600 at time instant $t = 300s$. The values in the legend is the same for all cases.

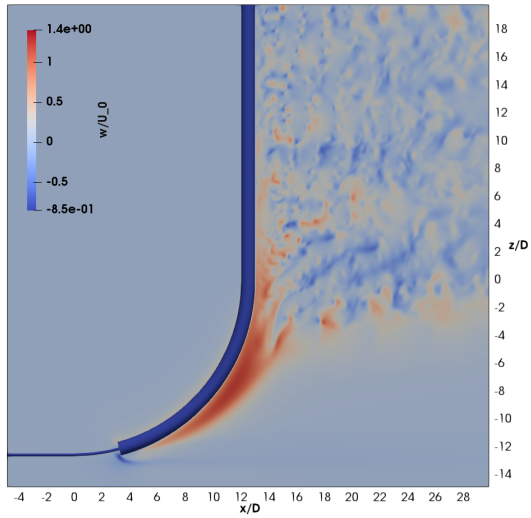

Figure C.15: Instantaneous distribution of the vertical velocity component w for case 1, $\alpha = 15°$. The distribution is sampled at Re = 600 at time instant $t = 300s$. The values in the legend is the same for all cases.

C.2.3 Iso-volume of λ_2

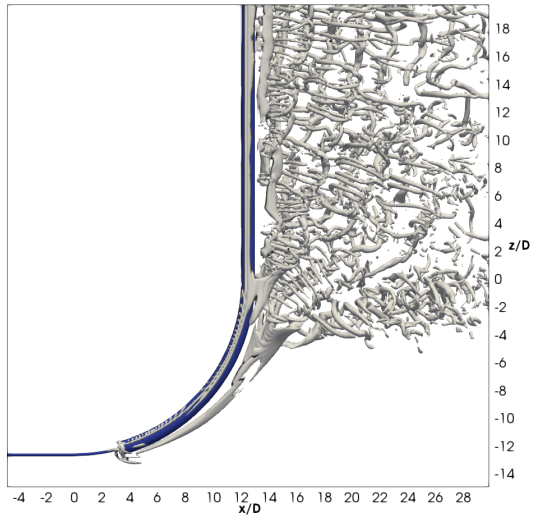

Figure C.16: Iso-contours of $\lambda_2 = -1$ for a fully developed flow for case 1, $\alpha = 15°$. The distribution is sampled at Re = 600 at time instant $t = 300s$.

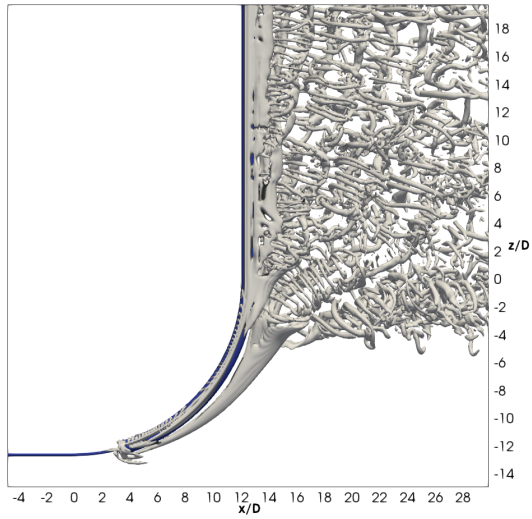

Figure C.17: Iso-contours of $\lambda_2 = -0.5$ for a fully developed flow for case 1, $\alpha = 15°$. The distribution is sampled at Re = 600 at time instant $t = 300s$.

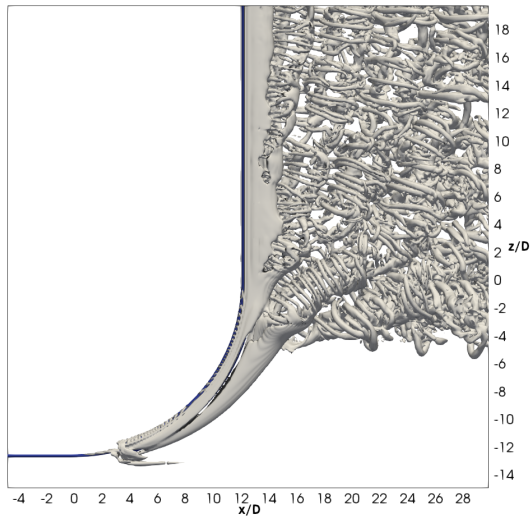

Figure C.18: Iso-contours of $\lambda_2 = -0.1$ for a fully developed flow for case 1, $\alpha = 15°$. The distribution is sampled at Re = 600 at time instant $t = 300s$.

C.2.4 Vorticity

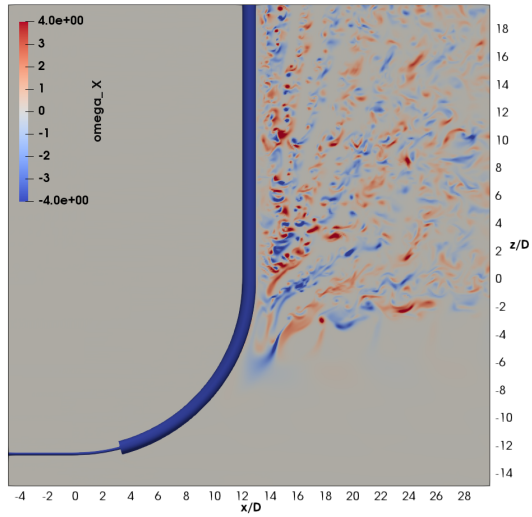

Figure C.19: Instantaneous distribution of the vorticity component ω_x for case 1, $\alpha = 15°$. The distribution is sampled at Re = 600 at time instant $t = 300s$. The values in the legend is the same for all cases.

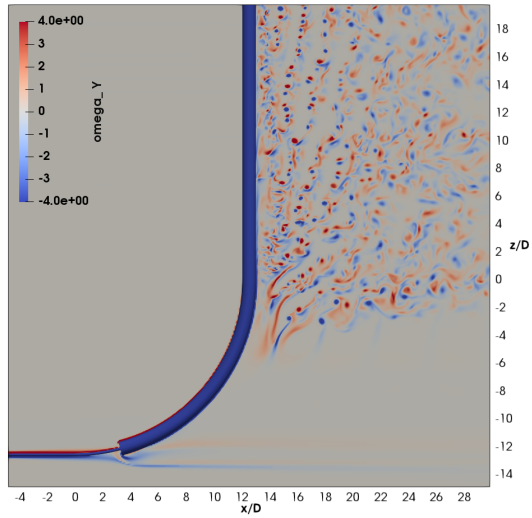

Figure C.20: Instantaneous distribution of the vorticity component ω_y for case 1, $\alpha = 15°$. The distribution is sampled at Re = 600 at time instant $t = 300s$. The values in the legend is the same for all cases.

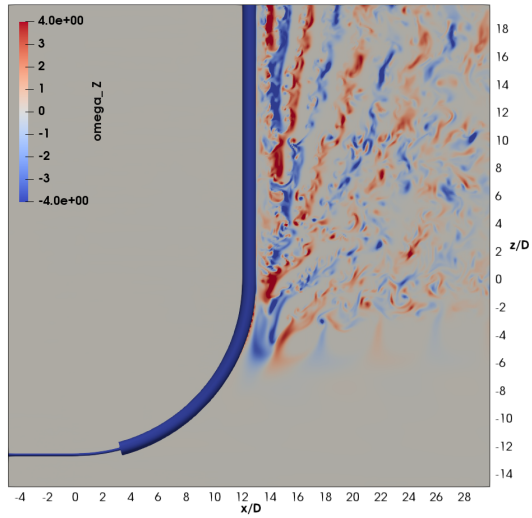

Figure C.21: Instantaneous distribution of the vorticity component ω_z for case 1, $\alpha = 15°$. The distribution is sampled at Re = 600 at time instant $t = 300s$. The values in the legend is the same for all cases.

C.2.5 Power Density Spectrum of Cross Flow Velocity v

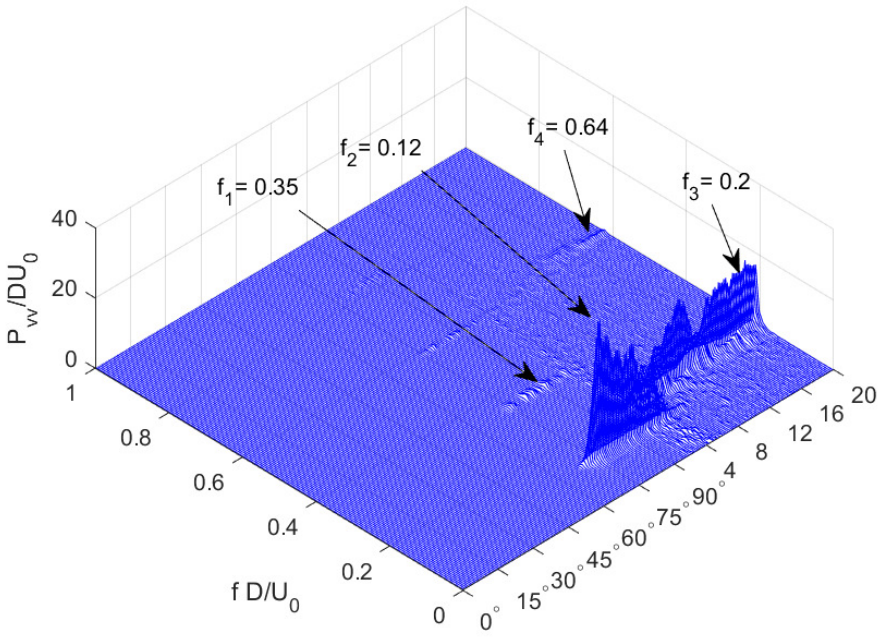

Figure C.22: Power density spectrum of the cross flow velocity for case 2, $\alpha = 15°$,.The cross flow velocity is sampled at a distance of 3.5 D behind the cylinder in the $y/D = 0$ plane. The text indicates the dominating frequencies at different regions in the simulation.The distribution is sampled at Re = 600 for 100 time units.

C.3 Case 3 - $\alpha = 30°$

C.3.1 Pressure

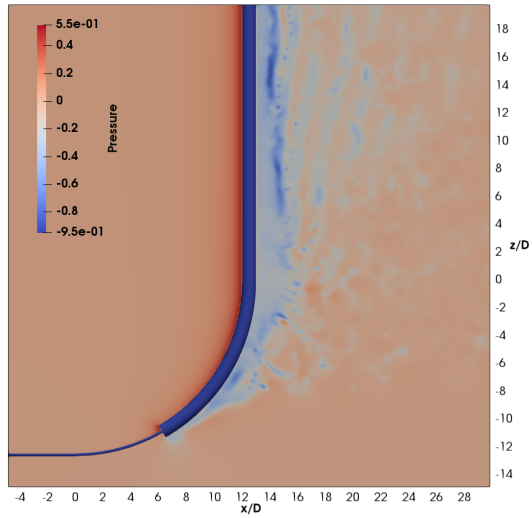

Figure C.23: Instantaneous pressure distribution in the $y/D = 0$ plane for case 3, $\alpha = 30°$. The distribution is sampled at Re = 600 at time instant $t = 300s$. The values in the legend is the same for all cases.

C.3.2 Velocity

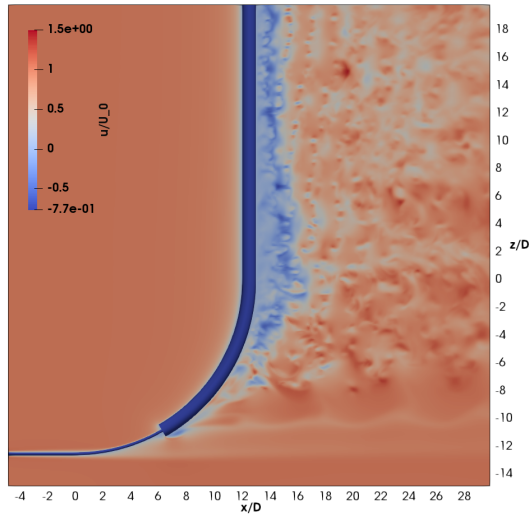

Figure C.24: Instantaneous distribution of the horizontal velocity component u for case 3, $\alpha = 30°$. The distribution is sampled at Re = 600 at time instant $t = 300s$. The values in the legend is the same for all cases.

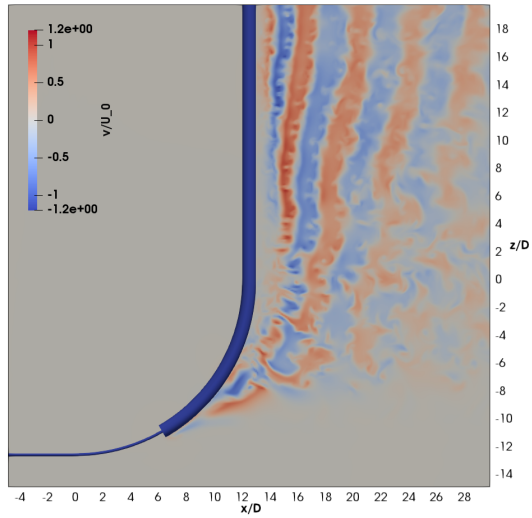

Figure C.25: Instantaneous distribution of the cross-flow velocity component v for case 3, $\alpha = 30°$. The distribution is sampled at Re = 600 at time instant $t = 300s$. The values in the legend is the same for all cases.

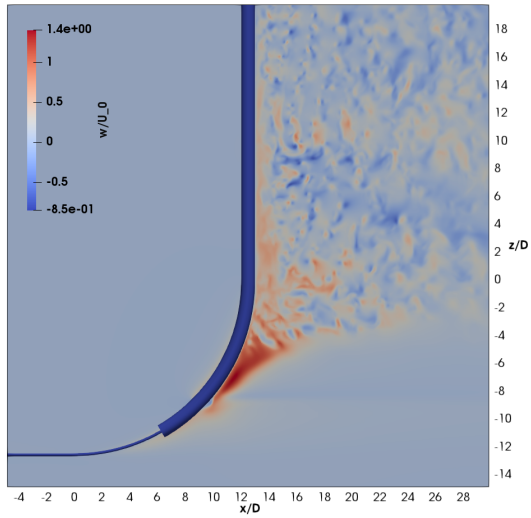

Figure C.26: Instantaneous distribution of the vertical velocity component w for case 3, $\alpha = 30°$. The distribution is sampled at Re = 600 at time instant $t = 300s$. The values in the legend is the same for all cases.

C.3.3 Iso-volume of λ_2

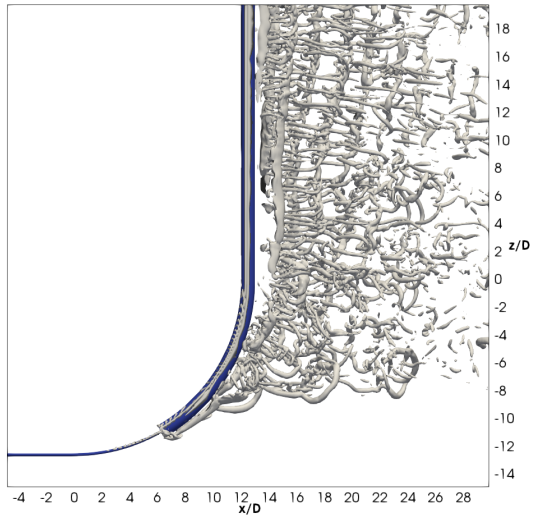

Figure C.27: Iso-contours of $\lambda_2 = -1$ for a fully developed flow for case 3, $\alpha = 30°$. The distribution is sampled at Re = 600 at time instant $t = 300s$.

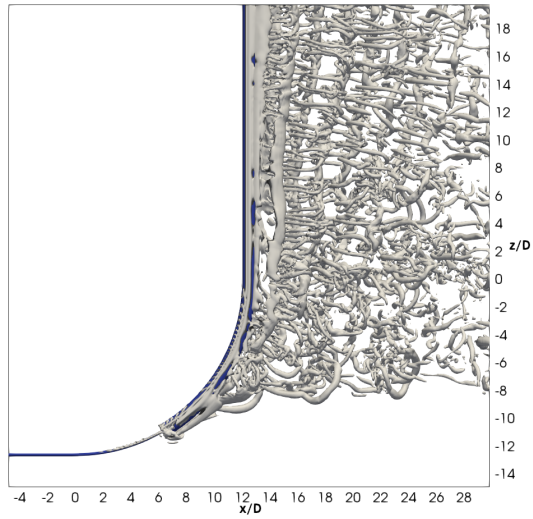

Figure C.28: Iso-contours of $\lambda_2 = -0.5$ for a fully developed flow for case 3, $\alpha = 30°$. The distribution is sampled at Re = 600 at time instant $t = 300s$.

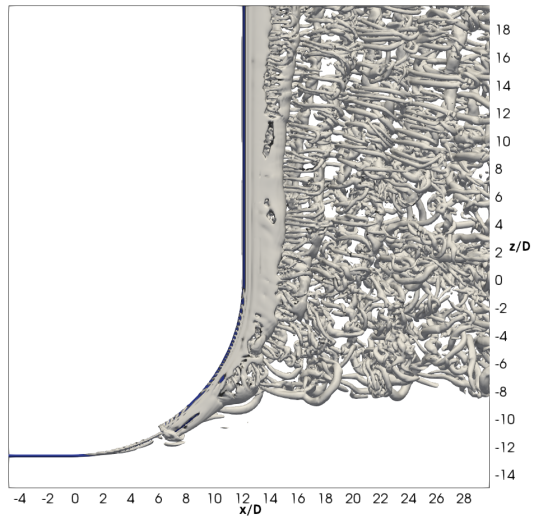

Figure C.29: Iso-contours of $\lambda_2 = -0.1$ for a fully developed flow for case 3, $\alpha = 30°$. The distribution is sampled at Re = 600 at time instant $t = 300s$.

C.3.4 Vorticity

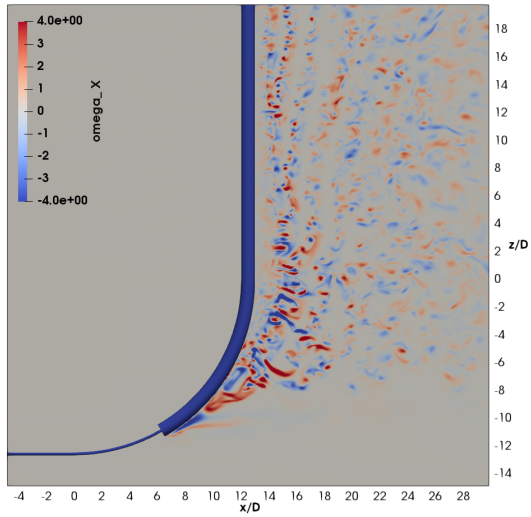

Figure C.30: Instantaneous distribution of the vorticity component ω_x for case 3, $\alpha = 30°$. The distribution is sampled at Re = 600 at time instant $t = 300s$. The values in the legend is the same for all cases.

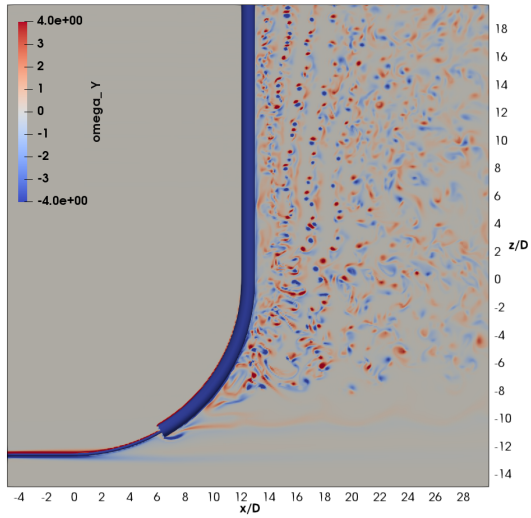

Figure C.31: Instantaneous distribution of the vorticity component ω_y for case 3, $\alpha = 30°$. The distribution is sampled at Re = 600 at time instant $t = 300s$. The values in the legend is the same for all cases.

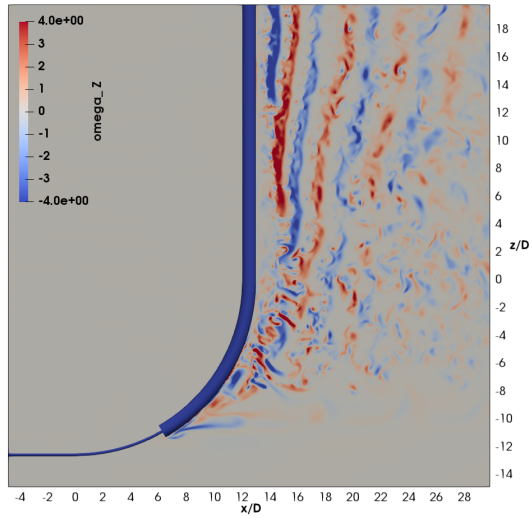

Figure C.32: Instantaneous distribution of the vorticity component ω_z for case 3, $\alpha = 30°$. The distribution is sampled at Re = 600 at time instant $t = 300s$. The values in the legend is the same for all cases.

C.3.5 Power Density Spectrum of Cross Flow Velocity v

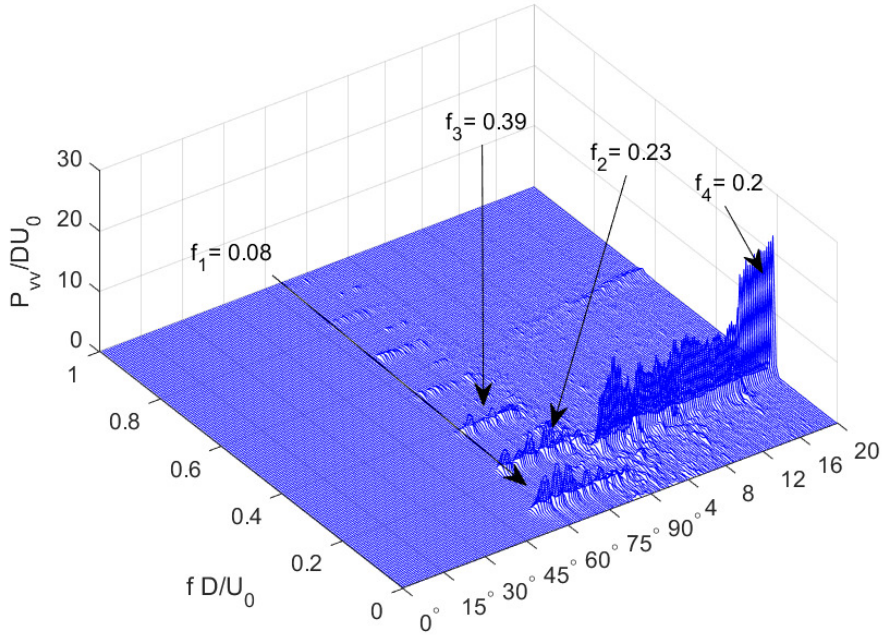

Figure C.33: Power density spectrum of the cross flow velocity for case 3, $\alpha = 30°$.The cross flow velocity is sampled at a distance of 3.5 D behind the cylinder in the $y/D = 0$ plane. The text indicates the dominating frequencies at different regions in the simulation.The distribution is sampled at Re = 600 for 100 time units.

C.4 Case 4 - $\alpha = 45°$

C.4.1 Pressure

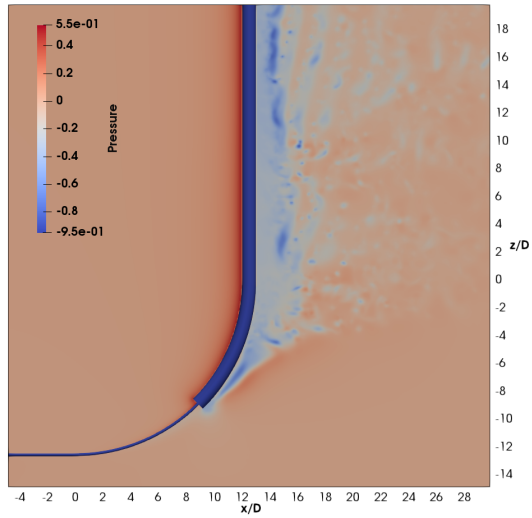

Figure C.34: Instantaneous pressure distribution in the $y/D = 0$ plane for case 4, $\alpha = 45°$. The distribution is sampled at Re = 600 at time instant $t = 300s$. The values in the legend is the same for all cases.

C.4.2 Velocity

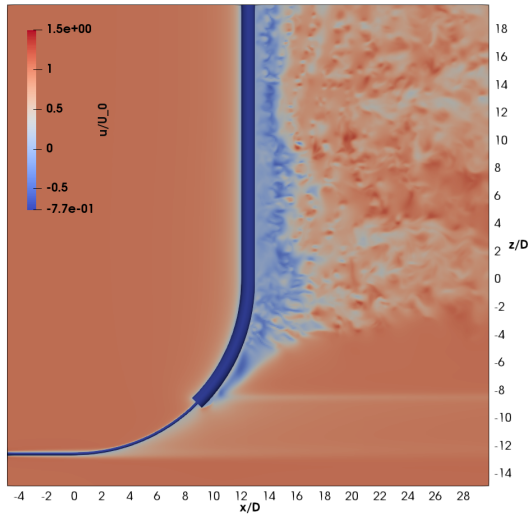

Figure C.35: Instantaneous distribution of the horizontal velocity component u for case 4, $\alpha = 45°$. The distribution is sampled at Re = 600 at time instant $t = 300s$. The values in the legend is the same for all cases.

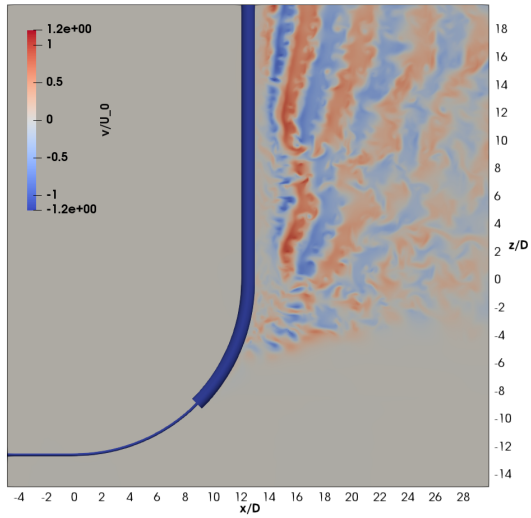

Figure C.36: Instantaneous distribution of the cross-flow velocity component v for case 4, $\alpha = 45°$. The distribution is sampled at Re = 600 at time instant $t = 300s$. The values in the legend is the same for all cases.

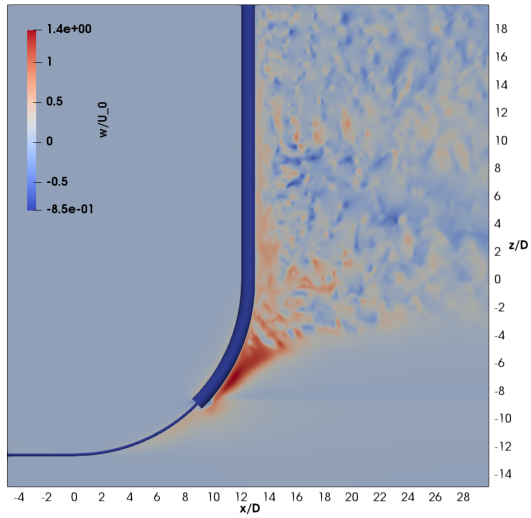

Figure C.37: Instantaneous distribution of the vertical velocity component w for case 4, $\alpha = 45°$. The distribution is sampled at Re = 600 at time instant $t = 300s$. The values in the legend is the same for all cases.

C.4.3 Iso-volume of λ_2

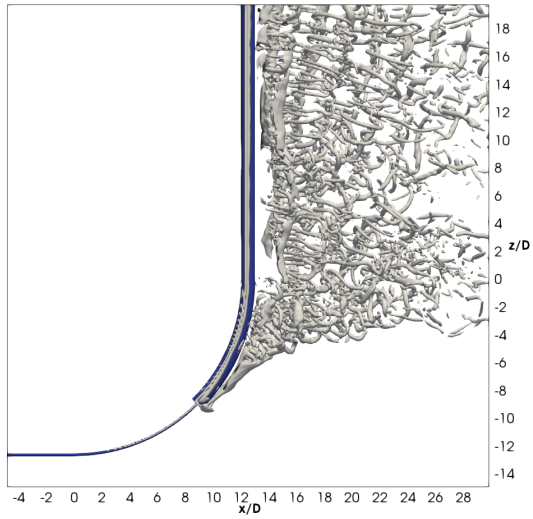

Figure C.38: Iso-contours of $\lambda_2 = -1$ for a fully developed flow for case 4, $\alpha = 45°$. The distribution is sampled at Re = 600 at time instant $t = 300s$.

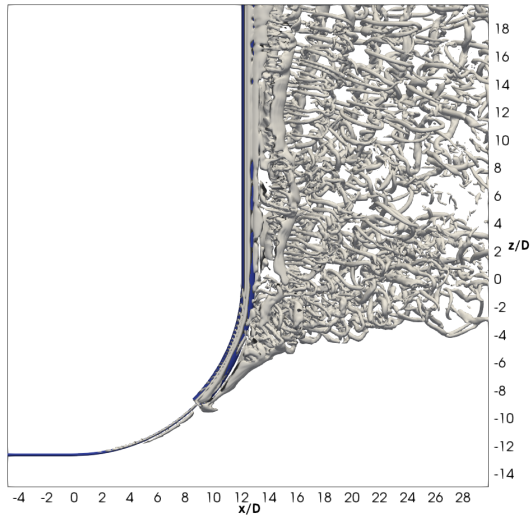

Figure C.39: Iso-contours of $\lambda_2 = -0.5$ for a fully developed flow for case 4, $\alpha = 45°$. The distribution is sampled at Re = 600 at time instant $t = 300s$.

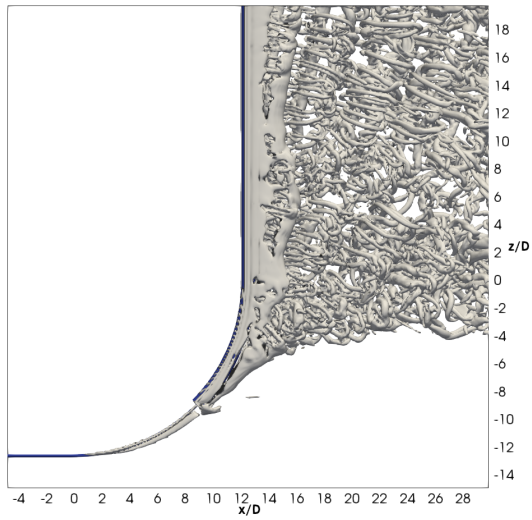

Figure C.40: Iso-contours of $\lambda_2 = -0.1$ for a fully developed flow for case 4, $\alpha = 45°$. The distribution is sampled at Re = 600 at time instant $t = 300s$.

C.4.4 Vorticity

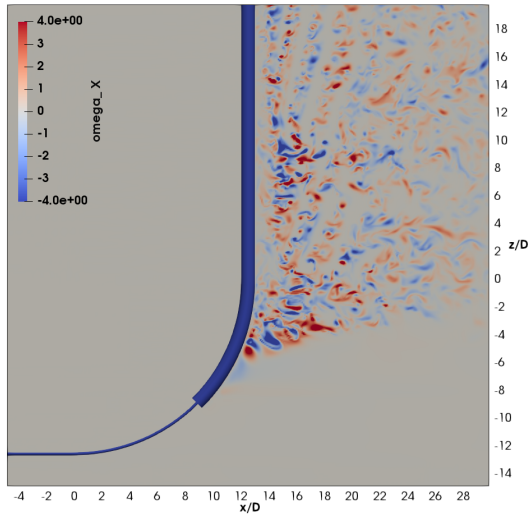

Figure C.41: Instantaneous distribution of the vorticity component ω_x for case 4, $\alpha = 45°$. The distribution is sampled at Re = 600 at time instant $t = 300s$. The values in the legend is the same for all cases.

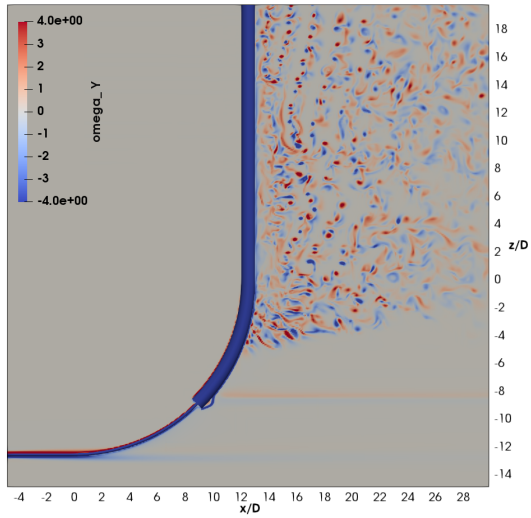

Figure C.42: Instantaneous distribution of the vorticity component ω_y for case 4, $\alpha = 45°$. The distribution is sampled at Re = 600 at time instant $t = 300s$. The values in the legend is the same for all cases.

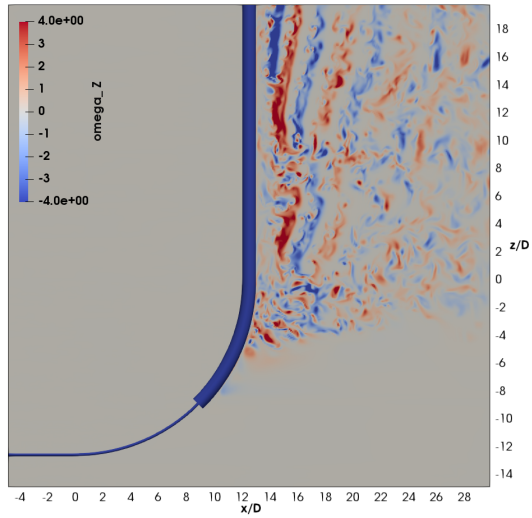

Figure C.43: Instantaneous distribution of the vorticity component ω_z for case 4, $\alpha = 45°$. The distribution is sampled at Re = 600 at time instant $t = 300s$. The values in the legend is the same for all cases.

C.4.5 Power Density Spectrum of Cross Flow Velocity v

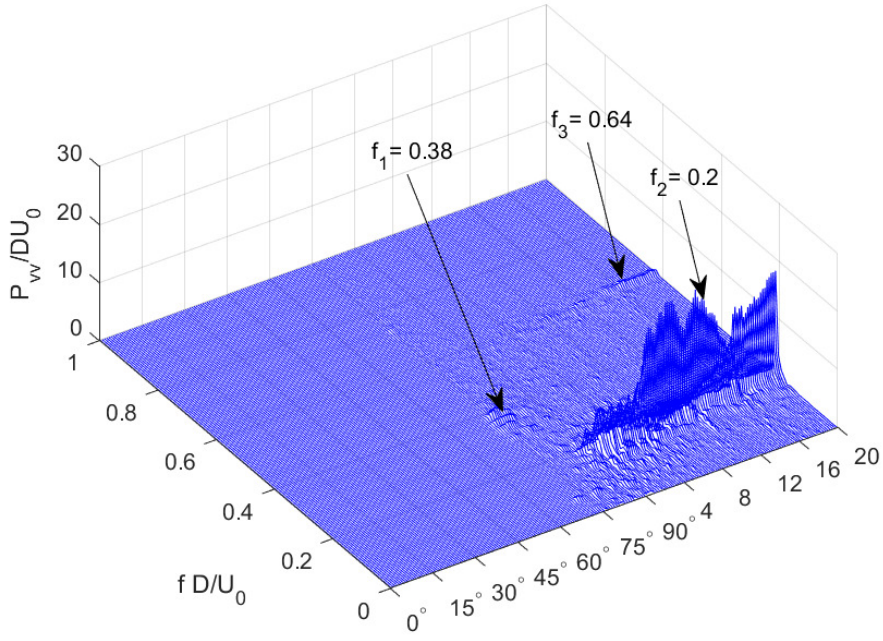

Figure C.44: Power density spectrum of the cross flow velocity for case 4, $\alpha = 45°$.The cross flow velocity is sampled at a distance of 3.5 D behind the cylinder in the $y/D = 0$ plane. The text indicates the dominating frequencies at different regions in the simulation.The distribution is sampled at Re = 600 for 100 time units.

C.5 Case 5 - $\alpha = 60°$

C.5.1 Pressure

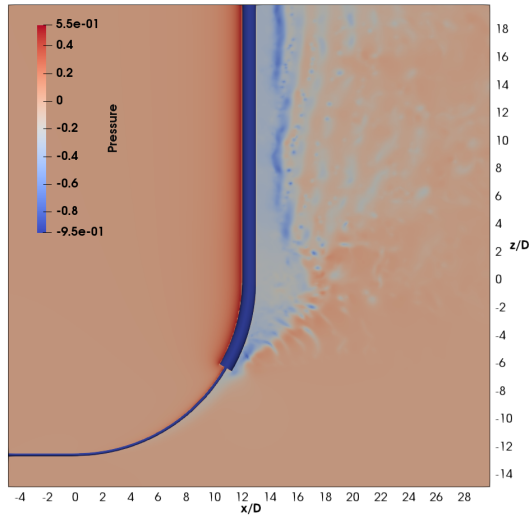

Figure C.45: Instantaneous pressure distribution in the $y/D = 0$ plane for case 5, $\alpha = 60°$. The distribution is sampled at Re = 600 at time instant $t = 300s$. The values in the legend is the same for all cases.

C.5.2 Velocity

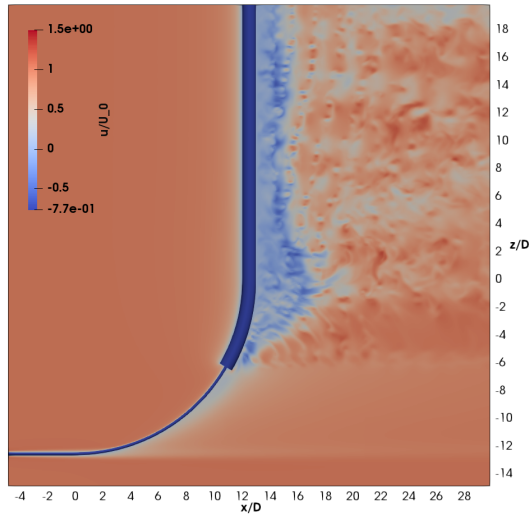

Figure C.46: Instantaneous distribution of the horizontal velocity component u for case 5, $\alpha = 60°$. The distribution is sampled at Re = 600 at time instant $t = 300s$. The values in the legend is the same for all cases.

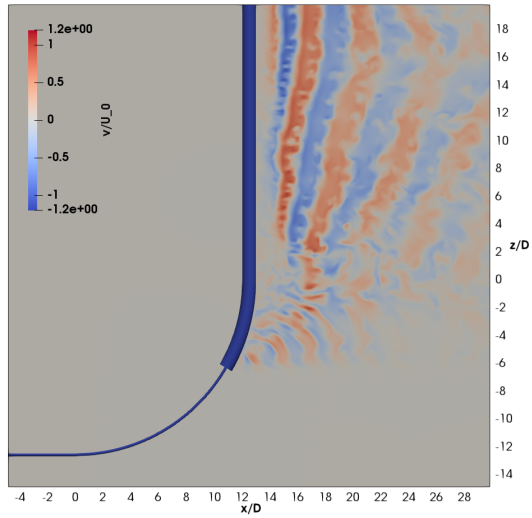

Figure C.47: Instantaneous distribution of the cross-flow velocity component v for case 5, $\alpha = 60°$. The distribution is sampled at Re = 600 at time instant $t = 300s$. The values in the legend is the same for all cases.

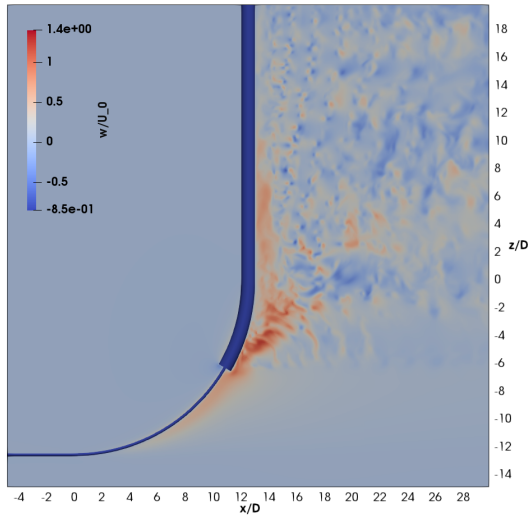

Figure C.48: Instantaneous distribution of the vertical velocity component w for case 5, $\alpha = 60°$. The distribution is sampled at Re = 600 at time instant $t = 300s$. The values in the legend is the same for all cases.

C.5.3 Iso-volume of λ_2

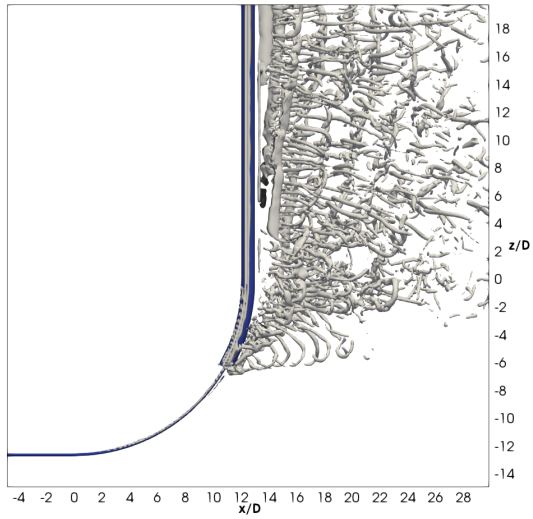

Figure C.49: Iso-contours of $\lambda_2 = -1$ for a fully developed flow for case 5, $\alpha = 60°$. The distribution is sampled at Re = 600 at time instant $t = 300s$.

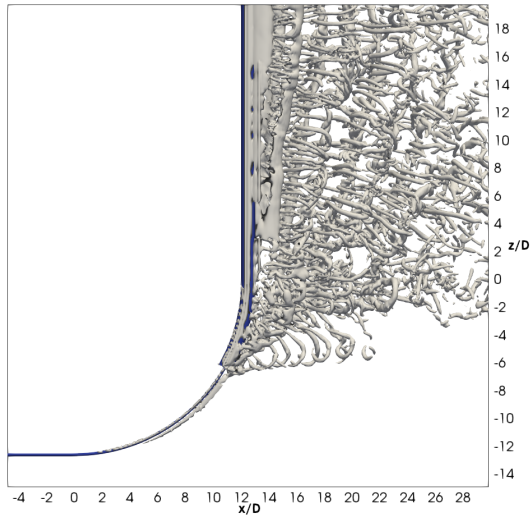

Figure C.50: Iso-contours of $\lambda_2 = -0.5$ for a fully developed flow for case 5, $\alpha = 60°$. The distribution is sampled at Re = 600 at time instant $t = 300s$.

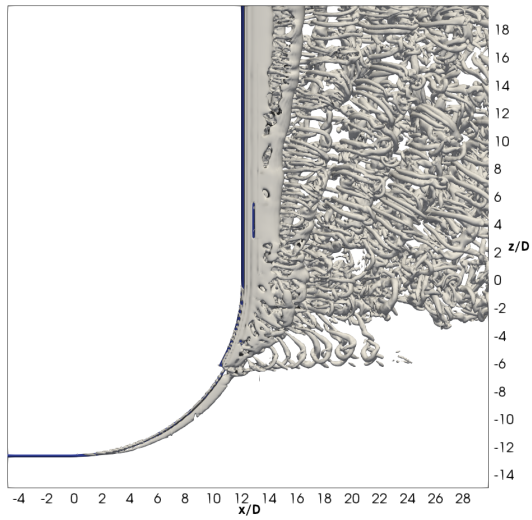

Figure C.51: Iso-contours of $\lambda_2 = -0.1$ for a fully developed flow for case 5, $\alpha = 60°$. The distribution is sampled at Re = 600 at time instant $t = 300s$.

C.5.4 Vorticity

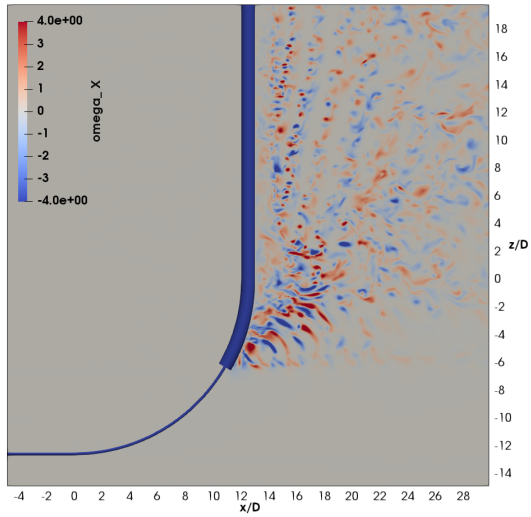

Figure C.52: Instantaneous distribution of the vorticity component ω_x for case 5, $\alpha = 60°$. The distribution is sampled at Re = 600 at time instant $t = 300s$. The values in the legend is the same for all cases.

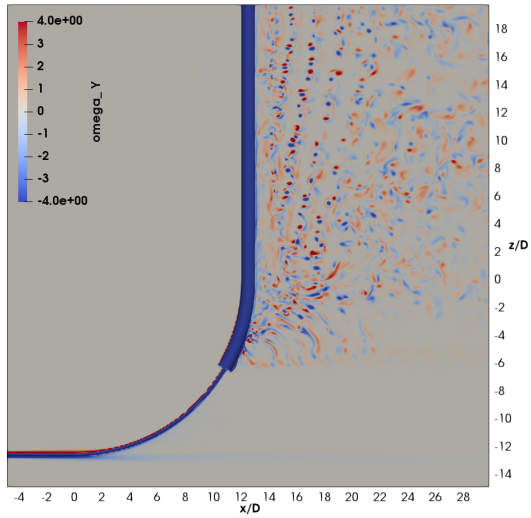

Figure C.53: Instantaneous distribution of the vorticity component ω_y for case 5, $\alpha = 60°$. The distribution is sampled at Re = 600 at time instant $t = 300s$. The values in the legend is the same for all cases.

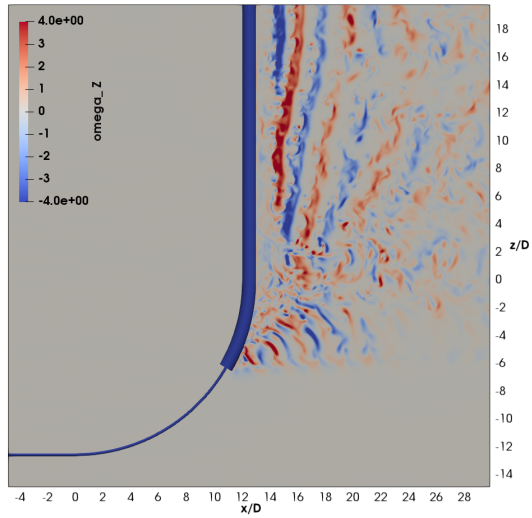

Figure C.54: Instantaneous distribution of the vorticity component ω_z for case 5, $\alpha = 60°$. The distribution is sampled at Re = 600 at time instant $t = 300s$. The values in the legend is the same for all cases.

C.5.5 Power Density Spectrum of Cross Flow Velocity v

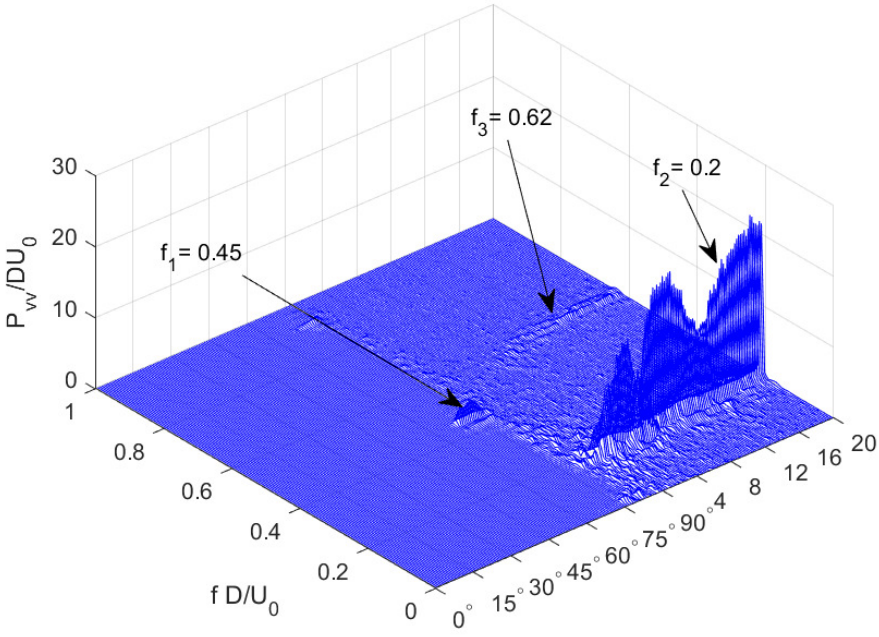

Figure C.55: Power density spectrum of the cross flow velocity for case 5, $\alpha = 60°$.The cross flow velocity is sampled at a distance of 3.5 D behind the cylinder in the $y/D = 0$ plane. The text indicates the dominating frequencies at different regions in the simulation.The distribution is sampled at Re = 600 for 100 time units.

C.6 Case 6 - $\alpha = 70°$

C.6.1 Pressure

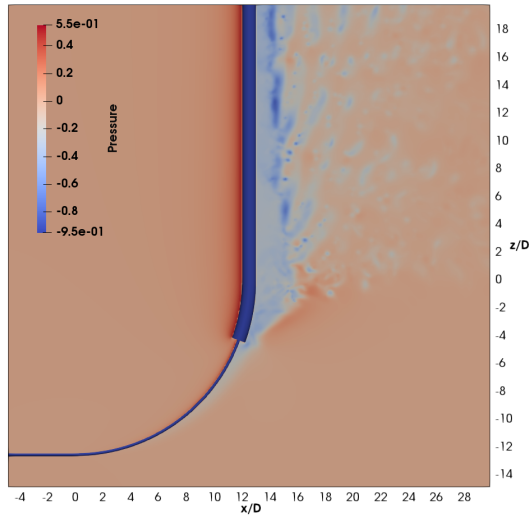

Figure C.56: Instantaneous pressure distribution in the $y/D = 0$ plane for case 6, $\alpha = 70°$. The distribution is sampled at Re = 600 at time instant $t = 300s$. The values in the legend is the same for all cases.

C.6.2 Velocity

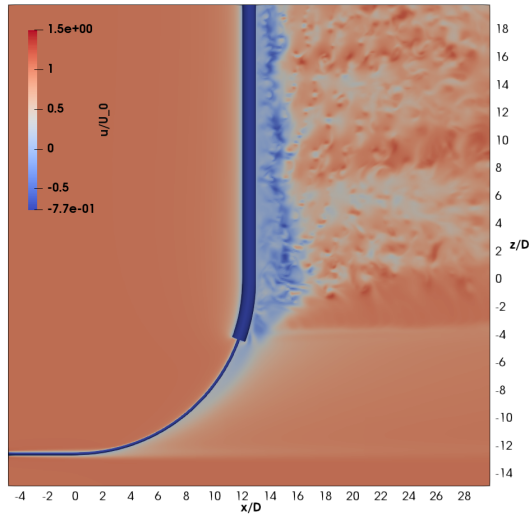

Figure C.57: Instantaneous distribution of the horizontal velocity component u for case 6, $\alpha = 70°$. The distribution is sampled at Re = 600 at time instant $t = 300s$. The values in the legend is the same for all cases.

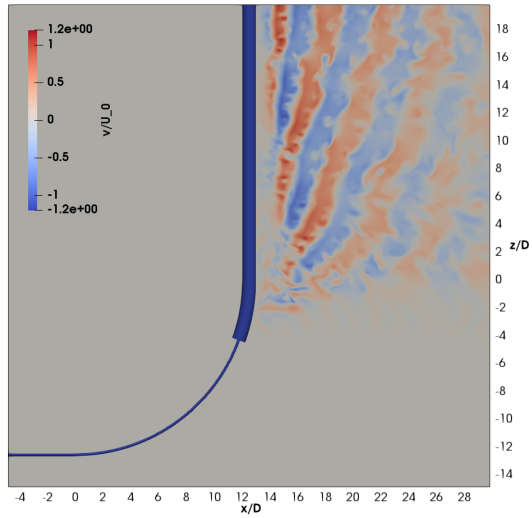

Figure C.58: Instantaneous distribution of the cross-flow velocity component v for case 6, $\alpha = 70°$. The distribution is sampled at Re = 600 at time instant $t = 300s$. The values in the legend is the same for all cases.

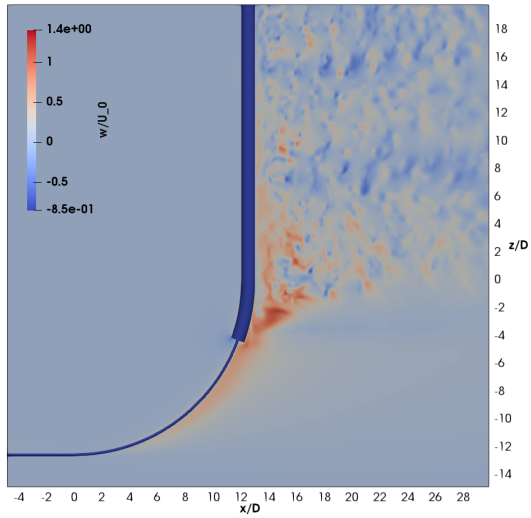

Figure C.59: Instantaneous distribution of the vertical velocity component w for case 6, $\alpha = 70°$. The distribution is sampled at Re = 600 at time instant $t = 300s$. The values in the legend is the same for all cases.

C.6.3 Iso-volume of λ_2

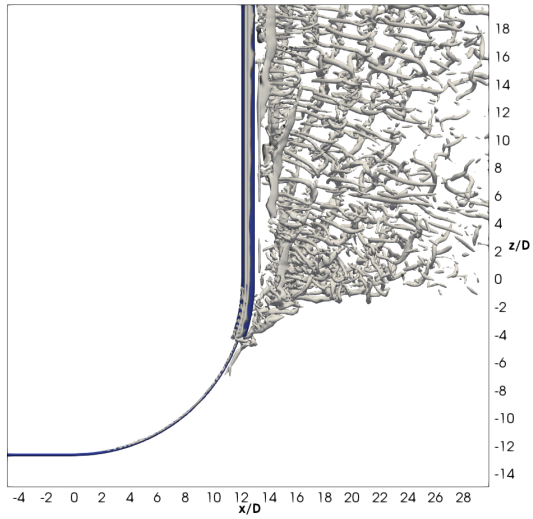

Figure C.60: Iso-contours of $\lambda_2 = -1$ for a fully developed flow for case 6, $\alpha = 70°$. The distribution is sampled at Re = 600 at time instant $t = 300s$.

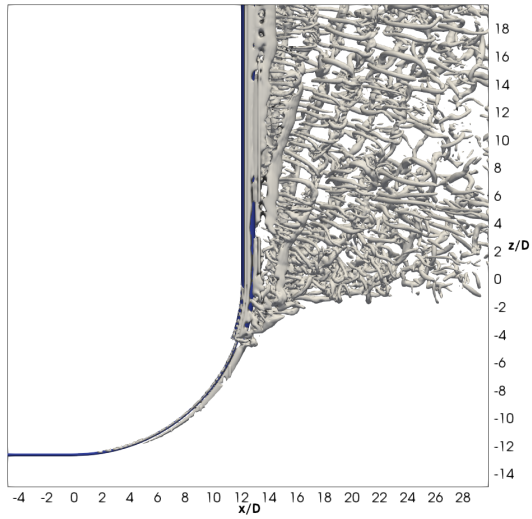

Figure C.61: Iso-contours of $\lambda_2 = -0.5$ for a fully developed flow for case 6, $\alpha = 70°$. The distribution is sampled at Re = 600 at time instant $t = 300s$.

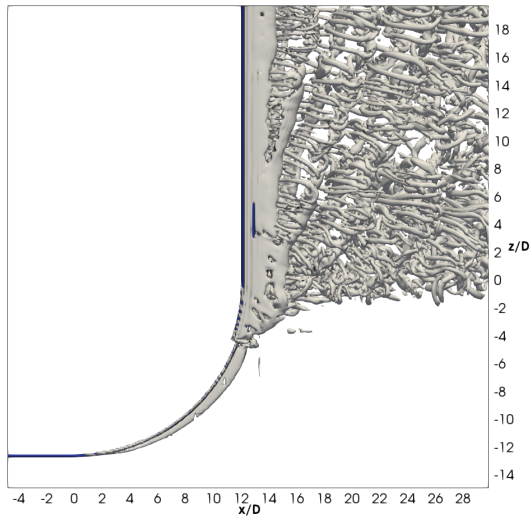

Figure C.62: Iso-contours of $\lambda_2 = -0.1$ for a fully developed flow for case 6, $\alpha = 70°$. The distribution is sampled at Re = 600 at time instant $t = 300s$.

C.6.4 Vorticity

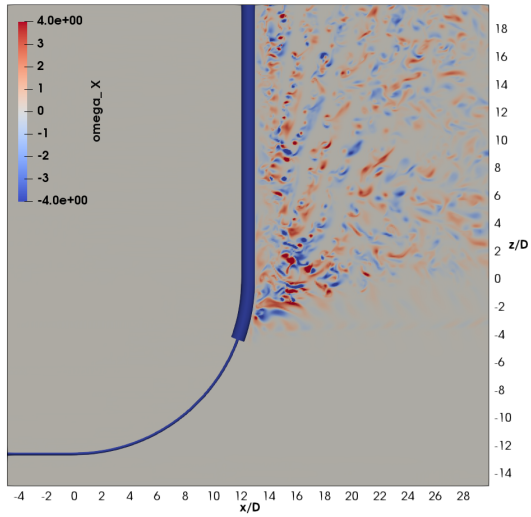

Figure C.63: Instantaneous distribution of the vorticity component ω_x for case 6, $\alpha = 70°$. The distribution is sampled at Re = 600 at time instant $t = 300s$. The values in the legend is the same for all cases.

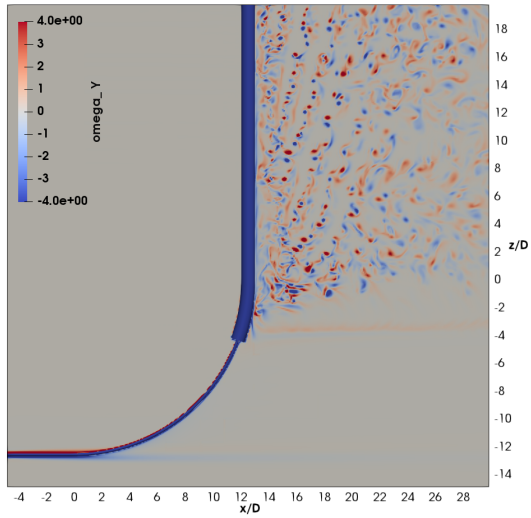

Figure C.64: Instantaneous distribution of the vorticity component ω_y for case 6, $\alpha = 70°$. The distribution is sampled at Re = 600 at time instant $t = 300s$. The values in the legend is the same for all cases.

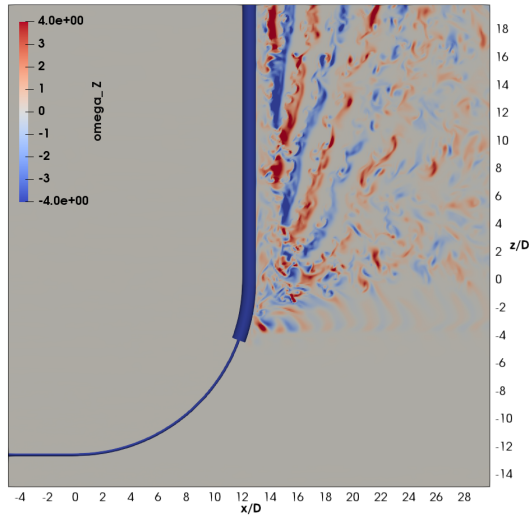

Figure C.65: Instantaneous distribution of the vorticity component ω_z for case 6, $\alpha = 70°$. The distribution is sampled at Re = 600 at time instant $t = 300s$. The values in the legend is the same for all cases.

C.6.5 Power Density Spectrum of Cross Flow Velocity v

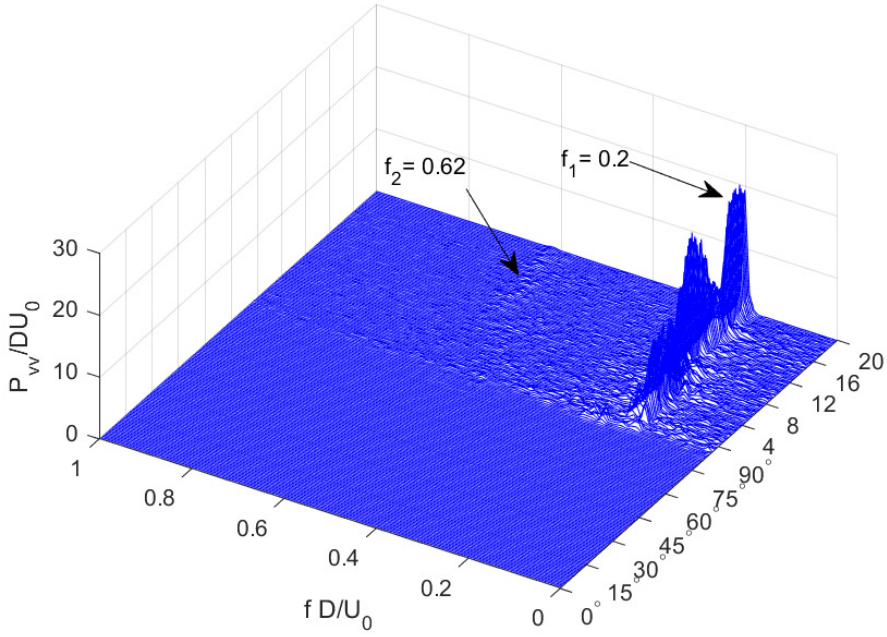

Figure C.66: Power density spectrum of the cross flow velocity for case 6, $\alpha = 70°$.The cross flow velocity is sampled at a distance of 3.5 D behind the cylinder in the $y/D = 0$ plane. The text indicates the dominating frequencies at different regions in the simulation.The distribution is sampled at Re = 600 for 200 time units.

C.7 Case 7 - $\alpha = 75°$

C.7.1 Pressure

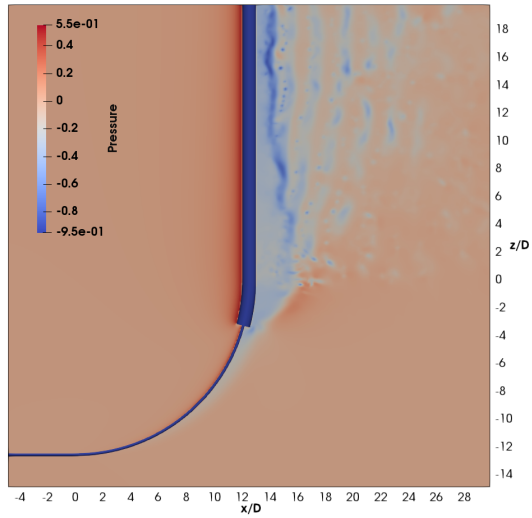

Figure C.67: Instantaneous pressure distribution in the $y/D = 0$ plane for case 7, $\alpha = 75°$. The distribution is sampled at Re = 600 at time instant $t = 300s$. The values in the legend is the same for all cases.

C.7.2 Velocity

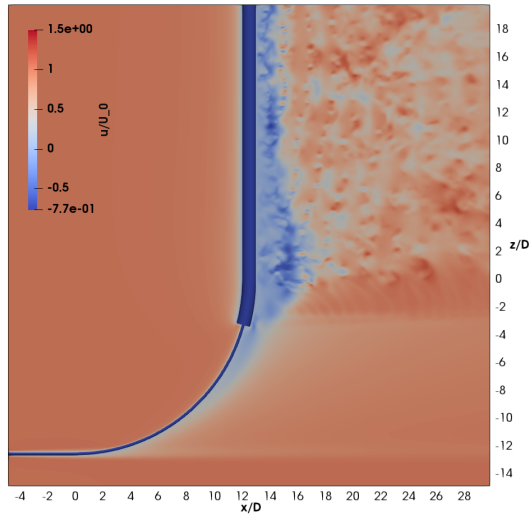

Figure C.68: Instantaneous distribution of the horizontal velocity component u for case 7, $\alpha = 75°$. The distribution is sampled at Re = 600 at time instant $t = 300s$. The values in the legend is the same for all cases.

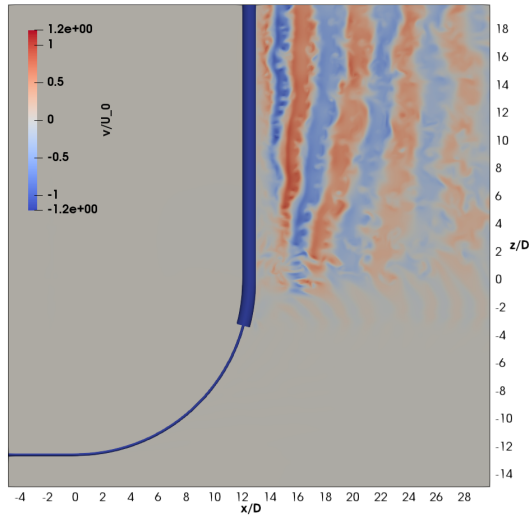

Figure C.69: Instantaneous distribution of the cross-flow velocity component v for case 7, $\alpha = 75°$. The distribution is sampled at Re = 600 at time instant $t = 300s$. The values in the legend is the same for all cases.

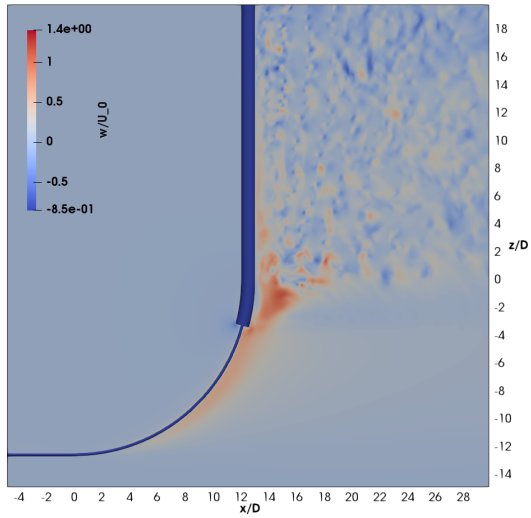

Figure C.70: Instantaneous distribution of the vertical velocity component w for case 7, $\alpha = 75°$. The distribution is sampled at Re = 600 at time instant $t = 300s$. The values in the legend is the same for all cases.

C.7.3 Iso-volume of λ_2

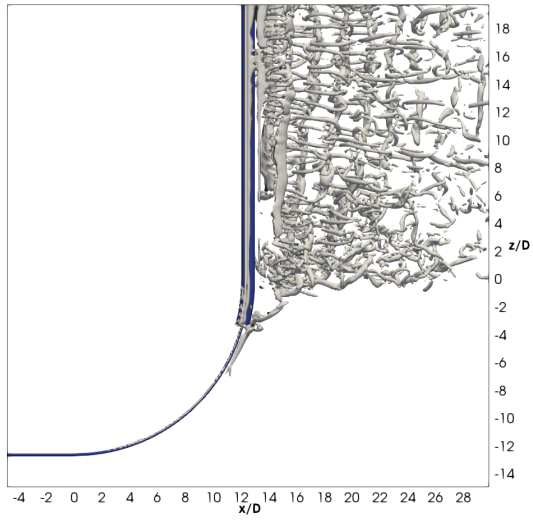

Figure C.71: Iso-contours of $\lambda_2 = -1$ for a fully developed flow for case 7, $\alpha = 75°$. The distribution is sampled at Re = 600 at time instant $t = 300s$.

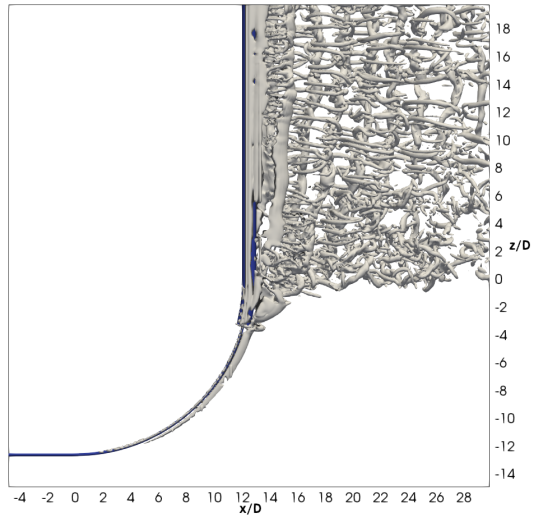

Figure C.72: Iso-contours of $\lambda_2 = -0.5$ for a fully developed flow for case 7, $\alpha = 75°$. The distribution is sampled at Re = 600 at time instant $t = 300s$.

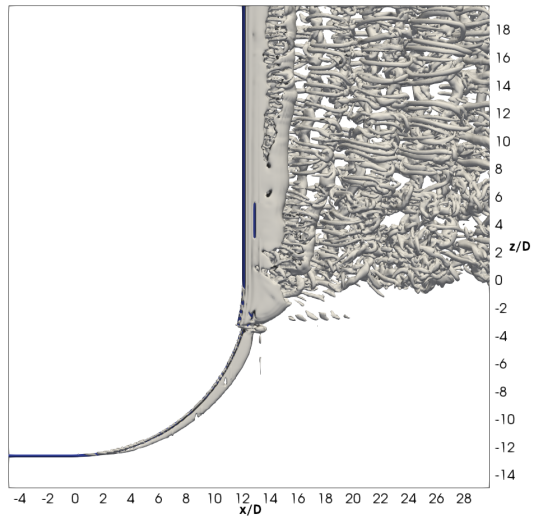

Figure C.73: Iso-contours of $\lambda_2 = -0.1$ for a fully developed flow for case 7, $\alpha = 75°$. The distribution is sampled at Re = 600 at time instant $t = 300s$.

C.7.4 Vorticity

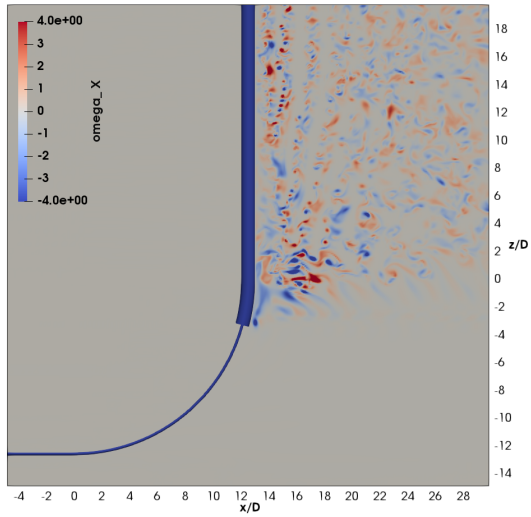

Figure C.74: Instantaneous distribution of the vorticity component ω_x for case 7, $\alpha = 75°$. The distribution is sampled at Re = 600 at time instant $t = 300s$. The values in the legend is the same for all cases.

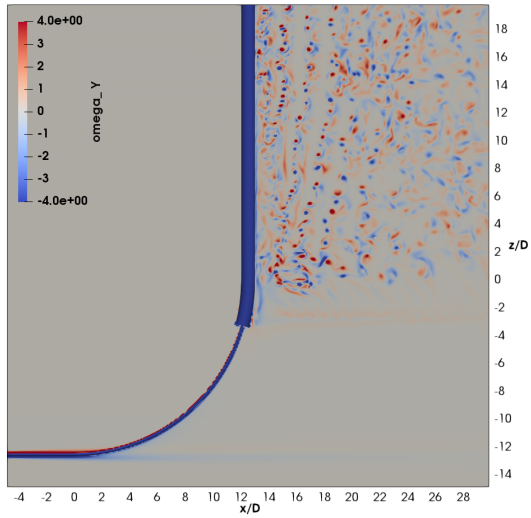

Figure C.75: Instantaneous distribution of the vorticity component ω_y for case 7, $\alpha = 75°$. The distribution is sampled at Re = 600 at time instant $t = 300s$. The values in the legend is the same for all cases.

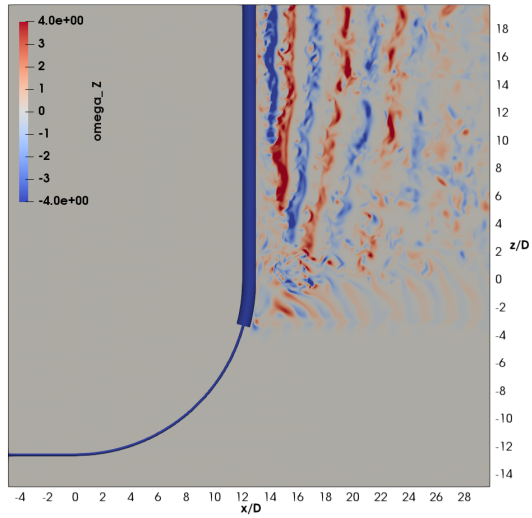

Figure C.76: Instantaneous distribution of the vorticity component ω_z for case 7, $\alpha = 75°$. The distribution is sampled at Re = 600 at time instant $t = 300s$. The values in the legend is the same for all cases.

C.7.5 Power Density Spectrum of Cross Flow Velocity v

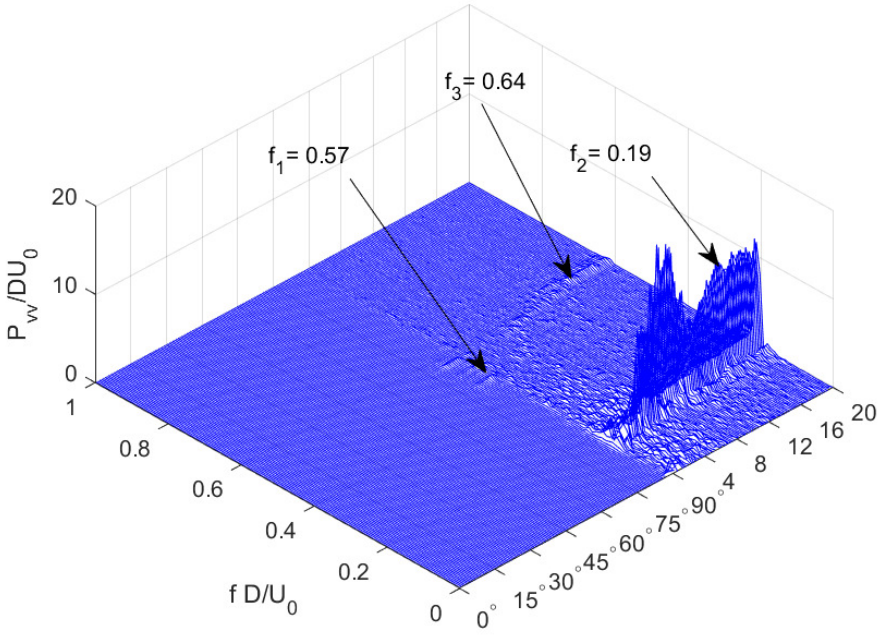

Figure C.77: Power density spectrum of the cross flow velocity for case 7, $\alpha = 75°$.The cross flow velocity is sampled at a distance of 3.5 D behind the cylinder in the $y/D = 0$ plane. The text indicates the dominating frequencies at different regions in the simulation.The distribution is sampled at Re = 600 for 100 time units.

C.8 Case 8 - $\alpha = 80°$

C.8.1 Pressure

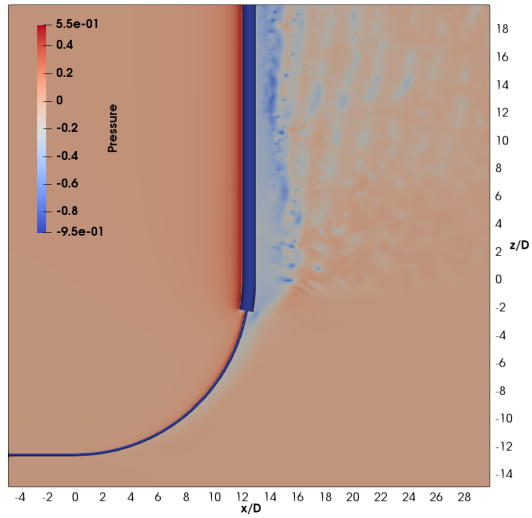

Figure C.78: Instantaneous pressure distribution in the $y/D = 0$ plane for case 8, $\alpha = 80°$. The distribution is sampled at Re = 600 at time instant $t = 300s$. The values in the legend is the same for all cases.

C.8.2 Velocity

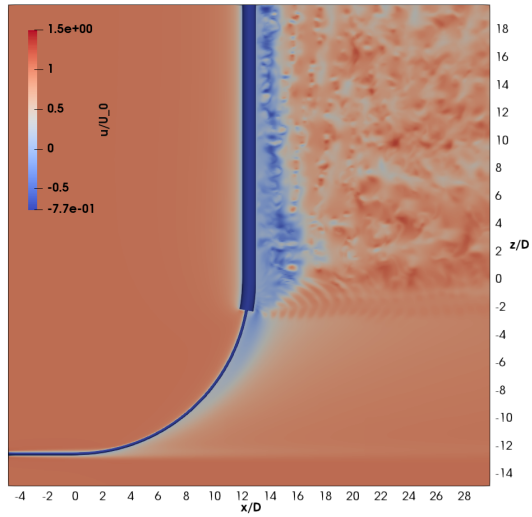

Figure C.79: Instantaneous distribution of the horizontal velocity component u for case 8, $\alpha = 80°$. The distribution is sampled at Re = 600 at time instant $t = 300s$. The values in the legend is the same for all cases.

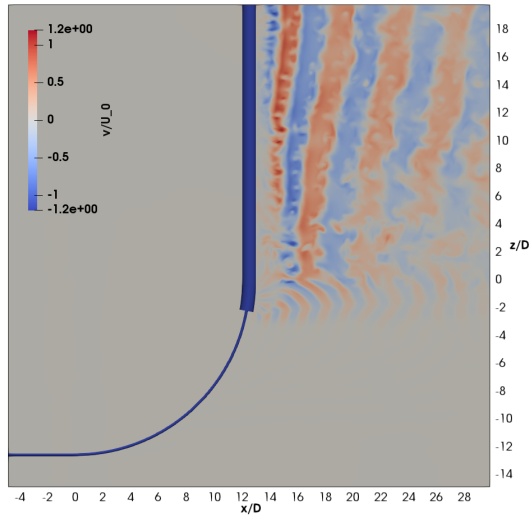

Figure C.80: Instantaneous distribution of the cross-flow velocity component v for case 8, $\alpha = 80°$. The distribution is sampled at Re = 600 at time instant $t = 300s$. The values in the legend is the same for all cases.

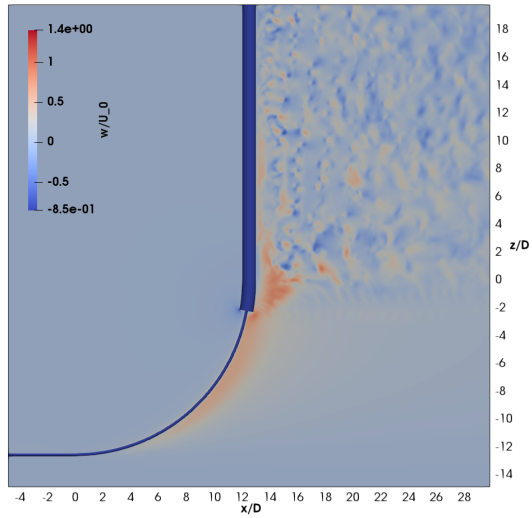

Figure C.81: Instantaneous distribution of the vertical velocity component w for case 8, $\alpha = 80°$. The distribution is sampled at Re = 600 at time instant $t = 300s$. The values in the legend is the same for all cases.

C.8.3 Iso-volume of λ_2

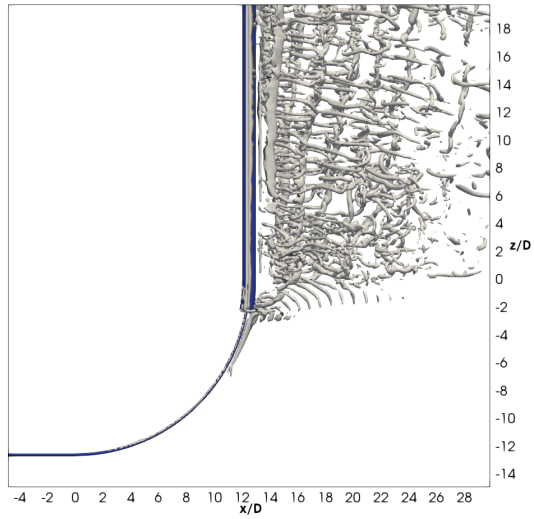

Figure C.82: Iso-contours of $\lambda_2 = -1$ for a fully developed flow for case 8, $\alpha = 80°$. The distribution is sampled at Re = 600 at time instant $t = 300s$.

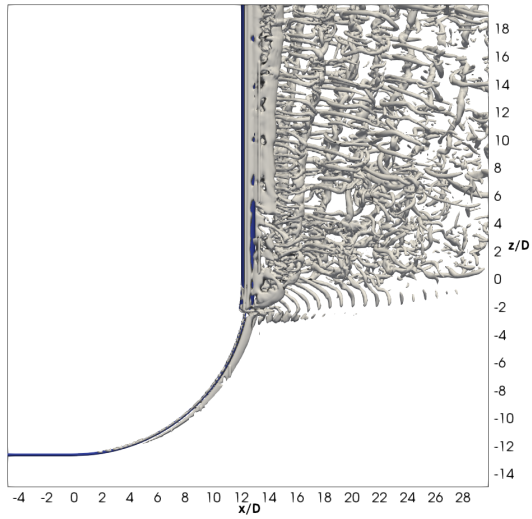

Figure C.83: Iso-contours of $\lambda_2 = -0.5$ for a fully developed flow for case 8, $\alpha = 80°$. The distribution is sampled at Re = 600 at time instant $t = 300s$.

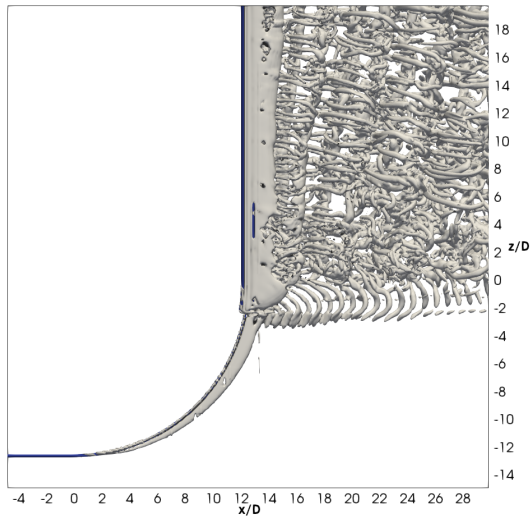

Figure C.84: Iso-contours of $\lambda_2 = -0.1$ for a fully developed flow for case 8, $\alpha = 80°$. The distribution is sampled at Re = 600 at time instant $t = 300s$.

C.8.4 Vorticity

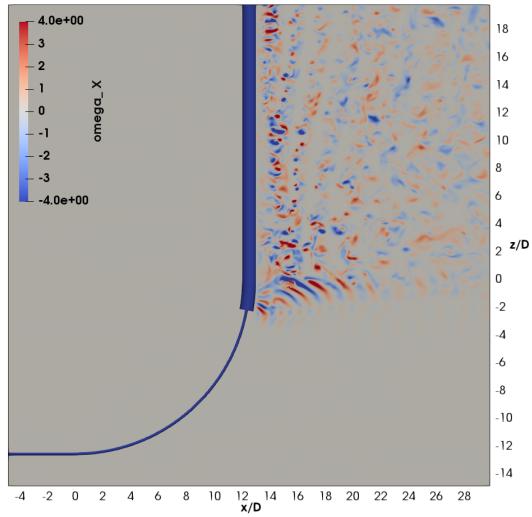

Figure C.85: Instantaneous distribution of the vorticity component ω_x for case 8, $\alpha = 80°$. The distribution is sampled at Re = 600 at time instant $t = 300s$. The values in the legend is the same for all cases.

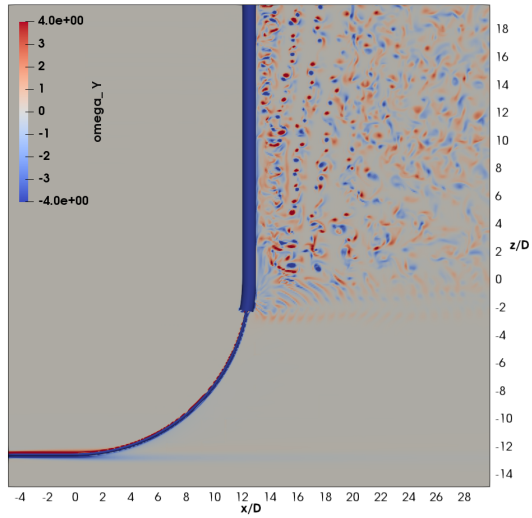

Figure C.86: Instantaneous distribution of the vorticity component ω_y for case 8, $\alpha = 80°$. The distribution is sampled at Re = 600 at time instant $t = 300s$. The values in the legend is the same for all cases.

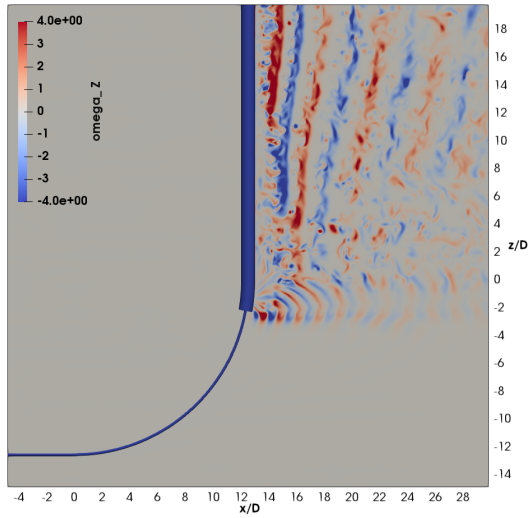

Figure C.87: Instantaneous distribution of the vorticity component ω_z for case 8, $\alpha = 80°$. The distribution is sampled at Re = 600 at time instant $t = 300s$. The values in the legend is the same for all cases.

C.8.5 Power Density Spectrum of Cross Flow Velocity v

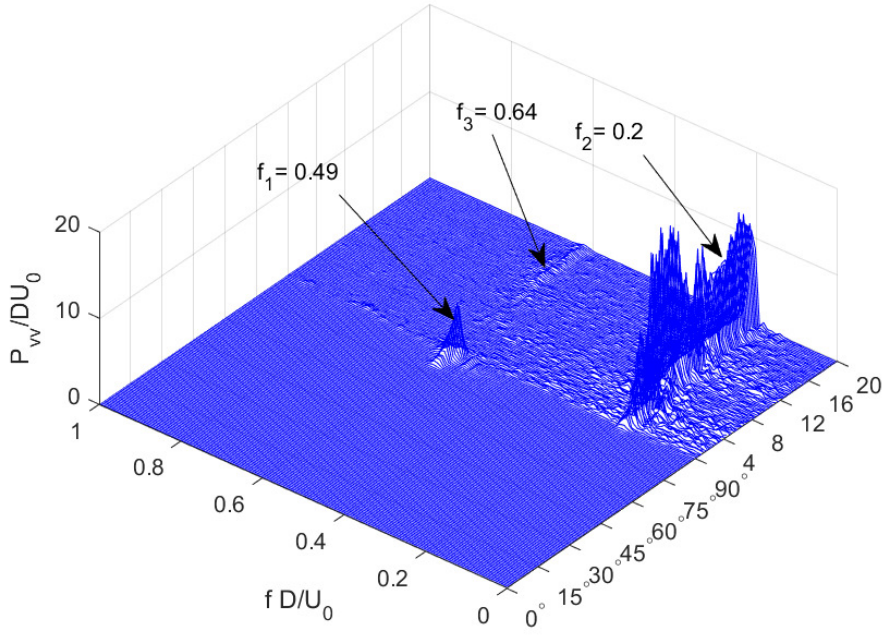

Figure C.88: Power density spectrum of the cross flow velocity for case 8, $\alpha = 80°$.The cross flow velocity is sampled at a distance of 3.5 D behind the cylinder in the $y/D = 0$ plane. The text indicates the dominating frequencies at different regions in the simulation.The distribution is sampled at Re = 600 for 100 time units.

C.9 Case 9 - $\alpha = 85°$

C.9.1 Pressure

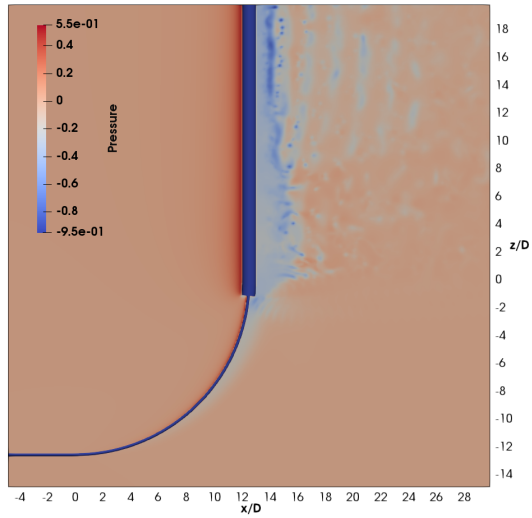

Figure C.89: Instantaneous pressure distribution in the $y/D = 0$ plane for case 9, $\alpha = 85°$. The distribution is sampled at Re = 600 at time instant $t = 300s$. The values in the legend is the same for all cases.

C.9.2 Velocity

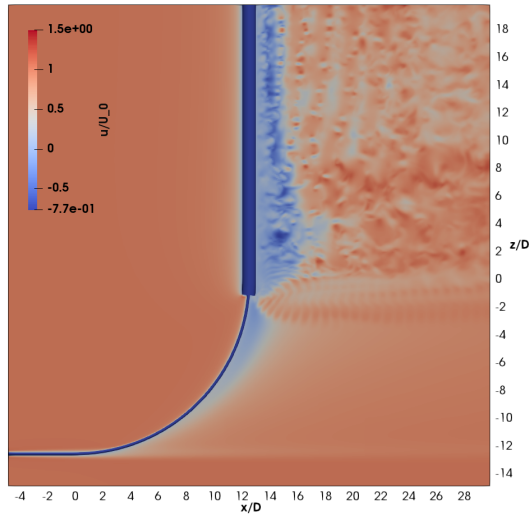

Figure C.90: Instantaneous distribution of the horizontal velocity component u for case 9, $\alpha = 85°$. The distribution is sampled at Re = 600 at time instant $t = 300s$. The values in the legend is the same for all cases.

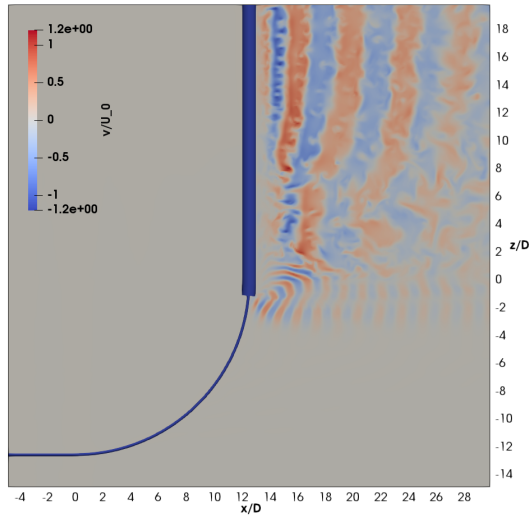

Figure C.91: Instantaneous distribution of the cross-flow velocity component v for case 9, $\alpha = 85°$. The distribution is sampled at Re = 600 at time instant $t = 300s$. The values in the legend is the same for all cases.

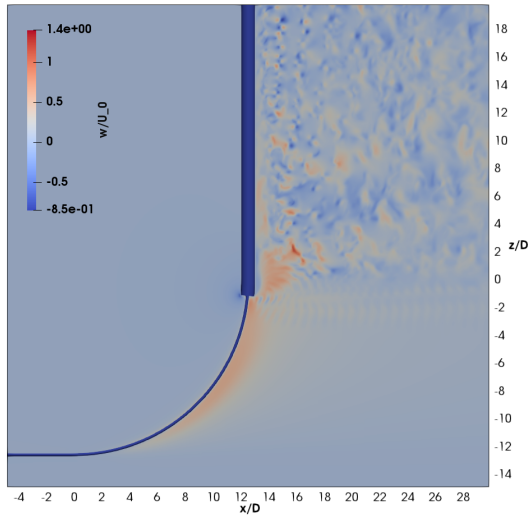

Figure C.92: Instantaneous distribution of the vertical velocity component w for case 9, $\alpha = 85°$. The distribution is sampled at Re = 600 at time instant $t = 300s$. The values in the legend is the same for all cases.

C.9.3 Iso-volume of λ_2

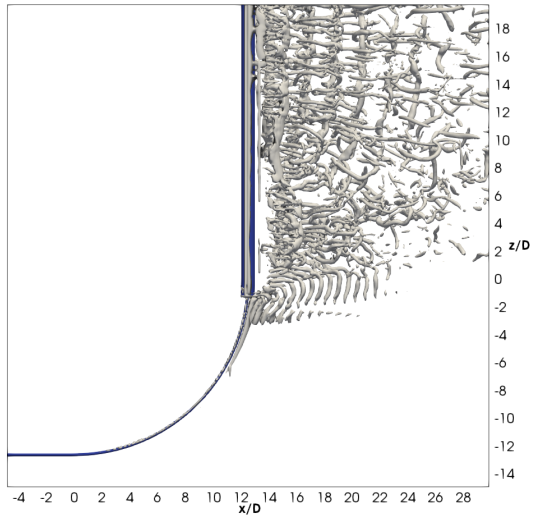

Figure C.93: Iso-contours of $\lambda_2 = -1$ for a fully developed flow for case 9, $\alpha = 85°$. The distribution is sampled at Re = 600 at time instant $t = 300s$.

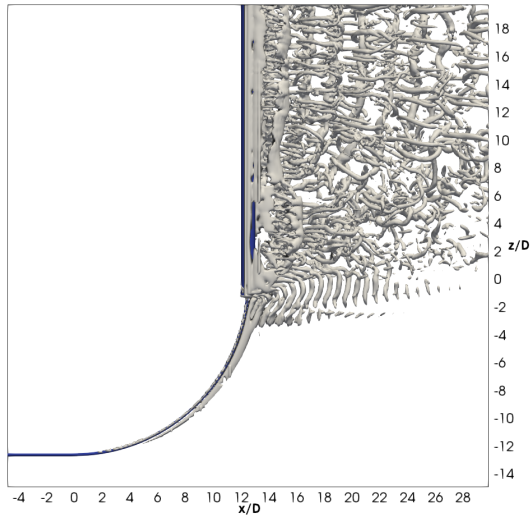

Figure C.94: Iso-contours of $\lambda_2 = -0.5$ for a fully developed flow for case 9, $\alpha = 85°$. The distribution is sampled at Re = 600 at time instant $t = 300s$.

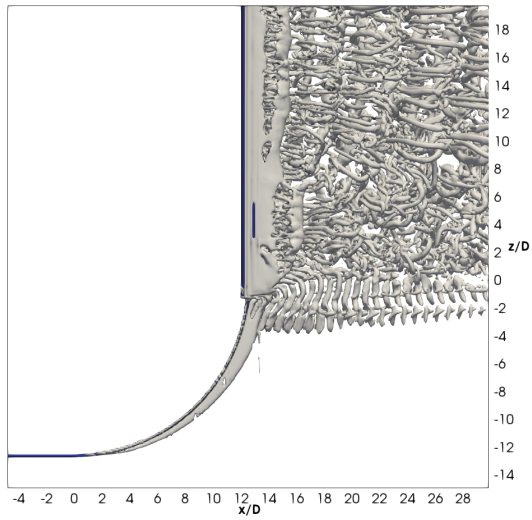

Figure C.95: Iso-contours of $\lambda_2 = -0.1$ for a fully developed flow for case 9, $\alpha = 85°$. The distribution is sampled at Re = 600 at time instant $t = 300s$.

C.9.4 Vorticity

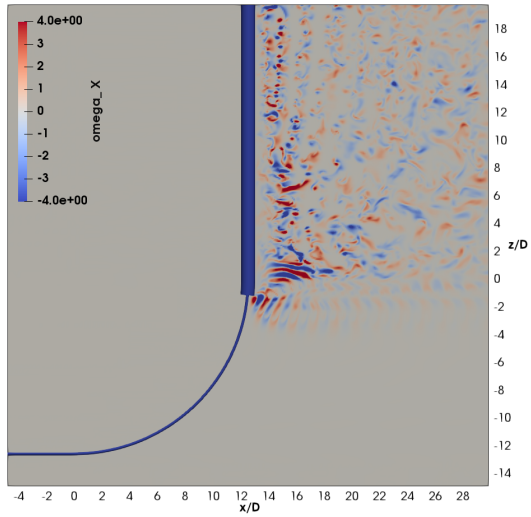

Figure C.96: Instantaneous distribution of the vorticity component ω_x for case 9, $\alpha = 85°$. The distribution is sampled at Re = 600 at time instant $t = 300s$. The values in the legend is the same for all cases.

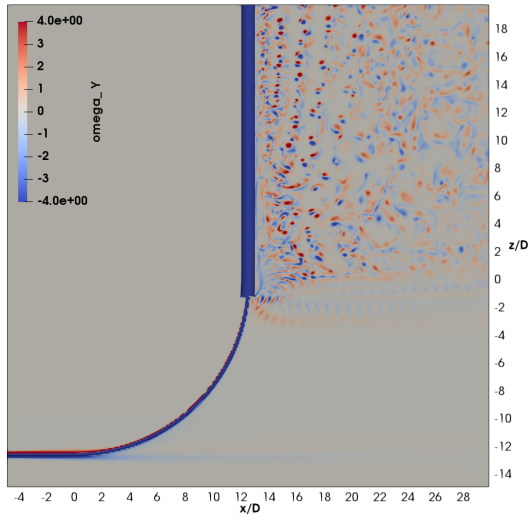

Figure C.97: Instantaneous distribution of the vorticity component ω_y for case 9, $\alpha = 85°$. The distribution is sampled at Re = 600 at time instant $t = 300s$. The values in the legend is the same for all cases.

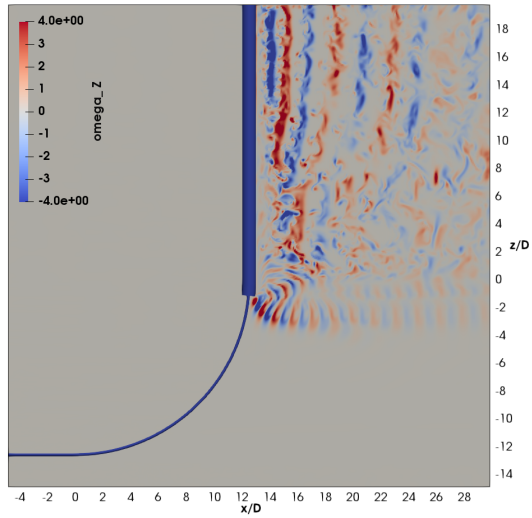

Figure C.98: Instantaneous distribution of the vorticity component ω_z for case 9, $\alpha = 85°$. The distribution is sampled at Re = 600 at time instant $t = 300s$. The values in the legend is the same for all cases.

C.9.5 Power Density Spectrum of Cross Flow Velocity v

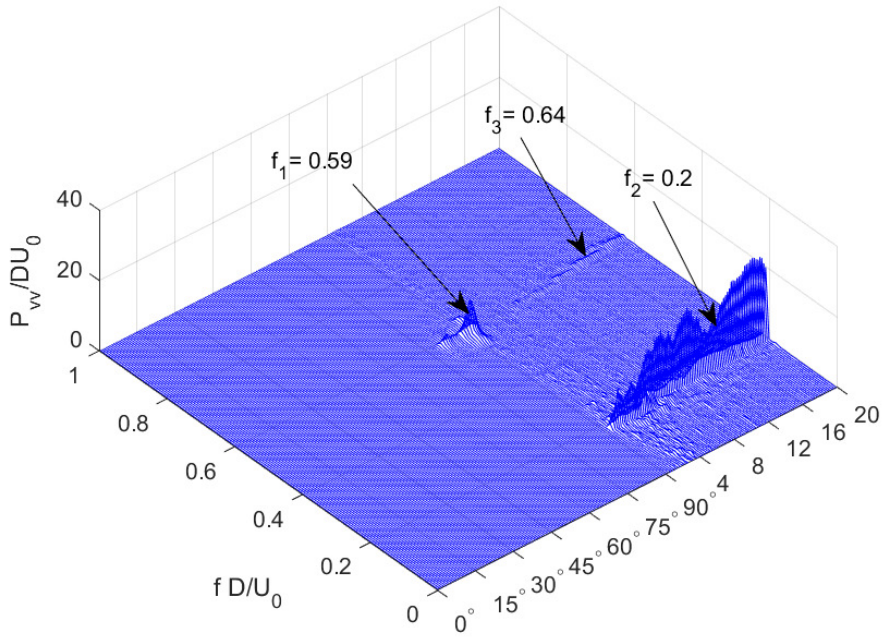

Figure C.99: Power density spectrum of the cross flow velocity for case 9, $\alpha = 85°$.The cross flow velocity is sampled at a distance of 3.5 D behind the cylinder in the $y/D = 0$ plane. The text indicates the dominating frequencies at different regions in the simulation.The distribution is sampled at Re = 600 for 100 time units.

C.10 Case 10 - $\alpha = 90°$

C.10.1 Pressure

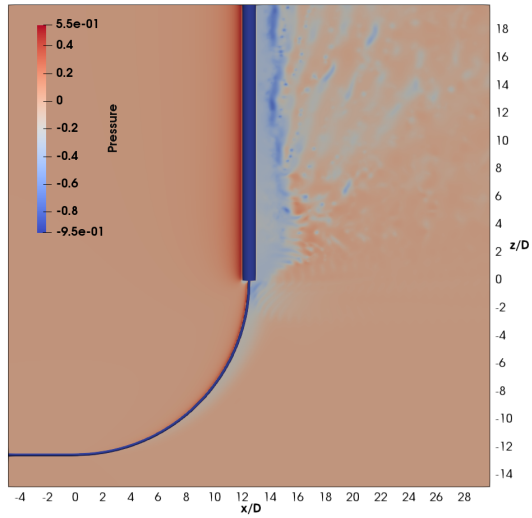

Figure C.100: Instantaneous pressure distribution in the $y/D = 0$ plane for case 10, $\alpha = 90°$. The distribution is sampled at Re = 600 at time instant $t = 300s$. The values in the legend is the same for all cases.

C.10.2 Velocity

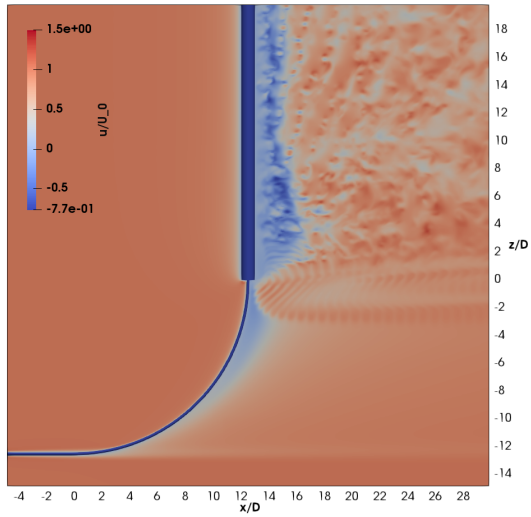

Figure C.101: Instantaneous distribution of the horizontal velocity component u for case 10, $\alpha = 90°$. The distribution is sampled at Re = 600 at time instant $t = 300s$. The values in the legend is the same for all cases.

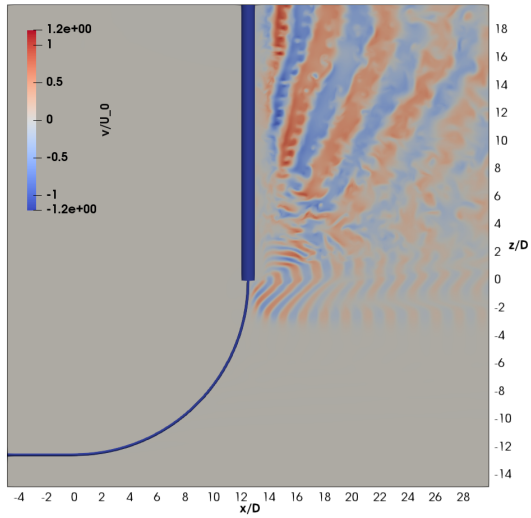

Figure C.102: Instantaneous distribution of the cross-flow velocity component v for case 10, $\alpha = 90°$. The distribution is sampled at Re = 600 at time instant $t = 300s$. The values in the legend is the same for all cases.

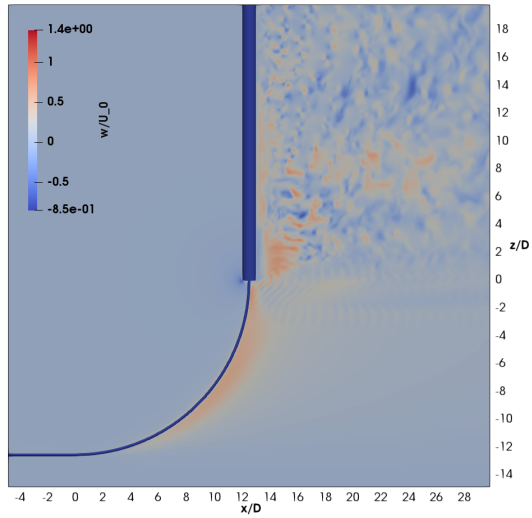

Figure C.103: Instantaneous distribution of the vertical velocity component w for case 10, $\alpha = 90°$. The distribution is sampled at Re = 600 at time instant $t = 300s$. The values in the legend is the same for all cases.

C.10.3 Iso-volume of λ_2

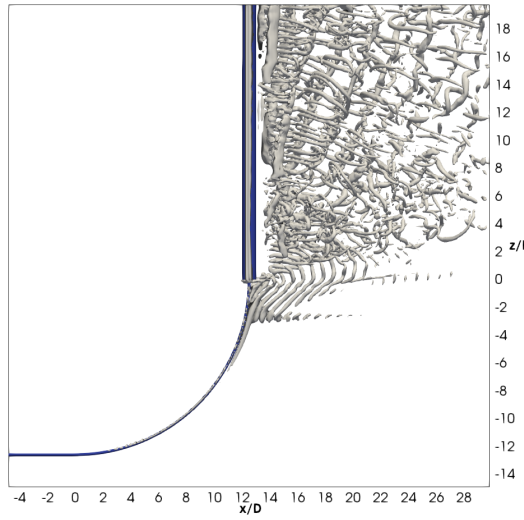

Figure C.104: Iso-contours of $\lambda_2 = -1$ for a fully developed flow for case 10, $\alpha = 90°$. The distribution is sampled at Re = 600 at time instant $t = 300s$.

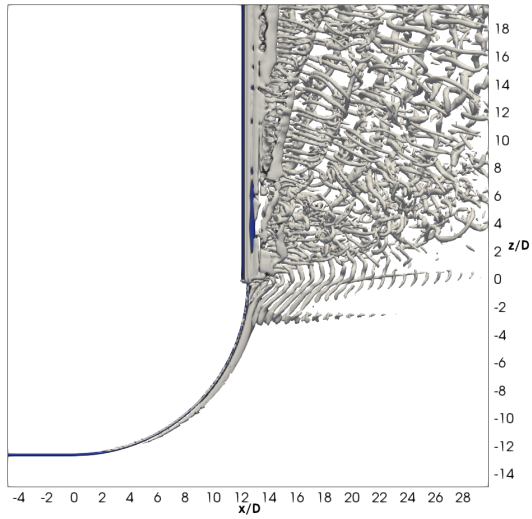

Figure C.105: Iso-contours of $\lambda_2 = -0.5$ for a fully developed flow for case 10, $\alpha = 90°$. The distribution is sampled at Re = 600 at time instant $t = 300s$.

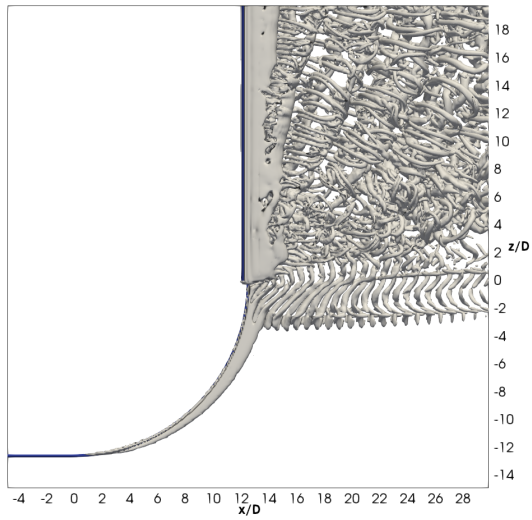

Figure C.106: Iso-contours of $\lambda_2 = -0.1$ for a fully developed flow for case 10, $\alpha = 90°$. The distribution is sampled at Re = 600 at time instant $t = 300s$.

C.10.4 Vorticity

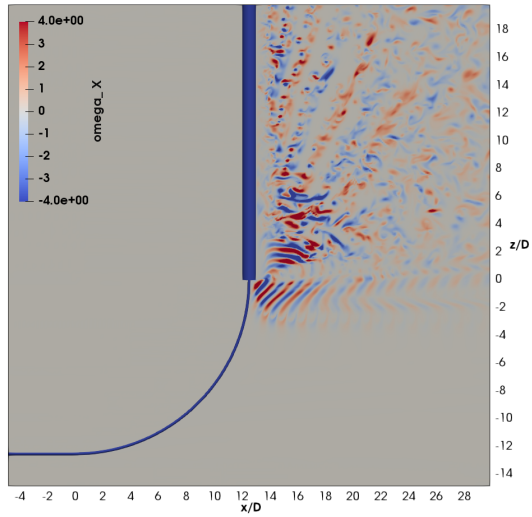

Figure C.107: Instantaneous distribution of the vorticity component ω_x for case 10, $\alpha = 90°$. The distribution is sampled at Re = 600 at time instant $t = 300s$. The values in the legend is the same for all cases.

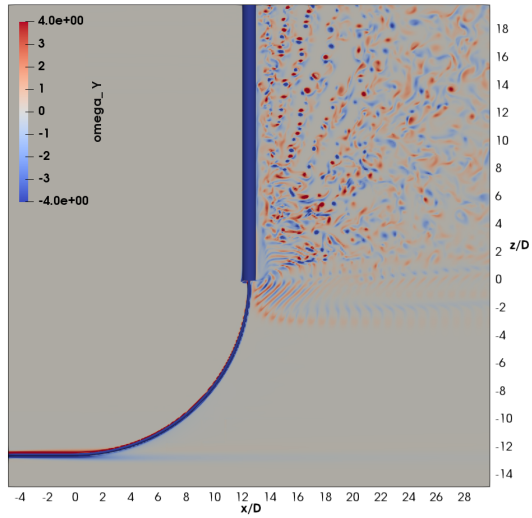

Figure C.108: Instantaneous distribution of the vorticity component ω_y for case 10, $\alpha = 90°$. The distribution is sampled at Re = 600 at time instant $t = 300s$. The values in the legend is the same for all cases.

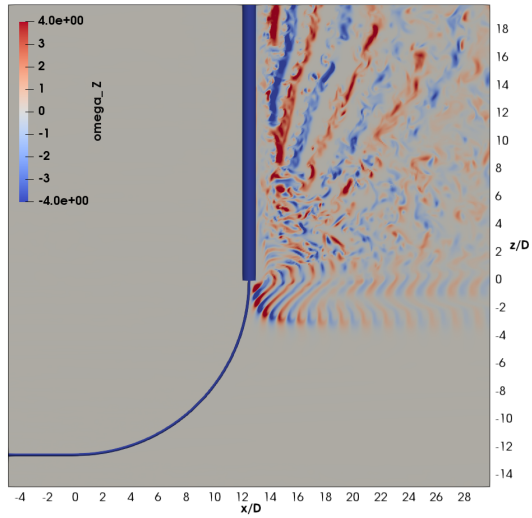

Figure C.109: Instantaneous distribution of the vorticity component ω_z for case 10, $\alpha = 90°$. The distribution is sampled at Re = 600 at time instant $t = 300s$. The values in the legend is the same for all cases.

C.10.5 Power Density Spectrum of Cross Flow Velocity v

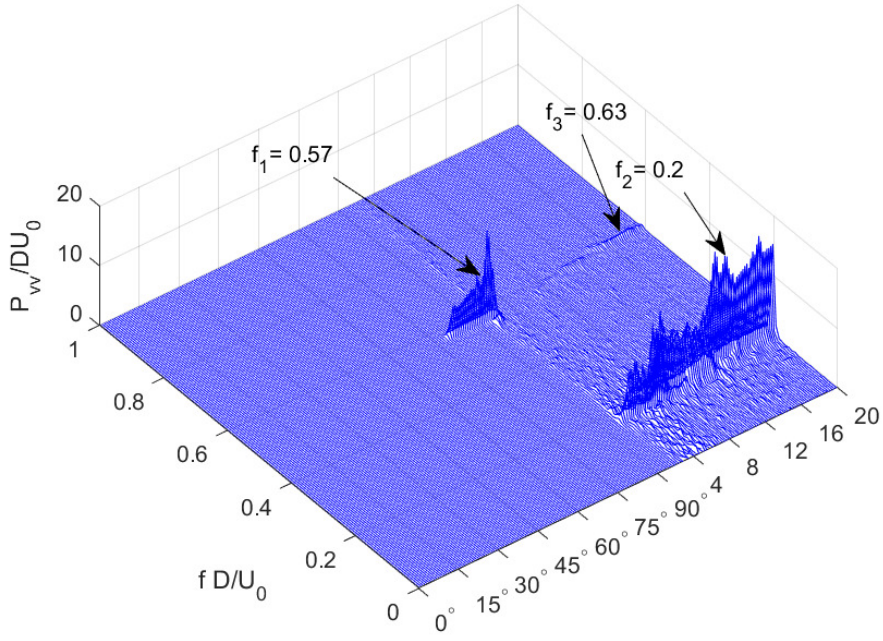

Figure C.110: Power density spectrum of the cross flow velocity for case 10, $\alpha = 90°$. The cross flow velocity is sampled at a distance of 3.5 D behind the cylinder in the $y/D = 0$ plane. The text indicates the dominating frequencies at different regions in the simulation.The distribution is sampled at Re = 600 for 100 time units.

Appendix D

Parameter Study Velocity and Pressure Profiles

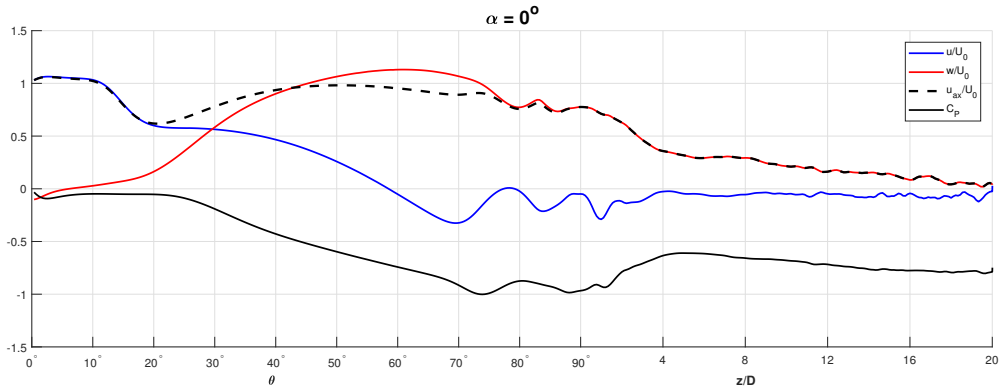

Figure D.1: Time averaged pressure and vertical, horizontal and axial velocity profiles, for case 1, $\alpha = 0°$. The values were sampled at $R = 13.2D$ i.e. $0.2D$ away from the large diameter cylinder surface ($0.6D$ from the small cylinder surface). The samples are located in the $y/D = 0$ plane along the the curvature from the start of the horizontal extension to at the end of the vertical extension. The velocities and pressure were time averaged for 100 seconds after the flow was fully developed

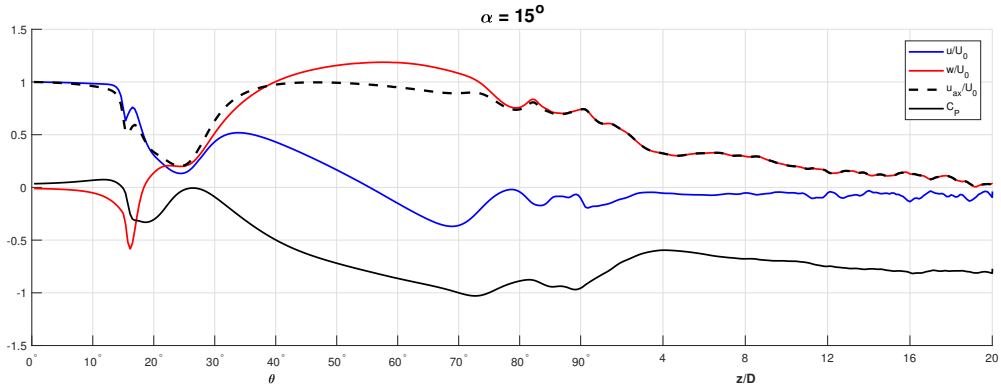

Figure D.2: Time averaged pressure and vertical, horizontal and axial velocity profiles, for case 2, $\alpha = 15°$. The values were sampled at $R = 13.2D$ i.e. $0.2D$ away from the large diameter cylinder surface ($0.6D$ from the small cylinder surface). The samples are located in the $y/D = 0$ plane along the the curvature from the start of the horizontal extension to at the end of the vertical extension. The velocities and pressure were time averaged for 100 seconds after the flow was fully developed

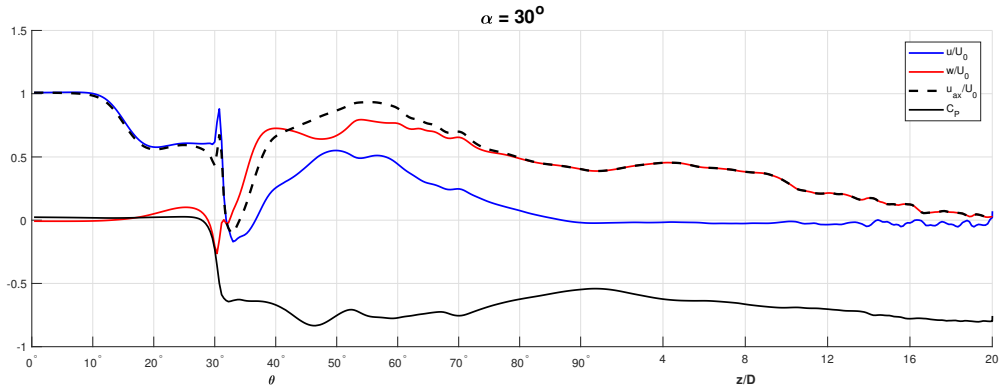

Figure D.3: Time averaged pressure and vertical, horizontal and axial velocity profiles, for case 3, $\alpha = 30°$. The values were sampled at $R = 13.2D$ i.e. $0.2D$ away from the large diameter cylinder surface ($0.6D$ from the small cylinder surface). The samples are located in the $y/D = 0$ plane along the the curvature from the start of the horizontal extension to at the end of the vertical extension. The velocities and pressure were time averaged for 100 seconds after the flow was fully developed

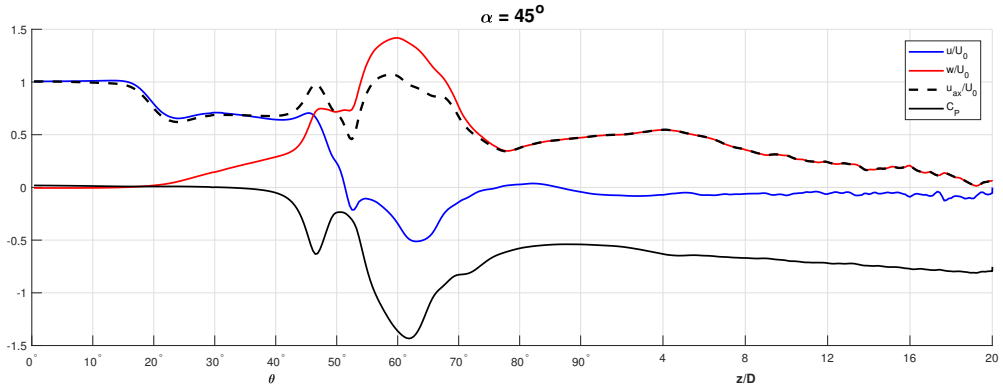

Figure D.4: Time averaged pressure and vertical, horizontal and axial velocity profiles, for case 4, $\alpha = 45°$. The values were sampled at $R = 13.2D$ i.e. $0.2D$ away from the large diameter cylinder surface ($0.6D$ from the small cylinder surface). The samples are located in the $y/D = 0$ plane along the the curvature from the start of the horizontal extension to at the end of the vertical extension. The velocities and pressure were time averaged for 100 seconds after the flow was fully developed

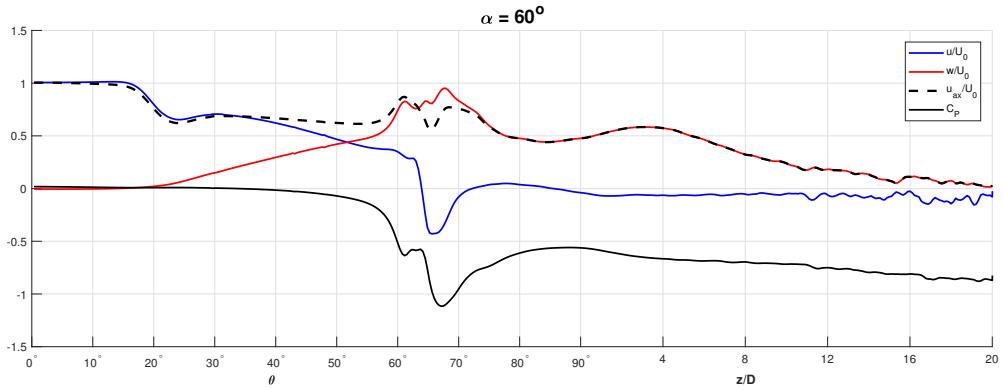

Figure D.5: Time averaged pressure and vertical, horizontal and axial velocity profiles, for case 5, $\alpha = 60°$. The values were sampled at $R = 13.2D$ i.e. $0.2D$ away from the large diameter cylinder surface ($0.6D$ from the small cylinder surface). The samples are located in the $y/D = 0$ plane along the the curvature from the start of the horizontal extension to at the end of the vertical extension. The velocities and pressure were time averaged for 100 seconds after the flow was fully developed

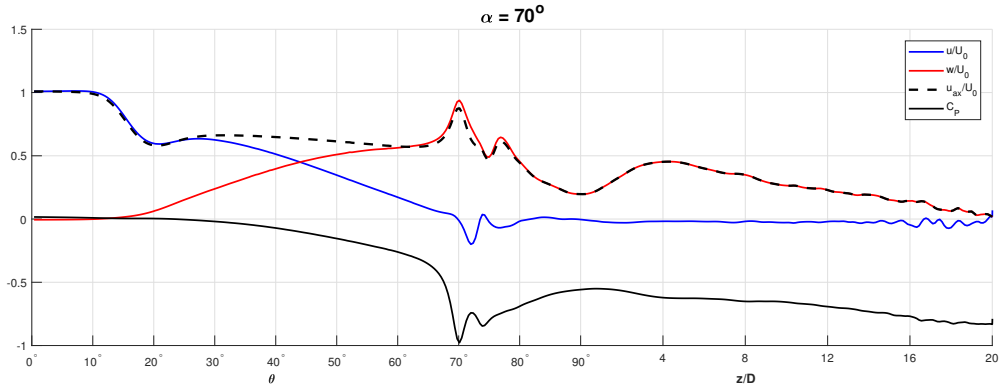

Figure D.6: Time averaged pressure and vertical, horizontal and axial velocity profiles, for case 6, $\alpha = 70°$. The values were sampled at $R = 13.2D$ i.e. $0.2D$ away from the large diameter cylinder surface ($0.6D$ from the small cylinder surface). The samples are located in the $y/D = 0$ plane along the the curvature from the start of the horizontal extension to at the end of the vertical extension. The velocities and pressure were time averaged for 100 seconds after the flow was fully developed

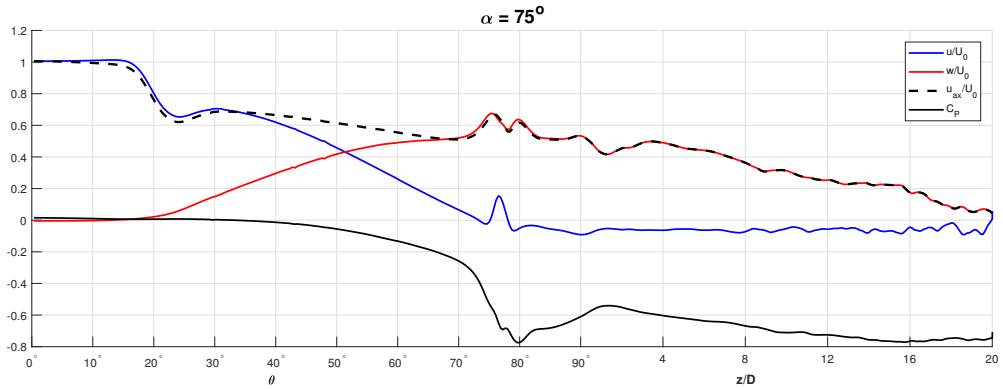

Figure D.7: Time averaged pressure and vertical, horizontal and axial velocity profiles, for case 7, $\alpha = 75°$. The values were sampled at $R = 13.2D$ i.e. $0.2D$ away from the large diameter cylinder surface ($0.6D$ from the small cylinder surface). The samples are located in the $y/D = 0$ plane along the the curvature from the start of the horizontal extension to at the end of the vertical extension. The velocities and pressure were time averaged for 100 seconds after the flow was fully developed

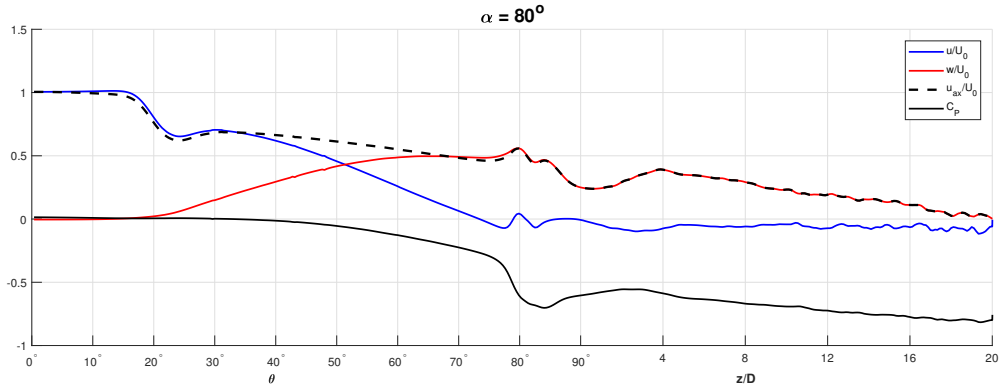

Figure D.8: Time averaged pressure and vertical, horizontal and axial velocity profiles, for case 8, $\alpha = 80°$. The values were sampled at $R = 13.2D$ i.e. $0.2D$ away from the large diameter cylinder surface ($0.6D$ from the small cylinder surface). The samples are located in the $y/D = 0$ plane along the the curvature from the start of the horizontal extension to at the end of the vertical extension. The velocities and pressure were time averaged for 100 seconds after the flow was fully developed

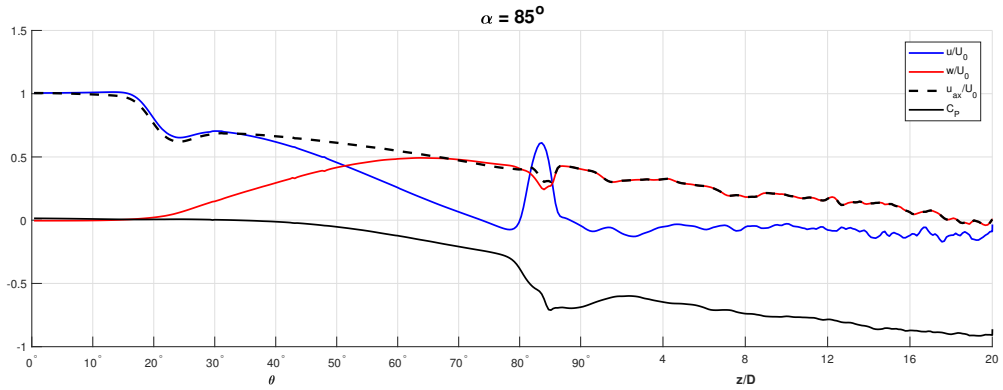

Figure D.9: Time averaged pressure and vertical, horizontal and axial velocity profiles, for case 9, $\alpha = 85°$. The values were sampled at $R = 13.2D$ i.e. $0.2D$ away from the large diameter cylinder surface ($0.6D$ from the small cylinder surface). The samples are located in the $y/D = 0$ plane along the the curvature from the start of the horizontal extension to at the end of the vertical extension. The velocities and pressure were time averaged for 100 seconds after the flow was fully developed

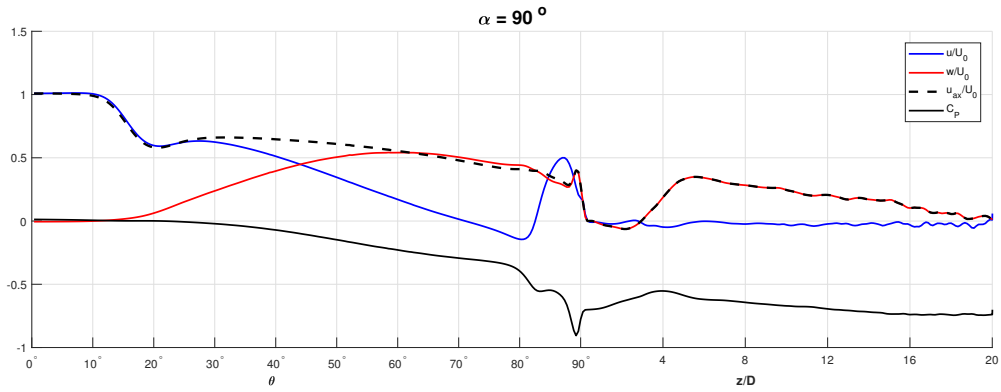

Figure D.10: Time averaged pressure and vertical, horizontal and axial velocity profiles, for case 10,$\alpha = 90°$. The values were sampled at $R = 13.2D$ i.e. $0.2D$ away from the large diameter cylinder surface ($0.6D$ from the small cylinder surface). The samples are located in the $y/D = 0$ plane along the the curvature from the start of the horizontal extension to at the end of the vertical extension. The velocities and pressure were time averaged for 100 seconds after the flow was fully developed

List of Tables

List of Figures

Emil Severin Moen Ramsvik

Numerical simulation of flow around a curved cylinder with varying diameter.

NTNU
Norwegian University of
Science and Technology